

DISS. ETH NO. 27083

**TIMBER-CONCRETE COMPOSITE SLABS WITH  
MICRO-NOTCHES**

A thesis submitted to attain the degree of

DOCTOR OF SCIENCES of ETH ZURICH

(Dr. sc. ETH Zurich)

presented by

Katharina Maria Müller

MSc ETH Civil Eng

born on 12.05.1990

citizen of

Mollis GL

accepted on the recommendation of

Prof. Dr. Andrea Frangi (ETH Zurich, Examiner)

Prof. Dr. Ingo Burgert (ETH Zurich, Co-Examiner)

Prof. Dr. Alfredo Dias (Universidade de Coimbra, Co-Examiner)



Mainly written during the first wave of the Coronavirus (COVID-19) pandemic.

To my mother and all the other intensive care unit nurses: DANKE.



# Acknowledgements

This thesis concludes my research activities on the concept of micro-notches of the past four years at the chair of Timber Structures at the Institute of Structural Engineering (IBK) at ETH Zurich. It has been a privilege to work and grow in this great environment and group of positive, forward-looking, pragmatic, skilful - and some of them simply brilliant - people.

I would like to thank Prof. Dr. Andrea Frangi for offering me the opportunity to work in his team and giving me his sincere trust and support during these years. His subtle guidance and unhesitating encouragement made it possible for me to face the challenges and obstacles along the way and emerge into and evolve in the amazing field of timber construction.

Further, I am grateful to Prof. Dr. Ingo Burgert for his insightful lectures on wood science at ETH and thus bringing me closer to this ingenious and fascinating material. Also, I would like to thank Prof. Dr. Alfredo Dias for the invitation to Coimbra to attend the well organised Training School and meet and exchange with experts from all over Europe. I'm honoured that both of them agreed on being a part of my PhD Examination Committee and thankful for their valuable inputs.

A big thank you also goes to all project partners from TS3.0 AG, Sidler Holz AG, Timbatec, and all the other companies I had the privilege to work with. The great interest and fruitful cooperation was both motivating and challenging and the exchange enriching on both technical and personal levels. My special thanks go to Stefan Zöllig, Marcel Herzog, René Wicki from TS3.0 AG, and Erich Sidler, Kurt Sidler, Marcel Frey, and Markus Beutler from Sidler Holz AG. Furthermore, I gratefully acknowledge the financial support by the Commission for Technology and Innovation (CTI).

Huge thanks go to the laboratory team at ETH, in particular Patrik Morf, Pius Herzog, Thomi Jaggi, Dominik Werne, Christoph Gisler, and Martin Viertel. Their technical support with exceptional engagement made the elaborate experimental investigations possible in the first place. Especially Pius and Thomi earn my sincere gratitude for helping me install the long-term tests during cold winter days in an unpleasantly dim and filthy cellar.

I would like to thank all the students who decided to write their master project thesis or master thesis with me: Alexander Keller, Philipp Limburg, Juli Simon Millet, Michael Merkli, Felix Stutz, Elia Quadranti, Luca Imfeld, Xavier Hitz, Manuel Schacher, and Marina Rella Diallo. Their work contributed to a large extent to the success of this research project. I greatly appreciated to work and learn together during the process of these theses.

Of irreplaceable value to me was the team of Group Frangi. I would like to thank everyone of the group with whom I was privileged to share a part of the journey. It was a pleasure being a part of this group and I learned a lot from every single one of my lab- and office mates. A very special thanks go to my TCC companion Benjamin Kreis and to the micro-notch inventor Marcel Muster. Without their proficient input in many insightful and enlightening discussions I probably would not have gotten very far. Many thanks also to all other colleagues from the IBK, in particular the steel guys, the concrete guys, and the wood science guys from the Institute

of Building Materials, for their open and unconditional help. A huge thanks goes to those colleagues and friends who proof-read individual parts of this thesis.

Finally, I would like to express my deepest gratitude to my friends and family for their faith and encouragement. Special thanks also go to Ralf for his delicious culinary supply, and above all to Oli for his understanding, his patience, and his never ending optimism.

# Abstract

The combined use of timber and concrete for slabs in buildings offers a range of advantages compared to timber-only slabs: increased stiffness and load-bearing capacity, improved sound insulation and vibration behaviour, and improved fire safety. Other substantial advantages are low self-weight, fast production, and significantly lower environmental impact compared to slabs made entirely of reinforced concrete. Timber-concrete composite (TCC) slabs have been used in Switzerland for several decades. The connection between timber and concrete is of significant importance for the load-bearing behaviour of the slab. In fact, there are various connection systems on the market which have different characteristics regarding connection stiffness, load-bearing capacity, and ductility. For example, notched connections achieve an almost rigid composite action and have a high load-bearing capacity. They are supplemented by screws or dowels, supposed to carry vertical tensile forces and prevent uplift of the concrete layer. However, the material and installation costs for the screws and milling process for the notches represent an economical disadvantage. This thesis therefore presents a novel connection system called micro-notches enabling a composite slab of timber and concrete only, without additional metal connectors.

The concept of micro-notches was developed in an extensive experimental program, supplemented by analytical and numerical investigations. In a first step, the connection with micro-notches was tested in local shear tests in a symmetrical push-out test setup. The objectives of these investigations were to determine the connection properties of different micro-notch configurations and to find an optimum configuration. This optimum configuration was then tested in global 4-point bending tests to assess the realistic structural behaviour of the novel connection system in TCC slabs. The tested beams showed a very stiff, linear elastic load-bearing behaviour with brittle ultimate failure in the timber cross-section at mid-span. The failure mode observed in the micro-notches was for both local and global tests a shear failure of the concrete notches and, in some places, also a shear failure of the timber notches. Two models were developed to assess the global load-bearing behaviour, including an analytical model based on the  $\gamma$ -method and a numerical model based on a strut-and-tie approach. The global load-bearing behaviour was then compared with the local load-bearing behaviour observed in the local shear tests. With these results, the connection properties of the micro-notches were adjusted. To assess the influence of rheological phenomena in timber, concrete, and the connection, a long-term test series was installed and first results are presented. As a further field of application for TCC slabs, a two-span beam test series was performed to evaluate the positive effect of continuous systems on the deflections. The cracking of concrete over the middle support greatly influences the beam stiffness and needs to be considered in the calculation models. The tests showed that micro-notches are also functioning in cracked concrete and that the multi-span system reduces deflections. The findings of the experimental investigations and the developed models described above are summarised in design and production recommendations.

The research work showed that micro-notches are suitable as a connection system for TCC slabs. They have a very stiff (approximately rigid) connection behaviour and sufficient shear resistance for the application in residential and office buildings with spans up to 10 m and heavy floor structures. The failure modes observed in global bending tests were brittle. Ductility of the connection was not a criteria for the investigated TCC slabs since the decisive failure mode of TCC slabs, subjected to the loading situation in practice, is bending tension in timber. Micro-notches are a valid replacement for conventional notches for TCC slabs, providing several advantages. The composite action of micro-notches can be assumed rigid, no additional screws or dowels are needed, and the timber cross-section is less compromised than with conventional notches. The principle of operation of micro-notches is similar to that of glued connections, where the micro-notches have a lower, still sufficient strength, but operate without any adhesive.



# Zusammenfassung

Der Verbund von Holz und Beton für Geschossdecken bietet eine Reihe von Vorteilen im Vergleich zu reinen Holzdecken: höhere Steifigkeit und Tragfähigkeit, verbesserte Schallschutz- und Schwingungseigenschaften und besseres Verhalten im Brandfall. Zudem zeichnen sie sich durch ein geringeres Eigengewicht, schnelleren Baufortschritt und wesentlich tiefere Umweltbelastung im Vergleich zu reinen Stahlbetondecken aus. Holz-Beton Verbunddecken (HBV-Decken) werden in der Schweiz seit einigen Jahrzehnten angewendet. Die Verbindung zwischen Holz und Beton ist von grosser Bedeutung für das Tragverhalten der Decke. Eine Vielzahl an verschiedenen Verbindungsmitteln mit unterschiedlichen Eigenschaften bezüglich Verbundsteifigkeit, Tragfähigkeit und Duktilität wurde mittlerweile entwickelt. Dabei zeichnen sich Verbindungen mit Kerben durch eine annähernd starre Verbundwirkung und hohe Tragfähigkeit aus. Meistens werden sie mit zusätzlichen Schrauben oder Dübeln kombiniert, um vertikale Zugkräfte aufzunehmen und Abheben der Betonplatte zu verhindern. Die Material- und Installationskosten der Schrauben sowie die Fräsarbeiten der Kerben fallen kostentesischnisch stark ins Gewicht. In dieser Dissertation wird ein neuartiges Verbindungsmittel namens Mikrokerben vorgestellt, das den reinen Verbund von Holz und Beton ohne zusätzliche Stahlteile ermöglicht.

Die Entwicklung der Mikrokerben erfolgte in einem ausführlichen experimentellen Versuchsprogramm, ergänzt durch analytische und numerische Untersuchungen. Im ersten Schritt wurde die Verbindung mit Mikrokerben in lokalen Scherversuchen in einem symmetrischen Push-Out Aufbau getestet. Das Ziel dieser Untersuchungen war die Ermittlung der Verbundeigenschaften von verschiedenen Konfigurationen von Mikrokerben und die Bestimmung einer optimalen Konfiguration. Diese optimale Konfiguration wurde dann in grossformatigen 4-Punkt Biegeversuchen getestet, um das realistische globale Tragverhalten der neuen Verbindung in HBV-Decken zu beurteilen. Die getesteten Träger wiesen ein sehr steifes, linear-elastisches Tragverhalten mit sprödem Endversagen im Holz in der Feldmitte auf. Die beobachteten Versagensarten in den Mikrokerben waren sowohl in den lokalen Scherversuchen als auch in den globalen Biegeversuchen eine Kombination aus mehrheitlich abgescherten Betonkerben und stellenweise abgescherten Holzkerben. Zwei Berechnungsmodelle, eines analytisch basierend auf dem  $\gamma$ -Verfahren und eines numerisch basierend auf einem Stabwerkmodell, wurden entwickelt, um das globale Tragverhalten bemessen zu können. Das globale Tragverhalten wurde dann mit dem lokalen Tragverhalten verglichen und die Verbundeigenschaften wurden entsprechend angepasst. Eine Langzeitversuchsserie wurde aufgesetzt, um den Einfluss von rheologischen Prozessen im Holz, im Beton und in der Verbindung zu untersuchen. Als weiteren Anwendungsbereich für HBV-Decken wurden Zweifeldträger getestet, um den positiven Einfluss der Durchlaufwirkung auf die Durchbiegungen zu evaluieren. Das Reißen des Betons über dem Mittelaufleger hat dabei einen entscheidenden Einfluss auf die Steifigkeit und muss in den Berechnungsmodellen berücksichtigt werden. Die Versuche zeigten, dass Mikrokerben auch in gerissenem Beton funktionieren und dass Durchlaufträger die Durchbiegungen reduzieren. Die Erkenntnisse aus den

durchgeführten experimentellen Versuchen und den entwickelten Berechnungsmodellen wurden in Empfehlungen für die Ausführung und die Bemessungen zusammengefasst.

Die Forschungsarbeit konnte zeigen, dass Mikrokerben als Verbundmittel für HBV-Decken ein sehr steifes, annähernd starres Verbundverhalten und ausreichende Tragfähigkeit bezüglich Schubübertragung in der Verbundfuge für die Anwendung in Wohn- und Bürogebäuden für Spannweiten bis 10 m aufweisen. Die beobachteten Versagensarten waren dabei spröde. Die Duktilität der Verbindung war jedoch kein Kriterium für die untersuchten HBV-Decken, da die massgebende Versagensart in Geschossdecken das kombinierte Biegezugversagen im Holz ist. Mikrokerben sind demnach eine valide Alternative für konventionelle Kerben, wobei sie einige Vorteile mitbringen. Die Verbundwirkung von Mikrokerben darf als starr angenommen werden, keine zusätzlichen Verbundmittel wie Schrauben oder Dübel sind notwendig und der Holzquerschnitt wird nur minimal beeinträchtigt. Die Wirkungsweise von Mikrokerben ist vergleichbar mit jener von verklebten Verbindungen mit geringerer, doch ausreichender Schubfestigkeit und ohne Klebstoff.

# Contents

<b>1</b>	<b>Introduction</b>	<b>1</b>
1.1	Motivation . . . . .	1
1.2	Objective . . . . .	1
1.3	Thesis outline . . . . .	2
1.4	Limitation of the work . . . . .	5
1.5	Terminology . . . . .	5
<b>2</b>	<b>Timber-concrete composite slabs</b>	<b>7</b>
2.1	General information . . . . .	7
2.1.1	Historical background . . . . .	7
2.1.2	Concept and advantages of TCC as slabs . . . . .	8
2.1.3	Timber-concrete composite systems . . . . .	9
2.1.4	Connection systems and connection behaviour . . . . .	11
2.2	Calculation models . . . . .	12
2.2.1	Development and overview of different calculation models . . . . .	12
2.2.2	Detailed description of the $\gamma$ -method . . . . .	14
2.2.3	Detailed description of the strut-and-tie model . . . . .	23
2.3	Interlocking connection system for composite beams . . . . .	25
2.3.1	Historical background of interlocking . . . . .	25
2.3.2	Notched TCC connections . . . . .	28
2.3.3	Micro-notches . . . . .	28
<b>3</b>	<b>Local behaviour of micro-notches</b>	<b>31</b>
3.1	Introduction and literature review . . . . .	31
3.1.1	Overview . . . . .	31
3.1.2	Previous experimental and numerical research . . . . .	32
3.1.3	Mechanical models for notched TCC connections . . . . .	35
3.1.4	Friction and adhesion . . . . .	39
3.1.5	Models on the determination of the connection properties . . . . .	39
3.2	Experimental push-out test series I & II . . . . .	42

3.2.1	Materials and methods . . . . .	42
3.2.2	Results . . . . .	49
3.3	Modelling local micro-notch behaviour . . . . .	57
3.3.1	Local forces and stresses on one individual micro-notch . . . . .	57
3.3.2	Local failure loads in timber . . . . .	59
3.3.3	Local failure loads in concrete . . . . .	60
3.3.4	Comparison with experimental data . . . . .	60
3.4	Determination of connection properties . . . . .	63
3.4.1	Distance between connectors . . . . .	63
3.4.2	Shear resistance . . . . .	63
3.4.3	Connection stiffness . . . . .	64
3.4.4	Comparison with literature results . . . . .	65
3.5	Influence of different parameters . . . . .	66
3.5.1	Test-setup . . . . .	66
3.5.2	Material properties . . . . .	66
3.5.3	Notch geometry . . . . .	66
3.5.4	Wood species . . . . .	68
3.5.5	Treatment of the timber surface before concreting . . . . .	69
3.5.6	Concrete treatment . . . . .	70
3.5.7	Direction of load to grain . . . . .	70
3.6	Specifying the design of micro-notches as TCC connection system . . . . .	71
3.7	Conclusions . . . . .	74
<b>4</b>	<b>Global behaviour of micro-notches</b>	<b>77</b>
4.1	Introduction and literature review . . . . .	77
4.1.1	Overview . . . . .	77
4.1.2	Previous experimental and numerical research . . . . .	77
4.1.3	Analytical and numerical models for TCC slabs . . . . .	81
4.2	Experimental 4-point bending test series . . . . .	82
4.2.1	Materials and methods . . . . .	82
4.2.2	Results . . . . .	88
4.3	Modelling TCC slabs with micro-notches . . . . .	93
4.3.1	General assumptions . . . . .	93
4.3.2	Analytical approach with the $\gamma$ -method . . . . .	94
4.3.3	Numerical approach with the strut-and-tie model . . . . .	100
4.3.4	Comparison of models and validation of experimental results . . . . .	102
4.4	Influence of different parameters . . . . .	105
4.4.1	Comparison of global behaviour of all configurations . . . . .	105
4.4.2	Notch front angle . . . . .	105
4.4.3	Treatment of the timber surface . . . . .	106
4.4.4	Additional screws . . . . .	106

4.4.5	Duration of load / short-term creep . . . . .	107
4.4.6	CLT element . . . . .	108
4.4.7	Cracking of concrete . . . . .	109
4.5	Comparison of global and local load-bearing behaviour . . . . .	109
4.5.1	Connection stiffness . . . . .	110
4.5.2	Load-bearing capacity . . . . .	110
4.5.3	Ductility . . . . .	112
4.5.4	Discussion . . . . .	112
4.6	Conclusions . . . . .	113
<b>5</b>	<b>Long-term investigations of micro-notches</b>	<b>115</b>
5.1	Introduction and literature review . . . . .	115
5.1.1	Overview . . . . .	115
5.1.2	Rheological phenomena in timber and concrete . . . . .	115
5.1.3	Interaction in timber-concrete composite slabs . . . . .	118
5.1.4	Models and simplified approaches for codes . . . . .	119
5.1.5	Previous experimental research . . . . .	121
5.2	Installation of a long-term test series . . . . .	122
5.2.1	Objective of the experimental program . . . . .	122
5.2.2	Materials and methods . . . . .	123
5.2.3	Results to date . . . . .	130
5.3	Outlook . . . . .	134
<b>6</b>	<b>Two-span TCC beams with micro-notches</b>	<b>135</b>
6.1	Introduction and literature review . . . . .	135
6.1.1	Overview . . . . .	135
6.1.2	Previous experimental and numerical research . . . . .	135
6.2	Experimental two-span beam tests . . . . .	138
6.2.1	Materials and methods . . . . .	138
6.2.2	Results . . . . .	144
6.3	Modelling two-span TCC beams with micro-notches . . . . .	148
6.3.1	General assumptions . . . . .	148
6.3.2	Analytical approach with the $\gamma$ -method . . . . .	148
6.3.3	Numerical approach with the strut-and-tie model . . . . .	152
6.3.4	Comparison of the models and the experimental data . . . . .	156
6.4	Influence of different parameters . . . . .	157
6.4.1	Comparison of configurations . . . . .	157
6.4.2	Reinforcement over the middle support . . . . .	157
6.4.3	MOE of the timber . . . . .	158
6.5	Conclusions . . . . .	159

<b>7</b>	<b>Design recommendations for TCC slabs with micro-notches</b>	<b>161</b>
7.1	General information . . . . .	161
7.2	Properties of the materials . . . . .	161
7.2.1	Timber . . . . .	161
7.2.2	Concrete . . . . .	162
7.3	Properties of micro-notches as a TCC connection system . . . . .	162
7.4	Structural behaviour of TCC slabs with micro-notches . . . . .	164
7.5	ULS verifications . . . . .	165
7.6	SLS verifications . . . . .	165
7.6.1	Deflections . . . . .	165
7.6.2	Vibrations . . . . .	166
7.7	Sound insulation . . . . .	166
7.8	Fire Safety . . . . .	166
7.9	Conclusions . . . . .	166
<b>8</b>	<b>Summary and conclusions</b>	<b>169</b>
8.1	Overview . . . . .	169
8.2	Local and global load-bearing behaviour . . . . .	170
8.3	Short-term and long-term behaviour . . . . .	171
8.4	Single-span and two-span beams . . . . .	171
<b>9</b>	<b>Outlook</b>	<b>173</b>
<b>A</b>	<b>Elastic bands as lateral supports for push-out test series II</b>	<b>175</b>
<b>B</b>	<b>Results for connection properties in push-out series I &amp; II</b>	<b>179</b>
<b>C</b>	<b>Derivation of cracked concrete height</b>	<b>181</b>
	<b>Nomenclature</b>	<b>185</b>
	<b>Bibliography</b>	<b>189</b>
	<b>Curriculum Vitae</b>	<b>203</b>

# Chapter 1

## Introduction

### 1.1 Motivation

The idea of combining timber and concrete in a resourceful way was first developed around 100 years ago in Europe and the USA. Detailed studies and thus more projects have been carried out again in the last few decades in Europe and in recent years also overseas. The timber-concrete composite (TCC) system has since become more and more popular, combining the advantages of both materials and providing a clever alternative to the prevalent concrete jungle in slab construction. But the combination of timber and concrete has by no means exhausted its potential in research and practice. For almost all of the composite systems and connection systems developed to date, TCC still requires a third material - steel for screws, dowels, metal plates, plastic for separation layers, or chemicals for adhesives. The additional material and subsequent time, costs, and complications do not correspond to the idea of combining building materials in a statically fully exploited and economically reasonable way. The motivation of this study was to tackle this potential to develop a TCC system with optimum production and performance using timber and concrete without additional materials.

### 1.2 Objective

The objective of this study was to develop a connection system for TCC slabs in office and residential buildings without additional dowel-type fasteners. The concept of micro-notches (see Chapter 2.3.3) was used as a starting point. The overall aim of the research project was to establish a novel connection system for market-ready application. The thesis therefore also intends to provide practical recommendations for the design and production in practice. The main goals were:

- development of a connection system for TCC slabs in office and residential buildings
- practice-relevant investigations to establish the optimum production of the connection system and to assess the connection properties and the performance in various structural systems

- development of analytical models to describe the structural behaviour of TCC slabs with the connection system
- development of design recommendations

### 1.3 Thesis outline

In this study, micro-notches as novel TCC connection system were developed and investigated in an extensive experimental program supported by analytical and numerical models. The concept of micro-notches was studied and tested as a connection system for the use in TCC slabs. The concept and production was optimised in local experiments and then tested for various aspects in different configurations and time-spans in a practice-oriented size scale. This thesis gives an overview of the relevant experimental series, a summary of the results obtained in these experimental series and their evaluations, as well as the underlying considerations and investigations in analytical and numerical models. The work is structured chronologically according to the progress of the investigations on the connection system micro-notch, preceded by a chapter with necessary background knowledge, and concluded by a summary of the most important aspects investigated.

The following Chapter 2 provides an introduction to the topic of composite slabs in general. A short summary of the historical development of TCC, of various construction systems, and of various connection systems is given. Various calculation models for composite slabs are described with a closer look to the commonly used  $\gamma$ -method and the strut-and-tie model. The concept of interlocking connection is described in a separate chapter, introducing the micro-notches as novel interlocking connection system for TCC applications.

The Chapters 3 to 6 treat different features of practical application. A literature recap for the respective application field regarding experimental and numerical studies as well as analytical approaches is found at the beginning of each of these chapters.

In Chapter 3, the investigations regarding the local behaviour of micro-notches as a connection system for TCC are presented. Two experimental push-out series have been carried out to assess the connection behaviour of micro-notches. The local behaviour of timber and concrete are analytically described. The influence of the variety of parameters tested are evaluated. The criteria for the optimum connection are described and the optimum parameters for the geometry and production are defined.

Chapters 4, 6, and 5 describe the subsequent implementation of the connection system micro-notches on a larger scale with practice-oriented dimensions:

In Chapter 4, an experimental series with 4-point bending tests are described and analysed. The analysis of the results is done by the analytical model approach using the  $\gamma$ -method and a numerical model approach using the strut-and-tie model. The influence of the tested parameters is described. The global load-bearing behaviour is compared to the local load-bearing behaviour.

In Chapter 5, the setup of a long-term test series for micro-notches as a connection system for TCC is described. A literature review and introduction over the different long-term phenomena



are given. The installation of the specimens and the measurements and analytical considerations are described. First results after half a year of loading are presented.

In Chapter 6, the novel connection system is tested on a two-span beam system. Two specimens as two-span beams with a total length of 12 m with different reinforcement over the middle support were tested. The results are evaluated and analysed with the same models used in the single-span application field. The influence of the material properties and the concrete reinforcement in the area of the middle support are discussed. The load-bearing and connection behaviour of two-span TCC beams is compared to single-span TCC beams.

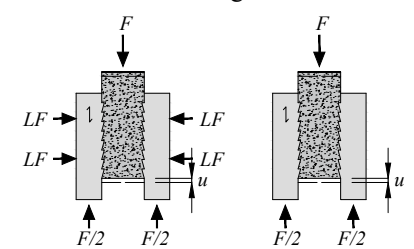
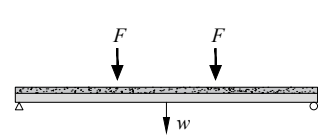
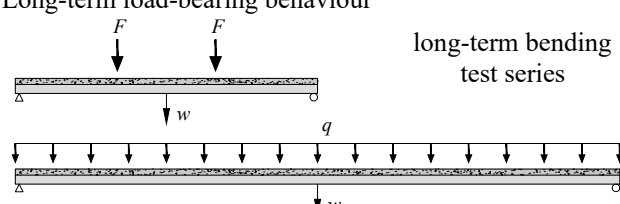
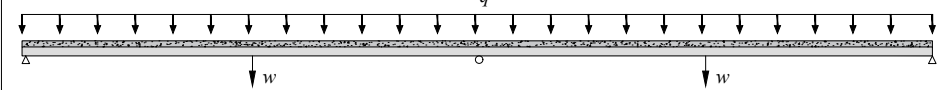
In Chapter 7, the characteristics of micro-notches as a novel connection system for TCC slabs are adapted from the experimental to a design stage. The general requirements for timber and concrete and for the production of the micro-notches are stated. The properties found for slip modulus and shear strength are adapted to design level. The relevant verifications for the ultimate limit state and the serviceability limit state are listed. The performance of the micro-notch connection system for TCC system with regard to vibration, sound insulation, and fire safety is briefly addressed.

A summary and the conclusions follow in Chapter 8 with a comparative review of the three main aspects on which micro-notches as TCC connection system were investigated:

- local/global load-bearing behaviour
- short-term/long-term load-bearing behaviour
- single-span/two-span load-bearing systems

The thesis is concluded with an outlook in Chapter 9.

Fig. 1.1 gives a graphic overview of the structure of the thesis.

<b>1 Introduction</b>	
<b>2 Timber-concrete composite slabs</b>	
<b>Investigation aspects on TCC with micro-notches</b>	
<b>local</b>	<p><b>3 Local load-bearing behaviour</b></p> <div style="display: flex; align-items: center;">  <div style="margin-left: 20px;"> <p>Push-Out tests Series I + II</p> </div> </div> <div style="text-align: right; margin-top: 10px;"> <p style="border: 1px dashed black; padding: 2px;">literature review</p> <p>determination of connection properties</p> <p>determination of optimum micro-notch configuration</p> </div>
<b>global</b>	<p><b>4 Global load-bearing behaviour</b></p> <div style="display: flex; align-items: center;"> <div style="writing-mode: vertical-rl; transform: rotate(180deg); font-size: small; margin-right: 5px;">short-term</div>  <div style="margin-left: 20px;"> <p>4-Point Bending test series with BST</p> </div> </div> <div style="text-align: right; margin-top: 10px;"> <p style="border: 1px dashed black; padding: 2px;">literature review</p> <p>modelling of structural behaviour</p> <p>comparison to local load-bearing behaviour</p> </div>
	<p><b>5 Long-term load-bearing behaviour</b></p> <div style="display: flex; align-items: center;"> <div style="writing-mode: vertical-rl; transform: rotate(180deg); font-size: small; margin-right: 5px;">long-term</div>  <div style="margin-left: 20px;"> <p>long-term bending test series</p> </div> </div> <div style="text-align: right; margin-top: 10px;"> <p style="border: 1px dashed black; padding: 2px;">literature review</p> <p>installation of long-term tests series</p> <p>first results</p> </div>
	<p><b>6 Two-span TCC beams</b></p> <div style="display: flex; align-items: center;"> <div style="writing-mode: vertical-rl; transform: rotate(180deg); font-size: small; margin-right: 5px;">two-span beam</div>  <div style="margin-left: 20px;"> <p>Two-span beam test series</p> </div> </div> <div style="text-align: right; margin-top: 10px;"> <p style="border: 1px dashed black; padding: 2px;">literature review</p> <p>modelling of structural behaviour</p> <p>comparison to single-spans</p> </div>
<b>7 Design Recommendations</b>	
<b>8 Summary &amp; Conclusions</b>	
<p>local - global</p> <p>short-term - long-term</p> <p>single span - two-span</p>	
<b>9 Outlook</b>	

**Fig. 1.1:** Overview of the thesis with chapter numbers. Boxes with dashed lines contain state-of-the-art content, boxes with solid lines contain original work.

## 1.4 Limitation of the work

This thesis focuses on the development of micro-notches as novel connection system for planar TCC slabs with *Brettstapel* elements. The boundary conditions for the material of the investigated systems were given by a system already used in practice: normal strength concrete and spruce/fir of strength class C24 for the timber elements.

The focus of this research was on application-based practicality. The ductility of the connection system was not a priority criteria, because the decisive failure mode of the investigated TCC slabs is the brittle failure due to bending tension in timber. Ductility is therefore only marginally discussed in this thesis.

The investigations conducted to develop the micro-notch system strongly rely on experimental investigations to authentically assess the material behaviour and interaction. Analytical and numerical investigations were conducted as prognosis for the tests and to assess the load-bearing behaviour.

The micro-notch system was developed for slabs bearing in one direction. The focus of the investigations summarised in this thesis is on the short-term local and global load-bearing behaviour. The long-term behaviour is addressed with a literature review and with the description of the installed long-term test series. However, because of the very recent installation and difficulties with data evaluation, the thesis is limited to the description of the test series and plain results of the first months. No prognosis or detailed models are presented.

The experimental program presented in this thesis summarise the most important investigations performed during the research project.

## 1.5 Terminology

All abbreviations and symbols used in this thesis are listed in the nomenclature. Frequently used terms are explained in the following:

Timber-concrete composite is referred to in the following as **TCC**. The **composite action** is a term to describe the efficiency of the composite. The **composite joint** denotes the interface between the two components timber and concrete. The **connection system** includes all possible systems to connect timber and concrete, while **connectors** refer to individual, local fasteners such as screws, dowels, or nails. The **connection stiffness** is a term for the load-deformation relation of a connection system. It is measured by the **slip modulus**  $K$  (in kN/mm/m) or the **joint stiffness**  $k$  (in kN/mm<sup>2</sup>/m). In this thesis, *Brettstapel* is abbreviated and denoted as **BST** as it is referred to by the producer. *Brettstapel* elements are planar timber elements made of upright lamellas put next to each other and connected by dowels or nails. The elements investigated in this research project are made out of spruce and/or fir lamellas connected only with kiln-dried beech dowels. *Brettstapel* is the term used in Switzerland, Germany and Austria. In North America, this timber element is known as *dowel laminated timber* or short DLT. Cross-laminated timber is denoted as **CLT**.



## Chapter 2

# Timber-concrete composite slabs

### 2.1 General information

#### 2.1.1 Historical background

The first combined use of timber and concrete for structural members dates back to the beginning of the 20<sup>th</sup> century. At that time, a shortage of steel due to the aftermath of World War I was the main motivation for combining these two materials. Efforts were made to replace the reinforcing steel in reinforced concrete components. This was profitable in the case of floor slabs by replacing the lower part of the slab cross-section exposed to tensile stresses. One of the first known documents regarding timber-concrete composite was a patent by Paul Müller granted in 1921 for a “Slab made of upright standing wooden planks or boards and concrete top layer (*Decke aus hochkantig stehenden Holzbohlen oder Holzbrettern mit Betondeckschicht*)” [118]. The connection between timber and concrete consisted of steel stirrups also acting as shear and tension reinforcement for the concrete [136]. Further patents were granted to Otto Schaub in 1931 for a “Wood reinforced concrete structural member” [140] in the United States and in 1939 for a “Composite floor made of wooden ribs and concrete slab (*Verbunddecke aus Holzrippen und Betonplatte*)” in Germany [141]. The connection was realised by steel I- or Z-profiles embedded into the timber. Schaub also identified a second motive for the combination of timber and concrete in structural members: to refurbish existing timber slabs with a top layer of concrete.

The further development of timber-concrete composites (hereafter called TCC) mainly advanced in North America in the 1930s, where various systems and connectors were tested [106; 129; 147]. The investigations led to the evolution of an efficient design for bridge structures. Until 1943, more than 180 TCC structures and bridges were realised [136], some of which are still in operation today [130]. The US National Bridge Inventory reports that most TCC bridges still in service were built shortly after World War I and again shortly after World War II [164]. In the 1950s, TCC was also used in bridge construction in Australia and New Zealand [130; 168].

In the 1960s, the construction of TCC bridges started to decrease in the US [164], whereas in Europe, the use of TCC for building construction was rediscovered [168]. TCC was found to be an excellent method to reinforce existing timber slabs and was implemented first in this way in Eastern Europe [126; 54]. The interest in TCC structures increased significantly since the 1980s and 1990s [86; 69] throughout several European countries, including Switzerland, Austria, Italy, and Finland [168]. In addition to the previous applications, including reinforcement of existing timber slabs and bridges, TCC is used more and more for slabs in new buildings. In the recent past, a large variety of different TCC systems and TCC connection systems have been investigated in research and applied in practice. TCC is used mainly for slabs or bridges, but also wall systems [27]. TCC systems generally encourage the use of timber in construction, as they extend the field of application [32].

### 2.1.2 Concept and advantages of TCC as slabs

TCC structures consist of three components: timber, concrete, and the connection. These three components are intended to be used in such a way that their advantages are combined and their disadvantages are neutralised as much as possible. The original idea of replacing the steel bars in reinforced concrete slabs was created as a logical consequence of the optimal use of the specific properties of each building material. According to Eurocode 2 [22] and SIA 262 [150] design, tensile stresses occur in approximately the lower two thirds of the cross-section of single-span reinforced concrete slabs. Concrete cracks under very low tensile stresses. It is even often assumed that only concrete under compressive stresses can transfer forces and bending moments. The cracked concrete cross-section is therefore mainly acting as a static height. The concept of TCC is to substitute this cracked concrete cross-section with timber which can also carry and transfer tensile stresses. Hence, the timber element is below and takes the tensile forces occurring in slabs resulting from bending. The concrete element is above and takes the compressive forces in the slab. The connection transfers shear forces and thus ensures the composite action. Ideally, all components are dimensioned in a way that they fulfil their specific task in the best possible way.

At present, slabs for residential and office buildings in Switzerland are commonly made of reinforced concrete. Concrete is available everywhere in Switzerland and is extremely low-cost due to the industrially optimised production of large quantities and the high competition in the construction sector. However, there are severe disadvantages of concrete for the use of slabs. As described above, the replacement of the tensile-exposed concrete cross-section by timber is statically reasonable and provides further advantages. The construction process of TCC is significantly faster because the timber element below acts as formwork and can also serve as a finished ceiling for the room below. Furthermore, replacing the lower part of the concrete slab with timber decreases the overall weight of the slab. The weight of the slabs is often the governing part of the weight of the whole building. This is especially relevant for tall buildings. Lower construction weight represents less weight on foundations and is highly beneficial for transport to and on the construction site. The environmental impact of concrete regarding

energy consumption, CO<sub>2</sub>-emissions, and embodied energy of concrete is several times larger than the environmental impact of timber. Depending on how the boundaries of the Life Cycle Analysis are set, even the CO<sub>2</sub> sequestration of timber can be taken into account at least as storage during the period of the service life of the building.

The combination of timber and concrete also outperforms timber-only slabs. The concrete part enhances the load-bearing behaviour of the slab, improving its stiffness and load-bearing capacity. Furthermore, the concrete slab improves the sound insulation and vibration behaviour of the slab. In addition, the concrete slab, which is often realised monolithic or connected subsequently, acts as an airtight barrier, protects the timber below, and thus enhances the fire resistance of the slab.

Table 2.1 lists the advantages of TCC slabs compared to timber-only slabs and reinforced concrete slabs:

**Tab. 2.1:** Advantages of TCC slabs

<b>compared to timber-only slabs</b>	<b>compared to concrete slabs</b>
increased stiffness	lower self-weight
increased load-bearing capacity	faster construction process
improved sound insulation	lower primary energy consumption
improved vibration behaviour	reduced CO <sub>2</sub> -emissions
improved fire resistance	high level of prefabrication

To obtain the best performance of timber-concrete composite slabs, the thickness of the two components and the material properties have to be chosen carefully. However, the connection between the two components is the most important consideration for the composite performance.

### 2.1.3 Timber-concrete composite systems

TCC slabs can be constructed in a variety of designs. A general differentiation can be made on the connected surface, the ratio of section thicknesses, or the production.

The connected surface between timber and concrete is defined by the used timber element, which can be linear or planar. A **linear TCC system** essentially consists of timber beam elements and the planar concrete slab above. Timber beams can be made out of solid timber, glued laminated timber, LVL beams, or any other timber beam element. An intermediate layer between timber beams and the concrete slab such as a formwork timber panel or a separating foil is optional. The concrete plate can be casted in-situ or prefabricated and connected on site. The applicable width of the timber part corresponds to the width of the timber beam and the applicable width of the concrete part is defined as the effective width activated by shear according to SIA 265 [149]. Linear TCC systems offer the advantage of space and access for pipes and cables for building services. Linear TCC systems are thus suitable for industrial or office buildings, where the wider spans can be realised by beams with larger height and thus offer an industrial appearance and even more flexibility for usable volume between the beams. A **planar TCC system** essentially consists of a planar timber element and the planar concrete slab on

top. Planar timber elements can be made out of *Brettstapel* elements (hereafter called BST), glued laminated timber (GLT), cross-laminated timber (CLT), solid timber boards, or other planar timber elements. An intermediate layer between timber element and the concrete slab, such as a separating foil, is optional. The concrete plate can be casted in-situ or prefabricated and connected on site. In this case, the applicable width of the timber part is the same as the width of the concrete part. Planar TCC systems are more eligible for office or residential buildings, where smaller spans and less building services are needed. However, planar TCC systems can also be an option for larger spans by using a hidden joist or multi-span systems.

Fig. 2.1 shows a planar and a linear TCC system. In this research project, planar TCC systems with BST elements were investigated.

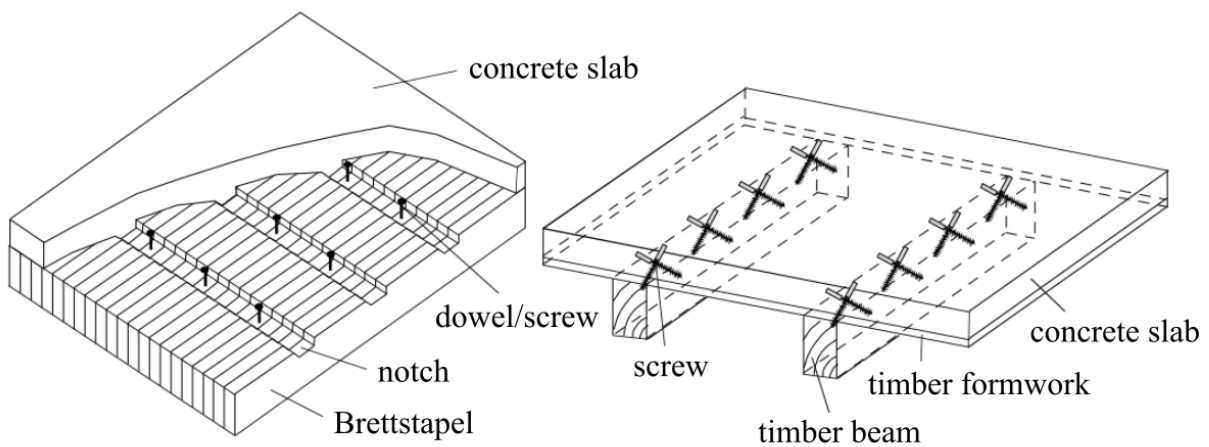


**Fig. 2.1:** Planar and linear TCC slab systems [45]

The ratio of the cross-section thicknesses is also a design parameter. Conventionally, the timber part substitutes the cracked concrete cross-section and thus makes up the major part of the total cross-section (Fig. 2.2a). However, the concrete part is often designed with a minimum height of 120 mm or more for production and acoustical reasons. Boccadoro [8] investigated a TCC system with a thin timber panel made out of beech laminated veneer lumber (*BauBuche* [125]) and a large concrete section (Fig. 2.2b). The system investigated by Kreis [89] optimises the material consumption as both the timber and the concrete cross-section are designed as thin chords. The connection is achieved with steel tubes and thus creates a large static height, which can be filled with insulation material as shown in Fig. 2.2c.

The production of TCC slabs can be prefabricated or made on site. The timber elements are produced in the workshop and transported to the site in a finished state. The connection system can be prefabricated or installed on site. The concrete can also be prefabricated or casted on site. Prefabricated TCC slabs have the advantage of less deflections, since the deflections during construction state are omitted. In-situ casted TCC slabs have the advantages of a lighter transport and better vibration behaviour as the concrete plate acts as a monolithic plane. Both construction types are wet, since the prefabricated TCC slabs also need to be connected with in-situ concrete or mortar.



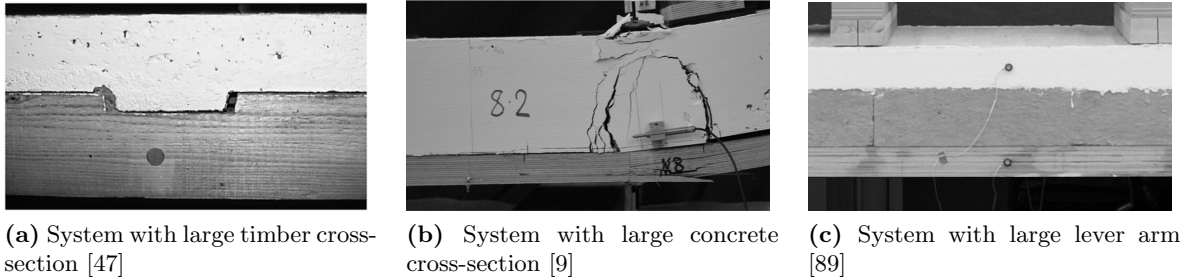


**Fig. 2.2:** Different timber-concrete composite cross-section designs

#### 2.1.4 Connection systems and connection behaviour

The load-bearing behaviour of TCC slabs is primarily guided by the efficiency of the connection between timber and concrete. The connection between timber and concrete transfers shear forces and thus enables the composite action. The load-bearing behaviour of a connection can be described by three characteristics:

- connection stiffness
- shear resistance
- ductility

The connection stiffness influences the effective bending stiffness of the composite slabs and thus has a large effect both on the deformations and the resulting stresses in the components. The shear resistance depends on the load-bearing capacity of the connection system. In conventional timber floor slabs, the ultimate limit state (ULS) is often not decisive and the shear stresses occurring in the connection joint are low (see Chapter 3.6). The shear resistance of the connection is therefore not of primary relevance, as long as the load-bearing capacity of the connection system exceeds the shear stresses in the composite joint. The ductility as a connection characteristic has gained in importance and attracted a lot of attention lately. Ductile connection systems enable a redistribution of forces which provides for alternative load paths and thus increases the robustness of the system. Furthermore, a ductile failure of the connection systems can indicate that the structure might fail ultimately. Boccadoro [8] developed a ductile connection behaviour between timber and concrete by using end-to-end screws, slotted holes, and polystyrene buffer areas to achieve a ductile failure mode in the notches.

An extensive variety of different connectors and connection systems have been subject to research and practice. An overview of the topic has been addressed in various studies [6; 31; 70; 168]. Various connection system concepts are shown in Fig. 2.3b and their corresponding load-slip behaviour in Fig. 2.3a) as described by Ceccotti [17]. Connection system group a) includes all dowel-type connectors such as nails, screws, dowels, or other dowel-type steel connectors such as bent reinforcement bars and glued-in rods [47; 8]. The corresponding load-slip behaviour indicates low connection stiffness and low load-bearing capacity, but large ductility. Connection system group b) includes steel connectors such as split rings, toothed

plates, tubes [89], or metal plates. The corresponding load-slip behaviour depends on the steel connector used (Fig. 2.3a). Connection system group c) includes all types of notches or indentations, in almost all cases combined with steel connectors such as screws, steel bars, or steel shear plates. The corresponding load-slip behaviour indicates high connection stiffness, medium load-bearing capacity, and ductility depending on the additional steel connector. Connection system group d) includes all types of continuous connection systems such as steel meshes or plates glued into the timber parallel to the span [3]. The corresponding load-slip behaviour indicates very high connection stiffness and load-bearing capacity, but small ductility.

The last connection system group d) of continuous connection systems with high stiffness but brittle failure behaviour also includes adhesives [14; 87; 136] and friction-based connection systems such as the *PlusMinus* system [78; 88], in some cases with additional transverse steel rods [134] or beech dowels [112].

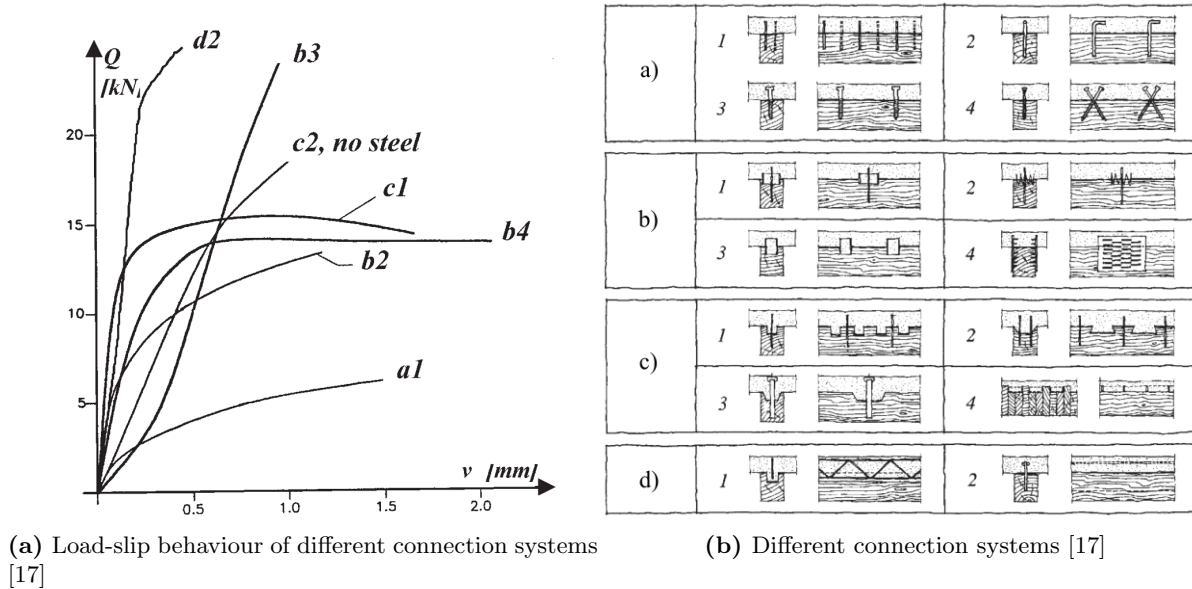


**Fig. 2.3:** Different connection systems and their connection behaviour

## 2.2 Calculation models

### 2.2.1 Development and overview of different calculation models

The calculation of internal forces and displacements of TCC systems must consider several phenomena: partial composite action between timber and concrete, non-linear behaviour and/or irregular arrangement of the connections, and differences in the long-term behaviour of the materials.

The first calculation models for TCC were adopted from calculation models for other composite systems with partial composite action, and adjusted with timber and concrete properties. An analytical solution can be found with the elastic differential equation for beams comple-

mented by equilibrium and deformation conditions in the connection joint [157]. Solutions for different loading and support conditions are deduced by Natterer & Hoefft [120]. The effort for the structural analysis using the differential equation rises considerably for multi-span beams, varying cross-sections or stiffness properties along the axis, or different spacing of the connectors. These aspects can be accounted for in the difference method described by Timmermann & Meierhofer [161] that is an approximate solution of the elastic differential equation. A further simplification was developed by Stüssi [157] and Möhler [113] based on a single-span, simply supported composite beam under sinusoidal line load with constant cross-sections and stiffness of the materials, linear elastic material behaviour, and constant joint stiffness along the beam axis. The boundary conditions of this specific composite beam configuration allow a particularly simple integration of the differential equation. The decreased bending stiffness caused by the partial composite action of the connection is considered with the reduction of the area moments of inertia according to the parallel axis theorem by the reduction factor  $\gamma$ . The so-called  $\gamma$ -method can be used as a good approximation for simple beams with uniform line loads, which represent by far the majority of slab systems in timber construction. Due to its practicality and convenience, the  $\gamma$ -method is widely used and adapted in Eurocode 5, Annex B [21].

The analytical models described above are not applicable with reasonable efforts or not applicable at all for irregularities of material, connectors, and loading situations or for non-linear effects. The neglect of non-linear effects of material and composite joint can, however, lead to non-conservative results under certain circumstances [29]. Therefore, and due to the rapid increase of computing power, numerical methods have become very popular. The strut-and-tie model developed by Rautenstrauch and Grosse [127; 58] is a low effort approach using a structural analysis software allowing to consider arbitrary arrangements, distances, and stiffness properties of connectors, as well as varying cross-sections and various static systems. This model is especially useful for local connectors, point loads, and multi-span systems. Another numerical model is the shear analogy developed by Kreuzinger [90]. The shear analogy model consists of two beams, where beam A presents the bending stiffness of the individual components and beam B presents the composite stiffness due to eccentricity of the single cross-sections [31]. The shear analogy is suitable to analyse composite beams of more than three components.

Even more computational aid is used in 3D finite element (FE) models, where both the timber and concrete components and the connection are modelled individually. FE models can simulate all kinds of irregularities and nonlinearities of materials. The computational effort is considerable, but modeling with FE programs is still especially worthwhile for parametric studies.

An extensive overview of different calculation models is given by Timmermann & Meierhofer [161]. An extensive overview, comparison and evaluation of different models including more recent approaches such as FE models and is presented in a report by COST Action FP1402 / WG 4 [31]. In this thesis, the calculation methods used for the analysis of TCC slabs with micro-notches were the  $\gamma$ -method and the strut-and-tie model, which are described in more detail in the following Chapters 2.2.2 and 2.2.3. The consideration of long-term effects in the models is addressed in an extended  $\gamma$ -method proposed by Schänzlin [138] and implemented in

the state-of-the-art Technical Specification on TCC CEN/TC 250/SC 5 [30]. It is treated in more detail in Chapter 5.1.

### 2.2.2 Detailed description of the $\gamma$ -method

The  $\gamma$ -factor is a reduction factor for the area moments of inertia according to the parallel axis theorem to account for the decrease of bending stiffness caused by the partial composite action of the connection. The value of  $\gamma$  is inverse to the reduction and has two limit states:  $\gamma = 0$  represents no composite action, where the effective beam stiffness consists of the individual stiffnesses of each beam without any coupling. At the other end,  $\gamma = 1$  represents full composite action, where the effective beam stiffness consists of the individual stiffnesses of each beam plus the full area moments of inertia according to the parallel-axis theorem, which equals the moment of inertia of the entire composite cross-section. A full composite action is called rigid connection. For two cross-sections with the same dimensions and properties, rigid connection leads to a stiffness four times higher than no connection of the same two cross-sections (Fig. 2.4). Most connection systems are not rigid, but have a  $\gamma$ -value between 0 and 1.

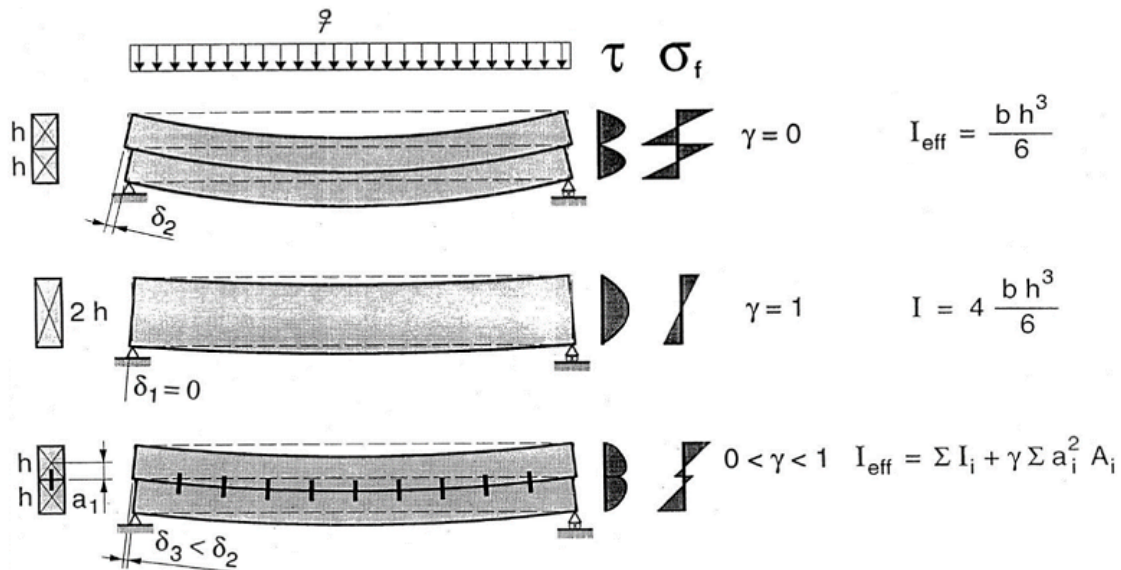


**Fig. 2.4:** Second moment of area  $I_{\text{eff}}$  of a composite beam with no connection ( $\gamma = 0$ ), with rigid connection ( $\gamma = 1$ ), and with flexible connection ( $0 < \gamma < 1$ ) [116]

The basics of the  $\gamma$ -method are found in the work of Stüssi and Dubas [37; 157; 158] as well as Möhler [113]. Stüssi and Dubas used a different reference axis than Möhler for the distances of the area moments of inertia. The approach of Möhler has become generally accepted, was adopted in the standard Eurocode 5, Annex B [22], and is therefore used in the vast majority of research work. The approach of Stüssi and Dubas is hardly used today.

The different approaches to calculate the  $\gamma$ -factors are briefly presented below with the reference axis as the main difference:

- **Neutral axis of one of the components as the reference axis**

The neutral axis is the axis free of stresses and strains in the composite beam subjected to bending. Both the timber and the concrete cross-section have a neutral axis in the composite beam. The approach of Möhler [113] takes the neutral axis in the timber cross-section as the reference axis for the distances  $a_1$  and  $a_2$ , which represent the distances of the centroids of the components to the centroid of the composite cross-section. Eurocode 5, Annex B [21] adapts this method and defines the reference axis as the neutral stress axis in the web of a linear composite cross-section with two or three parts. The  $\gamma$ -factor according to Eurocode 5, Annex B [21] is:

$$\gamma_i = \frac{1}{1 + \frac{\pi^2 E_i A_i s}{K l^2}} \quad (2.1)$$

where	$E_i$	MOE of component $i$ in [N/mm <sup>2</sup> ]
	$A_i$	cross-section area of component $i$ in [N/mm <sup>2</sup> ]
	$s$	spacing between connectors in [mm]
	$l$	span in [mm]
	$K$	slip modulus [kN/mm]

The index  $i$  in equation 2.1 is 1 for the upper flange and 3 for an additional lower flange. The second component (index  $i = 2$ ) is defined as the web of the composite cross-section. The  $\gamma$ -factor of this component equals 1 according to Eurocode 5:

$$\gamma_2 = 1 \quad (2.2)$$

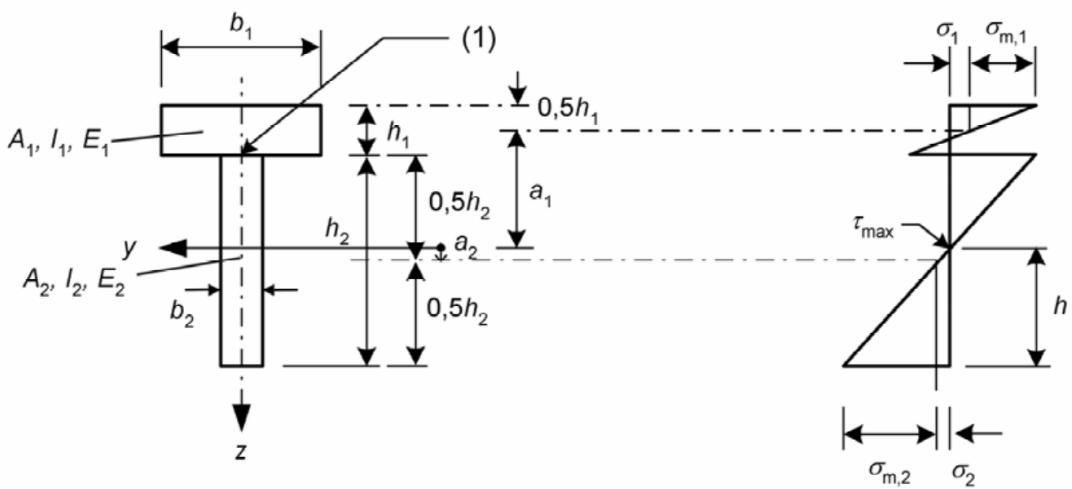


**Fig. 2.5:** Cross-section and stress distribution of a composite section with two components as defined by Eurocode 5, Annex B [21]

Adapted to TCC slabs, the indices are:

$i = 1$	for concrete
$i = 2$	for timber

The reference axis in this case is the neutral axis in timber and the  $\gamma$ -value defines the reduction of the area moment of inertia of the concrete cross-section. However, it is also possible to reduce the area moment of inertia of the timber cross-section. Boccadoro [8] suggests that the determination of the  $\gamma$ -factor depends on the ratio of the cross-sections. If the centroid of the composite cross-section is located in the timber section, the neutral axis of the timber should be considered as reference axis. If the centroid of the composite cross-section is located in the concrete section, the neutral axis of the concrete section should be considered as reference axis. For the TCC system investigated in [8], the concrete section measures 16 cm and the timber section 4 cm (see also Fig. 2.2b). The centroid of the cross-section is located in the concrete section. The  $\gamma$ -factors with the neutral axis of the concrete cross-section as the reference axis are determined as:

$$\gamma_1 = 1 \quad (2.3)$$

$$\gamma_2 = \frac{1}{1 + \frac{\pi^2 E_2 A_2 s}{K l^2}} \quad (2.4)$$

The distances  $a_1$  and  $a_2$  between the centroids of the components and the centre of gravity can be calculated for both approaches described above in the same way:

$$a_1 = \frac{\gamma_2 n_2 A_2 \cdot e}{\gamma_1 n_1 A_1 + \gamma_2 n_2 A_2} \quad (2.5)$$

$$a_2 = \frac{\gamma_1 n_1 A_1 \cdot e}{\gamma_1 n_1 A_1 + \gamma_2 n_2 A_2} \quad (2.6)$$

The  $n$ -value is defined as the ratio between the MOE of the two materials and again referencing on one of the components:

$$n_i = \frac{E_i}{E_{ref}} \quad (2.7)$$

The term  $e$  is the distance between the centroid of the timber cross-section and the centroid of the concrete cross-section. In case of an additional interlayer with thickness  $t$ ,  $e$  is:

$$e = \frac{h_1}{2} + t + \frac{h_2}{2} \quad (2.8)$$

The two approaches with the reference axis in the timber or the concrete cross-section deliver different  $\gamma$ -values and different values for the distances  $a_1$  and  $a_2$ . However, the

reduced distance  $\gamma_1 \cdot a_1$  from the timber reference is the same value as  $a_1$  from the concrete reference. Similarly, the reduced distance  $\gamma_2 \cdot a_2$  from the concrete reference is the same value as  $a_2$  from the timber reference. Thus, both approaches deliver the same results regardless of the ratio of the component thickness.

- **The centre of gravity of the composite cross-section as the reference axis**

The approach by Stüssi and Dubas [37; 157; 158], cited in [45; 46] takes the centre of gravity of the composite cross-section as reference axis. The  $\gamma$ -value is then defined as:

$$\gamma_i = \frac{1}{1 + \frac{\pi^2 E_i A_i s a_i}{K l^2 e}} \quad (2.9)$$

In this approach, the  $\gamma$ -factor acts as the reduction factor for the area moments of inertia and for both distances  $a_1$  and  $a_2$  between the centroids of the components and the centre of gravity. The reduction and thus the  $\gamma$ -factor is for both components the same:

$$\gamma_i = \gamma_1 = \gamma_2 \quad (2.10)$$

The distances  $a_1$  and  $a_2$  between the centroids of the components and the centre of gravity are defined as:

$$a_1 = \frac{n_2 A_2 \cdot e}{n_1 A_1 + n_2 A_2} \quad (2.11)$$

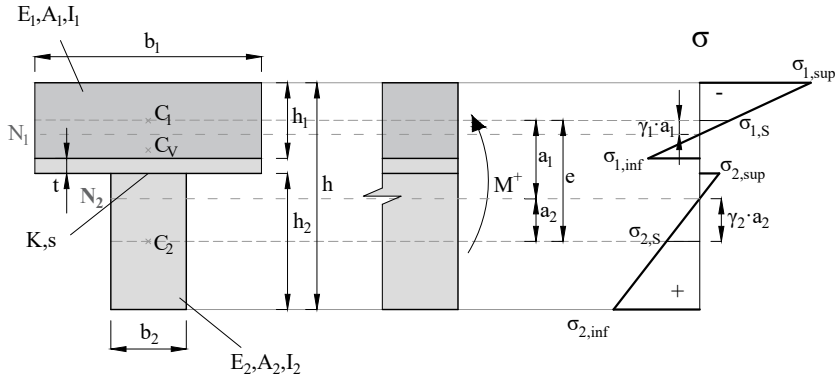
$$a_2 = \frac{n_1 A_1 \cdot e}{n_1 A_1 + n_2 A_2} \quad (2.12)$$

Equations 2.11 and 2.12 show that the distances  $a_1$  and  $a_2$  are independent of the  $\gamma$ -factor and therefore also independent of the span  $l$  and of the connection properties  $K$  and  $s$ .

- **Overview of different  $\gamma$ -values and their connection efficiency**

As shown above, there are three different definitions of the  $\gamma$ -factor: Two definitions are based on the neutral axis in one of the components while the third definition is based on the centre of gravity as reference axis. This results in different values in each case for  $\gamma_1$ ,  $\gamma_2$ ,  $a_1$ , and  $a_2$ . However, the resulting products of  $\gamma_i \cdot a_i$  are identical for all three approaches. The following equations are therefore valid for all three approaches. The context of the  $\gamma$ -values and the distances  $a_1$  and  $a_2$  for the three possible reference axes is shown in Fig. 2.6 for a linear composite cross-section with interlayer (thickness  $t$ ). The equations also apply to planar cross-sections with or without interlayer.

**$\gamma$ -factor with reference axis = neutral axis in timber:  $\gamma_2 = 1$**



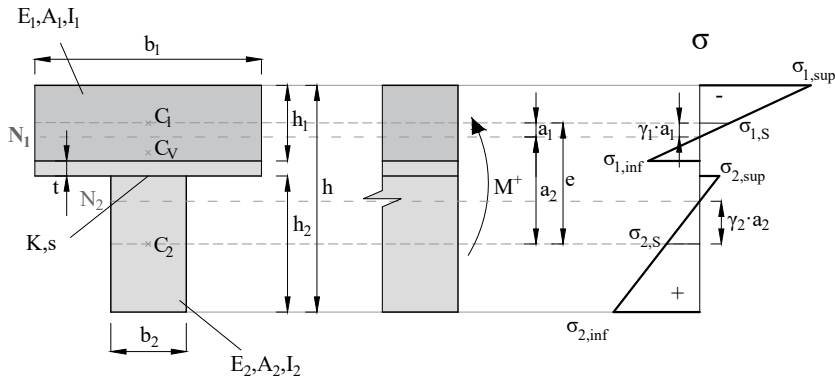
$$\gamma_1 = \frac{1}{1 + \frac{\pi^2 E_1 A_1 s}{K l^2}}$$

$$\gamma_2 = 1$$

$$a_1 = \frac{\gamma_2 E_2 A_2 \cdot e}{\gamma_1 E_1 A_1 + \gamma_2 E_2 A_2}$$

$$a_2 = \frac{\gamma_1 E_1 A_1 \cdot e}{\gamma_1 E_1 A_1 + \gamma_2 E_2 A_2}$$

**$\gamma$ -factor with reference axis = neutral axis in concrete:  $\gamma_1 = 1$**



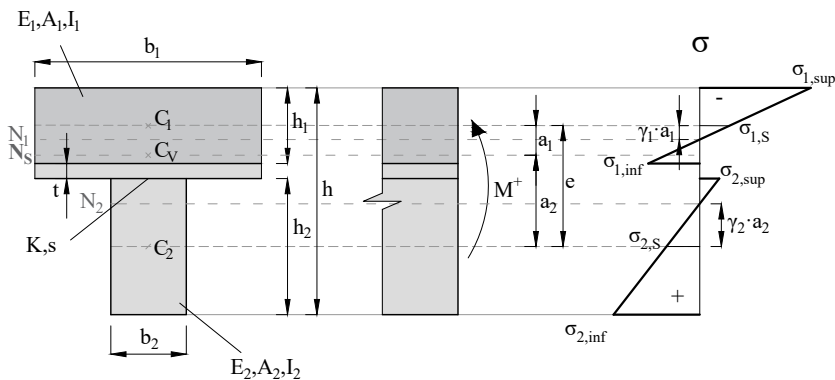
$$\gamma_1 = 1$$

$$\gamma_2 = \frac{1}{1 + \frac{\pi^2 E_2 A_2 s}{K l^2}}$$

$$a_1 = \frac{\gamma_2 E_2 A_2 \cdot e}{\gamma_1 E_1 A_1 + \gamma_2 E_2 A_2}$$

$$a_2 = \frac{\gamma_1 E_1 A_1 \cdot e}{\gamma_1 E_1 A_1 + \gamma_2 E_2 A_2}$$

**$\gamma$ -factor with reference axis = centroidal axis of composite cross-section:  $\gamma_1 = \gamma_2$**



$$\gamma_1 = \frac{1}{1 + \frac{\pi^2 E_1 A_1 s a_1}{K l^2 e}}$$

$$\gamma_2 = \gamma_1$$

$$a_1 = \frac{E_2 A_2 \cdot e}{E_1 A_1 + E_2 A_2}$$

$$a_2 = \frac{E_1 A_1 \cdot e}{E_1 A_1 + E_2 A_2}$$

**Fig. 2.6:** Overview of different reference axes to determine the  $\gamma$ -factor



- **Calculation of effective bending stiffness**

The resulting bending stiffness for composite cross-sections with two components is determined as:

$$EI_{eff} = \sum_{i=1}^2 (E_i I_i + \gamma_i E_i A_i a_i^2) \quad (2.13)$$

Taking the timber section as the reference section, the  $n$ -values result:

$$n_1 = \frac{E_1}{E_2} \quad (2.14)$$

$$n_2 = \frac{E_2}{E_2} = 1 \quad (2.15)$$

Equation 2.13 therefore evolves to:

$$EI_{eff} = E_2 \cdot \sum_{n=1}^2 (n_i I_i + \gamma_i n_i A_i a_i^2) \quad (2.16)$$

The effective moment of inertia of the composite cross-section is:

$$I_{eff} = \sum_{n=1}^2 (n_i I_i + \gamma_i n_i A_i a_i^2) \quad (2.17)$$

Applying equations 2.2 and 2.15, the effective moment of inertia simplifies to:

$$I_{eff} = n_1 I_1 + I_2 + \gamma_1 n_1 A_1 a_1^2 + A_2 a_2^2 \quad (2.18)$$

Using equations 2.5 and 2.6, the effective moment of area of a composite cross-section can be found as:

$$I_{eff} = n_1 I_1 + I_2 + \gamma_1 n_1 A_1 a_1 e \quad (2.19)$$

The derivation of this simplified equation for  $I_{eff}$  can be found in the same way for the  $\gamma$ -factor defined with the reference axis in concrete and the centroidal axis of the composite cross-section as the reference axis.

The effective bending stiffness of a composite cross-section with the timber as reference section results:

$$EI_{eff} = E_1 \cdot (n_1 I_1 + I_2 + \gamma_1 n_1 A_1 a_1 e) \quad (2.20)$$

The resulting effective moment of inertia and effective bending stiffness deliver the same values for all three approaches.

- **Connection efficiency and relation to the  $\gamma$ -value**

Fig. 2.7 shows for a numeric example the  $\gamma$ -values obtained from the three different approaches for different connection stiffnesses using the joint stiffness  $k$ , defined from the slip modulus  $K$ , and the distance between the connectors  $s$ :

$$k = \frac{K}{s} \quad (2.21)$$

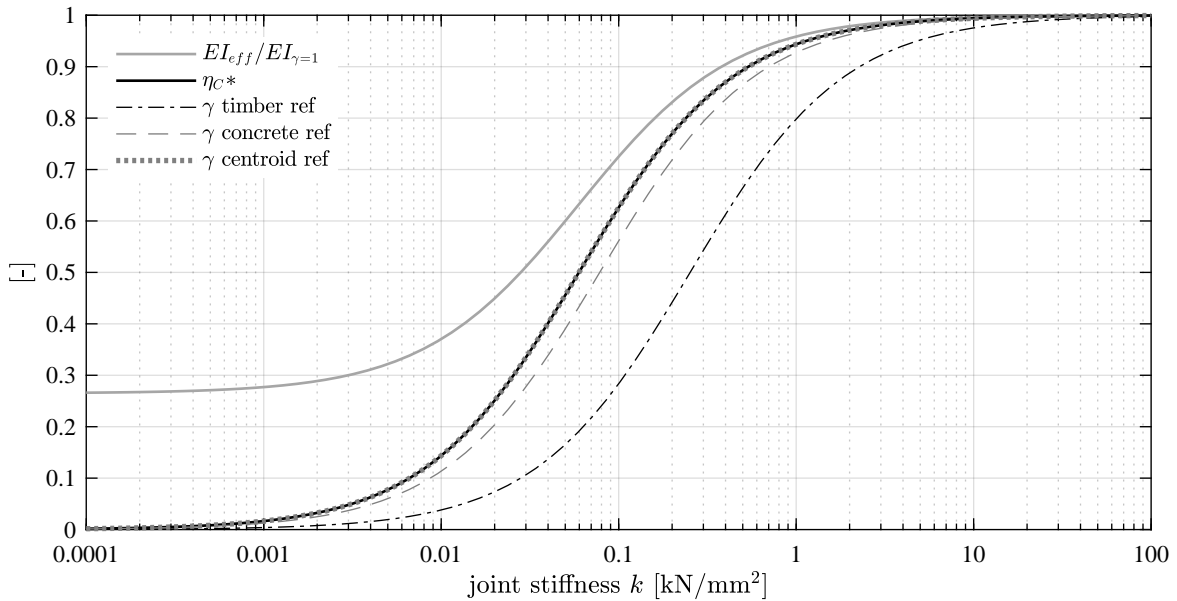
Fig. 2.7 also displays the connection efficiency  $\eta_C$  defined by Pault [124] using the deflections of a composite beam with no composite action  $w_{\gamma=0}$ , with full composite action  $w_{\gamma=1}$ , and with the composite action as a function of the joint stiffness  $w(k)$ :

$$\eta_C(k) = \frac{w_{\gamma=0} - w(k)}{w_{\gamma=0} - w_{\gamma=1}} \quad (2.22)$$

To exclude the influence of the loading situation and the span of the system, the connection efficiency  $\eta_{C^*}$  is defined using the effective bending stiffness  $EI_{eff}$  of the three states: no composite action  $EI_{\gamma=0}$ , full composite action  $EI_{\gamma=1}$ , and effective composite action  $EI_{eff}(k)$ :

$$\eta_{C^*}(k) = \frac{EI_{eff}(k) - EI_{\gamma=0}}{EI_{\gamma=1} - EI_{\gamma=0}} \quad (2.23)$$

The ratio between the effective bending stiffness  $EI_{eff}(k)$  and the bending stiffness at full composite action  $EI_{\gamma=1}$  is plotted as a reference. The value of this ratio depends on the material properties, cross-section dimensions, and thickness of the interlayer. The minimum value of this ratio is 0.25 as was shown in Fig. 2.4.



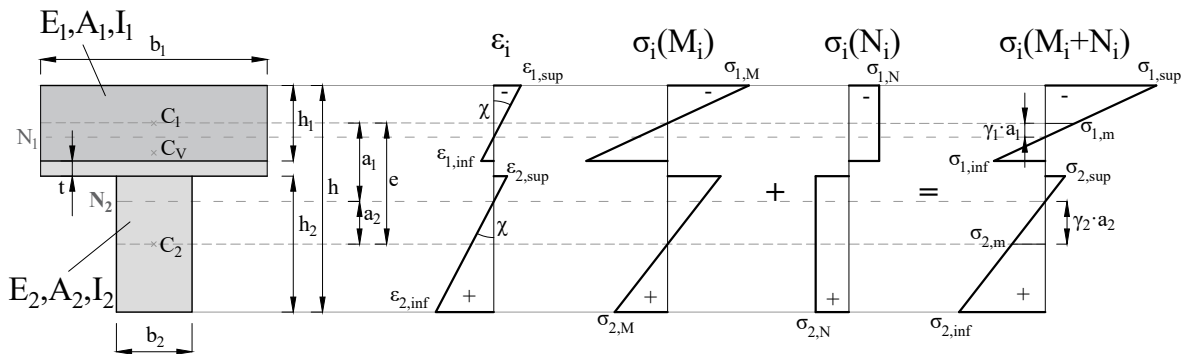
**Fig. 2.7:** Influence of the joint stiffness  $k$  on the effective bending stiffness and display of  $\gamma$ -factor according to different approaches

Fig. 2.7 shows that the  $\gamma$ -values obtained with the reference axis as the neutral axis in one of the components does not correlate with the connection efficiency  $\eta_{C^*}$ . The  $\gamma$ -values obtained with those two approaches cannot be taken as a factor which directly indicates the connection efficiency of the system. For the numeric example plotted in Fig. 2.7 which has a large timber cross-section and small concrete cross-section, the  $\gamma$ -values obtained with the commonly used approach by Möhler (timber as reference) show a very different progression. The  $\gamma$ -values obtained with the approach by Boccadoro (concrete as reference) shows a different curve. Only the approach by Stüssi and Dubas (centroidal axis as reference) correlates with the connection efficiency. Therefore, a  $\gamma$ -factor obtained with the centroidal axis of the composite cross-section is a direct indicator for the connection efficiency.

Although the Stüssi approach is more straightforward and a direct indicator for connection efficiency, the approach by Möhler has been established in research [6] and implemented in Eurocode 5 [21]. The majority of further research took the Möhler  $\gamma$ -method as basis. For example, the extended  $\gamma$ -method model to assess for the long-term behaviour developed by Schänzlin [138] was calibrated on the  $\gamma$ -factor obtained with the Möhler approach. It is therefore recommended to use the Möhler approach and determine the  $\gamma$ -factor according to equation 2.1 and the distances  $a_1$  and  $a_2$  according to equations 2.5 and 2.6 respectively. However, the other two approaches to obtain the  $\gamma$ -factor can be used equally for short-term investigations and turn out to be useful for some applications (see Chapter 6 and Appendix C). In this thesis, the calculations are by default based on the  $\gamma$ -method as developed by Möhler with the neutral axis in timber as the reference axis.

- **Calculation of strains and stresses**

Fig. 2.8 shows the strains  $\varepsilon$  and axial stresses  $\sigma$  in a composite cross-section subjected to a positive bending moment  $M$  as in a simple beam.



**Fig. 2.8:** Axial strains and stresses in a composite cross-section

The curvature  $\chi$  of the cross-section is:

$$\chi = \frac{M}{EI_{eff}} \quad (2.24)$$

Subsequently, the strains at the top edge  $\varepsilon_{i,sup}$  and at the bottom edge  $\varepsilon_{i,inf}$  of the component  $i$  ( $1 = \text{concrete}$  and  $2 = \text{timber}$ ) are determined from the curvature  $\chi$  and the respective distance to the neutral axis:

$$\varepsilon_{1,sup} = \chi \cdot \left( \frac{h_1}{2} + \gamma_1 \cdot a_1 \right) \quad (2.25)$$

$$\varepsilon_{1,inf} = \chi \cdot \left( \frac{h_1}{2} - \gamma_1 \cdot a_1 \right) \quad (2.26)$$

$$\varepsilon_{2,sup} = \chi \cdot \left( \frac{h_2}{2} - \gamma_2 \cdot a_2 \right) \quad (2.27)$$

$$\varepsilon_{2,inf} = \chi \cdot \left( \frac{h_2}{2} + \gamma_2 \cdot a_2 \right) \quad (2.28)$$

The total axial stresses  $\sigma$  are:

$$\sigma_{i,sup} = E_i \cdot \varepsilon_{i,sup} \quad (2.29)$$

$$\sigma_{i,inf} = E_i \cdot \varepsilon_{i,inf} \quad (2.30)$$

The axial stresses  $\sigma$  can be divided into a part due to internal normal forces  $\sigma_i(N_i)$  and a part due to internal bending moments  $\sigma_i(M_i)$ :

$$\sigma_i(N_i) = \frac{M}{I_{eff}} \cdot n_i \gamma_i a_i \quad (2.31)$$

$$\sigma_i(M_i) = \frac{M}{I_{eff}} \cdot n_i \frac{h_i}{2} \quad (2.32)$$

The maximum shear stress in timber  $\tau_{2,max}$  is:

$$\tau_{2,max} = \frac{V}{2 \cdot I_{eff}} \cdot \left( \gamma_2 n_2 a_2 + \frac{h_2}{2} \right)^2 \quad (2.33)$$

The shear stress in the composite joint  $\tau_v$  is:

$$\tau_v = \frac{V \cdot S_i}{I_{eff} \cdot b_2} \quad (2.34)$$

with the static moment  $S_i$ :

$$S_i = \gamma_i n_i a_i A_i \quad (2.35)$$

$$S_1 = S_2 \quad (2.36)$$

Equations 2.31, 2.32, and 2.34 show the influence of the connection stiffness. The higher the connection stiffness, the more force is transferred via the internal normal forces and the joint is

subjected to higher shear stress. The lower the connection stiffness, the more force is transferred via bending and the joint is less stressed.

### 2.2.3 Detailed description of the strut-and-tie model

A strut-and-tie model consists of an upper chord representing the concrete section, a lower chord representing the timber section, and the connection between these chords. There are several different modelling approaches for the connection. Bergfelder [4] developed a Vierendeel beam with the vertical struts at the location of the connectors and the connection stiffness defined by their connection to the chords. Kneidl & Hartmann [85] use a truss system with vertical struts modelled as hinged beam element at the position of the connectors and the axial stiffness of the diagonals simulating the connection stiffness. The most commonly used strut-and-tie model in Switzerland is the model developed by Rautenstrauch [127; 58]. In this model, the connection is implemented by a multitude of vertical elements along the span. Where no connection is assumed, the vertical element is a hinged beam element with infinite axial, shear, and bending stiffness. At the position of the connectors, the vertical element consists of two clamped lever arms meeting in a moment hinge at the level of the composite joint between the two chords. Fig. 2.9 shows an example of a strut-and-tie model for a TCC beam with notches as described in [92].

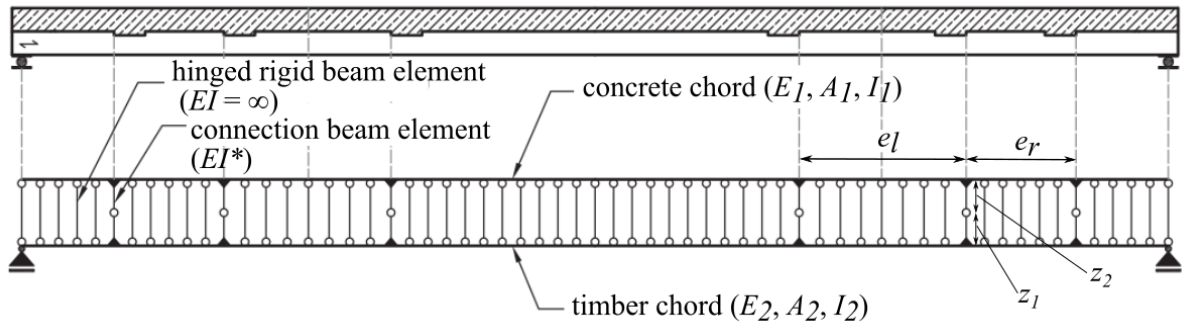


**Fig. 2.9:** Example of a strut-and-tie model for a TCC beam with notches, adapted from [92]

The equivalent bending stiffness of the connection element  $EI^*$  is defined by the length of the two lever arms and the slip modulus  $K$ :

$$EI^* = \frac{K}{3} \cdot (z_1^3 + z_2^3) \quad (2.37)$$

with

$$z_1 = \frac{h_1}{2} \quad (2.38)$$

$$z_2 = \frac{h_2}{2} \quad (2.39)$$

The stiffness of the chords can be taken into account with the distance of the connector to its left and right neighbour ( $e_l$  and  $e_r$ ), the material properties, and the dimensions of the chords:

$$EI^{**} = \frac{z_1^3 + z_2^3}{\frac{3}{K} - \frac{e_l^3 + e_r^3}{2 \cdot (e_l + e_r)^2} \cdot \left( \frac{z_1^3}{E_1 I_1} + \frac{z_2^3}{E_2 I_2} \right)} \quad (2.40)$$

Fig. 2.10 shows the influence of the distance of the connectors on the difference between the equivalent bending stiffness for the connector elements determined by equation 2.37 and equation 2.40 for a planar TCC system with a cross-sectional ratio 1:2 of concrete to timber. For connection systems with regular and small distances between the connectors, the influence of the chord stiffness can be neglected.

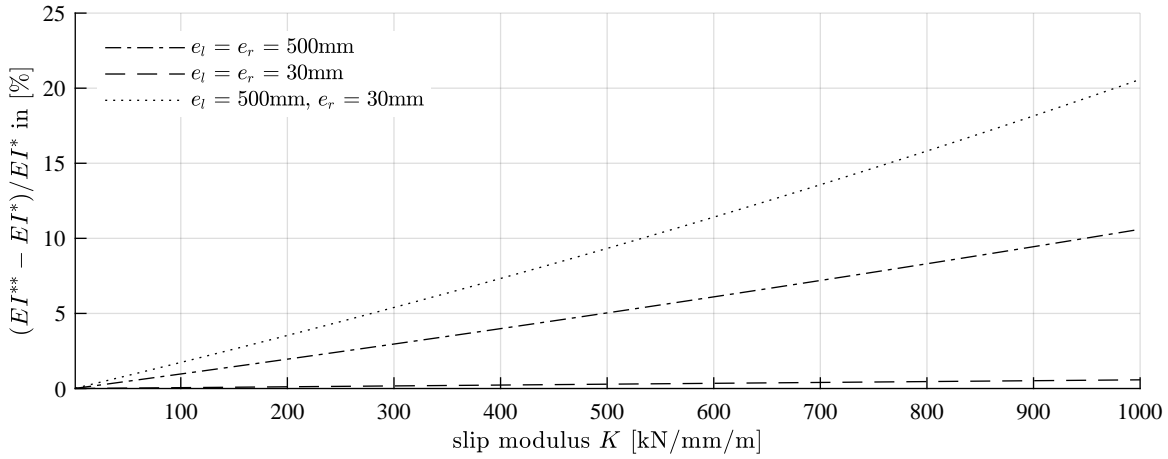


**Fig. 2.10:** Influence of connector distances on the equivalent bending stiffness  $EI^*$

The output of the strut-and-tie model are the internal forces and deflections of the concrete chord, the timber chord, and in the individual connectors. The strains and stresses in the components can be read out directly or calculated using the internal forces, depending on the structural analysis software used.

The strut-and-tie model can directly reproduce variable cross-sections or material properties over the span, the exact arrangement, and respective individual stiffness of local connectors as well as the exact loading situation. In addition, any other static systems such as two-span beams or cantilever beams can also be displayed without loss of accuracy. In many structural analysis programs, the design of the reinforcement for the concrete part can also be carried out directly. However, the computational effort for a strut-and-tie model is often not worthwhile in practice for unique systems; likewise, it is cumbersome to carry out parametric studies.

The main advantage of the strut-and-tie model over the  $\gamma$ -method is the correct implementation of local connectors and of the connector distances  $s$ . The state-of-the-art report on the design of TCC structures [31] summarises the parametric studies of different researchers and recommends to use the strut-and-tie model, if the distances between the connectors  $s$  exceed 5% of the span.

## 2.3 Interlocking connection system for composite beams

### 2.3.1 Historical background of interlocking

The interlocking of timber composite beams is known since the Middle Ages and was a common measure to improve the load-bearing capacity and stiffness of timber beams in order to build larger spans for slabs and bridges [55; 69; 71; 72]. Fig. 2.11 shows composite beams with three and five timber parts. Composite beams with three parts consist of one beam with full span below and two parts with half the span length on top. The interlocking joint is arranged at the position of the highest shear stress in the cross-section. The average cross-section height of the lower beam increases towards the middle of the span, where the highest bending moment occurs (Fig. 2.12 top). According to Gottgetreu [55], the interlocking teeth must be worked out as accurately as possible and all surfaces must be planed clean. The lower beam should be slightly bent and the upper beams are slightly shorter than half of the span. When the upper beams are fitted onto the lower beam, they are additionally connected with vertical dowels to prevent uplift. For longer spans, composite beams with five parts were interlocked, consisting of two beams with half the span length below and three beams above (Fig. 2.11 bottom). The lower two beams are connected and act as tension chord. The upper middle beam acts as an additional clamp for the two lower beams under tension. The interlocking of the upper middle beam is therefore not arranged according to the shear distribution in the global beam, but to clamp the lower beams under tension. The shear forces are transferred via compression from the upper middle beam directly to the upper outer beams, and then via interlocking to the lower beams.

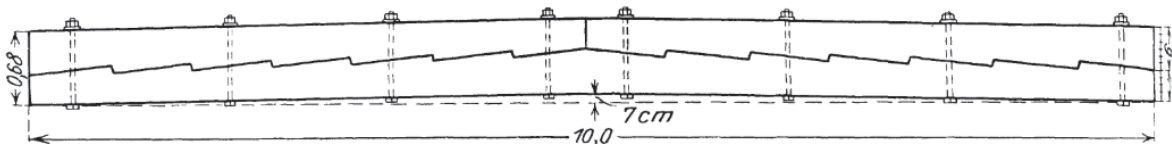


Abb. 143. Dreiteiliger verzahnter Träger.

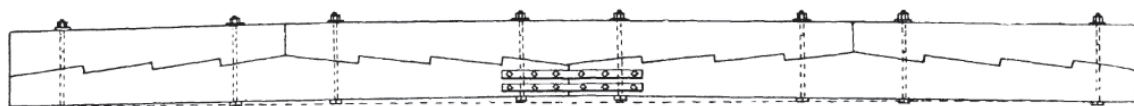


Abb. 144. Fünfteiliger verzahnter Träger.

**Fig. 2.11:** Composite beam consisting of three and five timber components [51]

The structural behaviour of composite beams with interlocking depends on correct processing of the interlocking surfaces, which was often considered one of the most difficult tasks for a carpenter. Small plates of zinc or iron, or wedges of hardwood were often inserted between the interlocking front sides. Those plates or wedges enabled a more uniform contact of the front sides and thus facilitated the difficult realisation of the contact surfaces, enhancing the composite action. The metal or hardwood plates also protected the interlocking front from local compression failure.

The geometry of the interlocking usually followed simple rules: the longest span was 10 m and the total height  $h$  of the composite beam usually  $1/15$  to  $1/12$  of the span. The interlocking notch length was usually  $1 \cdot h$  and the interlocking notch front depth  $1/10 \cdot h$  [51; 132].

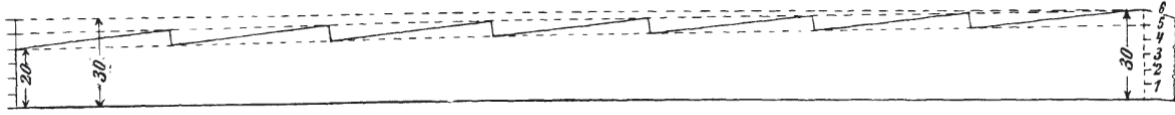


Abb. 149. Austeilung der Zähne des verzahnten Trägers.

**Fig. 2.12:** Geometry of interlocking notches in [cm] [51]

The composite action of such interlocked composite beams was usually considered by reducing the section modulus  $W$  by 15% for composite beams made of two parts and by 35% for composite beams made of three parts [132]. The connection behaviour of the interlocking connection was tested by Rug et al. [132] in push-out and bending tests as part of a restoration project of a church built in 1740.

With the increasing availability of steel and steel dowels, dowelled composite beams were more and more preferred due to their easier production and less material waste. At the end of the 19th century, the usage of interlocking for composite beams is already considered too complicated and thus rarely applied or reported. Later literature in timber engineering no longer mentions the interlocking technology and instead focuses on dowelled beams.

Interlocking or indented notches as a shear connection system for TCC are first mentioned in the patent of Schaub [140]. Schaub stated the need of “kerfed, indented, or perforated” surfaces for both timber and concrete to eliminate the longitudinal relative displacements. He suggested to arrange the indentations inclined to the transverse axis as shown in Fig. 2.13 of the beam to achieve a lasting contact even with strong timber swelling or shrinkage.

Richart and Williams [129] performed 4-point bending tests with 3.0 m span with “sloped daps” of 2.5 cm depth and 15 cm length, with and without additional “spikes” as shown in Fig. 2.14. The timber element was similar to the *PlusMinus* system [78] with lamellas of alternating height. The tests showed a low connection stiffness and low load-bearing capacity for the specimens without spikes. The specimens with spikes showed a significantly higher connection stiffness and also higher failure loads. The relevant findings of these 4-point bending tests on TCC slabs are summarised in Chapter 4.1.

Natterer and Hoefft [120] also show interlocking as a possible connection system for TCC (see Fig. 2.15). However, they do not recommend to use the illustrated interlocking system for TCC. They generally suggest a separation of timber and concrete to avoid unpleasant side effects like discoloration of the timber and damage to the concrete during hydration. The separation should be performed by a timber interlayer, which can be used as formwork in the investigated linear slab system. In the case of interlocking, however, the concrete should be casted directly onto the timber to get the required connection stiffness. Additional adhesives are mentioned to strengthen the connection and to protect the joint surfaces. The interlocking



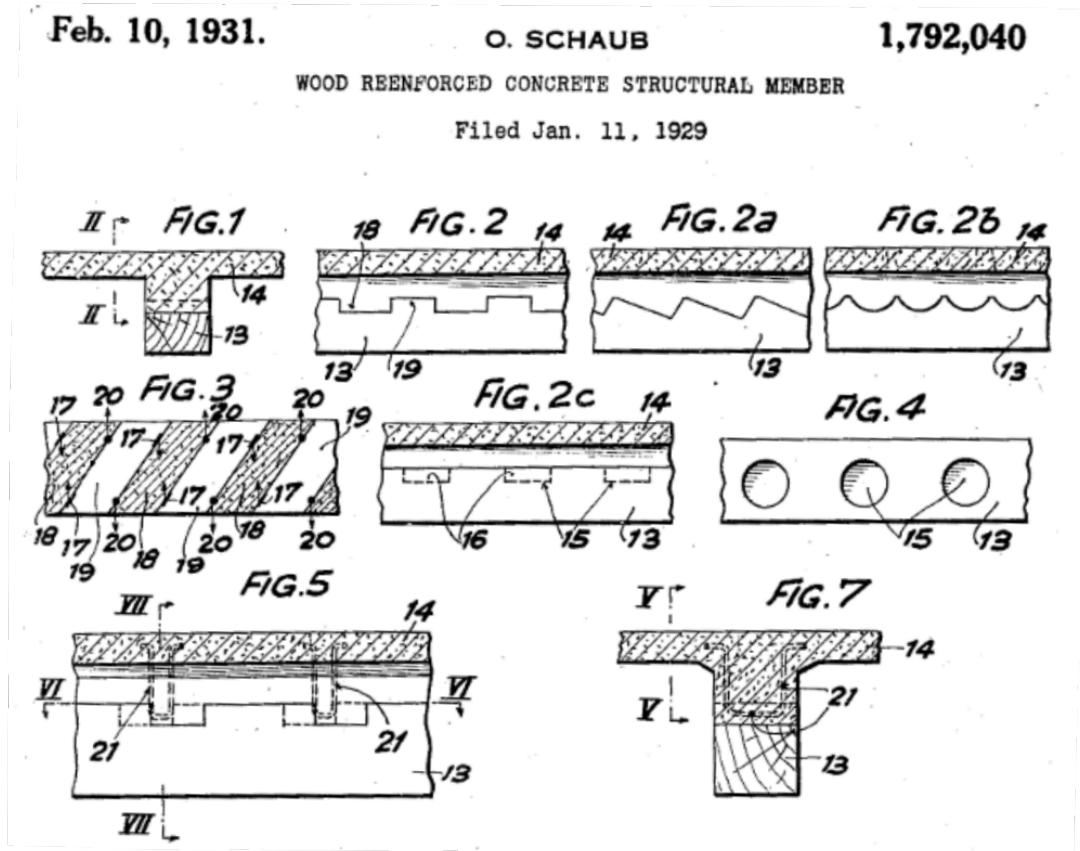


Fig. 2.13: Indented notches for TCC (FIG. 2a) in the patent of Schaub 1929/1931 [140]

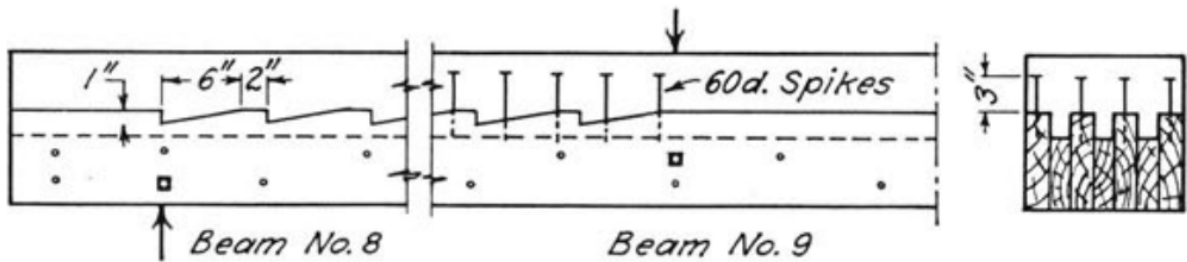


Fig. 2.14: Indented notches for TCC in the studies of Richart and Williams 1943 [129]

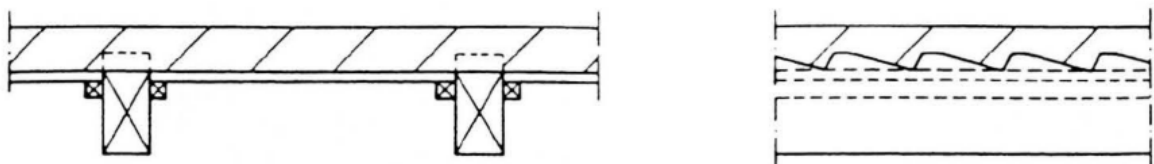


Fig. 2.15: Indented notches for TCC in the research report of Natterer & Hoeft 1987 [120]

connection is not recommended due to possible loss of contact over time regarding the different

shrinkage behaviour of the components. In addition, the notches protrude into the concrete cross-section and are thus statically not beneficial. They conclude that interlocking should only be implemented in TCC if the structural safety of the slab can be achieved without composite action and design constraints do not allow other connection systems.

### 2.3.2 Notched TCC connections

Notches are milled cut-outs in the timber cross-section. In TCC slabs, the concrete is casted on top of the timber element and flows into the notches, fills them, and thereby creates a form-fit connection. Notches for TCC were first mentioned in the patent of Schaub [140] (see Fig. 2.13: illustrated in *FIG. 2*, *FIG. 5*, and *FIG. 7*). Notches are the second-most used connection system for TCC after screws and dowels. Notches are usually combined with additional screws or dowels in order to increase ductility and shear resistance, and to prevent uplift of the concrete slab. In research, notches alone and notches combined with screws or dowels represent about a third of the connection systems investigated [31]. In practice, notches are widely used in Switzerland and Germany for slabs in residential and office buildings. Conventional notches have a notch depth of approximately  $t_N = 20$  mm to 40 mm, a notch length of  $l_N = 150$  mm to 400 mm, and the angle of the front notch is vertical ( $\alpha = 0^\circ$ ) or slightly inclined outwards of the notch ( $\alpha > 0^\circ$ ). The concrete in the notch can be reinforced to improve the shear resistance of the concrete notch [60]. Notched connections in TCC show a good balance between production simplicity and connection efficiency. Usually, notched connections show a high connection stiffness and high load-bearing capacity, but brittle failure (see also Fig. 2.3).

### 2.3.3 Micro-notches

The concept of micro-notches as shown in Fig. 2.16 was developed during a master thesis at ETH Zurich in 2015 [119]. A parametric study was carried out regarding the influence of the number and geometry of conventional notches for planar TCC with BST elements. The study showed significant improvements if the number of notches was increased, the notch depth decreased, and the shape of the notches was altered from rectangular to diagonal indentations.

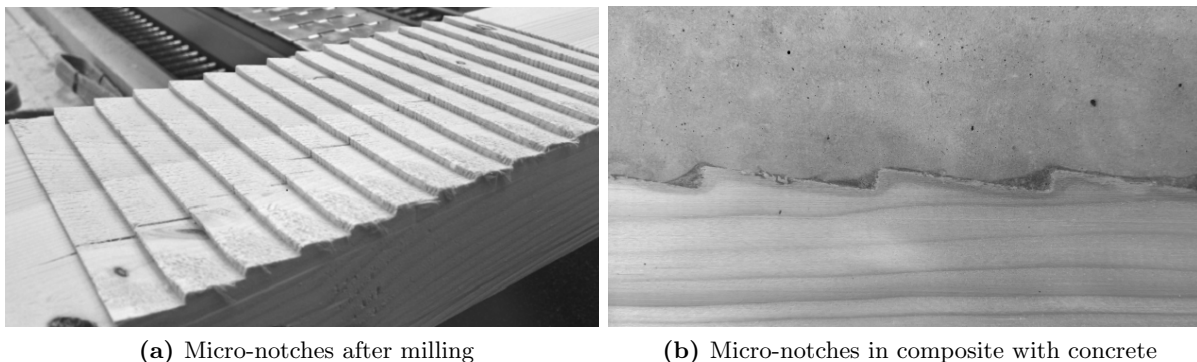


**Fig. 2.16:** Micro-notches in a BST element tested at ETH in the course of local shear tests

As a first point, the shear transmission via a multitude of notches is almost continuous and therefore beneficial. Conventionally, notches are arranged in small numbers near the supports and locally concentrated forces occur at the notch ends. These concentrated forces must be transferred to the concrete as tension or shear forces and can lead to a local crack in the concrete at the notch end [8]. For this reason, screws or dowels are used as an additional connector to take these local forces. In recent years, it has been repeatedly proven that these screws are not necessary [92; 110]. In practice, however, screws are still used for fear of uplift.

As a second point, a decreased notch depth proved to be an advantage if combined with a multitude of notches. The notch depth of conventional, local notches is usually chosen in the range of 20 mm to 30 mm and a higher notch depth correlates with a higher connection stiffness [110; 93]. However, the notch depth also causes a moment of eccentricity due to the resulting shear force that acts approximately in the middle of the notch front [8; 46]. The moment of eccentricity leads to tensile stresses perpendicular to the grain at the notch front. In combination with shear stresses, tensile stresses perpendicular to the grain represent a very unfavourable stress situation in timber. Smaller notch depths decrease this moment of eccentricity and the subsequent stresses perpendicular to grain. In terms of production, many notches with small depths save a considerable amount of milling time and volume compared to a few notches with large depths. In addition, the timber cross-section is less weakened by the smaller milling depths, which have a positive effect on the stiffness and load-bearing capacity of the timber element and on the fire safety of the slab.

As a third point, the indented shape of the notches optimises the available length to take up the shear force and the eccentricity moment while maximising the number of notches. The indentation in turn has a disadvantage for the design, since the notch can thus only transfer shear stresses in one direction - namely through the notch front facing in the opposite direction to the shear flow. On the other hand, the indentation does not clamp the concrete compared to rectangular notches and could therefore lead to less constraint during concrete shrinkage.

The in these ways modified notches were called micro-notches due to the small notch depth. In reality, they resemble less the traditional notches, but rather the historical interlocking. Interlocking was outdated because of its difficult craftsmanship by hand. Modern CNC technologies offer new possibilities in the production of timber elements with regard to precision, speed, and automatisisation, allowing again for an economically competitive use of this type of connection.



# Chapter 3

## Local behaviour of micro-notches

### 3.1 Introduction and literature review

#### 3.1.1 Overview

The first step to develop the micro-notch concept and to determine its connection properties was to separate the connection from the global structural system and to investigate its local connection properties in shear tests. Shear tests consist at least of two composite parts and the connection in the composite joint. The goal of local shear tests is to test the connection by pure shear, determine the failure load  $F_{max}$ , and the relation between the applied load  $F$  and the relative slip between the composite parts  $u$ . The slope of the load-slip curve represents the slip modulus  $K$  as a measure of the connection stiffness. Fig. 3.1 shows four shear test setups commonly used in TCC research: the vertical symmetric push-out test [129; 126; 169; 100; 29; 57; 110; 153; 167; 92; 115], the vertical asymmetric push-out test [64; 163; 2; 24; 19; 43; 102; 26], the inclined push-out test [90; 144], and the horizontal slip-block test [47; 99; 53; 9]. The advantages and disadvantages of those different test setups are often discussed in research [99; 53; 144].

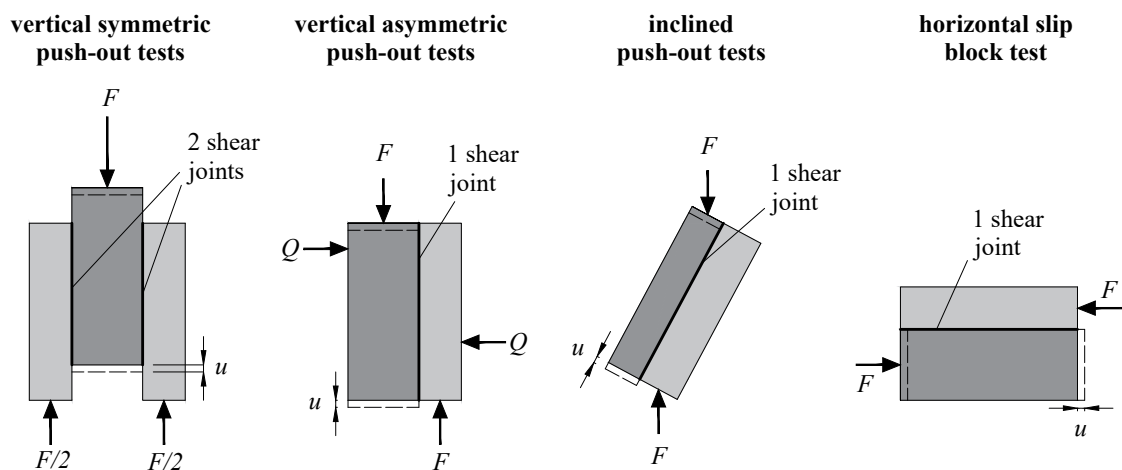
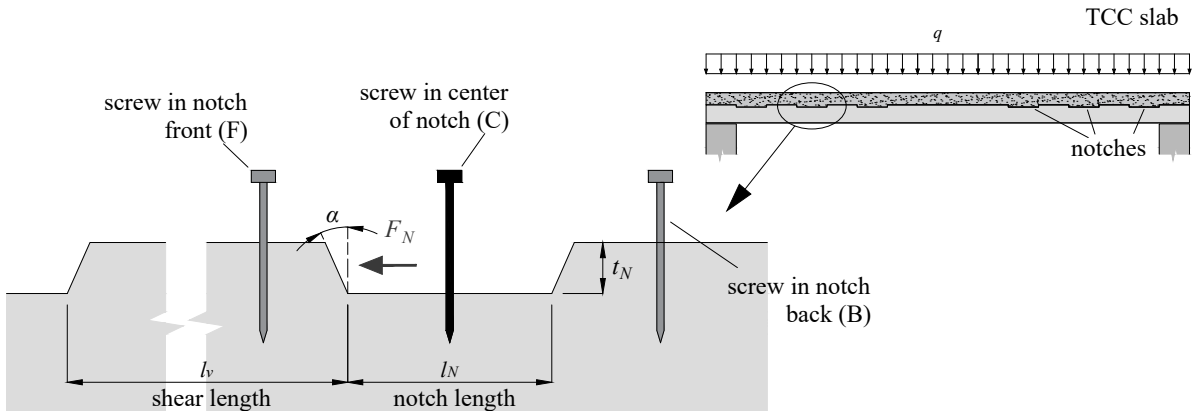


Fig. 3.1: Different test setups for shear tests

In this study, vertical symmetric push-out tests with two composite joints were conducted. This test setup has the advantage of symmetry, so that eccentricity moments can be largely avoided. The force offset between load introduction and supports generates a horizontal force component. These horizontal forces can be compensated by friction in the case of narrow and long test specimens; in the case of compact test specimens, horizontal fixing in the area of the supports is often necessary. Another disadvantage of this test set-up for TCC is the concreting direction, which can be vertical or horizontal, but not perpendicular to the composite joint as in practice. However, this influence can be neglected if the concrete is carefully casted and vibrated.

### 3.1.2 Previous experimental and numerical research

A large variety of local shear tests has been carried out in research for composite systems including TCC to test novel connection systems or assess established connections. Table 3.1 shows a selection of vertical symmetrical push-out tests on TCC specimens with notches and spruce/fir timber which can be found in the literature. These experimental studies have similar test setup dimensions, concrete and timber strength classes, and are all performed on notches with comparable geometries. The width  $b$  of the specimens of all series is around 200 mm with one optional screw. In Michelfelder [110], 500 mm wide specimens with two optional screws were tested. To standardise the results for the slip modulus  $K$  and the failure load  $F_{max}$ , the results of all test series are given for a width of 1 m. The notch front angle  $\alpha$  is the angle between the notch front and a line perpendicular to the specimen axis: a vertical notch front has an angle  $\alpha = 0^\circ$ . In practice, notch front angles are often reclined outwards from the notch  $\alpha > 0^\circ$  (as shown in Fig. 3.2), but can also be inclined into the notch  $\alpha < 0^\circ$  (undercut notch).



**Fig. 3.2:** Convention for notches used in this thesis

Additionally, Table 3.2 lists the local shear experiments conducted by **Rug** [132] regarding the historical interlocking for timber to timber beams as described in Chapter 2.3.1. No studies are known regarding the local load-bearing behaviour of interlocking (as indentations) between timber and concrete so far.

**Tab. 3.1:** Literature selection of experimental symmetric push-out test series for TCC with notches and spruce/fir timber. Every row corresponds to one test configuration.

Parameters altered in relation to the reference configuration are highlighted in gray .

source	concrete strength class	timber strength class	notch length	notch depth	shear length	notch front angle	screws/dowels <sup>a</sup>	no. of specimens	slip modulus	failure load
			$l_N$ [mm]	$t_N$ [mm]	$l_v$ [mm]	$\alpha$ [°]		$n$	$K$ [kN/mm/m]	$F_{max}$ [kN/m]
Zöllig [169]	B35/25 <sup>b</sup>	?	152	30	374	+14	-	3	631	(1081) <sup>c</sup>
	B35/25 <sup>b</sup>	?	177	30	362	+8	-	3	681	(1094) <sup>c</sup>
Grosse [57]	C35/45	C24	200	20	250	-10	-	5	719	568
	C35/45	C24	200	20	250	0	-	3	(1462) <sup>d</sup>	610
	C35/45	C24	200	20	250	+10	-	3	(1696) <sup>d</sup>	591
Michelfelder [110]	C20/25	C16	200	20	250	0	C <sup>e,i</sup>	1	852	866
	C20/25	C16	200	20	250	0	C <sup>f,i</sup>	2	842	760
	C20/25	C16	200	20	250	0	C <sup>g,i</sup>	2	810	819
	C20/25	C16	200	20	250	0	C <sup>h,i</sup>	3	816	829
	C20/25	C16	200	20	250	0	B <sup>e,i</sup>	2	884	786
	C20/25	C16	200	20	250	+45	C <sup>e,i</sup>	2	135	73
	C20/25	C16	200	20	150	0	C <sup>e,i</sup>	2	543	557
	C20/25	C16	200	40	250	0	C <sup>e,i</sup>	2	1424	1187
	C20/25	C16	200	20	250	0	B <sup>e</sup>	3	903	615
	C20/25	C16	200	20	250	0	C <sup>h</sup>	3	748	706
	C20/25	C16	200	20	250	0	-	3	953	821
	C12/15	C16	200	20	250	0	C <sup>e</sup>	3	921	542
Simon [153]	C25/30	GL28	200	20	250	+10	-	4	737	588
Kudla [92]	C30/37	GL24	160	20	300	0	C <sup>j</sup>	7	1372	545
	C30/37	GL24	120	20	300	0	C <sup>j</sup>	3	1571	600
	C30/37	GL24	200	20	300	0	C <sup>j</sup>	3	1971	585
	C30/37	GL24	160	20	300	0	-	4	1629	510
	C30/37	GL24	200	20	300	0	F <sup>j</sup>	3	2816	660
Mönch [115]	C30/37	GL24	160	20	160	0	C <sup>j</sup>	3	908	946
	C30/37	GL24	*160	20	160	0	C <sup>j</sup>	3	781	922.5
	C30/37	GL24	160	20	300	0	C <sup>j</sup>	3	1223	1033
	C30/37	GL24	*160	20	300	0	C <sup>j</sup>	3	1287	1097
Loebus [101]	C20/25	CLT <sup>  </sup>	200	20	250	0	-	2	371	760
	C20/25	CLT <sup>⊥</sup>	200	20	250	0	-	2	125	83

Footnotes on next page

**Tab. 3.2:** Literature on symmetric push-out tests for interlocking (historical indentations). Every row corresponds to one test configuration.

	middle part	side parts	notch length	notch depth	shear length	notch front angle	screws/dowels	no. of specimens	slip modulus	failure load
source			$l_N$ [mm]	$t_N$ [mm]	$l_v$ [mm]	$\alpha$ [°]		$n$	$K$ [kN/mm/m]	$F_{max}$ [kN/m]
Rug [132]	pine	pine	800	36	180	0	-	12	179	~ 900
	pine	pine	?	18	?	0	-	3	147	?

Footnotes for Tables 3.1 and 3.2:

<sup>a</sup> position of the screw: C = center, B = back, F = as reinforcement of the notch front, see also Fig. 3.2

<sup>b</sup> corresponds approximately to the current strength class C25/30

<sup>c</sup> shear failure of timber prevented by test setup

<sup>d</sup> concrete quality uneven, stiffness results invalid according to [57]

<sup>e</sup> screw  $\varnothing 16$  mm, <sup>f</sup> screw  $\varnothing 12$  mm, <sup>g</sup> screw  $\varnothing 12$  mm prestressed, <sup>h</sup> wood construction screw  $\varnothing 12$  mm

<sup>i</sup> screw with sheathing tube allowing prestressing

<sup>j</sup> self-drilling washer head screw  $\varnothing 8$  mm

\* lying lamellas

<sup>⊥</sup> perpendicular to grain

**Richard et al.** [128] and **Sikora et al.** [152] investigated a similar form to historical interlocking in TCC with very small, inclined notches. They performed vertical symmetric and asymmetric inclined push-out tests on small notches as TCC connection system. Five different geometry configurations were tested with notch depths of 5 mm, various inclinations, and varying distances between the notches. Larch from Northeastern China was used for the timber part and three types of concrete mixtures for the concrete part. Failure was observed exclusively in the concrete notches. Since shear failure of the timber was prevented by the test set-up, the results for the shear resistance are not valid. The load-slip behaviour showed curves with widely dissimilar appearance even in one configuration and thus huge scattering regarding the connection stiffness. Therefore, the results of this study are not considered in this thesis.

In addition to the results from experimental tests summarised in Tables 3.1 and 3.2, there is a variety of numerical local shear tests, often as validation to the experimental series:

**Grosse** [57] performed push-out tests to investigate different angles of the notch front ( $\alpha = -10^\circ, 0^\circ$ , and  $10^\circ$ ). He was able to reconstruct the failure modes in a FE model. He observed a distinct peak of compression stresses and compression failure at the top of the timber notch for the angle leaning inwards the notch ( $\alpha = -10^\circ$ ). He also observed a distinct shear stress peak at the bottom of the timber notch and reported timber shear failure of individual lamellas. However, he found that both timber and concrete exhibit a sufficiently ductile behaviour subjected to



compression and that this local stress peaks are plasticised onto the whole notch front area. He concluded that both experimental and numerical investigations show no significant influence of the notch front angle on the load-bearing behaviour.

**Michelfelder** [110] validated the results of some of her experimental push-out series in a FE-model. She found that the slip modulus  $K$  tends to be underestimated by the FE-model. Also, she proved in both experimental and numerical investigations that additional screws are not necessary. She also investigated the progression of shear stress close to the notch and confirmed findings from previous studies [154; 25] that the shear stress in timber approach zero after a length of approximately 8 times the notch depth.

**Kuhlmann and Aldi** [95; 94] built numerical FE models for the push-out tests performed by Grosse [58], Michelfelder [110], and Simon (former Döhner) [153]. They found good agreement of the failure modes in the experiments and the simulations. The FE model, however, overestimated the connection stiffness and the load-bearing capacity for all test series.

**Kudla** [93] used a FE model to numerically investigate notched TCC connections with different notch depths and the position of optional screws. Elasto-plastic material models were used in the model to retrace the linear elastic, nearly ideal plastic load-slip behaviour of the notches observed in the experiments. The model was verified with experimental data [92] and then used for parametric studies. In both experimental and numerical investigations, she observed two failure states: At first, compression failure in timber occurred followed by plastic deformations. Second, at a certain deformation, the timber showed a hardening behaviour and the compressive strength could be increased by 10 %, reaching a plateau. She also observed in experiments and could reconstruct in the FE model the formation of a crack in the concrete at the upper end of the notch front. In a parametric study, she found that the variation of the notch length in the range of 160 mm to 200 mm does not have an influence on the connection stiffness or the load-bearing capacity. The increase of the notch depth showed a positive correlation with connection stiffness and load-bearing capacity up to a notch depth of 30 mm.

### 3.1.3 Mechanical models for notched TCC connections

The mechanical analysis of the local behaviour of timber and concrete in notches and the behaviour of TCC connection systems has been examined in many studies. Detailed models of the local timber and concrete behaviour can be found in [8; 136; 144].

Timber and concrete in TCC slabs are subjected to different stresses. In the notch, stresses occur due to the shear transfer in the joint, direct vertical loads from the self-weight of the concrete and the floor construction, and direct shear transfer into the support. The Technical Specification [30] lists four verifications for notched connections: a) shear of concrete, b) crushing of concrete, c) shear of timber, and d) crushing of timber. Fig. 3.3 shows the four failure modes for a rectangular notch with vertical notch front ( $\alpha = 0^\circ$ ). The following paragraphs list the stress states and verifications in the four failure modes, extended by considerations of combined stresses.

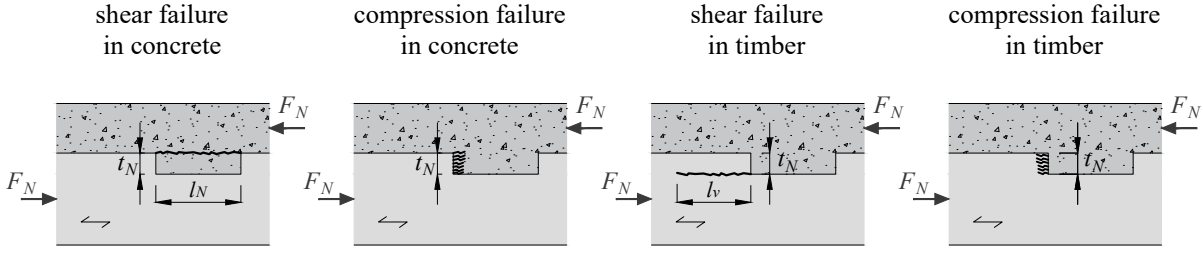


**Fig. 3.3:** Failure modes in notched TCC connections according to [30]

a) **Shear failure in the concrete**

Shear failure in the concrete occurs when the shear stresses  $\tau$  exceed the shear strength  $\tau_{1,v}$  of the concrete. The shear stress is given by the shear force on the notch  $F_N$  and the available shear area:

$$\tau = \frac{F_N}{l_N \cdot b_N} \quad (3.1)$$

Additional stresses parallel to the beam axis  $\sigma_x$  or perpendicular to the beam axis  $\sigma_y$  in combination with the shear stress  $\tau_v$  can lead to a reduced load-bearing resistance in concrete. Boccardo [8] suggests to consider the combined stress state with a modified version of the failure criterion of COULOMB [104]. The modification includes the additional condition

$$f_{1,t} = \frac{2 \cdot c \cdot \cos \varphi}{1 + \sin \varphi} \quad (3.2)$$

to consider the low tensile strength of concrete  $f_{1,t}$ . This criterion is then more generalised formulated with the envelope curve of MOHR.

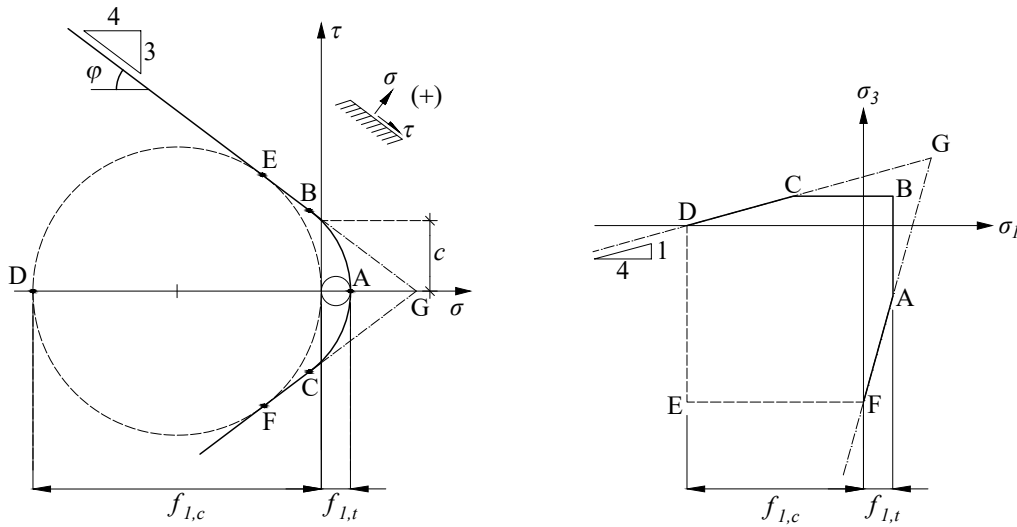


**Fig. 3.4:** Modified MOHR-COULOMB failure criterion for concrete adapted from [80]

The principal stresses  $\sigma_1$  and  $\sigma_3$  as well as the failure criterion result as:

$$\sigma_{1,3} = \frac{\sigma_x + \sigma_y}{2} \pm \sqrt{\left(\frac{\sigma_x - \sigma_y}{2}\right)^2 + (\tau_{xy})^2} \leq f_{1,t} \quad (3.3)$$

b) **Compression failure in the concrete**

Compression failure in the concrete occurs when the axial stresses on the notch front  $\sigma_x$  exceed the compressive strength of the concrete  $f_{1,c}$ . The compressive stress is given by the shear force on the notch  $F_N$  and the area of the notch front:

$$\sigma_{1,x} = \frac{F_N}{t_N \cdot b_N} \quad (3.4)$$

c) **Shear failure in the timber**

Shear failure in the timber occurs when the shear stresses  $\tau$  exceed the shear strength  $\tau_{2,v}$  of the timber. The shear stress is given by the shear force on the notch  $F_N$  and the available shear area:

$$\tau = \frac{F_N}{l_v \cdot b_N} \quad (3.5)$$

The effective shear length  $l_v$  depends on the shear stress propagation in the timber (Fig. 3.5). Frangi [47] considers the whole length of the timber available. Several authors refer to an effective shear length of eight times the notch depth:  $l_v = 8 \cdot t_N$ , which was found by Staudacher [154] in experiments investigating slip joints. This effective length of  $l_v = 8 \cdot t_N$  is then documented in various timber engineering textbooks [39; 25; 66]. As stated above, Michelfelder [110] proved this effective shear length in numerical investigations. Schönborn [144] suggests a shear length of at least  $l_v = 12.5 \cdot t_N$  for the design, which was included in the Technical Specification [30]. An often cited study is the work by Stephan [155] on the shear stress distributions in the timber behind the notch front for different notch front angles. He reported a distinct peak directly behind the notch front and a rapid decrease of the shear stresses with increasing distance to the notch front. Other than often cited, he did not find an effective shear length, but the critical lengths in front of the notch that have an influence on the shear stress peak. For notch front angles of  $0^\circ$ , the maximum shear stress does not increase anymore if the length before the notch is increased above  $l_{crit} = 4.9 \cdot t_N$ . For the value of the peak shear stress he found:

$$\tau_{max} = \frac{\sigma_x}{\pi} \quad (3.6)$$

Additional tensile stresses perpendicular to the beam axis  $\sigma_z$  in combination with the shear stress  $\tau$  can lead to a reduced load-bearing resistance in the timber. In notched connections, vertical tensile stresses occur because of the eccentricity moment generated by the shear force  $F_N$  acting on the middle of the notch front. This phenomenon was idealised by Steurer [156] and is also described by Boccadoro [10]. The decisive tensile

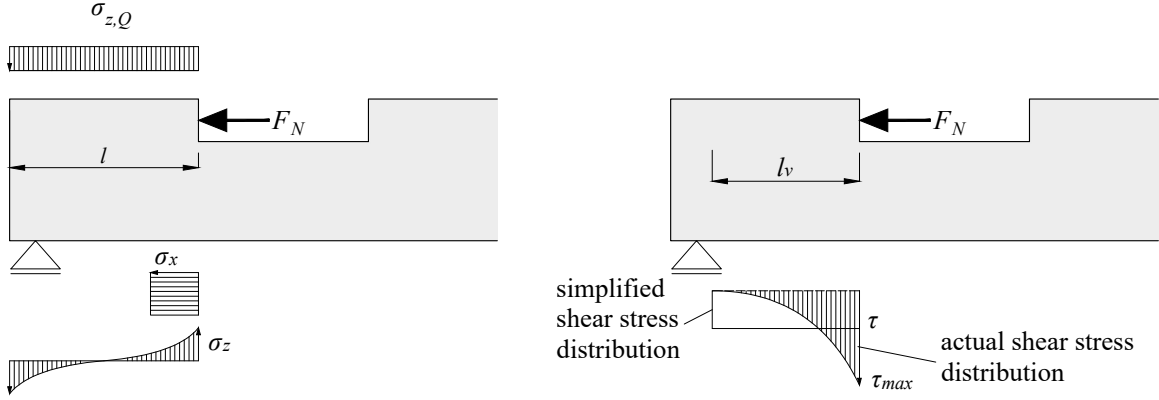


**Fig. 3.5:** Axial stresses  $\sigma_i$  and shear stress  $\tau$  in a timber notch

stress at the notch front can be found with the eccentricity moment  $M_{Ecc}$  and the section modulus  $W_N$ :

$$M_{Ecc} = F_N \cdot \frac{t_N}{2} \quad (3.7)$$

$$W_N = \frac{b_N \cdot l^2}{6} \quad (3.8)$$

$$\sigma_z \approx \frac{M_{Ecc}}{W_N} \quad (3.9)$$

Additional compressive stresses perpendicular to the beam axis  $\sigma_{z,Q}$  result from the self-weight of the concrete, superimposed loads, or from the introduction of the forces into the support (Fig. 3.5). Compressive stresses perpendicular to the beam axis have a beneficial effect on the shear stress state and can increase the load-bearing capacity.

The combination of shear  $\tau$  and compression or tension perpendicular to grain  $\sigma_z$  is verified according to SIA 265 [149] with the strength properties in compression and tension perpendicular to grain  $f_{2,c,\perp}$  and  $f_{2,t,\perp}$ , as well as the shear strength  $f_{2,v}$ :

$$\left( \frac{f_{2,c,\perp} + \sigma_z}{f_{2,c,\perp} + f_{2,t,\perp}} \right)^2 + \left( \frac{\tau}{f_{2,v}} \right)^2 \cdot \left[ 1 - \left( \frac{f_{2,c,\perp}}{f_{2,c,\perp} + f_{2,t,\perp}} \right)^2 \right] \leq 1.0 \quad (3.10)$$

#### d) Compression failure in the timber

Compression failure in the timber occurs when the axial stresses on the notch front  $\sigma_x$  exceed the compressive strength of the timber  $f_{2,c}$ . The compressive strength of the timber strongly depends on the direction of the grain, the compressive strength parallel to grain  $f_{2,c,\parallel}$  is significantly higher than the compressive strength perpendicular to grain  $f_{2,c,\perp}$ . The compressive stress is given by the shear force on the notch  $F_N$  and the area of the notch front:

$$\sigma_{2,x} = \frac{F_N}{h_N \cdot b_N} \quad (3.11)$$

### 3.1.4 Friction and adhesion

The influence of forces due to friction and adhesion between timber and concrete and other mineral top layers was investigated in detail by Lehmann [99]. He quantified the additional shear strength due to these surface contact effects and proposed to take them into account for the design. The value for the shear strength due to adhesion  $f_{j,s}$  was determined in experiments. For a connection of timber to concrete, he found a characteristic shear strength of  $f_{j,s} = 0.42 \text{ N/mm}^2$ . The value for the shear strength due to friction depends on the friction coefficient  $\mu_f$  and the stresses vertical to the composite joint  $\sigma_{j,A,d}$ . His proposal for the shear strength due to adhesion and friction is:

$$f_{j,s,\mu,d} = \frac{f_{j,s} \cdot k_{mod}}{\gamma_M} + \mu_f \cdot \sigma_{j,A,d} \quad (3.12)$$

However, these values strongly depend on the material properties and production conditions. Usually, the contribution of adhesion and friction are not taken into account in the design [88].

### 3.1.5 Models on the determination of the connection properties

The relevant properties of a connection are the shear resistance (load-bearing capacity of the connection system)  $F_{v,R}$ , the connection stiffness described by the slip modulus  $K$ , and the ductility as described in Chapter 2.1.4. The load-slip behaviour of TCC connection systems was studied in detail by Dias [29] in experimental and numerical tests and by fitting different analytical models onto experimental load-slip curves. The load-slip behaviour is often non-linear and there are different approaches on how to determine the relevant connection properties.

#### Determination of the shear resistance

In symmetrical push-out tests, it is generally assumed that the applied force  $F$  on the middle part is equally distributed to the two side parts:

$$F_{joint} = \frac{F}{2} \quad (3.13)$$

The shear resistance of a local connector is then given by:

$$F_{v,R} = F_{joint,max} \quad (3.14)$$

SIA 265 [149] also introduces the yield load  $F_y$  as the turning point of non-linear load-slip behaviour, where the connection stiffness decreases significantly.

In case of a continuous or extensive connection system such as adhesives or to evaluate a smeared shear strength, the shear resistance of the connection  $f_{v,R}$  can be defined by the applied load  $F_{joint}$  and the shear area  $A_{joint}$ :

$$f_{v,R} = \frac{F_{joint}}{A_{joint}} \quad (3.15)$$

### Determination of the slip modulus

The connection stiffness is characterised by the slip modulus  $K$ , which generally describes the slope of the load-slip curve in the linear elastic range. There are different methods to determine the slip modulus  $K$  from experimental data using load-slip curves:

- The method described in SIA 265:2012 [149] is used for timber to timber connections mostly with steel connectors. The slip modulus for the serviceability state  $K_{ser}$  is defined with the terms used in Fig. 3.6 as

$$K_{ser} = \frac{F_y}{w_y} \quad (3.16)$$

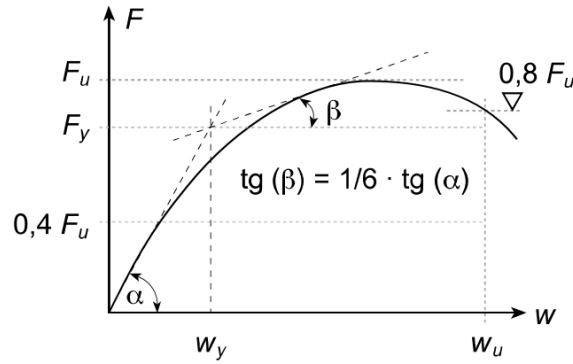


**Fig. 3.6:** Determination of slip modulus  $K$  with slip denoted as “ $w$ ” according to SIA 265 [149]

- DIN EN 26891 [20] defines an initial slip modulus  $k_i$  and an elastic slip modulus  $k_s$  (Fig. 3.7). The definition for  $k_s$  considers and removes the influence of initial slip. This definition of the slip modulus is also part of the Technical Specification [30]. The elastic slip modulus  $k_s$  is defined with the terms used in Fig. 3.7 as:

$$k_s = K_{ser} = \frac{0.4 \cdot F_{est}}{\frac{4}{3} \cdot (v_{0.4} - v_{0.1})} \quad (3.17)$$

Equation 3.17 shows that the slip modulus  $k_s$  depends on the estimated failure load  $F_{est}$ . Depending on the connection system, the load-slip curve can show a bi-linear behaviour with a distinct deformation plateau. In these cases, the determination based on the estimated failure load  $F_{est}$  might lead to inaccurate results. A better accuracy with the curve slope can be found when using the actual failure load  $F_{max}$  [29].

- In some studies, the connection stiffness was determined from the slope between 10% and 40% of  $F_{est}$ :

$$K_s = K_{ser} = \frac{F_{0.4} - F_{0.1}}{u_{0.4} - u_{0.1}} \quad (3.18)$$

- Another approach to find the relevant slope of the load-slip curves is described by Brandner et al. [12] by plotting the load increments and defining the relevant linear elastic area

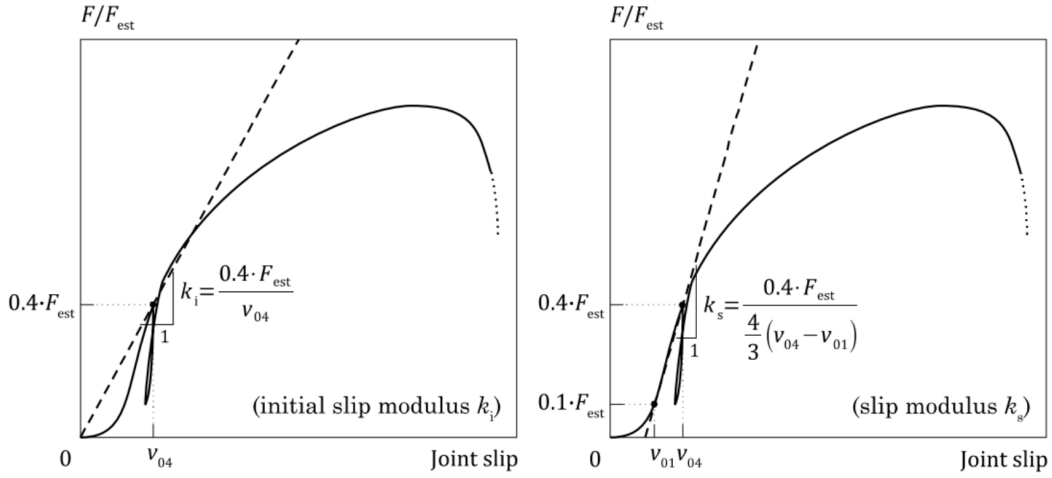


**Fig. 3.7:** Determination of slip modulus  $K$  with slip denoted as “ $v$ ” according to DIN 26891 [20; 123]

graphically as the curve section with constant progression (Fig. 3.8). The slip modulus is then determined as the slope in the load-slip diagram on the length found as relevant in the load increment-slip diagram.

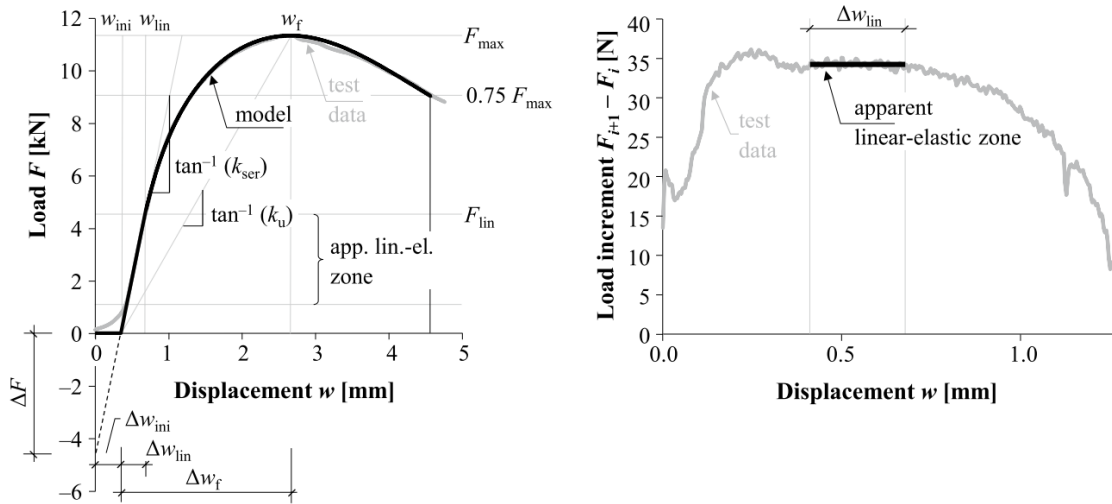


**Fig. 3.8:** Graphic determination of slip modulus  $K$  with slip denoted as “ $w$ ” [12]

Since the system investigated in this research project was developed for the Swiss market, the definition according to SIA 265 was chosen to determine the slip modulus  $K$ . For connection systems with distinct non-linear load-slip behaviour (almost no linear elastic phase), the connection stiffness for the ULS can be found as:

$$K_u = \frac{2}{3} \cdot K_{ser} \tag{3.19}$$

For connection systems with a high stiffness and a distinct linear elastic phase, such as notches or adhesives, the connection stiffness for the ULS does not need to be reduced [29; 110; 93]:

$$K_u = K_{ser} \quad (3.20)$$

### Determination of the ductility

The evaluation of the ductility is defined in SIA 265 [149] for steel connectors such as dowels or screws. The ductility  $D$  is defined as the ratio between deformations at yielding of the connection and at 80 % of the maximum load in the post-peak softening behaviour. The definition with the terms used in Fig. 3.6 is:

$$D = \frac{w_u}{w_y} \quad (3.21)$$

Ductility can also be seen as the dissipated energy, outlined as the fracture energy [5]. The fracture energy corresponds to the area under the load-slip curve: the larger the area, the higher the fracture energy and the corresponding ductility of the connection.

## 3.2 Experimental push-out test series I & II

### 3.2.1 Materials and methods

#### Test setup push-out series I and improved test push-out setup series II

Two series of vertical symmetric push-out tests were performed to assess the connection behaviour of micro-notches. The test setups of both series are shown in Fig. 3.9. The test machine was a universal tension and compression testing machine with two pressure plates. A calotte was installed at the top pressure plate to avoid moment restraints at the load introduction. A steel plate and neoprene rubber layer between calotte and specimen ensure a uniform force application without grinding the surface of the concrete middle parts. The concrete middle part is offset by 5 cm from the timber side parts to enable sufficient displacements. The test setup was altered and improved from the first series (PO1) to the second series (PO2). In push-out series I (PO1), steel profiles and threaded rods with attached load cells were installed as lateral restraints (Fig. 3.9a). The lateral restraints turned out to be a time-consuming setup and had a strong influence on the test results. Due to its high weight, the prepared specimen could only be lifted into the testing machine by forklift. In push-out series II (PO2), the lateral restraints were replaced by belts of elastic bands (Fig. 3.9b). These elastic bands were TheraBands<sup>®</sup> with black color. The color corresponding to a “strength class” [133] and the dimensions of the belts were chosen to simulate the transverse compression forces on the joint usually expected in practice due to superimposed load and live load (see Appendix A). In addition, the specimens in push-out series II were reduced in width by 20% in comparison to the specimens in push-out series I, so they could be lifted by hand, allowing a much faster testing preparation and procedure.



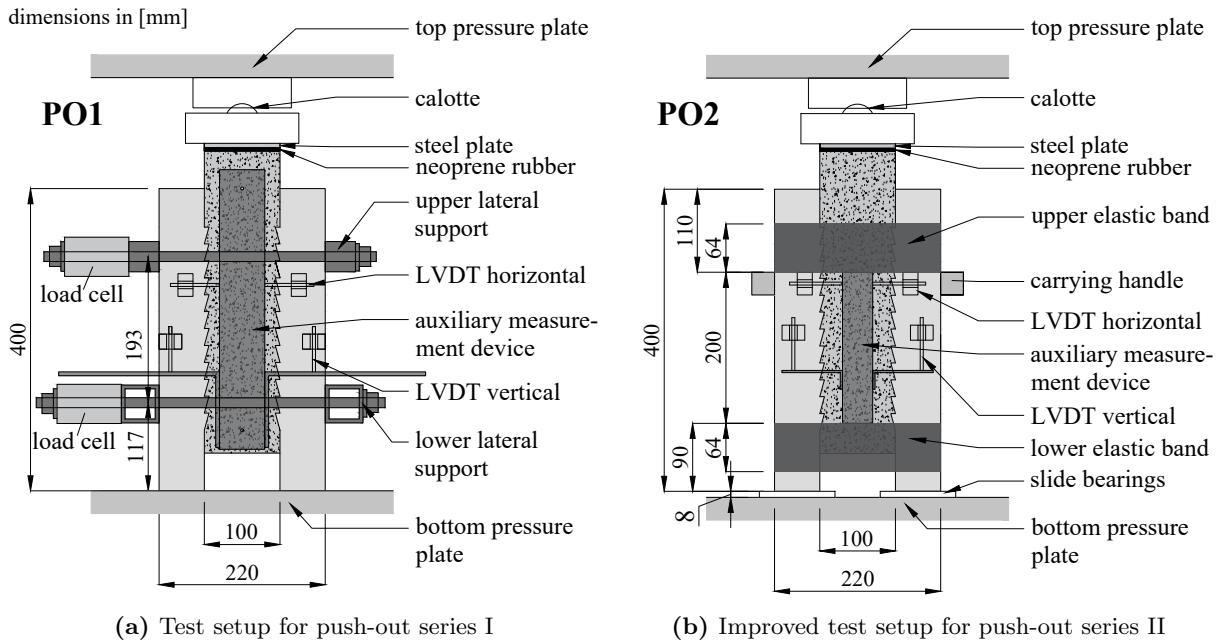


**Fig. 3.9:** Test setups for push-out tests

## Specimens

Fig. 3.10 shows the design and dimensions of the specimens of push-out series I and II. The specimens consist of a concrete middle part and two timber side parts. The two joints are realised with micro-notches on approximately  $270 \text{ mm} \pm 20 \text{ mm}$  of the total of  $350 \text{ mm}$  joint length, depending on the micro-notch geometry. The rest of the joint length is planed evenly. The micro-notches were milled protruding to allow shear failure in the timber. The dimensions of the specimens in push-out series I and II are equal except for the width of the specimen: the timber side elements in series I consist of 5 lamellas of  $40 \text{ mm}$  each and in series II of 4 lamellas of  $40 \text{ mm}$  each. The lamellas are solely connected by kiln-dried beech dowels as it is carried out in practice for BST slabs.

The materials used for the push-out tests were normal-strength concrete and spruce/fir timber lamellas. The specimens were produced in two steps: the production of the timber side parts and milling of the micro-notches in the company of the BST producer as well as the mixing and casting of the concrete at the laboratories at ETH Zurich.

First, the timber side parts were assembled, the lamellas connected by beech dowels, and their surface was planed. Then, the protruding micro-notches were milled by a CNC milling machine using a dovetail tool. The timber sides were then cut to length, combined in pairs, and set in place with the formwork for the concrete. The timber is of strength class C24. The material properties of timber were tested in detail for push-out series II. The average density of the timber was  $458 \text{ kg/m}^3$  according DIN 52182 [33] and the average moisture content was  $12.3\%$  according to DIN 52183 [34]. The average local MOE was  $11812 \text{ N/mm}^2$  determined according to EN 408 [36].

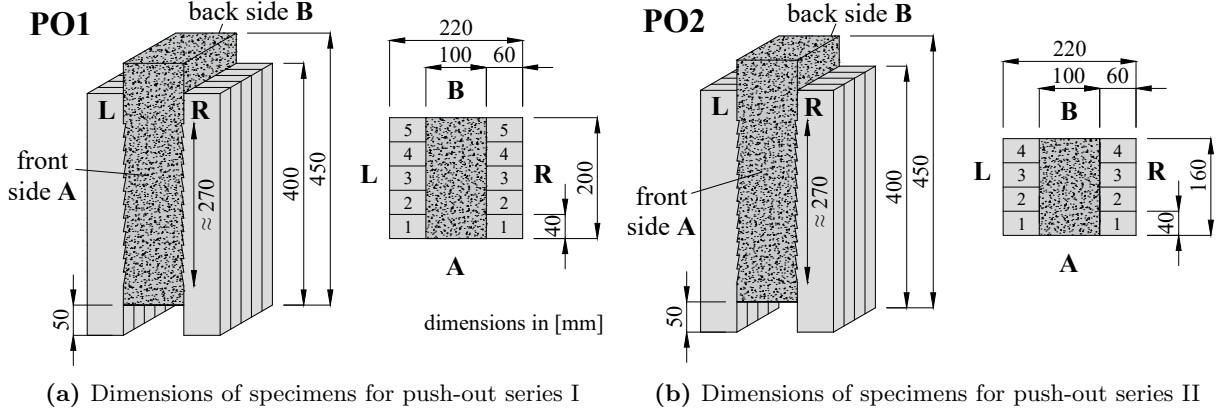


**Fig. 3.10:** Specimens for push-out tests

The concrete mixture was prepared for a concrete strength class C25/30 with maximum grain size 16 mm. No shrinkage reducer was added. Air void content, flow spread, and density of the fresh concrete were determined to assess the quality of the concrete before casting. Concrete samples in form of cubes and cylinders were casted from the same batch as the specimens to assess the properties of the hardened concrete. The specimens were concreted upright like their final position in the test setup (see Fig. 3.10) and vibrated on a vibration table. For series I, the determined concrete strength after 28 d corresponded to strength class C30/37. For series II, the determined concrete strength corresponded to C40/50 with a MOE of  $37\,597\text{ N/mm}^2$ . The concrete qualities were therefore higher than expected in both series I and II.

The configurations tested in the push-out series I & II are listed in Table 3.3. In series I, two different micro-notch geometries were tested. In series II, six different micro-notch geometries were tested. For the reference geometry 4-7.5, three different wood types, three different treatments of the timber surface before concreting, the concrete vibration treatment, and the load to grain direction were tested. All tested parameters are described in detail below:

- The **geometry** of the micro-notch is defined by the notch depth  $t_{MN}$  and the angle of the notch front  $\alpha$ . The opening angle (angle between notch bottom and notch front) is for all specimens  $75^\circ$  due to the geometry of the milling tool available at that time. The specimen geometries are denoted with the notch depth  $t_{MN}$  and the notch front angle  $\alpha$ : configuration 4-2.5 has a notch depth of  $t_{MN} = 4\text{ mm}$ , a notch front angle of  $\alpha = -2.5^\circ$ , and thus a notch bottom angle of  $\beta = 12.5^\circ$ . The reference configuration is the 4-7.5 configuration. In this case, the notch front angle is  $\alpha = -7.5^\circ$  and the notch bottom angle  $\beta = 7.5^\circ$ . Fig. 3.11 shows the six different geometries tested plus the geometry used for the specimen with load direction perpendicular to the grain (PO2 qF).

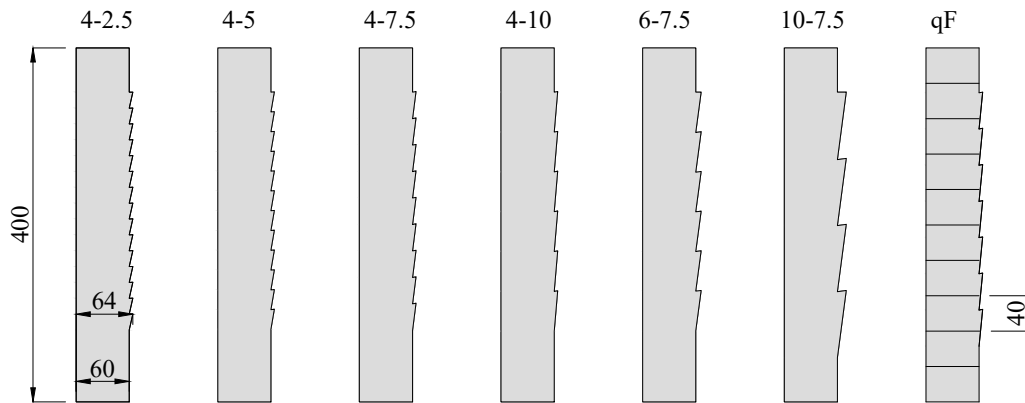


**Fig. 3.11:** Geometries of micro-notches for push-out test series

- The **timber surface** of TCC slabs in practice usually is watered a few hours before concreting. Timber is hygroscopic and can extract the mixing water from the concrete, which can lead to inferior hydration and thus to inferior strength development in the concrete. Two configurations with three specimens each were tested with different treatment: no watering of the timber surface (PO2 oW) and treatment of the timber surface with a hydrophobic primer (PO2 hP). The hydrophobic primer was developed by Kostic [87] and consists of ethanol, ammonia hydroxide, and tetraethyl orthosilicate.
- The **wood species** used for BST elements in Switzerland are usually made from spruce (*Picea abies* Karst.) and/or from the mechanically and optically very similar wood of the silver fir (*Abies alba* L.). One specimen was produced out of European beech (*Fagus sylvatica* L.) and one out of European ash (*Fraxinus excelsior* L.).
- The concrete was carefully **vibrated** and compacted with a vibrating table for all test specimens. For one specimen (PO2 nv), the concrete was simply filled into the formwork and neither compacted nor vibrated.
- The **load direction** is usually perpendicular to the notch front, meaning that the load direction is parallel to the grain of the wood. One configuration (PO2 qF) with three specimens with load direction perpendicular to the grain was tested. The timber lamellas for these specimens were stacked vertically to obtain this grain direction. The geometry was chosen so that no notch fronts occurred at the transition between the lamellas (Fig. 3.11).

**Tab. 3.3:** Specimen configurations of push-out series I & II. Every row corresponds to one test configuration.

Parameters altered in relation to the reference configuration are highlighted in gray

	timber	timber treatment <sup>a</sup>	direction of grain	concrete age	concrete treatment <sup>b</sup>	specimen width	notch depth	notch length	front angle	bottom angle	notches per joint	no. of specimens
name				[d]		$b$ [mm]	$t_{MN}$ [mm]	$l_{MN}$ [mm]	$\alpha$ [°]	$\beta$ [°]	$n$ [-]	[-]
PO1 4-10	C24	w		28	v	200	4	45	-10	5	6	3
PO1 4-5	C24	w		29	v	200	4	22.3	-5	10	12	3
Total specimens in push-out series I												<b>6</b>
PO2 4-10	C24	w		30	v	160	4	45	-10	5	6	3
PO2 4-7.5	C24	w		29	v	160	4	29.9	-7.5	7.5	9	3
PO2 4-5	C24	w		30	v	160	4	22.3	-5	10	12	3
PO2 4-2.5	C24	w		33	v	160	4	17.9	-2.5	12.5	15	3
PO2 6-7.5	C24	w		33	v	160	6	44.8	-7.5	7.5	6	3
PO2 10-7.5	C24	w		34	v	160	10	74.6	-7.5	7.5	4	3
PO2 oW	C24	-		36	v	160	4	29.9	-7.5	7.5	9	3
PO2 hP	C24	hP		36	v	160	4	29.9	-7.5	7.5	9	3
PO2 Bu	beech	w		34	v	160	4	29.9	-7.5	7.5	9	1
PO2 Es	ash	w		34	v	160	4	29.9	-7.5	7.5	9	1
PO2 nv	C24	w		34	nv	160	4	29.9	-7.5	7.5	9	1
PO2 qF	C24	w	⊥	37	v	160	4	40.9	-5.5	9.5	7	3
Total specimens in push-out series II												<b>30</b>

<sup>a</sup> treatment of the timber surface before concreting: w = water, - = no water, hP = hydrophobic primer [87]

<sup>b</sup> treatment of the concrete: v = vibrated, nv = non-vibrated

### Measurement points and testing procedure

The measurement points for series I & II are listed in Table 3.4. The position of the measurement points for series I and for series II are shown in Fig. 3.12 and Fig. 3.13 respectively. In both push-out test series, the induced compression load on the concrete  $F$  is measured by the universal testing machine as well as the vertical path traversed by the upper pressure plate of the testing machine  $u_S$ . In both push-out series, the relative slip between timber and concrete was measured with linear variable differential transformers (LVDT) on both the front side A and the back side B of the specimens. On both sides, the vertical relative slip  $u$  and the horizontal relative slip  $v$  were measured for both joints left L and right R. The counterpart for the LVDTs was for both series I & II a sword-shaped auxiliary measurement device (Fig. 3.9). In push-out series I, the forces on the lateral restraints  $LF$  were measured ( $LF_t$  for top restraint

and  $LF_b$  for bottom restraint) on both the front side A and the back side B of the specimens. In push-out series II, the lateral forces induced by the elastic bands were not measured, but can be back-calculated as a function of the measured horizontal slip (see Appendix A).

**Tab. 3.4:** Measurement points for push-out series I & II

measurement	position	name	PO1	PO2	device	capacity	accuracy
vertical load		$F$	✓	✓	Schenck <sup>a</sup>	450 kN	± 0.2 %
machine path		$u_S$	✓	✓	Schenck <sup>a</sup>	± 125 mm	± 0.2 %
vertical slip	front right	$u_{RA}$	✓	✓	LVDT	± 5 mm	± 0.2 %
	front left	$u_{LA}$	✓	✓	LVDT	± 5 mm	± 0.2 %
	back right	$u_{RB}$	✓	✓	LVDT	± 5 mm	± 0.2 %
	back left	$u_{LB}$	✓	✓	LVDT	± 5 mm	± 0.2 %
horizontal slip	front right	$v_{RA}$	✓	✓	LVDT	± 5 mm	± 0.2 %
	front left	$v_{LA}$	✓	✓	LVDT	± 5 mm	± 0.2 %
	back right	$v_{RB}$	✓	✓	LVDT	± 5 mm	± 0.2 %
	back left	$v_{LB}$	✓	✓	LVDT	± 5 mm	± 0.2 %
lateral forces	front top	$LF_{tA}$	✓	-	load cell	150 kN	± 0.2 %
	front bottom	$LF_{bA}$	✓	-	load cell	150 kN	± 0.2 %
	back top	$LF_{tB}$	✓	-	load cell	150 kN	± 0.2 %
	back bottom	$LF_{bB}$	✓	-	load cell	150 kN	± 0.2 %

<sup>a</sup> universal compression and tension testing machine Schenck

The loading procedure was conducted according to DIN EN 26891 [20]. Deviating from this standard, the load was applied in a displacement-controlled mode at a speed of 3 mm/s. The test was stopped and the load released as soon as one of the joints failed. After the tests, the measurement equipment was disassembled and the lateral restraints removed. With one or even two failed joints, the specimens were still holding together and could easily be lifted out of the testing machine. The timber side parts were detached from the concrete middle part with a hammer stroke, striking in the opposite direction to the micro-notches so as not to damage the notches any further.

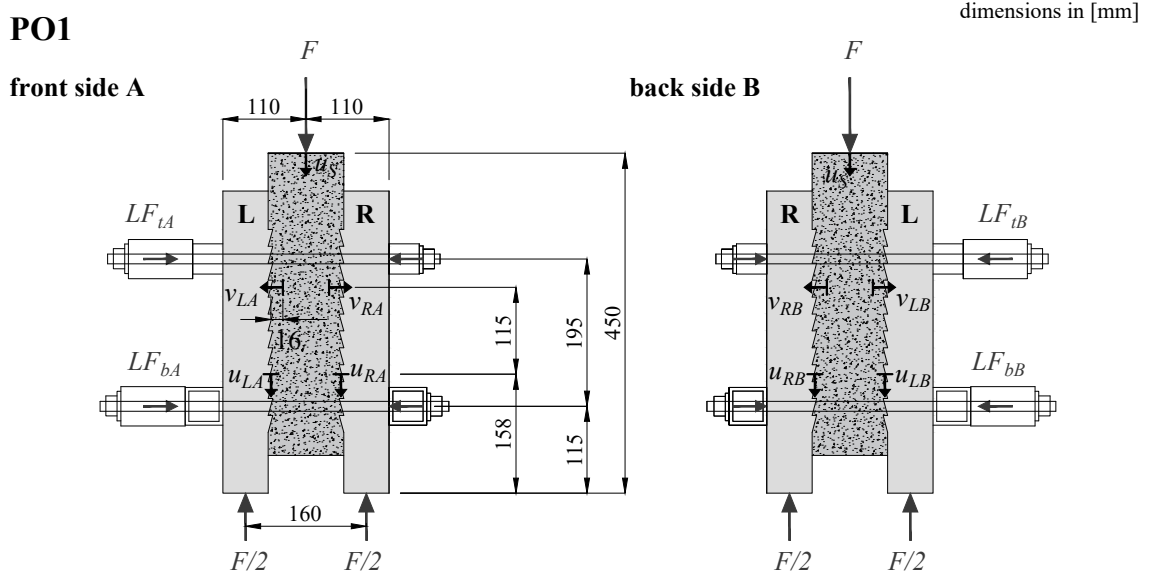


**Fig. 3.12:** Measurement points for push-out series I

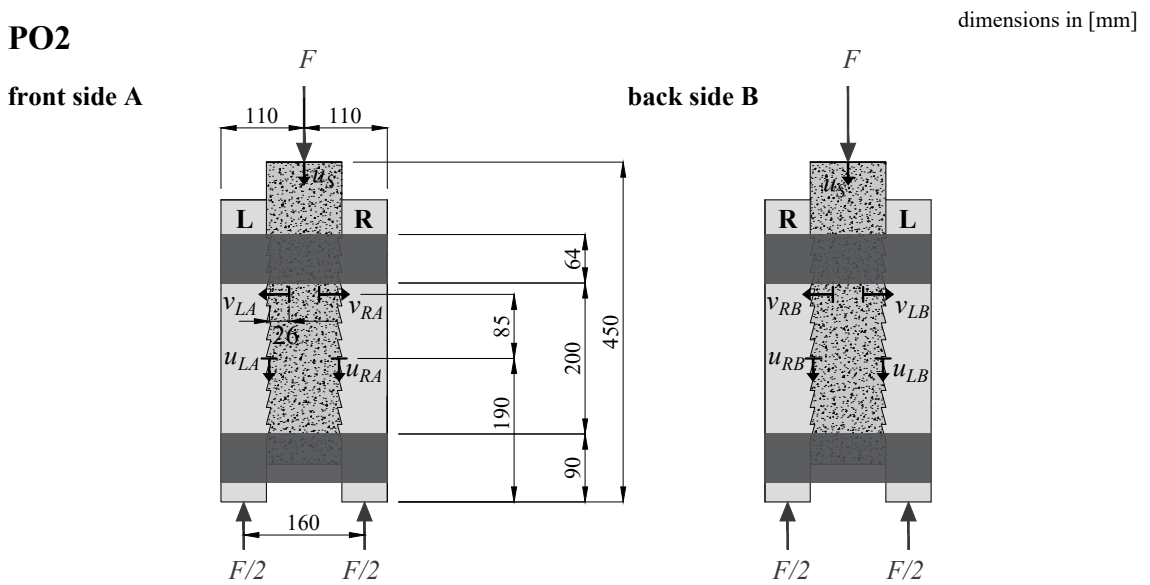


**Fig. 3.13:** Measurement points for push-out series II

### 3.2.2 Results

#### Failure modes and fracture patterns

Fig. 3.14 shows the failure patterns that were visible during and after the testing before opening the specimens. During the test and before opening the specimens (detaching the timber side parts from the concrete middle part), concrete spalling was observed in the area of the joints (Fig. 3.14a). This concrete spalling was superficial.

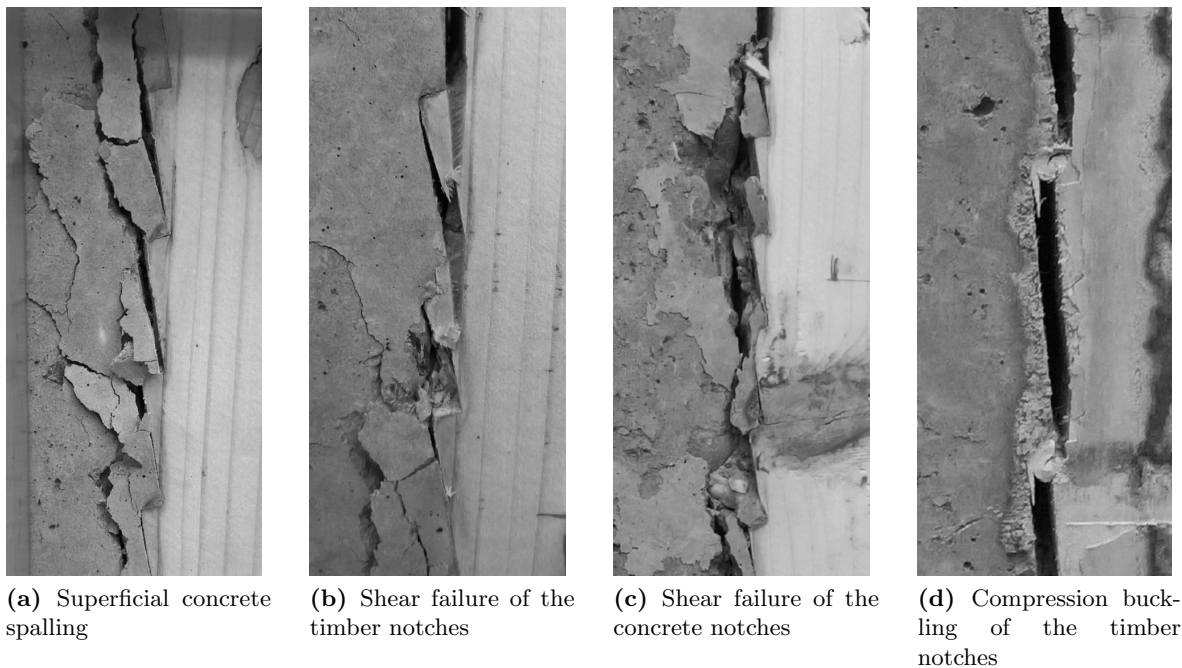


**Fig. 3.14:** Externally visible fracture patterns

The actual failure modes and fracture patterns can only be determined inside the joint (Fig. 3.15). The observed failure modes inside the joints in the push-out series I & II were:

- shear failure of the timber notches
- compression buckling of the timber notches
- shear failure of the concrete notches

The occurred failure modes were visually assessed using the fracture patterns (Fig. 3.15). The local failure mode was classified in the failed joint left L or right R of every specimen. If both joints failed, the visually more destroyed joint was considered.

The percentage distribution of areas per failure mode is shown in Fig. 3.16 for the different micro-notch geometries and in Fig. 3.17 for the different configurations tested on geometry 4-7.5 according to Table 3.3. Fig. 3.16 shows that the setup of the push-out series I mainly led to shear failure in the concrete in combination with compression buckling of the timber notch fronts. This is due to the restrictive lateral restraints (rigid steel profiles). The limited horizontal slip led to the fact that with increasing load, the joint surfaces of the two components ground against each



(a) Concrete shear and timber shear (b) Intact notches and timber shear (c) No mechanical connection shear

**Fig. 3.15:** Internal fracture patterns

other with large lateral load. In contrast to this, timber compression buckling was much less observed in push-out series II (Fig. 3.16 and 3.17). Timber compression buckling only occurs if the joint is held laterally, otherwise the shearing failure of the timber notch occurs first. In push-out series II, a large part of the micro-notches stayed intact on both the timber and the concrete side. The failure of the joint happened only in certain areas. As soon as the joint fails in one area, the timber side part slides over the concrete part and the remaining micro-notches stay intact.



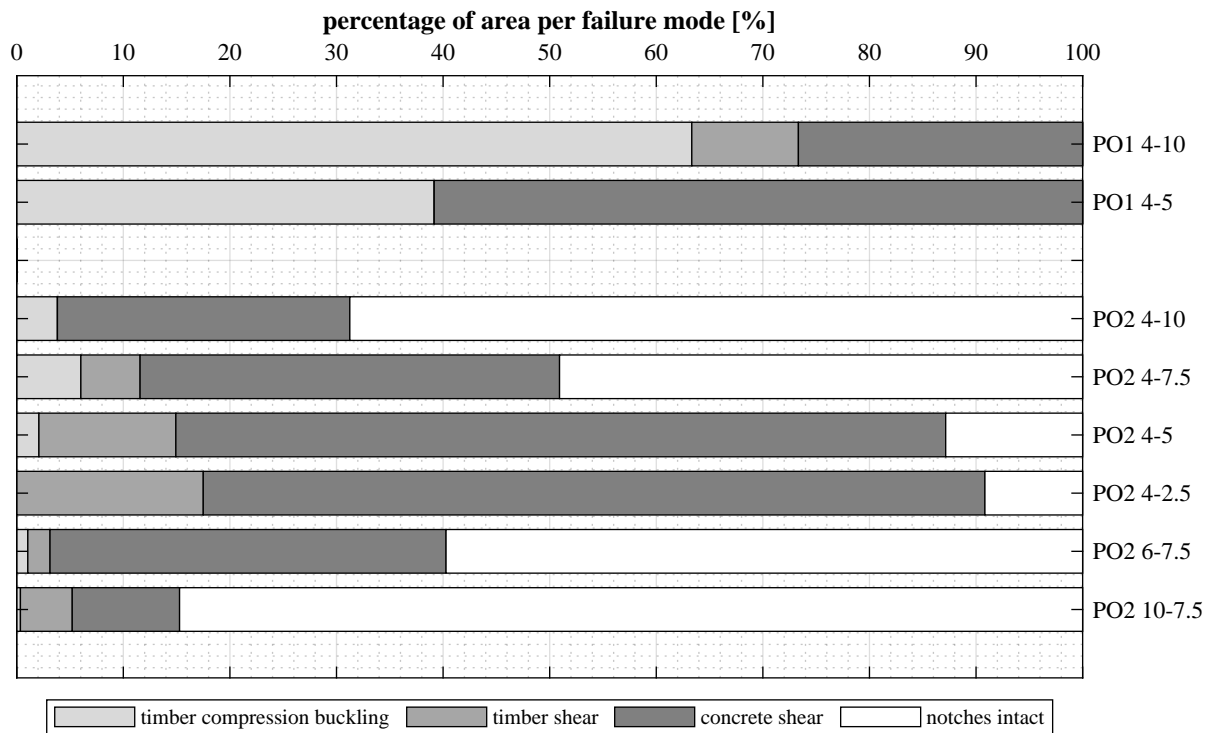


**Fig. 3.16:** Relative share of joint area per failure mode for specimen with different geometries (only failed joint considered)

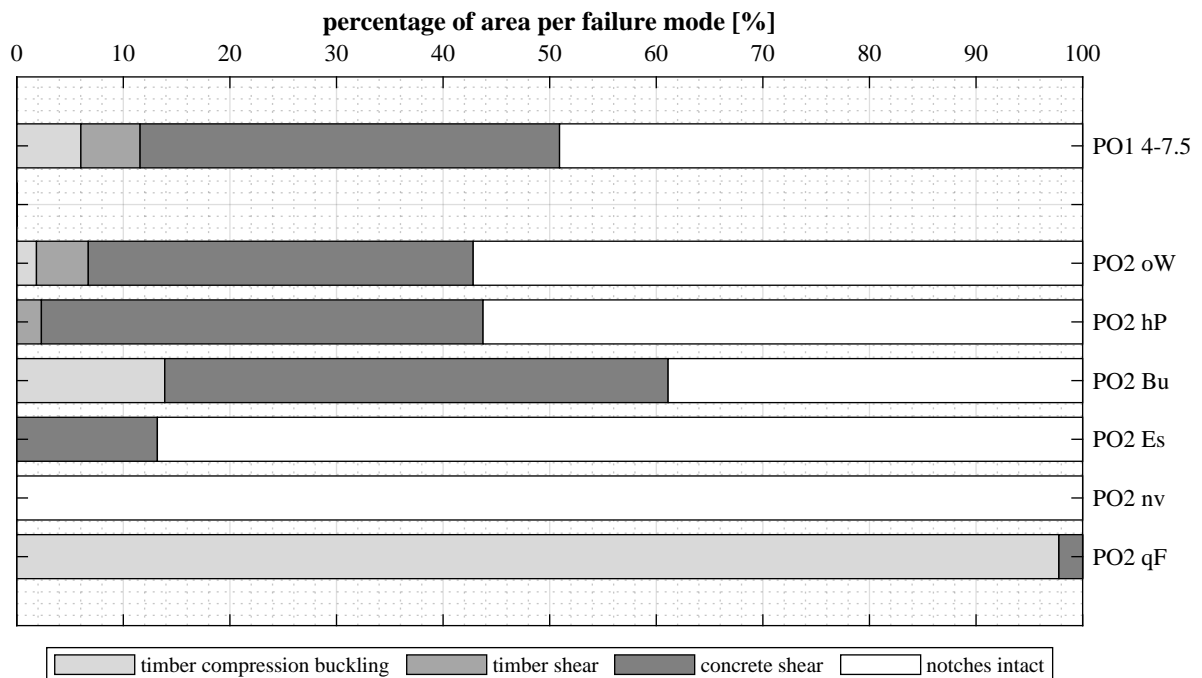


**Fig. 3.17:** Relative share of joint area per failure mode for specimen with geometry 4-7.5 and different configurations (only failed joint considered)

## Displacements

The averaged vertical slip  $u$  corresponds to:

$$u = \frac{u_{RA} + u_{LA} + u_{RB} + u_{LB}}{4} \quad (3.22)$$

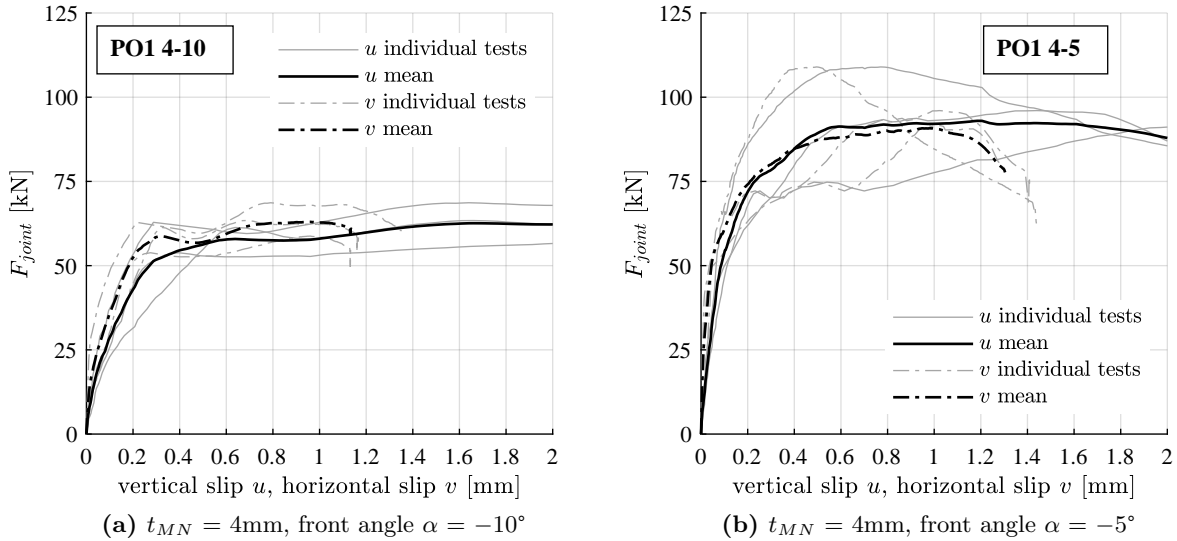
The averaged horizontal slip  $v$  corresponds to:

$$v = \frac{v_{RA} + v_{LA} + v_{RB} + v_{LB}}{4} \quad (3.23)$$

The load per joint  $F_{joint}$  corresponds to half of the total load applied:

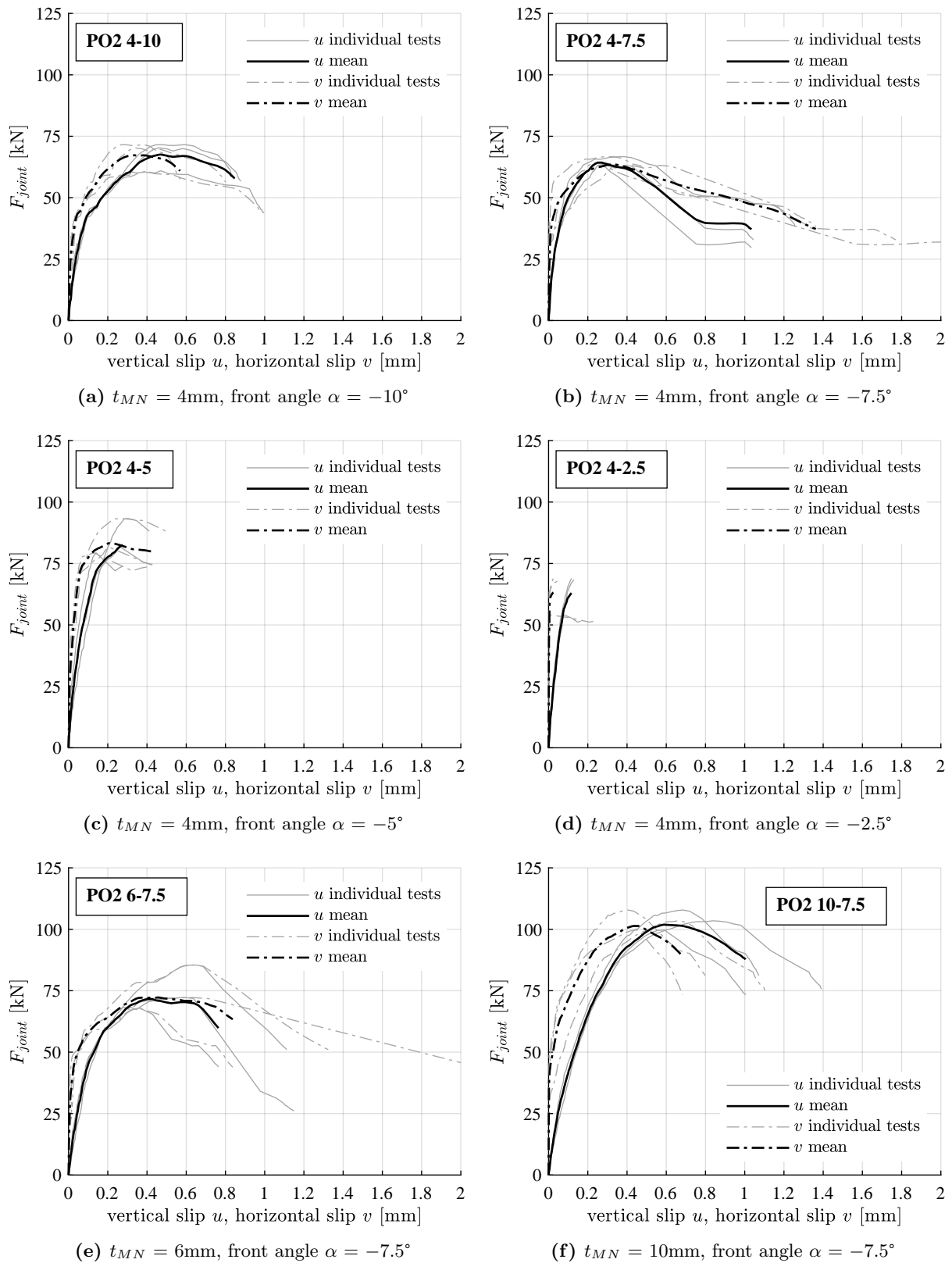
$$F_{joint} = \frac{F}{2} \quad (3.24)$$

The following Figure 3.18 shows the averaged vertical slip  $u$  and the averaged horizontal slip  $v$  for all configurations of push-out series I for individual specimen in gray and the mean of all specimens in black.

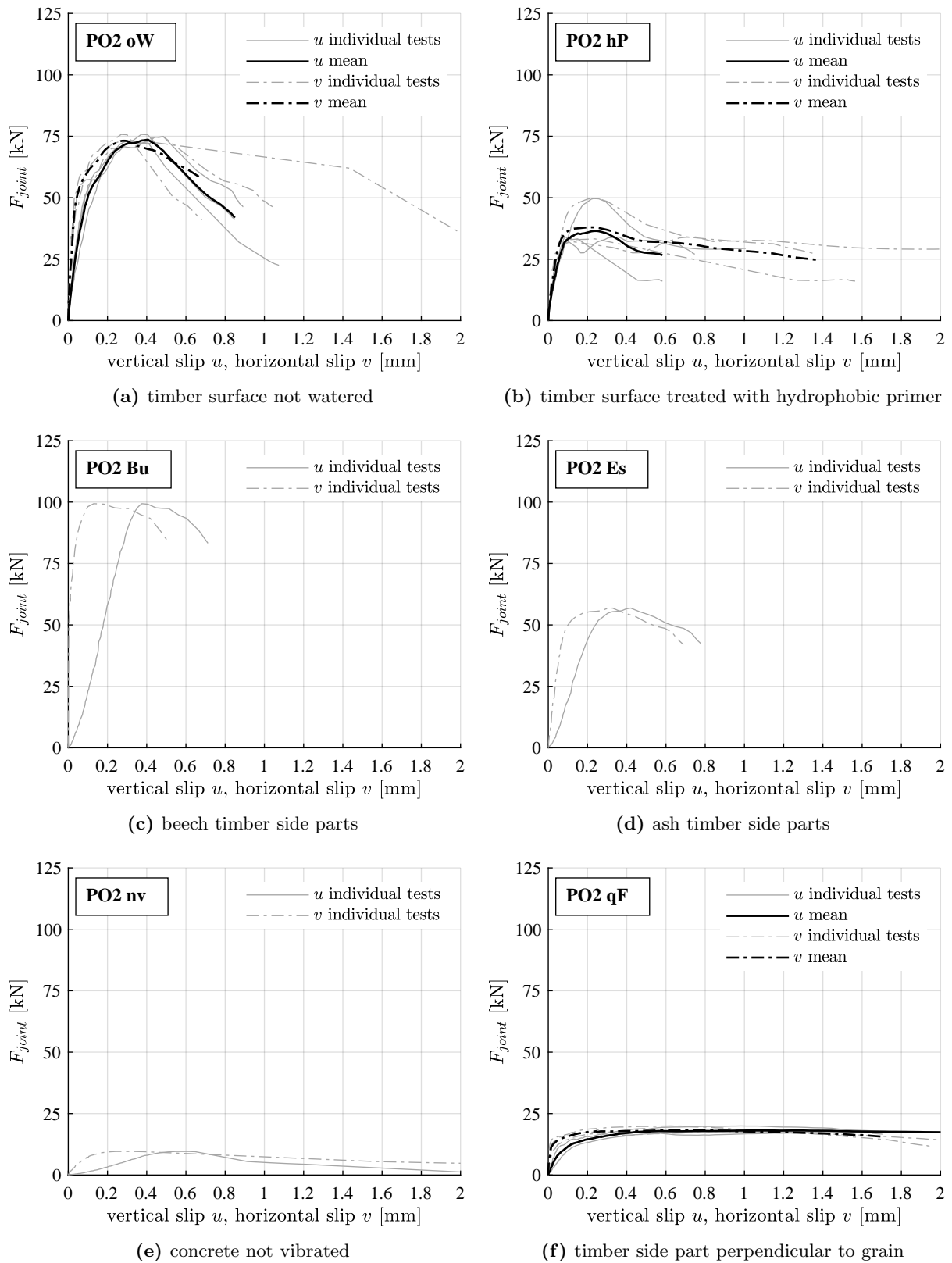


**Fig. 3.18:** Load-slip curves of push-out series I - different micro-notch geometries

The following Figures 3.19 and 3.20 show the averaged vertical slip  $u$  and the averaged horizontal slip  $v$  for all configurations of push-out series II for individual specimen in gray and the mean of all specimens in black.



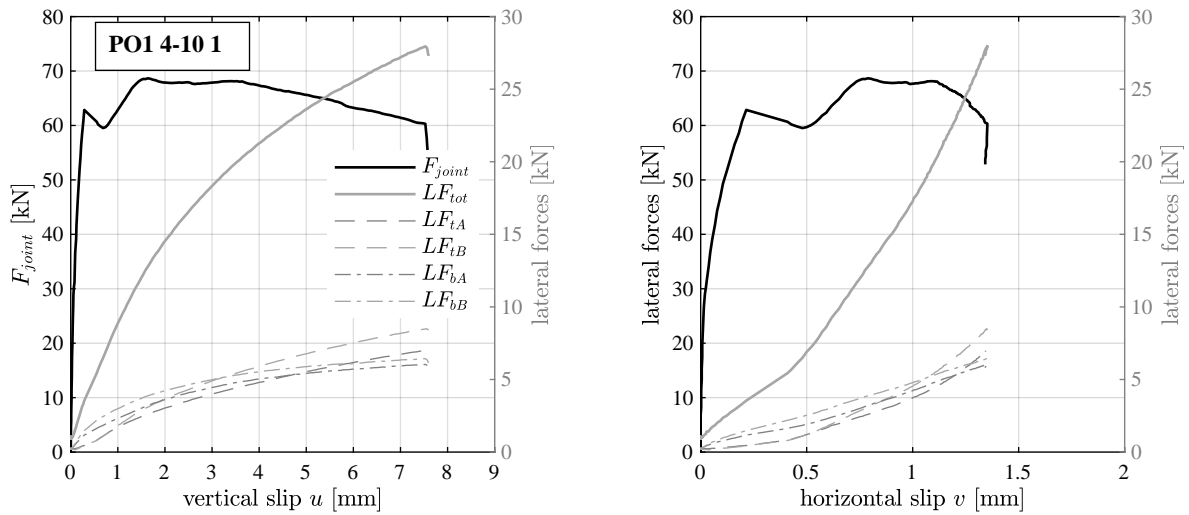
**Fig. 3.19:** Load-slip curves of push-out series II - different micro-notch geometries



**Fig. 3.20:** Load-slip curves of push-out series II - different parameters on geometry 4-7.5

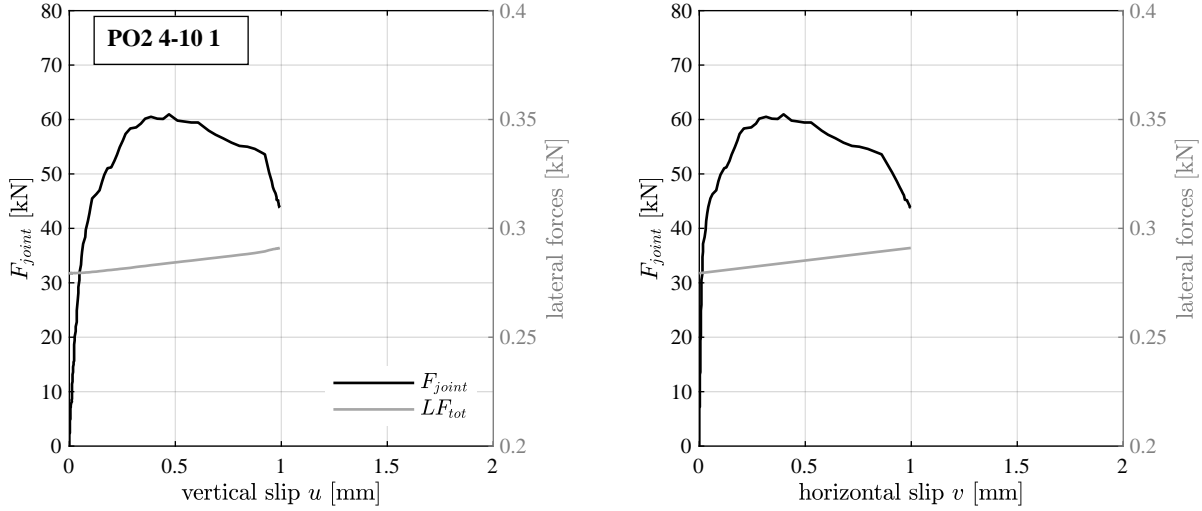
### Influence of lateral forces on the deformation behaviour

Fig. 3.21 shows the lateral forces in the steel rods that were installed as lateral restraint in push-out test series I using the example of specimen PO1 4-10 1. The other specimens of this test series show similar curves for the lateral forces. The lateral forces increase in approximately linear correlation with the vertical displacements measured. The distinct displacements up to 8 mm at approximately constant load  $F_{joint}$  pretend a high ductility, but this only occurs due to the lateral restraints. The horizontal displacements  $v$  also increase approximately linear with the lateral forces. It can be seen that the upper lateral forces  $LF_{tA}$  and  $LF_{tB}$  increase faster than the lower lateral forces  $LF_{bA}$  and  $LF_{bB}$ . At failure load level, the total lateral forces  $LF_{tot}$  smeared onto the area of the two joints result as the transverse compressive stress  $\sigma_Q = 0.241 \text{ N/mm}^2$  which would be the equivalent of a superimposed load of  $241 \text{ kN/m}^2$ .



**Fig. 3.21:** Progression of lateral forces on the load-slip diagrams for specimen PO1 4-10 1

Fig. 3.22 shows the lateral forces in the same specimen geometry PO2 4-10 1 tested in push-out series II with elastic bands used as supports. The lateral forces are back-calculated from the horizontal displacements and the corresponding strain on the elastic bands (Appendix A). The data for specimen PO2 4-10 1 was used as example, the other specimens show similar curves. The scale of the diagrams is different from Fig. 3.21, because much less vertical displacements occurred and the lateral forces were many times lower. Because of the initial prestressing of the elastic bands (see Appendix A), the lateral force starts at  $0.275 \text{ kN}$ . The lateral forces increase slightly with increasing horizontal displacement, but always stay in the range  $0.275 \text{ kN}$  to  $0.29 \text{ kN}$ . At failure load level, this lateral force smeared onto the area of the two joints results as the transverse compressive stress  $\sigma_Q = 0.0025 \text{ N/mm}^2$  which would be the equivalent of a superimposed load of  $2.5 \text{ kN/m}^2$ .



**Fig. 3.22:** Progression of lateral forces on the load-slip diagrams for specimen PO2 4-10 1

### Summary of results

The results regarding the loads applied  $F$  (reaching a yielding behaviour  $F_y$  and reaching its maximum value  $F_{max}$ ) as well as the corresponding vertical slip  $u$  is given in Appendix B for every individual specimen in Table B.1 for push-out series I and in Table B.2 for push-out series II. The following Table 3.5 gives an overview of the the maximum load  $F_{max}$ , the maximum vertical slip  $u_{max}$ , the maximum horizontal slip  $v_{max}$ , and the maximum lateral force  $LF_{max}$  as mean values of all specimens per configuration. The data shows that the test setup of push-out test series I resulted in similar shear resistance values as in push-out series II. In contrast, the achieved relative slip values are much higher due to the large lateral restraining forces.

**Tab. 3.5:** Results of push-out tests

configuration	$F_{max}$ [kN]	$u_{max}$ [mm]	$v_{max}$ [mm]	$LF_{max}$ [kN]	prevailing failure mode
PO1 4-10	63	7.7	1.2	28	timber compression buckling
PO1 4-5	93	3.3	1.4	29	concrete shear, timber compression
PO2 4-10	67	0.9	0.6	0.29	notches intact, concrete shear
PO2 4-7.5	64	1.0	1.4	0.30	notches intact, concrete shear
PO2 4-5	83	0.3	0.4	0.28	concrete shear
PO2 4-2.5	63	0.1	0.0	0.28	concrete shear
PO2 6-7.5	72	0.8	0.8	0.30	notches intact, concrete shear
PO2 10-7.5	102	1.0	0.7	0.29	notches intact
PO2 oW	73	0.9	1.4	0.30	notches intact, concrete shear
PO2 hP	38	0.6	0.5	0.30	notches intact, concrete shear
PO2 Bu	99	0.7	0.7	0.29	concrete shear, notches intact
PO2 Es	57	0.8	0.2	0.29	notches intact
PO2 nv	10	2.9	5.1	0.34	notches intact
PO2 qF	18	2.6	1.7	0.31	timber compression buckling

### 3.3 Modelling local micro-notch behaviour

#### 3.3.1 Local forces and stresses on one individual micro-notch

In the following considerations a single micro-notch is examined. The shear force  $F$  applied on the composite joint is distributed onto the number of micro-notches  $n$  so that each micro-notch is subjected to the same shearing force:

$$F_{MN} = \frac{F_{joint}}{n} \quad (3.25)$$

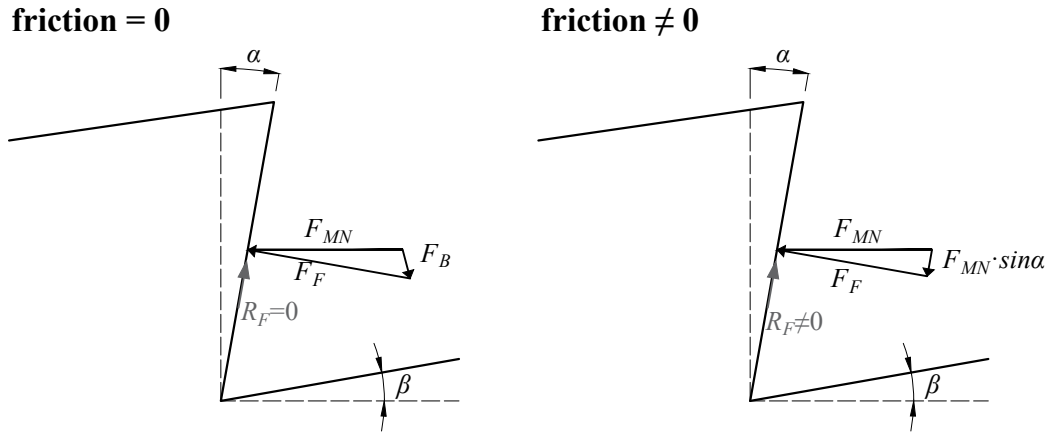


**Fig. 3.23:** Forces on one individual micro-notch

If there would be no friction between timber and concrete, the micro-notch could only take forces perfectly perpendicular to its front plane. Due to the inclination of the front, the arising forces with vertical components are taken by the bottom of the notch (Fig. 3.23 left). In this case, the force acting perpendicular on the notch front results:

$$F_F = \frac{F_{MN}}{\cos \alpha - \sin \alpha \cdot \tan \beta} \quad (3.26)$$

In reality, the friction coefficient between timber and concrete is in the range of  $\eta = 0.62 \dots 0.92$  [74; 114], depending on the moisture content of the timber and the concreting procedure. In this case, the full force on the notch can be carried by the notch front as shown in Fig. 3.23 right and the force perpendicular to the notch front is:

$$F_F = F_{MN} \cdot \cos \alpha \quad (3.27)$$

The full force on the notch can be carried by the notch front if the frictional force  $R_F$  is larger than the force parallel to the notch front:

$$R_F > F_{MN} \cdot \sin \alpha \quad (3.28)$$

with  $R_F$  depending on the force perpendicular to the notch  $F_F$ :

$$R_F = \eta \cdot F_F = \eta \cdot F_{MN} \cdot \cos \alpha \quad (3.29)$$

From equations 3.28 and 3.29, the requirement for the friction coefficient  $\eta$  can be defined:

$$\eta > \frac{\sin \alpha}{\cos \alpha} = \tan \alpha \quad (3.30)$$

This condition for friction results for the notch front angle  $\alpha$ :

$$\alpha < \arctan(\eta) \quad (3.31)$$

A very low friction coefficient of  $\eta = 0.62$  can be assumed for friction between plane timber and concrete surfaces without the adhesion through casting the concrete directly onto the timber [114]. This would still allow front notch angles up to  $\alpha \leq 31.8^\circ$  to fulfil equation 3.31. For the more authentic high friction coefficient  $\eta = 0.92$  for friction between rough sawn timber surface and insitu concrete, the notch front angle can be increased up to  $\alpha \leq 42.6^\circ$ . The largest inclination of the notch front shows configuration PO1 4-10 and PO2 4-10 with  $\alpha = 10^\circ$  (Table 3.3). The assumption of friction between timber and concrete is therefore confirmed for all tested specimens.

With friction in the connection, the relevant force on the notch front is  $F_{MN}$  and the notch front does not have an influence on the stresses. The stresses on the notch are due to the force on the notch front  $F_{MN}$  and can be described as horizontal and vertical stresses:

The horizontal stresses are compressive stresses on the notch front and can be determined as:

$$\sigma_x = \frac{F_{MN}}{t_{MN} \cdot b} \quad (3.32)$$

The vertical stresses result from the moment of eccentricity on the notch generated by the force on the notch front  $F_{MN}$ . The vertical stress on the notch front resulting from the eccentricity moment is:

$$\sigma_{z,Ecc} = F_{MN} \cdot \frac{3 \cdot t_{MN}}{(l_{MN})^2 \cdot b} \quad (3.33)$$

Any transverse compressive stresses  $\sigma_{z,Q}$  from external transverse loads on the composite joint result in a reduction of the transverse tensile stresses. The total vertical tensile stresses on the notch front are therefore calculated as:

$$\sigma_z = \sigma_{z,Ecc} - \sigma_{z,Q} \quad (3.34)$$

The shear stress over the length of the notch depends on the shear area available:

$$\tau = \frac{F_{MN}}{l_v \cdot b} \quad (3.35)$$



The available shear length  $l_v$  is assumed as  $8 \cdot t_{MN}$  as described in Chapter 3.1.3. The available shear length  $l_v$  is then:

$$l_v = \min(l_{MN}, 8 \cdot t_{MN}) \quad (3.36)$$

However, the peak shear stress right behind the notch front is (Fig. 3.5):

$$\tau_{max} = \frac{\sigma_x}{\pi} \quad (3.37)$$

### 3.3.2 Local failure loads in timber

To address the local verifications for the ULS required by the Technical Specification [30], the four expected failure modes and the corresponding failure loads described in Chapter 3.1.3 are established in the following chapters. Additional to the Technical Specification, combined stress states due to vertical stresses in the notch front are also considered. The strength values were taken as the mean values calculated according to the Joint Committee on Structural Safety JCSS [75].

#### Compression failure of the timber notch

The compression stress on the timber notch front is:

$$\sigma_{2,x} = \sigma_x = \frac{F_{MN}}{t_{MN} \cdot b} \quad (3.38)$$

The failure load for compression failure for load transfer parallel to the grain in timber is:

$$F_{2C,\parallel} = f_{2,c,\parallel} \cdot t_{MN} \cdot b \quad (3.39)$$

and for load transfer perpendicular to the grain:

$$F_{2C,\perp} = f_{2,c,\perp} \cdot t_{MN} \cdot b \quad (3.40)$$

#### Shear and tension failure of the timber

Assuming that the shear stress peak in timber can be mainly plasticised, the shear stress in the timber notch can be simplified as rectangular shear stress along the available shear length  $l_v$ :

$$\tau_2 = \frac{F_{MN}}{l_v \cdot b} \quad (3.41)$$

The failure load for pure timber shear failure is then:

$$F_{2S} = f_{2,v} \cdot l_v \cdot b \quad (3.42)$$

The combination of shear and tension perpendicular to grain is verified according to SIA 265 4.2.7.1 [149]:

$$\left(\frac{f_{c,\perp} + \sigma_{2,z}}{f_{c,\perp} + f_{t,\perp}}\right)^2 + \left(\frac{\tau_2}{f_v}\right)^2 \cdot \left[1 - \left(\frac{f_{c,\perp}}{f_{c,\perp} + f_{t,\perp}}\right)^2\right] \leq 1.0 \quad (3.43)$$

The vertical stresses  $\sigma_{2,z}$  in timber are all vertical stresses in the notch as derived in Equations 3.33 and 3.34:

$$\sigma_{2,z} = \sigma_z \quad (3.44)$$

The failure load for shear failure  $F_{2ST}$  due to combined shear and tensile stresses in the timber results from equation 3.43.

### 3.3.3 Local failure loads in concrete

#### Compression failure of the concrete notch

The compression stress on the concrete notch front is:

$$\sigma_{1,x} = \sigma_x = \frac{F_{MN}}{t_{MN} \cdot b} \quad (3.45)$$

The failure load for compression failure in concrete is:

$$F_{1C} = f_{1,c} \cdot t_{MN} \cdot b \quad (3.46)$$

#### Shear and tension failure of the concrete

In concrete, it can not be assumed that the shear peak stress  $\tau_{max}$  is plasticised. The shear stress in concrete is therefore

$$\tau_1 = \tau_{max} = \frac{\sigma_{1,x}}{\pi} \quad (3.47)$$

The failure load for concrete due to pure shear failure is then:

$$F_{1S} = f_{1,v} \cdot t_{MN} \cdot b \cdot \pi \quad (3.48)$$

The combination of shear and tension in the concrete notch is verified with the MOHR-COULOMB criterion (equation 3.3, where the axial stresses  $\sigma_y = 0$ ):

$$\sigma_{1,3} = \frac{\sigma_{1,z}}{2} \pm \sqrt{\left(\frac{\sigma_{1,z}}{2}\right)^2 + (\tau_1)^2} \leq f_{1,t} \quad (3.49)$$

The failure load for shear failure  $F_{1ST}$  due to combined shear and tensile stresses in the concrete results from equation 3.49.

### 3.3.4 Comparison with experimental data

The failure loads of the different failure modes described in Chapter 3.1.3 and the previous Chapter 3.3.2 are compared with the experimental data from push-out test series II. The experimental data from push-out test series I is not considered further, as the lateral restraints

impaired the load-bearing behaviour. Fig. 3.24 shows the load-slip curves from the configurations with different geometries from push-out test series II and the estimated failure loads.

The observed failure mode for all geometries in push-out series II showed a decisive failure due to shear in the concrete (Fig. 3.16). This failure mode corresponds to the failure load  $F_{1S}$  due to the peak shear stress right behind the notch front or the combined failure load  $F_{1ST}$ . Fig. 3.24 shows that both estimated failure loads  $F_{1S}$  and  $F_{1ST}$  are in the range of the failure loads observed in the tests. The estimated failure load for combination of shear and vertical stresses in concrete  $F_{1ST}$  is higher than the failure due to pure shear  $F_{1S}$ . The vertical tensile stresses resulting from the eccentricity moment  $\sigma_{z,Ecc}$  are low. The shear peak behind the notch has a much higher influence.

The estimated failure load in timber due to shear and tension  $F_{2ST}$  underestimates the shear loads observed in the tests. Failure in timber was only observed partially in all geometries (Fig. 3.16). The estimated failure load  $F_{2ST}$  largely depends on the assumed tensile strength perpendicular to grain  $f_{2,t,\perp}$ . The value of  $0.3 \text{ N/mm}^2$  for  $f_{2,t,\perp}$  taken from JCSS [75] is probably set too low. Considering the small scale in the micro-notches, the JCSS values for structural elements are likely to underestimate the real material properties. The shear strength values perpendicular to grain for small-scale timber without faults is in the range of  $3.1 \text{ N/mm}^2$  -  $4.0 \text{ N/mm}^2$  [121], the values found by Blass [7] in tests were  $1.8 \text{ N/mm}^2$  for tangential direction and  $2.6 \text{ N/mm}^2$  for radial direction. The shear strength perpendicular to grain  $f_{2,t,\perp}$  taken from JCSS underestimates the real shear strength in the timber micro-notches.

The estimated compression failures in concrete  $F_{1C}$  or timber  $F_{2C}$  are not decisive for any of the geometries. Observed compression failure patterns in timber in push-out series II are probably due to local faults in the timber. In push-out series I, the lateral restraint enabled large plastic deformations and thus led to compression failure in the timber notch.

The effects of adhesion and friction are not taken into account in the failure loads shown in Fig. 3.24. Considering the joint area without micro-notches as plane surface and the area with micro-notches including the bottom and front length of the notches, a total area of  $58\,800 \text{ mm}^2$  to  $67\,680 \text{ mm}^2$  (depending on the specimen) is available for adhesion and friction effects. The friction is dependent on the transverse stresses applied which are low and the shear resistance due to friction therefore negligible. The shear resistance due to adhesion, however, results around  $30 \text{ kN}$  for the bond shear resistance of  $0.42 \text{ N/mm}^2$  found by Lehmann [99]. If this estimated adhesion shear resistance would be added to the estimated loads above, the estimated failure loads would significantly overestimate the shear resistance measured in the experimental tests. The model described above is either wrong or the quantification of adhesion forces by Lehmann [99] can not be applied to this system.

The failure loads shown in Fig. 3.24 determined with the mechanical considerations described in Chapter 3.3.2 show no good agreement with the failure loads measured in the experimental tests. The analytical model developed above does not consider surface effects such as friction and adhesion. These effects have a great influence on the load-bearing behaviour of the small-scale micro-notches. However, their quantification is difficult. The shear strength due to adhesion

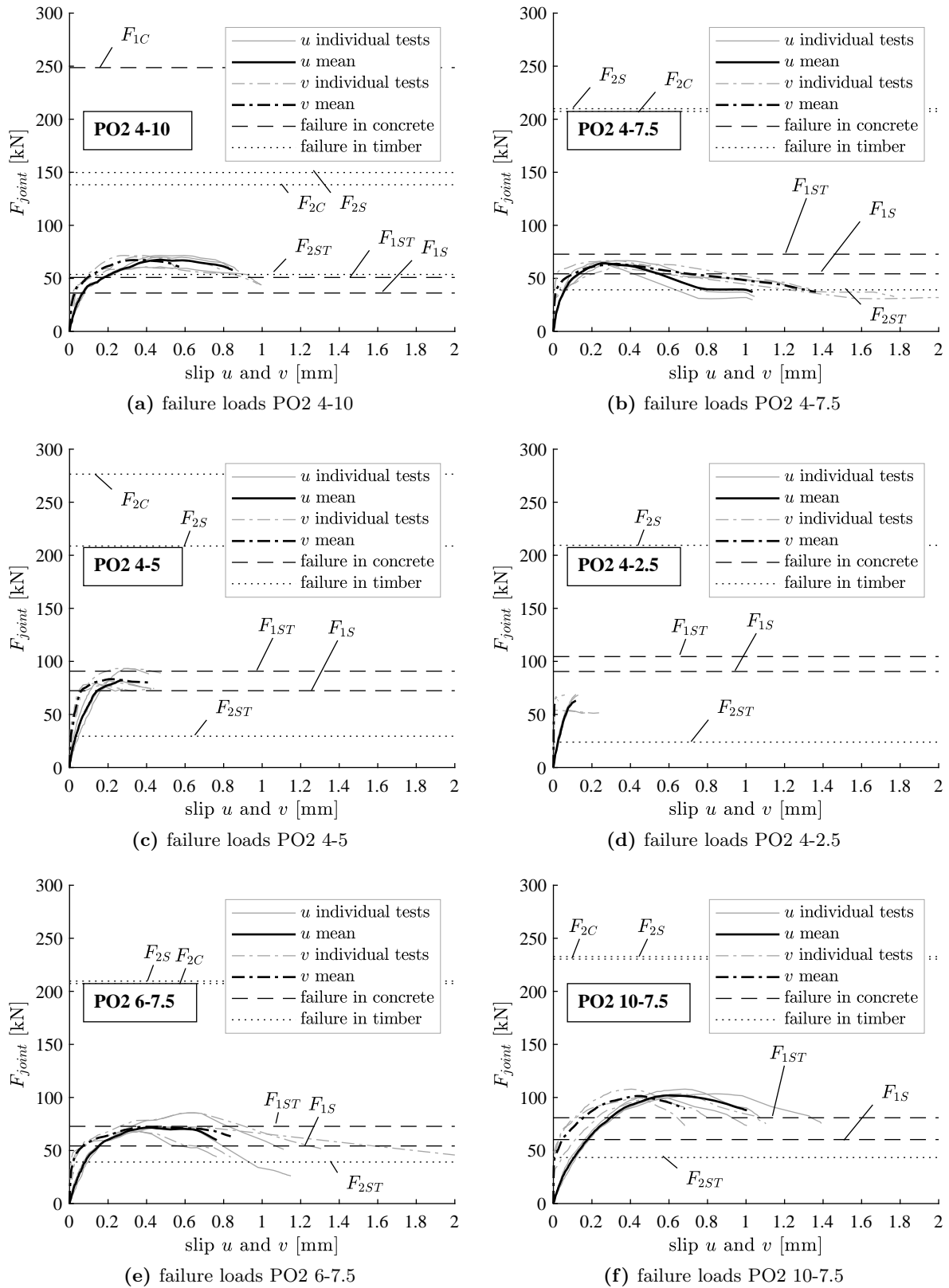


**Fig. 3.24:** Experimental load-slip curves and estimated failure loads for push-out series II

highly depends on the material and the production conditions. The analytical model described above was therefore only used to predict the estimated failure load  $F_{max,est}$  in the experiments.

## 3.4 Determination of connection properties

### 3.4.1 Distance between connectors

The distance between the connectors  $s$  for micro-notches arranged over a continuous area corresponds to the length of the micro-notches  $l_{MN}$ :

$$s = l_{MN} \quad (3.50)$$

### 3.4.2 Shear resistance

The shear resistance of the micro-notch system was determined using the measured load  $F$ . The total load  $F$  is assumed to be distributed equally into both joints, given the symmetric setup of the push-out tests. The force on the joints results then as:

$$F_{joint} = F_R = F_L = \frac{F}{2} \quad (3.51)$$

No accurate analytical model was found to describe the shear resistance of the different configurations of micro-notches (Chapter 3.3.4). The effect of adhesion has a non-negligible influence and has to be considered, but is difficult to quantify with the present knowledge. Therefore, the shear resistance of the micro-notch system was not defined as a decisive failure load but as a shear strength value. Micro-notches are a continuous connection system and the best way to determine its shear resistance is as a shear strength smeared over the whole area.

In literature, the shear resistance of a connection is commonly determined from the measured load at maximum  $F_{max}$ . In push-out series I, the steel rods as lateral restraints restricted a softening behaviour after reaching the load  $F_y$ , where the connection started yielding (Figs 3.18a and 3.18b). In this series, the reached maximum load  $F_{max}$  in the tests is usually higher than the yielding load  $F_y$ . On this account, both the yielding load  $F_y$  and maximum load  $F_{max}$  were determined for all test configurations. The shear strength  $f_v$  was then determined for both yield shear resistance  $F_y$  and maximum shear resistance  $F_{max}$  in relation to the total shear area  $A_{joint}$ :

$$f_{v,y} = \frac{F_y}{A_{joint}} \quad (3.52)$$

$$f_{v,max} = \frac{F_{max}}{A_{joint}} \quad (3.53)$$

The shear strengths  $f_{v,y}$  and  $f_{v,max}$  are listed for all configurations tested in push-out series I & II in Table 3.6. The results for the yielding load  $F_y$ , maximum load  $F_{max}$ , the relative slip at maximum load, and the maximum slip at the end of the test is listed for each specimen of push-out series I & II in Appendix B.

### 3.4.3 Connection stiffness

The slip modulus  $K$  of the micro-notches was determined per failed joint of each specimen according to SIA 265 [149] (see also Chapter 3.1.5). The values for the slip modulus  $K$  are listed for every individual specimens of push-out series I & II in the Appendix B. Table 3.6 shows the slip modulus  $K$  normalised to 1 m width and per micro-notch, enabling a comparison of the values obtained in the two push-out series and with literature data. The joint stiffness  $k$  for a continuous area of micro-notches is calculated from the slip modulus  $K$  and the notch length  $l_{MN}$  as:

$$k = \frac{K}{s} = \frac{K}{l_{MN}} \quad (3.54)$$

**Tab. 3.6:** Connection properties for push-out test series I & II

	yield shear strength	maximum shear strength	notch length	slip modulus per notch	joint stiffness
<b>configuration</b>	$f_{v,y}$ [N/mm <sup>2</sup> ]	$f_{v,max}$ [N/mm <sup>2</sup> ]	$l_{MN}$ [mm]	$K$ [kN/mm/m]	$k$ [kN/mm <sup>2</sup> ]
PO1 4-10	0.69	0.91	45.0	253	5.6
PO1 4-5	0.88	1.41	22.3	264	11.9
PO2 4-10	0.72	1.21	45.0	693	15.4
PO2 4-7.5	0.74	1.16	29.9	656	21.9
PO2 4-5	1.20	1.51	22.3	432	20.7
PO2 4-2.5	1.01	1.14	17.9	391	21.8
PO2 6-7.5	0.95	1.34	44.8	554	12.4
PO2 10-7.5	1.42	1.85	74.6	631	8.5
PO2 oW	0.95	1.33	29.9	473	15.8
PO2 hP	0.58	0.70	29.9	403	13.5
PO2 Bu	1.77	1.77	29.9	181	6.1
PO2 Es	0.96	1.02	29.9	137	4.6
PO2 nv	0.17	0.17	29.9	12	0.4
PO2 qF	0.20	0.33	40.9	168	4.1

The values for the joint stiffness  $k$  are very high for all configurations, except the configurations PO2 nv. The highest joint stiffness  $k$  was obtained for the configuration PO2 4-7.5. If this micro-notch geometry is used on a continuous area of a slab, a connection efficiency  $\eta_{C^*}$  of 0.997 (equation 2.23) can be achieved. This micro-notch geometry can therefore be assumed to be a rigid connection. The test results confirm the high connection stiffness observed in notched TCC connections and confirm the recommendation of Kudla [92], that the slip modulus  $K$  can be taken equal for both SLS and ULS:

$$K_{ser} = K_u \quad (3.55)$$

### 3.4.4 Comparison with literature results

It would be appropriate to compare the shear strength values of TCC with micro-notches (Table 3.6) to values from TCC with adhesive connections. However, in TCC systems with normal-strength concrete and adhesive connections, the shear failure in concrete is always decisive as stated by Schäfers [137], so no shear strength values of the connection alone are available. The available data is for TCC with ultra high performance concrete: Schäfers reported shear strength values of  $11.5 \text{ N/mm}^2$  for epoxy resin as connection between spruce and ultra high performance concrete. The failure occurred in timber. Kostic et al. [87] reported shear strength values of around  $5 \text{ N/mm}^2$  for epoxy resin used as connection between beech laminated veneer lumber and ultra high performance concrete. The shear strength values obtained for the micro-notches are considerably lower than the shear strength of those experiments with adhesives.

On the other hand, the connection stiffness can directly be compared to literature data (see Tab. 3.1). The connection stiffness highly depends on the distance of the connectors  $s$ : The slip modulus  $K$  alone is not comparable, only the joint stiffness  $k$  according to equation 2.21. Fig. 3.25 shows the joint stiffness and corresponding connection efficiency for a numerical example (planar TCC system with concrete height  $h_1 = 80 \text{ mm}$ , timber height  $h_2 = 120 \text{ mm}$ , and width  $b = 1 \text{ m}$ ) for the values obtained in the micro-notch shear tests and for a conventional TCC system with notches with slip modulus  $K = 1000 \text{ kN/mm/m}$  and the limit distances  $s_{min} = 250 \text{ mm}$  and  $s_{max} = 1000 \text{ mm}$ . The  $\gamma$ -value is determined with the approach of Möhler and the connection efficiency  $\eta_{C^*}$  with equation 2.23. All the configurations, except for PO2 nv, show a comparable or higher joint stiffness than the conventional notches.

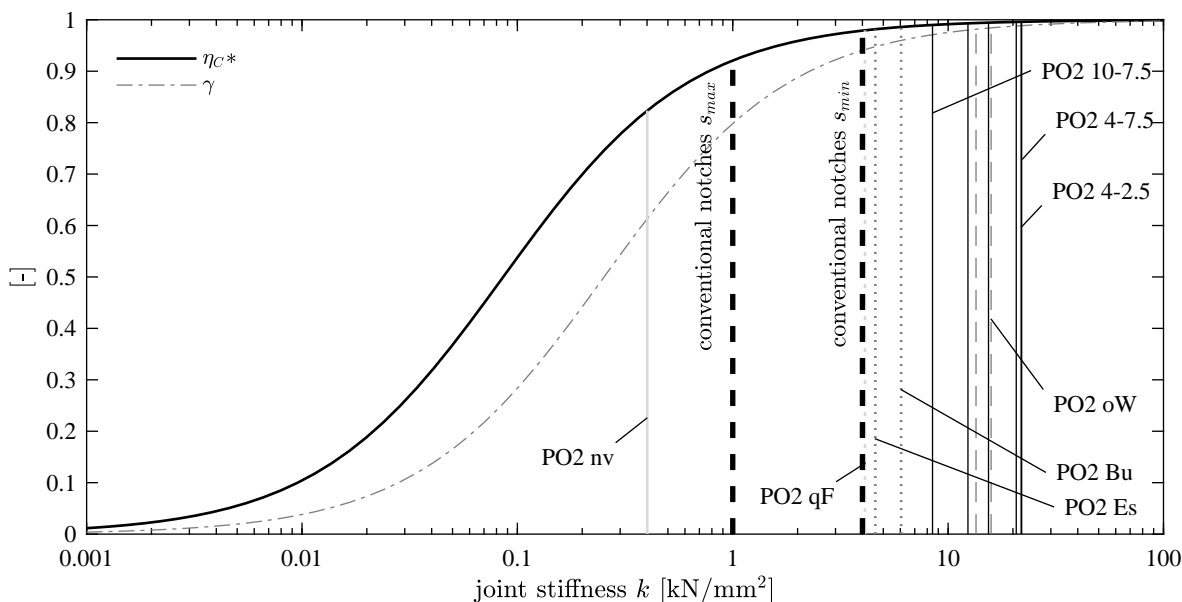


**Fig. 3.25:** Comparison of the joint stiffness  $k$  of micro-notches (push-out test series II) with a conventional TCC system with notches with slip modulus  $K = 1000 \text{ kN/mm/m}$ .

## 3.5 Influence of different parameters

### 3.5.1 Test-setup

The test setup for both series was chosen as symmetric push-out test setup. Both test series had the same dimensions regarding the height and the thickness of the timber and the concrete cross-sections. The width of the specimens was 200 mm for push-out series I and 160 mm for push-out series II. The results obtained in both test series do not indicate an influence of this difference in width. The presence of the lateral restraints in push-out series I had a large influence on the load-bearing behaviour of the connection joint (see Chapter 3.4). The lateral restraints lead to an approximate ideal-plastic load-slip behaviour of the micro-notches (see Chapter 3.2.2 and Fig. 3.18). As stated in the introduction (Chapter 3.1), the influence of the test setup itself and the chosen dimensions is an often discussed issue in research. Especially the thickness of the cross-sections and the length of the connection joint are assumed to have a non-negligible influence on the connection behaviour. In this study, this influence was not analysed in detail. The results obtained in push-out series I & II must be understood with regard to the test setup presented in Fig. 3.9a and 3.9b.

### 3.5.2 Material properties

The materials used for the push-out series were C24 for timber and a normal-strength concrete (concrete mixture for strength class C25/30). The material tests showed that the material properties of the concrete in push-out test series I correspond to a strength class higher (C30/37) and in push-out test series II even to two strength classes higher (C40/50) than expected with the chosen concrete mixture. The influence of this concrete with higher strength and stiffness values must be considered for the obtained results. It must be assumed that lower strength classes (C25/30) would lead to even more shear failure of the concrete notches. However, it must be stated that strength classes higher than planned or ordered are also common in practice. The findings of the push-out test series are therefore realistic with regard to the application in practice.

### 3.5.3 Notch geometry

Six different micro-notch geometries were tested in order to assess the influence of the micro-notch depth, length, and front angle on the connection behaviour.

#### Notch depth

Three different micro-notch depths  $t_{MN}$  were tested: 4 mm, 6 mm, and 10 mm. Fig. 3.26 shows the load-slip curves of the specimens and Table 3.7 shows the determined connection properties. The shear resistance increases and the stiffness of the connection decreases with increasing micro-notch depth. The higher shear resistance for deeper notch fronts can be explained by the increased notch front area. The lower stiffness for deeper notches does not correspond



with findings from Michelfelder [110] and Kudla [91; 92]. However, the stiffness behaviour of the indented micro-notches cannot be directly compared with the stiffness behaviour of conventional rectangle shear notches. The joint stiffnesses found for all three notch depths are very high and the stiffness is approximately rigid.

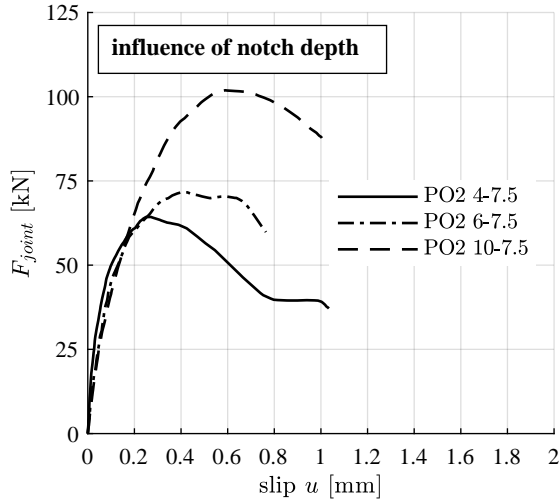


**Fig. 3.26:** Load-slip curves for different notch depths  $t_{MN}$

	micro-notch depth	shear strength	joint stiffness
name	$t_{MN}$ [mm]	$f_{v,max}$ [N/mm <sup>2</sup> ]	$k$ [kN/mm <sup>2</sup> ]
PO2 4-7.5	4	1.16	22.0
PO2 6-7.5	6	1.34	12.4
PO2 10-7.5	10	1.85	8.5

**Tab. 3.7:** Connection properties

### Notch front angle and notch length

Four different micro-notch front angles  $\alpha$  were tested:  $-10^\circ$ ,  $-7.5^\circ$ ,  $-5^\circ$ , and  $-2.5^\circ$  (all with negative sign according to the convention shown in Fig. 3.2). Fig. 3.27 shows the load-slip curves of the specimens and Table 3.8 shows the connection properties.

The analytical considerations show that the vertical component of the force on the notch front resulting from the incline can be taken by friction. The notch front angle has therefore no influence on the connection properties neither in the experimental nor in the analytical investigations. Due to the fixed opening angle of  $75^\circ$ , the notch front angle  $\alpha$  influences the notch length  $l_{MN}$ . The influence of the notch length  $l_{MN}$  can be assessed with the four specimens shown in Fig. 3.27 and Table 3.8. The values for shear strength and joint stiffness are similar for all specimens. However, there is a tendency on the ductility: the shorter the notch length  $l_{MN}$ , the more brittle is the failure after the linear elastic phase. The failure modes observed were mainly concrete shear and a small share of timber shear failure in the failed joints (Fig. 3.16).

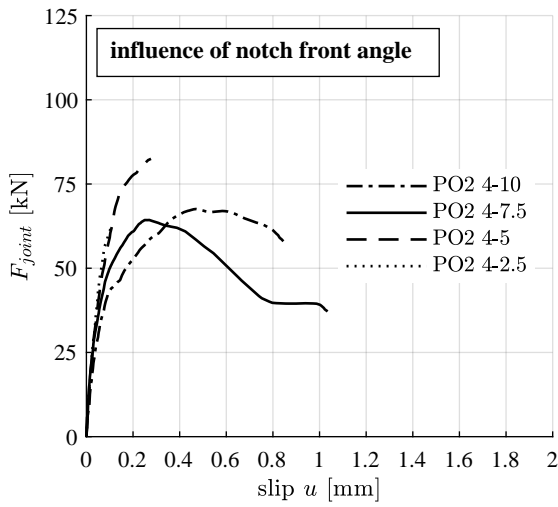


**Fig. 3.27:** Load-slip curves for different notch front angles  $\alpha$  and notch lengths  $l_{MN}$

	front angle	notch length	shear strength	joint stiffness
name	$\alpha$ [°]	$l_{MN}$ [mm]	$f_{v,max}$ [N/mm <sup>2</sup> ]	$k$ [kN/mm <sup>2</sup> ]
PO2 4-10	-10	45	1.21	15.4
PO2 4-7.5	-7.5	29.9	1.16	22.0
PO2 4-5	-5	22.3	1.51	20.7
PO2 4-2.5	-2.5	17.9	1.14	21.8

**Tab. 3.8:** Connection properties

### 3.5.4 Wood species

Three different wood species for the timber side elements were tested: spruce, beech, and ash. Fig. 3.28 shows the load-slip curves of the specimens and Table 3.9 shows the connection properties.

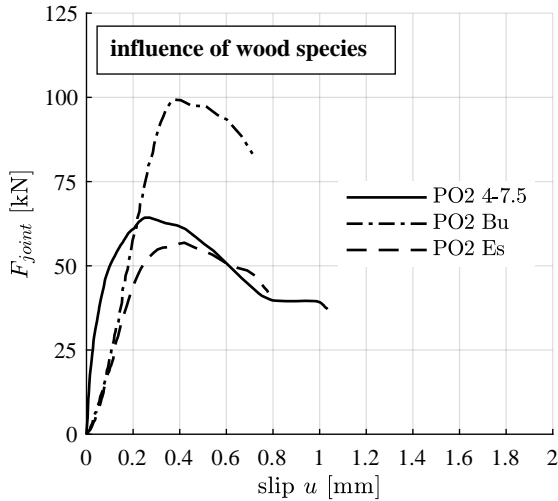


**Fig. 3.28:** Load-slip curves for different wood species: spruce, beech, and ash

	wood species	shear strength	joint stiffness
name		$f_{v,max}$ [N/mm <sup>2</sup> ]	$k$ [kN/mm <sup>2</sup> ]
PO2 4-7.5	spruce	1.16	22.0
PO2 Bu	beech	1.77	6.1
PO2 Es	ash	1.02	4.6

**Tab. 3.9:** Connection properties

The specimens with spruce side parts show a significantly higher connection stiffness than the specimens with beech and ash side parts. The shear resistance of the specimen with beech side parts is approximately 53% higher than the shear resistance of the specimen with spruce side parts. The specimen with ash side parts shows a slightly lower shear resistance compared to the

specimens with spruce side parts. The connection behaviour of the specimens with hardwood side elements shows an initial slip, whereas the specimens with spruce side elements show no visible initial slip.

Since the geometry of the specimens was the same for all three wood species, the differences in the connection behaviour must be due to the different mechanical strength and stiffness properties as well as the influence of surface effects. The separation of the timber side parts from the concrete middle part after testing took much less energy for the hardwood side part specimens. It can be assumed that the adhesion shear resistance of spruce is much higher than for beech and ash.

### 3.5.5 Treatment of the timber surface before concreting

Three different treatments of the timber joint surface before casting the concrete were tested: watering the timber shortly before concreting, no treatment, and the treatment of the timber with a hydrophobic primer. Fig. 3.29 shows the load-slip curves of the specimens and Table 3.10 shows the connection properties.

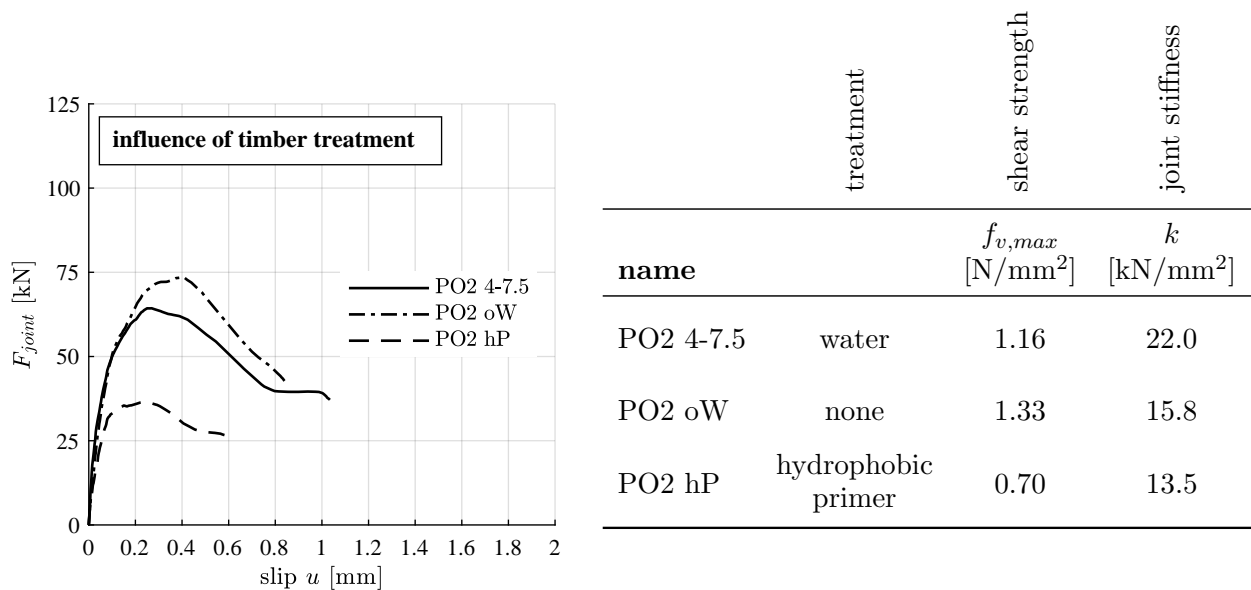


**Fig. 3.29:** Load-slip curves for different timber surface treatments before concreting

**Tab. 3.10:** Connection properties

The shear resistance of the specimens with no special treatment of the timber surface before concreting is the highest. The reference specimens with watered timber surface shows a slightly lower shear resistance, but a higher connection stiffness. In fact, the quality of connection achieved by the specimens without watering is comparable with the specimens with watering. The specimens with the hydrophobic primer show a much lower shear resistance and a lower connection stiffness. The weak connection properties of the specimens with the hydrophobic primer might be due to the poor execution of the primer application. After applying the primer, the specimens were stored in an oven over night to activate the chemical reaction. After the

wetting and drying in a short period, the timber side elements exhibited cracks and large gaps between the lamellas, which might have had a negative effect on the connection behaviour. Another possible explanation for the weak connection behaviour might be the primer itself, that prevents the adhesion effect of spruce and thus lowers the shear resistance.

### 3.5.6 Concrete treatment

Two different treatments of the concrete were tested: normal concrete vibration with a vibrating table and no vibration at all. Fig. 3.30 shows the load-slip curves of the specimens and Table 3.11 shows the connection properties.

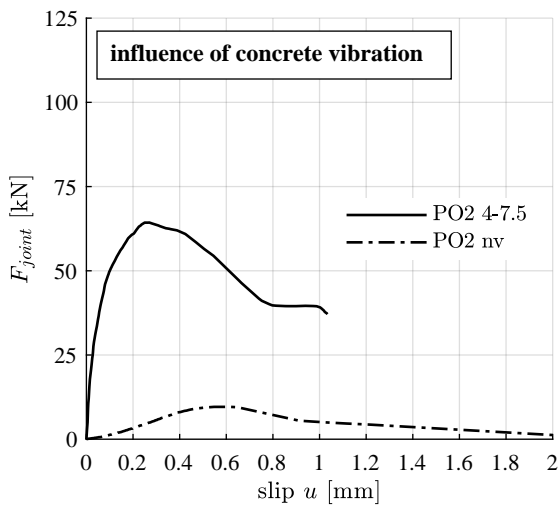


**Fig. 3.30:** Load-slip curves for different concrete treatments

	concrete treatment	shear strength	joint stiffness
name		$f_{v,max}$ [N/mm <sup>2</sup> ]	$k$ [kN/mm <sup>2</sup> ]
PO2 4-7.5	vibrated	1.16	22.0
PO2 nv	not vibrated	0.17	0.4

**Tab. 3.11:** Connection properties

The shear resistance and connection stiffness of the specimen with non-vibrated concrete is much lower than the connection properties of the reference specimen, where the concrete was vibrated. The connection of the non-vibrated concrete of specimen PO2 nv to the timber side parts was only punctual, because the concrete did not flow into the timber notches and therefore could not form concrete notches.

### 3.5.7 Direction of load to grain

Notches are ideally milled in such a way that the shear forces to be transferred to the notch front are parallel ( $\parallel$ ) to the grain direction of the wood. Therefore, the notches ideally run transverse to the lamellas and the notch front corresponds to the end grain. One configuration with three specimens (PO2 qF) was prepared with lamellas rotated by 90°, resulting in notch fronts where the shear forces must be transferred perpendicular ( $\perp$ ) to the grain. Fig. 3.31 shows the load-slip curves of the specimens and Table 3.12 shows the connection properties.

The specimens perpendicular to the grain show a clearly different load-slip behaviour than the reference specimens parallel to the grain. Both the shear resistance and the connection

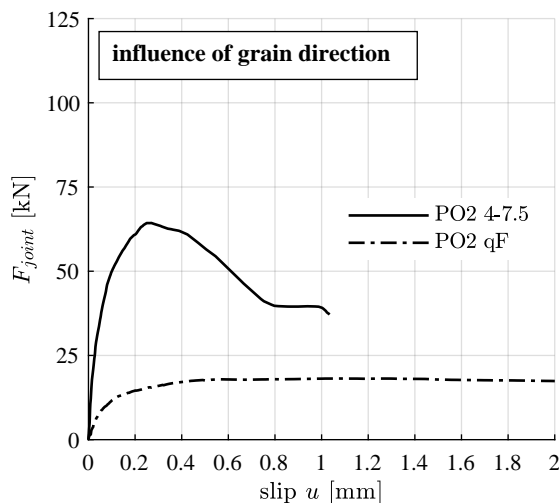


**Fig. 3.31:** Load-slip curves for different load directions to grain

	grain direction	shear strength	joint stiffness
name		$f_{v,max}$ [N/mm <sup>2</sup> ]	$k$ [kN/mm <sup>2</sup> ]
PO2 4-7.5		1.16	22.0
PO2 qF	⊥	0.33	4.1

**Tab. 3.12:** Connection properties

stiffness are significantly lower. The shear resistance of the specimens perpendicular to the grain is approximately 28% of the shear resistance of the specimens parallel to the grain. The connection stiffness of the specimens perpendicular to the grain is approximately 19% of the connection stiffness of the specimens parallel to the grain. However, the mean load-slip curve of the specimens perpendicular to the grain shows a much higher ductility. The reference specimens parallel to the grain have a maximum vertical slip of 1.26 mm, the specimens perpendicular to the grain showed a much higher deformation capacity with maximum vertical slip of 3.42 mm.

### 3.6 Specifying the design of micro-notches as TCC connection system

The two push-out series I & II were used to determine the optimum configuration for micro-notches as novel connection system for TCC slabs. Push-out series I was mainly a preliminary test series. The findings from this first push-out series I enabled the improvement of the test setup for push-out series II. Only results from push-out series II were used to specify the design of micro-notches for the further development of the concept.

The specifications of the design are based on the results presented in Chapters 3.4 and 3.5 and cover the geometry, the materials, and the production of the connection. The choice of the optimum geometry for the micro-notches is based on the three main criteria for connection systems as described in Chapter 2.1.4. The priorities for the application as connection system for TCC slabs in residential and office buildings were defined as follows:

1. **Shear resistance:** The connection must have sufficient shear strength to transfer the shear forces occurring in residential and office buildings. This criterion is part of the ultimate limit state (ULS). The verification of the load-bearing capacity of the joint must

be able to be carried out with design values. As a comparative value for the required shear strength of the joint, the design value of the shear load for the extreme case of a floor slab with very large span and high loads was determined. This lower boundary for the shear strength was determined as the stress occurring in a worst case scenario  $\tau_{v,WCS}$  for a slab of 10 m, the cross-sections thickness for concrete  $h_1 = 150$  mm and for timber  $h_2 = 210$  mm with a superimposed load of  $q_A, k = 2.0$  kN/m, a service load of  $q_N, k = 5.0$  kN/m, and a stiff connection, which results in the highest shear stresses in the joint. This design shear stress results with the span, cross-section, and loads described above and using the  $\gamma$ -method as described in Chapter 2.2.2 as:

$$\tau_{v,WCS} = 0.34 \text{ N/mm}^2 \quad (3.56)$$

If a global safety factor of  $\gamma_F = 1.7$  after SIA 265 [149] is assumed for the micro-notches, the characteristic shear strength must be at least:

$$f_{v,k} \geq \tau_{v,WCS} \cdot 1.7 = 0.59 \text{ N/mm}^2 \quad (3.57)$$

To compare this characteristic value to the experimental values obtained from the push-out tests, a factor of 1.545 is assumed according to JCSS [75] for the conversion from a characteristic (5% fractile) value to a mean value (shear strength, lognormal distribution, CoV  $\approx 25\%$ ):

$$f_{v,req} = f_{v,k} \cdot 1.545 = 0.91 \text{ N/mm}^2 \quad (3.58)$$

A connection with a shear strength larger than or equal  $f_{v,req}$  is sufficient. A higher shear strength does not bring further value, since bending tensile failure in timber becomes decisive.

2. **Connection stiffness:** A high connection stiffness of the connection system is favourable for the serviceability limit state (SLS), which governs the design of TCC slabs. A high connection stiffness leads to a higher bending stiffness of the composite slab. The higher bending stiffness leads to lower deflections and better vibration behaviour and thus enables more slender cross-sections. The higher the connection stiffness, the more load is taken by the connection. Since the bending tension failure of the timber cross-section is often decisive for ULS, the bending and tensile stresses in the timber bottom edge should be kept as low as possible. A high connection is thus not only favourable for the SLS, but also for the ULS. The connection with the highest connection stiffness is therefore the most favourable regarding this criterion.
3. **Ductility:** The advantages of the ductility of connection systems were presented in Chapter 2.1.4. In this study, however, ductility is of minor importance: The design for planar TCC system used in residential and office buildings is governed by the requirements to fulfil the SLS verifications. With the cross-sections of the components determined accord-

ing to the SLS requirements, the decisive verification for the ULS is the combination of bending and tension in the timber. The utilisation of the shear strength in timber and joint always remains below the utilisation of the combined stress from tension and bending. Bending tension is a very brittle failure. In the study of Boccadoro [8], ductility of the slab could be achieved with great effort by clever design of the cross-section and connecting them with end-to-end screws, elongated screw holes, and using polystyrene buffers on the notch fronts. In this study, the focus was on the practicality of a TCC slab with the novel connection system. Therefore, ductility was not set as a mandatory criterion for the micro-notches.

Fig. 3.32 shows the connection properties for the different configurations evaluated from the push-out series II. The mean value for each configuration is shown with a marker: plus sign for geometry, square for timber surface treatment, diamond for wood species, asterisk for concrete treatment, and cross for direction to grain. The error bars depict the range of values obtained in the configurations with three specimens. The lower boundary shear strength  $f_{v,req}$  can be covered by all configurations except for the specimen with non-vibrated concrete (PO2 nv), the specimens with the shear forces transferred perpendicular to grain (PO2 qF) and the specimens treated with hydrophobic primer (PO2 qF). All other configurations fulfil the shear resistance requirements. Configurations PO2 4-7.5 and PO2 4-2.5 show the highest connection stiffness and similar shear resistance. The load-slip behaviour of configuration PO2 4-7.5 is, however, much more ductile than the very brittle behaviour of configuration PO2 4-2.5 (Fig. 3.27). Configuration PO2 4-7.5 was therefore chosen as optimum geometry.

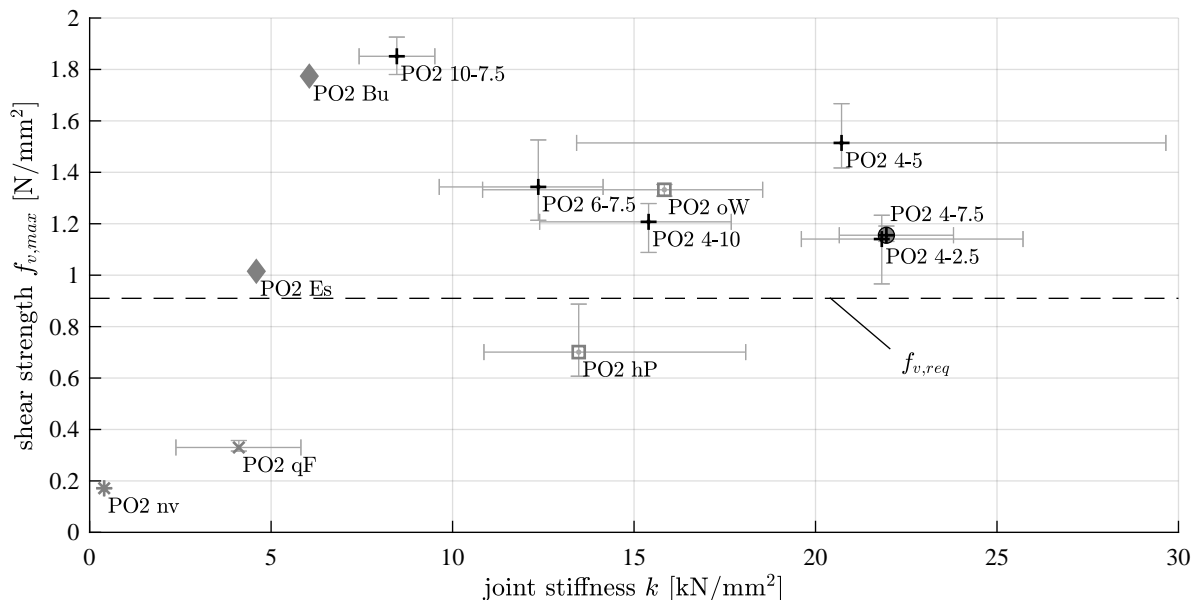


**Fig. 3.32:** Comparison of the connection properties of all configurations tested in push-out series II. The reference configuration PO2 4-7.5 is marked with a circle.

The evaluation of the treatment of the timber surface before concreting showed similar results for both watered and non-watered specimens. The shear resistance of the specimens

with non-watered timber surfaces was higher in all three specimens than the shear resistance of the specimens with watered timber surfaces (see Table B.1). The situation is reversed with the connection stiffness. However, the connection stiffness of both configurations is very high and can be considered as almost rigid. Thus, no clear statement can be made as to whether the watering of the timber surface before concreting has a positive effect on the connection properties. At least, no negative effect was observed. However, the use of a hydrophobic primer is not recommended.

The choice of the materials for the design of micro-notches as connection system for TCC slabs is straightforward: For TCC slabs with BST elements, spruce is distinctly better suited for the connection with concrete than the hardwood species beech and ash. Although the beech specimen displayed a higher shear resistance, the connection stiffness of the spruce specimens was higher and their shear resistance suffices the requirement described in equation 3.57. For the concrete part, normal-strength concrete with maximum grain size  $D_{max} = 16$  mm was used which developed good strength and stiffness properties and formed a neat interlocking in the notches.

The thorough vibration of the concrete is of great importance. If the concrete is not vibrated, it must be assumed that no interlocking can be formed and that the connection properties are substantially inferior.

The transfer of shear loads perpendicular to grain is possible, but the connection behaviour shows a significantly lower shear resistance and connection stiffness.

### 3.7 Conclusions

The investigations on the local load-bearing behaviour of micro-notches as a connection system for TCC slabs showed:

- a very high connection stiffness (joint stiffness  $k$  values over  $10 \text{ kN/mm}^2$  for most configurations)
- sufficient shear strength for the application in residential and office buildings with spans up to 10 m and high loads
- some ductility in form of a deformation capacity up to 1.26 mm for the shear transfer parallel to grain (specimen PO2 4-7.5 1) and up to 3.42 mm for the shear transfer perpendicular to grain (specimen PO2 qF 1) on a joint length of 350 mm.

The optimum of the tested geometries for micro-notches was determined with a notch depth of  $t_{MN} = 4$  mm and inclination of the notch bottom of  $\beta = 7.5^\circ$ , leading to a notch front angle of  $\alpha = -7.5^\circ$  and a notch length of  $l_{MN} = 29.9$  mm. Spruce as timber material and carefully vibrated normal-strength concrete with maximum grain size  $D_{max} = 16$  mm are well suited for a well-established formation of the interlocking connection.



The influence of the notch front angle and the influence of water treatment of the timber surface before concreting could not yet be fully assessed. These two parameters were therefore included in the further investigations.



## Chapter 4

# Global behaviour of micro-notches

### 4.1 Introduction and literature review

#### 4.1.1 Overview

The connection properties (consisting of the shear capacities  $f_{v,y}$  and  $f_{v,max}$  and the connection stiffness  $K$ ) have been determined for various geometries and other configuration parameters in Chapter 3. The local connection behavior can be considered as a system cut out of a floor slab, but this system only gives information about the local effects. To fully understand the performance of micro-notches in TCC slabs, the micro-notches must be tested in the entire composite system in the real situation of a vertically loaded beam. Bending tests in a practice-oriented scale can correctly represent the effects of size, bending moments as well as subsequent curvature, and the load transfer into the supports.

A series of 4-point bending tests was performed to assess the global behaviour of TCC slabs with micro-notches as connection system [117]. The focus of this series was to investigate the influence of the notch front angle on the load-bearing behaviour in a beam. Further test parameters were the influence of the timber surface treatment before concreting, the duration of load application, and the influence of additional screws. The transfer of shear forces was parallel to the grain. Six specimens with BST elements and one specimen with a CLT element were tested.

#### 4.1.2 Previous experimental and numerical research

Table 4.1 lists a selection of experimental bending tests on planar TCC slabs with BST elements with notches that can be found in the literature. All studies were performed in a 4-point bending test setup.

**Tab. 4.1:** Literature selection of experimental 4-point bending test series for TCC with notches and softwood BST elements. Every row corresponds to one test configuration.

Parameters altered in relation to the reference configuration are highlighted in gray

source	span		concrete thickness	concrete class	reinforcement	timber thickness	timber class or $E_2$	specimen width		notch depth	notch length	no. of notches <sup>a</sup>	screws <sup>b</sup>	front angle	no. of specimens
	$l$ [m]	$h_1$ [cm]			$A_{s,l}$ [mm <sup>2</sup> ]	$h_2$ [cm]		$b$ [mm]	$t_{MN}l_{MN}$ [mm][mm]					$\alpha$ [°]	$n$
Richart [129]	3	13	?	?	?	9/18 <sup>P</sup>	14GPa	292	25	152	5	-	-	0	2
	3	13	?	?	?	9/18 <sup>P</sup>	14GPa	292	25	152	5	spikes	-	0	2
Braun [13]	5.2	6	?	?	?	14	?	500	15	?	3	C	?	?	1
Zöllig [169]	8	13	B45/35	118	118	17	?	336	30	160	2	B	+8	+8	2
	8	13	B45/35	118	118	17 <sup>c</sup>	?	336	20	160	2	B	+8	+8	1
Frangi [47]	5.6	8	C30/37	98	98	10	C22	690	20	160	4	rods	+10	+10	1
	5.6	8	C30/37	98	98	10	C22	690	20	160	4	dowels	+10	+10	1
	5.6	8	C30/37	98	98	10/12 <sup>P</sup>	C22	690	20	160	-	-	-	-	2
	5.6	8	C30/37	98	98	10/12 <sup>P</sup>	C22	690	20	160	1	-	+10	+10	1
Gutkowski [61]	3.5	6.4	?	118	118	8.9	? <sup>G</sup>	267	32	127	2	C	+15	+15	10
	3.5	6.4	?	118	118	8.9	? <sup>N</sup>	305	32	127	2	C	+15	+15	10
Michelfelder [110]	4.8	8	C35/45	79	79	12	C16	500	30	200	3	C	0	0	1
	4.8 <sup>d</sup>	8	C35/45	79	79	12	C16	500	20	200	3	C	0	0	1
Kudla [92]	3.8 <sup>d</sup>	12	C30/37	151	151	12	GL24h	400	20	160	1	C	0	0	3
	3.8 <sup>d</sup>	12	C30/37	151	151	12	GL24h	400	20	160	1	-	0	0	3
	3.8 <sup>d</sup>	12	C30/37	151	151	12	GL24h	400	20	160	1	F	0	0	3
	5.8	12	C30/37	151	151	12	GL24h	400	20	160	3	C	0	0	3
	5.8	12	C30/37	151	151	12	GL24h	400	20	160	3	B	0	0	3
	5.8	12	C30/37	151	151	12	GL24h	400	20	160	3	-	0	0	3

<sup>a</sup> number of notches per side

<sup>b</sup> position of the screw: C = center, B = back, F = as reinforcement of the notch front, see also Fig. 3.2

<sup>c</sup> BST element specially milled for good acoustics, notched support

<sup>d</sup> 4-point bending with loads near to the supports

<sup>P</sup> alternating height of lamellas

<sup>G</sup> lamellas connected by adhesive

<sup>N</sup> lamellas connected by nails

**Richart et al.** [129] tested different connection systems for TCC bridges on beams with 3 m span. They measured strains at mid-span at four different positions of the cross-section, the horizontal slip between timber and concrete directly over the supports, and the global deflection at mid-span. Apart from composite beams connected with screws and nails, they tested two

beam configurations with indentations that they called saw-tooth “daps” cut into the timber as shown in Fig. 4.1. For the specimens with “daps” only, they observed a high initial slip, low connection stiffness, and low load-bearing capacity. For the specimens with additional spikes, the connection stiffness and load-bearing capacity were considerably higher, as could be seen on the six times lower horizontal slip measured. For both configurations, the failure occurred first in the timber due to bending tension or by shearing off of the concrete “daps”.

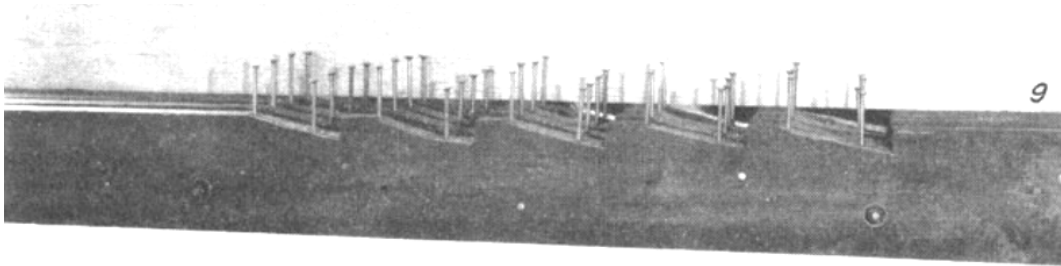


**Fig. 4.1:** “Daps” with spikes in timber specimens for TCC bending tests from Richart et al. [129]

**Braun** [13] tested one TCC beam with 5.2 m span. The connection was realised with three notches per side and one additional screw in the center of each notch (center position C according to Fig. 3.2). The screws were installed on the finished TCC beam from the top of the concrete. The load-bearing behaviour was linear elastic, but the failure load was not reached.

**Zöllig** [169] tested three specimens with 8 m span, two notches per side, and screws positioned 300 mm near to each notch towards mid-span (back position B according to Fig. 3.2). One of the three specimens had a special timber cross-section with millings for an improved acoustic performance and notched supports. The two specimens with the non-compromised timber cross-section failed in the finger-joints in timber at mid-span. The specimen with special millings failed at a 10% lower load due to tensile failure perpendicular to the grain in the area of the supports.

**Frangi** [47; 45] tested four different configurations of BST-concrete elements with 5.6 m span. Two specimens were tested with four notches per side and additional glued-in rods or dowels in the center of the notch. Three specimens had BST elements with alternating lamellas and the connection due to adhesion and friction was tested. One of these specimens had an additional notch per side near the supports. The beams were tested in >1000 load cycles to 30% of the estimated failure load and then loaded to failure. The specimens with alternating lamellas showed a rigid connection throughout the testing, until the ultimate failure of the timber due to bending tension. The specimens with notches and screws showed a rigid connection in the lower load levels and low horizontal slip in the higher load levels until bending tension failure in timber. The tests showed that screws do not increase the load-bearing capacity or the connection stiffness.

**Gutkowski et al.** [60; 61; 62] tested 20 specimens with 6.4 m span in 4-point bending tests. The connection was realised with two notches per side and additional dowel-type connectors. The dowel-type connectors had a plastic tube around the thread in the area of the concrete cross-

section. They were accessible from the top of the concrete layer and tightened after concrete curing. Ten specimens had BST elements made of eight lamellas nailed together with a total width of 305 mm. The other ten specimens had BST elements made of three boards glued together with a total width of 267 mm. The main failure observed was bending tension failure in the timber at mid-span. Some specimens failed due to timber shear between the last notch and the beam end or concrete shear in the notches near to the load application points.

**Michelfelder** [110] tested three specimens with 4.8 m span in 4-point bending tests with two different positions of the loads. The connection was realised for all specimens with three notches per side with additional self-tapping wood screws in the center of each notch. Two specimens were tested with the two loads in the approximate third points of the span. This load position led to bending tension failure in the timber. The corresponding load-bearing behaviour was linear elastic to failure. One specimen was tested with the two loads positioned nearer to the supports. This load position led to a combination of failure modes: bending tension failure in the timber in the area between the load applications points, shear failure of the timber in the last notch, and shear failure of the concrete at the top edge of the two inner notches. The corresponding load-bearing behaviour was linear elastic until shear failure of the timber notch, followed by distinct deformations until the ultimate failure due to bending tension in the timber. All specimens showed a very stiff connection behaviour at service load level. She also modelled the TCC beams using a finite element model to assess the influence of additional screws. As a verification, she simulated the experiments by Braun [13] and Frangi [47] and found good agreement of the predicted load-deflection curves. She was able to reconstruct the observed failure modes for both load positions. The evaluation of the shear force transfer showed that the screws take approximately 20 % and the notch front the remaining 80 % of the shear forces. Notches with or without screws showed both a very stiff, linear load-deflection behaviour. The screws decreased the deflection by only 6 %. No uplift occurred for both systems with or without screws.

**Kudla** [92] performed two types of beam tests in 4-point bending test setups: 9 specimens with a short span of 3.8 m called “shear beams” and 9 specimens with a longer span of 5.8 m called “bending beams”. Both beam types were tested with three configurations of three specimens each. The “shear beams” were connected by only one notch and one optional screw in the center or as reinforcement of the notch front (front position F according to Fig. 3.2). The objective of these tests was to investigate the behaviour of one notch subjected to bending without the load-sharing effects of multiple notches. The “bending beams” were connected by three notches and one optional screw in the center of the notch or in the back of the notch (back position B according to Fig. 3.2). The “shear beams” showed linear elastic load-bearing behaviour until the first failure in the notch due to concrete shear, then ultimate failure due to bending tension in the timber at mid-span. The “bending beams” showed linear elastic behaviour until the timber notch front of the outer notches start to deform under compression. With increasing load, the timber compression failure extended to the inner notches and the effective bending stiffness of the beam decreased continuously. The beams ultimately failed in bending tension of the timber at mid-span. She validated the experimental bending tests with strut-and-tie models

and reconstructed the linear elastic phase of the behaviour observed. She found that for a slip modulus  $K \geq 1000 \text{ kN/mm/m}$ , the forces in the beam do not significantly change anymore. Because of this very high stiffness of the connection, she could also find no influence of the screws used as reinforcement in the notch front. She investigated the influence of the shear deformations in the components and developed an effective spring stiffness by superposition of the shear stiffness and the connection stiffness. Using this superposed spring stiffness, she found good agreement of load-deflection curves with the experimental data.

The studies about notch connections of TCC beams with BST elements and normal-strength concrete described above show the high connection stiffness and linear global load-bearing behaviour of notches. In most studies, the governing failure was the failure due to combined bending tension in timber. In some studies, the redundancy of additional screws could be proven in experimental and numerical investigations.

### 4.1.3 Analytical and numerical models for TCC slabs

Models to predict or assess the load-bearing behaviour of TCC slabs are described in Chapter 2.2. The most commonly used is the  $\gamma$ -method that outputs the effective bending stiffness  $EI_{eff}$ . This method is a simplified method that considers the elastic range and is applicable for the design of single-span, uniform loaded TCC slabs with approximately continuous connections and constant material properties along the span. An extended version of the gamma method was developed by Frangi and Fontana [49] to relate to the behaviour of notches with dowel-type fasteners with a distinct linear elastic phase followed by a distinct plastic phase. A detailed consideration of the different states and failure loads of TCC slabs with notches was developed by Boccadoro [8]. This model considers the cracking of concrete, the yielding of the connection, the yielding of the concrete due to compression, and the bending tension failure of the timber. The TCC system and the notches studied to develop this model were designed to provoke the most ductile failure, namely the compression failure of the timber front notch, to obtain a ductile global behaviour of the TCC slab. In various other studies, the structural behaviour of TCC slabs is predicted or assessed with strut-and-tie models [169; 110; 93]. These models are well suited for point load situations and locally arranged connectors with large distances between them.

Most of the experimental studies described above focused on the global load-bearing behaviour of the TCC slab with notches in general and the composite joint was not specifically tested. As a consequence, the first failure mode observed was often bending tension in timber. The 4-point bending tests with load application points close to the supports as performed by Michelfelder [110] and Kudla [93] were aimed to test the connection system by reducing the ratio of the bending moment to the shear force. The 4-point bending tests described in the following also focused on testing the micro-notches by provoking the failure in the composite joint as first failure.

## 4.2 Experimental 4-point bending test series

### 4.2.1 Materials and methods

#### Test setup

The bending tests were conducted as 4-point bending tests, which has some advantages compared to other bending test setups: The area between load application points and supports is exposed to constant shear. All connectors in this area are subjected to the same shear load. The positioning of the load application points allows the regulation of the ratio between bending moment and shear forces. This advantage was of great importance in this test series because the objective was to test the micro-notches. The cross-sections and the loading situation were dimensioned so that the failure first occurred in the composite joint. The test setup with two cylinders as load application points is also less costly to install than a test setup for a uniform load situation. The load situation with two point loads represents an unfavourable load arrangement compared to the situation in practice, where the majority of the loads is distributed along the span. The results obtained in 4-point bending tests are therefore on the conservative side compared to the usual loading situation in practice.

Figure 4.2 shows the test setup for the 4-point bending tests. The composite beams were mounted over a span of 3.7 m on a fixed support with hinge on the left and a rolling support on the right. The two point loads were introduced with hydraulic cylinders arranged symmetrically with a distance of 1.33 m to the supports. The hydraulic cylinders were operated load-controlled using a pendulum manometer. The pressure load of the manometer was divided equally between the two cylinders.

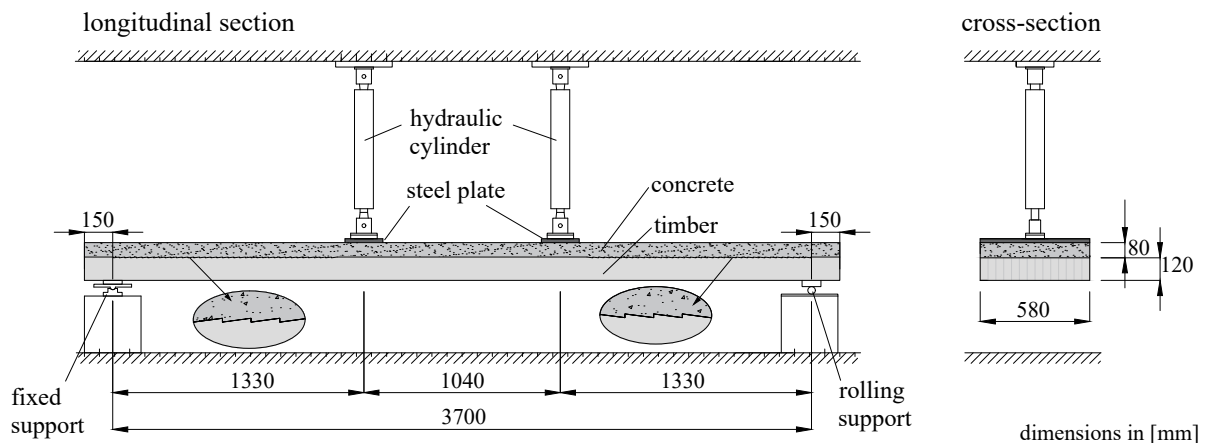
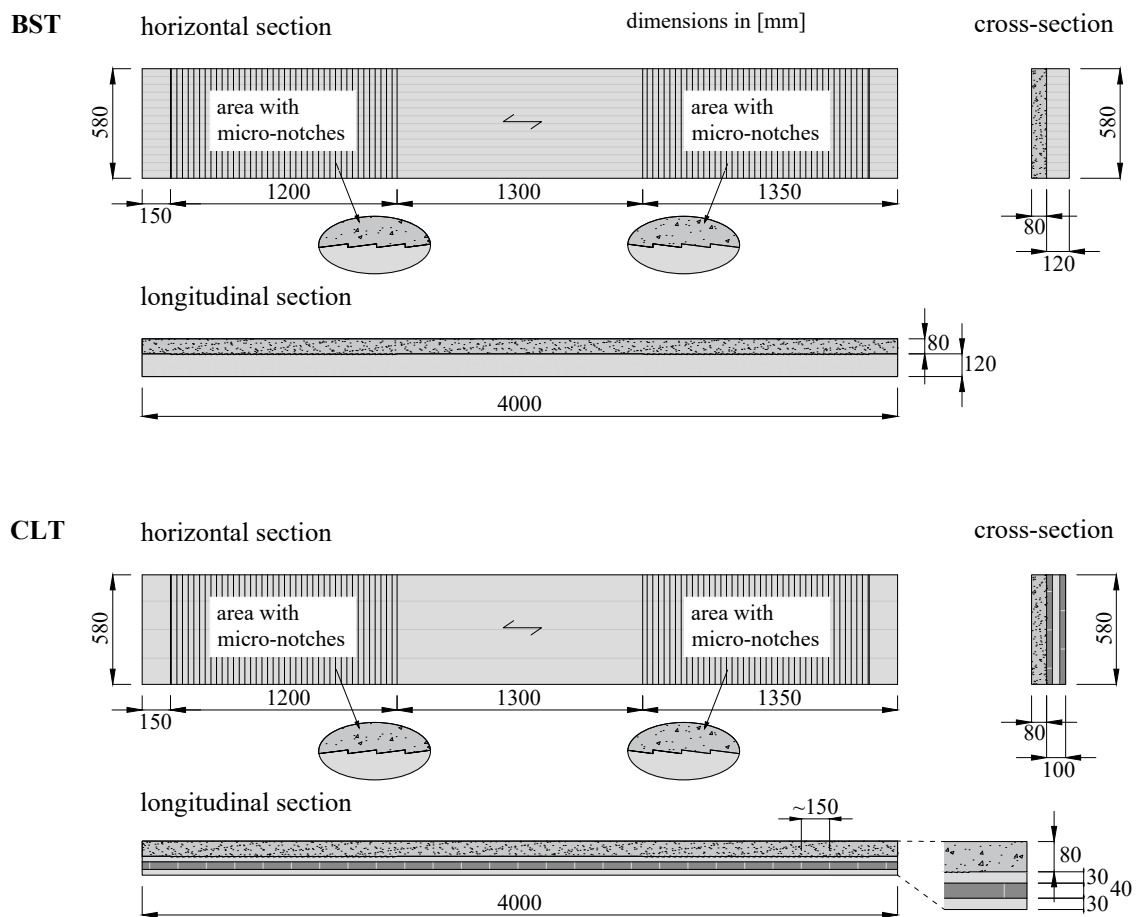


Fig. 4.2: Test setups for 4-point bending tests



## Specimens

Seven composite beam specimens were tested in the 4-point bending test series. The design and dimensions of the specimens are shown in Fig. 4.3. Six specimens featured a BST element with a total length of 4 m, a thickness of 120 mm, and a width of 580 mm composed of 14 lamellas of approximately 41 mm width each. The lamellas were solely connected by kiln-dried beech dowels. One specimen featured a CLT element with the same width and length and total thickness of 100 mm, composed of a symmetrical layup of 30-40-30 [mm]. The micro-notches were milled into the timber surface on a length of 1.2 m in the shear areas between the support and load application points on both sides of the beam. The rest of the joint length was planed evenly. The concrete layer was cast on top with the same length and width as the timber elements. The concrete thickness  $h_1$  was 80 mm. Figure 4.3 shows the horizontal section of the BST and CLT elements with the areas milled with micro-notches and the cross-sections of the composite beam.



**Fig. 4.3:** Specimens for 4-point bending tests with BST elements

The materials used for the bending tests were normal-strength concrete and spruce/fir timber. The specimens were produced in two steps: the production of the timber elements and milling of the micro-notches in the company of the BST producer as well as the casting of the concrete at ETH Zurich.

In the first step, the timber lamellas were assembled to elements, connected by beech dowels, and their surface was planed. The width of 580 mm corresponds to one standard element width of the BST producer [151]. The CLT element was taken from an existing stock (several months of storage). The timber elements were cut to length and the micro-notches were milled into the planed timber surface by a CNC milling machine using a dovetail tool. The fully prepared timber elements were then transported to ETH Zurich. The moisture content was determined with electric moisture meters. The MOE of each timber element was determined according to EN 408 [36]. The mean moisture content at three points of time and the mean value of the MOE for all timber elements are given in Table 4.2.

**Tab. 4.2:** Material properties of timber elements for 4-point bending test series

elements	$n$	mean moisture content			mean MOE $E_2$ [N/mm <sup>2</sup> ]
		upon arrival in the lab [%]	before concreting [%]	after stripping of formwork [%]	
BST	6	13.0	12.9	16.5	10'583
CLT	1	15.1	10.6	22.9	10'726

In the second step, the concrete slab was casted on top. A reinforcing mesh of type K335 was placed in the center of the concrete height. The longitudinal reinforcement were four bars of  $\varnothing$  8 mm resulting in a total area of  $A_{s,l} = 201 \text{ mm}^2$ . The timber surface was watered one day before and approximately one hour before casting the concrete. The concrete mixture was prepared for a concrete strength class C25/30 with a maximum grain size of 16 mm and the shrinkage reducer MasterLife SRA 895. Air void content, flow spread, and density of the fresh concrete were determined to assess the quality of the concrete before casting. Concrete samples in form of cubes and cylinders were casted from the same batch as the specimens to assess the properties of the hardened concrete. The concrete strength determined from the hardened cube and cylinder samples at age 31 days corresponds to strength class C30/37 with a MOE of  $34\,992 \text{ N/mm}^2$ . The mean value of concrete tension strength was  $f_{ctm} = 3.0 \text{ N/mm}^2$ , determined in double-punch tests [23]. The concrete age at the time of testing was 31 to 121 days, depending on the test specimen.

Table 4.3 lists the configurations tested in the 4-point bending tests. The main testing parameter was the angle of the notch front and the treatment of the timber surface before concreting. Besides, two other parameters were investigated. All tested parameters are briefly outlined below.

**Tab. 4.3:** Specimen configurations of bending tests series I. Every row corresponds to one specimen.

Parameters altered in relation to the reference configuration are highlighted in gray

name	concrete thickness	concrete age <sup>a</sup>	timber thickness	timber	timber treatment <sup>b</sup>	direction of grain	specimen width	span	load situation <sup>c</sup>	duration of load	notch depth	notch length	additional screws	front angle	no. of specimens
	$h_1$ [mm]	[d]	$h_2$ [mm]				$b$ [mm]	$l$ [mm]		[h]	$t_{MN}$ [mm]	$l_{MN}$ [mm]		$\alpha$ [°]	
H0-1	80	41	120	BST	w		580	370	4PB	0	4	30	-	0	1
H0-2	80	45	120	BST	w		580	3700	4PB	<span style="background-color: #cccccc;">72</span>	4	30	-	0	1
H5-1	80	31	120	BST	w		580	3700	4PB	0	4	30	-	<span style="background-color: #cccccc;">-5</span>	1
H5-2	80	121	120	BST	w		580	3700	4PB	<span style="background-color: #cccccc;">72</span>	4	30	-	<span style="background-color: #cccccc;">-5</span>	1
H0-oW	80	31	120	BST	-		580	3700	4PB	0	4	30	-	0	1
H0-S	80	35	120	BST	w		580	3700	4PB	0	4	30	<span style="background-color: #cccccc;">✓</span>	0	1
H0-CLT	80	35	<span style="background-color: #cccccc;">100</span>	<span style="background-color: #cccccc;">CLT</span>	w		580	3700	4PB	0	4	30	-	0	1
Total specimens in 4-point bending test series															<b>7</b>

<sup>a</sup> concrete age at day of testing to failure<sup>b</sup> treatment of the timber surface before concreting: w = water, - = no water, hP = hydrophobic primer<sup>c</sup> load situation: 4PBB = 4-point-bending, UL = uniform load

- The **angle of the front notch**  $\alpha$  has already been investigated in the small-scale push-out tests. However, no direct tendency regarding the connection properties was observed. Because of the fixed opening angle of the notch at  $75^\circ$  in the push-out test series, the notch front angle  $\alpha$  determined the length of the notch  $l_{MN}$  and was therefore not an independent parameter. Shorter notches led to more brittle failure, whereas the influence on shear resistance and connection stiffness could not be assessed. An undercut notch front (notch front angle  $\alpha < 0^\circ$ ) has an increased vertical force component leading to tension perpendicular to the grain in the timber. However, there are different hypotheses on how an undercut notch front may have a positive effect against uplift of the concrete layer: First, the friction force in the notch front is higher with an undercut notch front angle. Second, due to the curvature in loading situations where the beam is subjected to bending, the undercut notches may lead to a clamping effect. Therefore, two different notch front angles  $\alpha$  were investigated in the bending tests: no undercutting ( $\alpha = 0^\circ$ ) and slight undercutting ( $\alpha = -5^\circ$ ) as illustrated in Fig. 4.4. Due to milling difficulties, a planned configuration with  $\alpha = -10^\circ$  could not be produced properly.
- The **treatment of the timber surface** has also already been investigated in the small-scale push-out tests. The push-out test results showed that the watered and non-watered specimens had the best connection properties and the specimens with hydrophobic primer

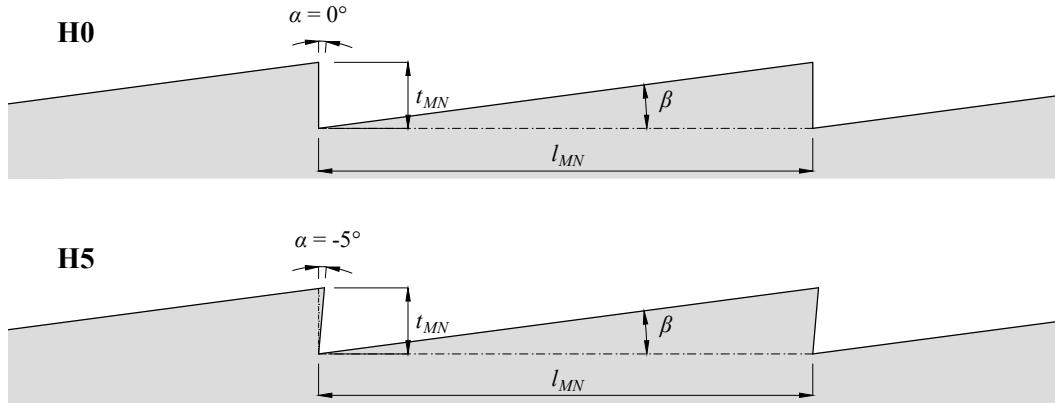


**Fig. 4.4:** Notch front angle  $\alpha = 0^\circ$  (specimens H0) and undercut  $\alpha = -5^\circ$  (specimens H5)

on the timber surface showed less shear resistance and less connection stiffness. No significant difference between the watered and the non-watered specimens regarding their connection behaviour could be observed. In the bending tests, one specimen was produced without watering the timber surface before concreting to further test this parameter on the global scale.

- To investigate the influence of additional dowel-type fasteners, one specimen was produced with **screws as additional connector**, supplementing the micro-notch system. Screws of type VB-48-7.5 X 100 [28] were used. In the shear areas, the screws were installed crosswise in pairs at an angle of  $45^\circ$ . In the middle area with no shear, the screws were installed single and vertically. The screws or screw pairs were arranged at an approximate distance of 50 cm along the span in two rows with a distance of 32 cm. A total of 22 screws were installed.
- The **duration of loading (DOL)** in the bending tests was usually approximately 30 min until reaching the failure load. To investigate the influence of longer exposition to load, the two specimens H0-2 and H5-2 were loaded during 72 h with increasing load levels.

### Measurement points and testing procedure

The measurement points for the bending test series are listed in Table 4.4. The positions of the measurement points are shown in Fig. 4.5. The induced pressure load  $F_{tot}$  is measured directly by a pendulum manometer. The global deflections  $w_i$  are measured in the center of the transverse section at mid-span  $w_M$  and underneath both load application points  $w_L$  and  $w_R$ . The relative slip between timber and concrete was measured with linear variable differential transformers (LVDT) on the front side of the specimens. The vertical relative slip  $v$  and the horizontal relative slip  $u$  were measured for both shear areas left and right at decisive points: The vertical relative slip was measured at mid-span  $v_M$  and the middle of the shear areas left  $v_L$  and right  $v_R$ . The horizontal relative slip was measured at both ends of the specimens  $u_L$  and  $u_R$  and in the middle of the shear areas  $u_{LM}$  and  $u_{RM}$ .

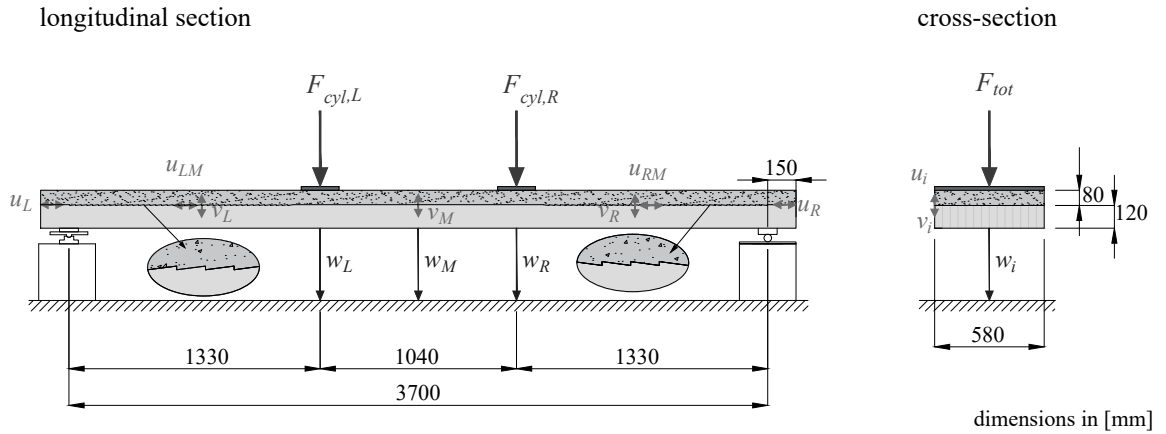


**Fig. 4.5:** Measurement points for the 4-point bending test series

**Tab. 4.4:** Measurement points for the 4-point bending test series

measurement	position	name	device	capacity	accuracy
hydraulic pressure		$F_{tot}$	PM <sup>a</sup>	220 bar	$\pm 0.5\%$
global deflection	left load	$w_L$	LVDT	$\pm 50$ mm	$\pm 0.3\%$
	mid-span	$w_M$	LVDT	$\pm 50$ mm	$\pm 0.3\%$
	right load	$w_R$	LVDT	$\pm 50$ mm	$\pm 0.3\%$
vertical slip	left shear area	$v_L$	LVDT	$\pm 5$ mm	$\pm 0.2\%$
	mid-span	$v_M$	LVDT	$\pm 5$ mm	$\pm 0.2\%$
	right shear area	$v_R$	LVDT	$\pm 5$ mm	$\pm 0.2\%$
horizontal slip	left end	$u_L$	LVDT	$\pm 5$ mm	$\pm 0.2\%$
	left shear area	$u_{LM}$	LVDT	$\pm 5$ mm	$\pm 0.2\%$
	right shear area	$u_{RM}$	LVDT	$\pm 5$ mm	$\pm 0.2\%$
	right end	$u_R$	LVDT	$\pm 5$ mm	$\pm 0.2\%$

<sup>a</sup> Pendulum manometer

The testing procedure was conducted based on DIN EN 26891 [20] with a first loading cycle to 40% of the estimated failure load  $F_{max,est}$ , discharge to 10% of  $F_{max,est}$ , and reloading cycle to failure. The tests were conducted load-controlled with an approximately constant load speed. Specimen H0-1 was tested until failure of the composite joint, then the load was discharged and the failed specimen was tested again to assess the residual load-bearing behaviour with no composite action in one shear field. This test is marked as H0-1 residual. Specimens H0-2 and H5-2 were loaded during a total time of 72 h. The first loading cycle was held at 30 kN for 24 h, then increased to 40 kN for 24 h, and 50 kN for 24 h. Before every load increase, the load was discharged to 10% of  $F_{max,est}$ . After 72 h, the specimens were loaded to failure.

## 4.2.2 Results

### Failure modes

The observed failure modes in the 4-point bending test series were:

- combined bending tension failure in the timber bottom fibre at mid-span, denoted as 2BT (Fig. 4.6a)
- failure of the micro-notches due to shear failure both in timber and concrete, denoted as MN (Fig. 4.6b)

In addition, cracking of the concrete, denoted as 1cr, occurred at mid-span and in the areas of the load application points (Fig. 4.6c). Cracking of concrete is not considered a failure mode of the beam.

The failure of the micro-notches in one of the shear areas (left or right side between the load application points and the supports) was the first failure to occur in most tests. As soon as the composite action on one side of the beam was lost, the bending stiffness of the beam decreased rapidly. The combined bending tension failure in the timber at mid-span followed shortly after the micro-notch failure. The concrete top layer remained mostly unharmed during the testing. Only at the very end of the testing, cracking occurred at the bottom of the concrete cross-section at mid-span and in the areas of the load application points (Fig. 4.7). The failure of the micro-notches was a combination of timber shear failure and concrete shear failure similar to the failure modes observed in the push-out tests. As soon as the connection began to fail due to shear in the timber or the concrete notches, the composite action failed and the concrete top layer was pushed over the timber bottom layer (Fig. 4.6b).

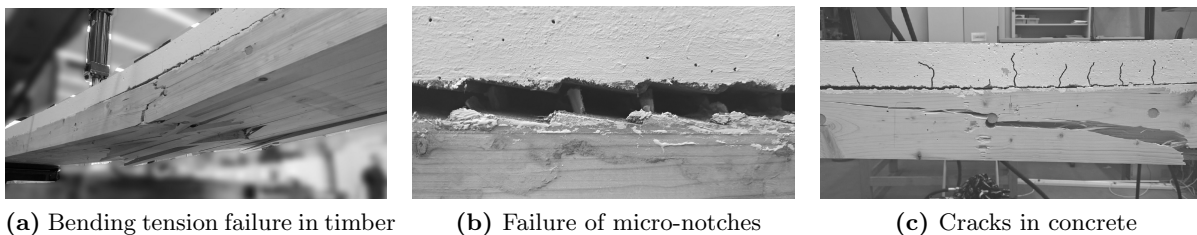
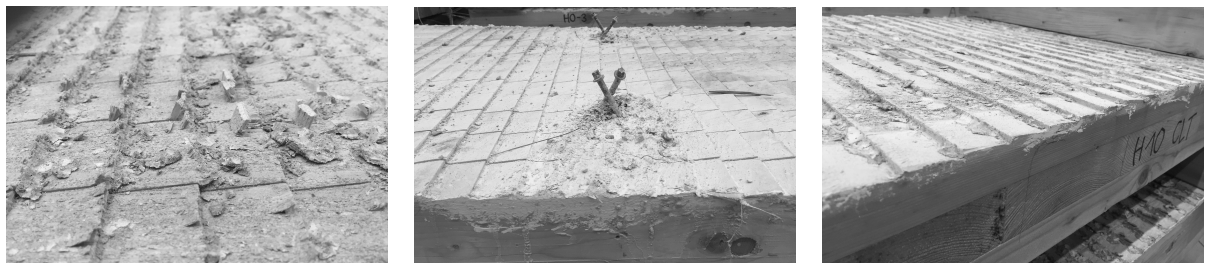


**Fig. 4.6:** Failure modes and concrete cracking observed during 4-point bending tests

After testing, the specimens were opened by removing the concrete layer from the timber element to investigate the fracture patterns in the composite joint. Fig. 4.8 shows the fracture patterns found inside the composite joint: notches sheared in timber and concrete (Fig. 4.8a), the mostly intact screws in specimen H0-S (Fig. 4.8b), and the intact notches found in all undamaged shear fields and in specimen H0-CLT (Fig. 4.8c).



**Fig. 4.7:** Specimen H0-1 after failure



(a) Timber notches shear failure in failed specimen H0-1      (b) Screws and intact notches in failed specimen H0-S      (c) Intact notches in failed specimen H0-CLT

**Fig. 4.8:** Fracture patterns on the timber element after testing

**Global deflections**

Figure 4.10 shows the global deflections  $w_i$  per test: deflections at mid-span  $w_M$ , below the left load application point  $w_L$ , and below the right load application point  $w_R$ .

**Relative slip between timber and concrete**

Figure 4.11 shows the relative vertical slip  $v_i$  in all positions as well as the relative horizontal slip  $u_i$  in all positions for all specimens. The respective slip measurement points are shown in Fig. 4.5 and 4.9, where the latter also shows the convention for negative and positive slip values of the vertical slip  $u_i$ .

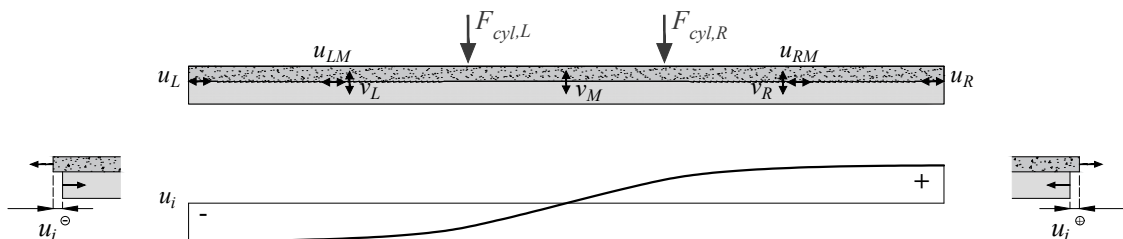


**Fig. 4.9:** Slip convention

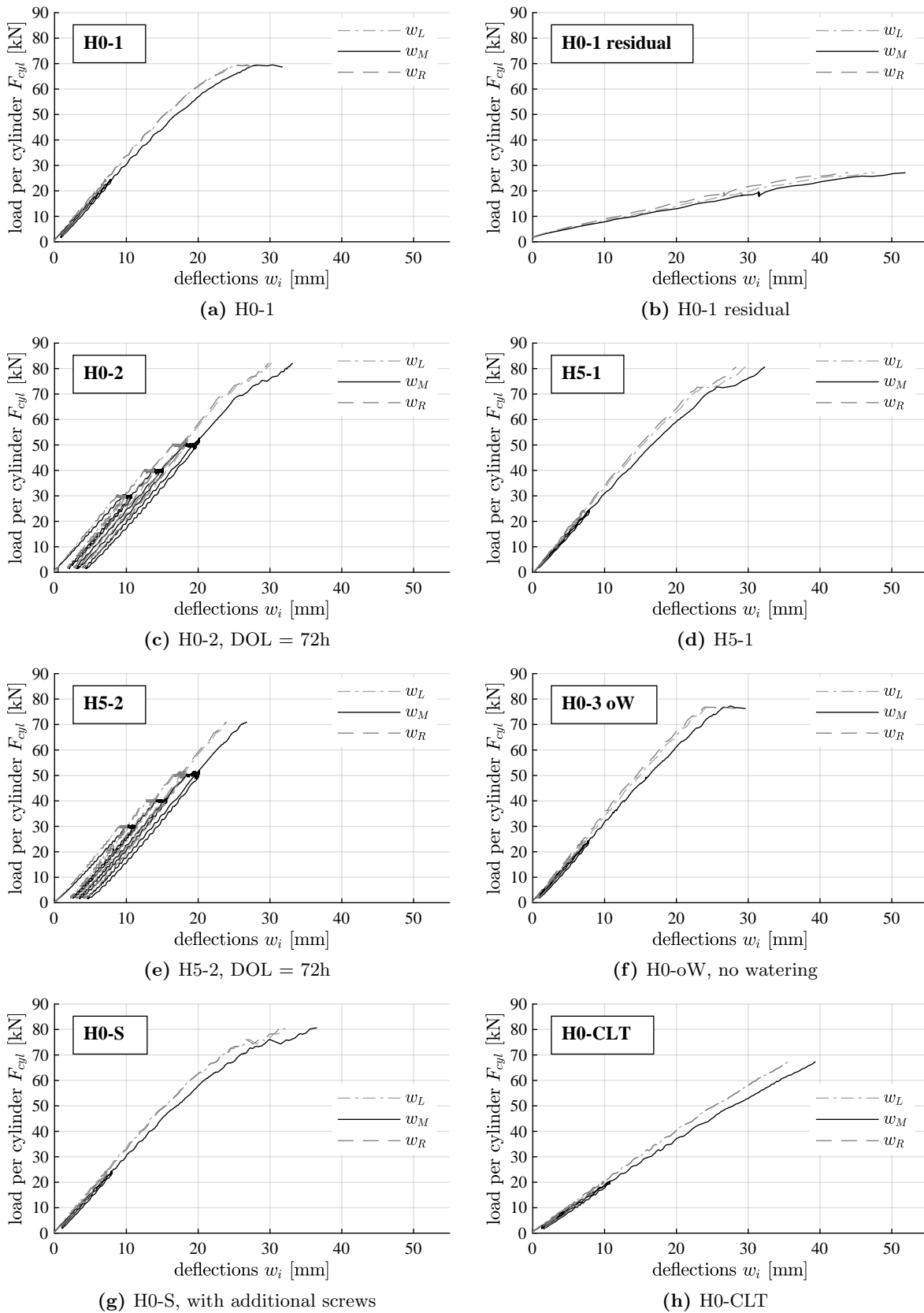


Fig. 4.10: Load-deflection curves of all tests in the 4-point bending test series



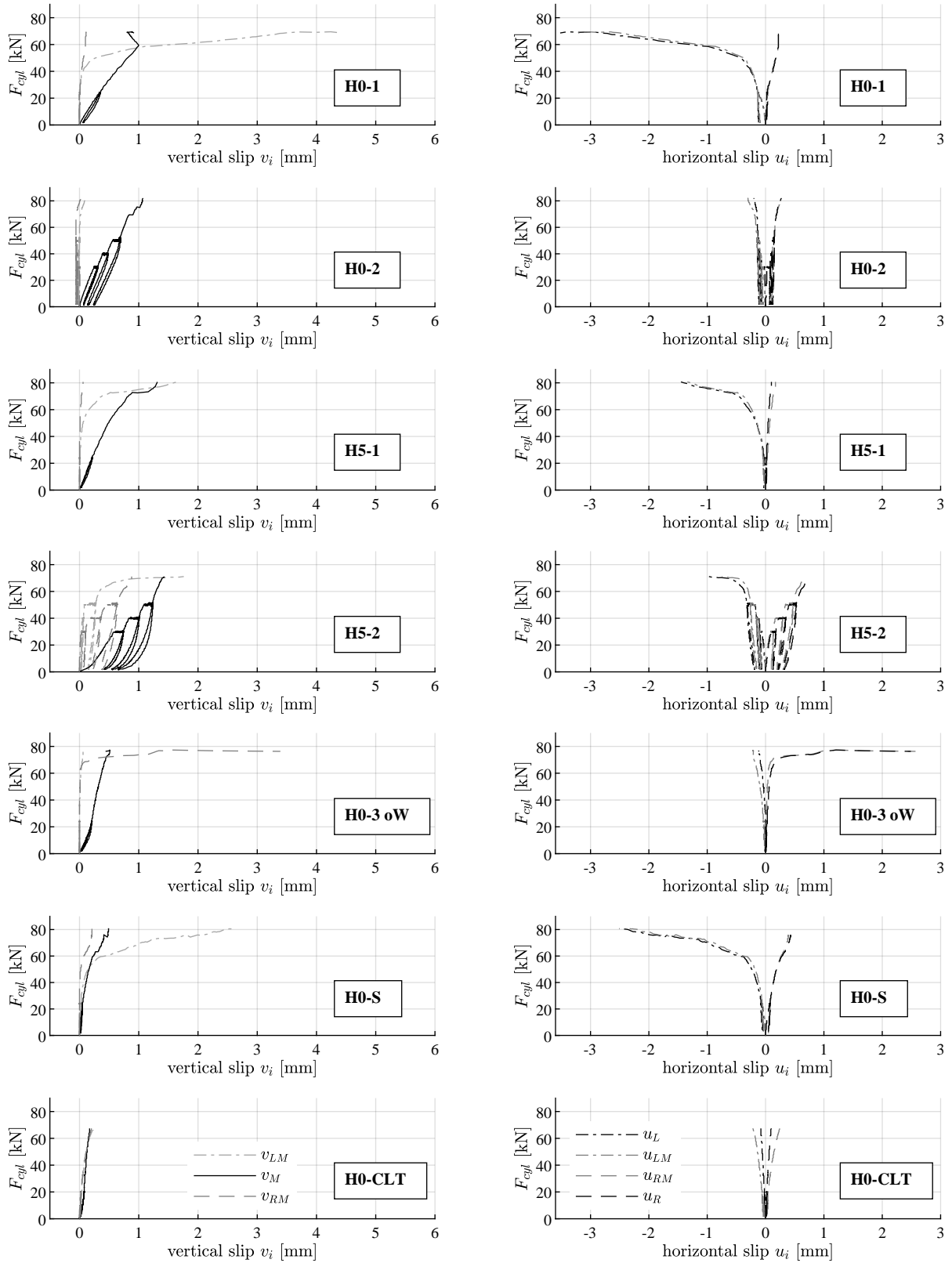


Fig. 4.11: Vertical and horizontal relative slip of all specimens in the 4-point bending tests

### Summary of results

Table 4.5 lists the relevant measurement results and the observed failure modes per test. The failure loads  $F_u$  and corresponding deflections at mid-span  $u(F_u)$  were of the same order of magnitude for all test specimens with BST elements (Fig. 4.10). The test H0-residual with the already failed specimen showed a much lower bending stiffness (see Fig. 4.10b) and failed after large deflections due to bending tension in timber. All specimens with BST elements failed first in the micro-notches and shortly after due to bending tension in the timber at mid-span. The specimen with the CLT element did not fail in the micro-notches, but directly due to bending tension in the timber. The vertical and horizontal slip measured at the beam ends and in the middle of the shear areas left and right show the relative displacements of timber and concrete for both the failed and the intact composite joint. The maximum horizontal slip in the composite joint was 3.5 mm for specimen H0-1. The corresponding load-deflection diagram in Fig. 4.10a shows a plateau before reaching failure, where this plastic deformation occurred. However, the plastic deformations are small and the global load-bearing behaviour of all specimens must be considered brittle. The composite joint with micro-notches sustains no more than a few millimetres of deformation. The vertical slip between timber and concrete at mid-span with no micro-notches was larger than in the shear areas. The vertical slip in the shear areas remained very small during the load increase and only propagated right before reaching the failure load of the micro-notches. At the end of testing, the vertical gap was in the range of some millimetres (Table 4.5 and Fig. 4.6b).

**Tab. 4.5:** Results of 4-point bending tests

Measurements on the side with failed composite joint are highlighted in gray

test	failure load	deflection at failure	vert. slip left	vert. slip mid-span	vert. slip right	hor. slip at left end	hor. slip left area	hor. slip right area	hor. slip at right end	failure mode <sup>a</sup> propagation
	$F_u$ [kN]	$w(F_u)$ [mm]	$v_{LM}$ [mm]	$v_M$ [mm]	$v_{RM}$ [mm]	$u_L$ [mm]	$u_{LM}$ [mm]	$u_{RM}$ [mm]	$u_R$ [mm]	
H0-1	68.6	32	4.4	0.9	0.1	3.5	3.2	0.2	0.2	MN
H0-1 residual	27.1	52								2BT
H0-2	82.1	33	0.1	1.1	0.0	0.2	0.3	0.3	0.3	MN, 2BT
H5-1	80.7	32	1.7	1.3	0.1	1.5	1.3	0.2	0.1	MN, 2BT
H5-2	71.1	27	1.8	1.4	0.9	1.0	0.8	0.7	0.7	MN, 2BT
H0-3 oW	76.3	30	0.1	0.4	3.4	0.1	0.2	2.6	2.5	MN, 2BT
H0-S	80.7	37	2.6	0.5	0.2	2.5	2.3	0.4	0.4	MN, 2BT
H0-CLT	67.4	39	0.2	0.2	0.2	0.1	0.2	0.2	0.1	2BT

<sup>a</sup> MN: failure of the micro-notches, 2BT: failure due to bending tension in the timber at mid-span

## 4.3 Modelling TCC slabs with micro-notches

### 4.3.1 General assumptions

The global load-bearing behaviour of TCC slabs with micro-notches as connection system can be modelled with the methods described in Chapter 2.2. The global load-bearing behaviour observed in the experimental investigations was linear elastic with brittle failure in the composite joint with micro-notches or due to bending tension in the timber cross-section at mid-span. Therefore, the models do not need to be extended by considering any non-linearities or plasticity.

The models are based on the connection properties obtained from the local shear tests in Chapter 3.4. The values for the slip modulus  $K$  and the shear strength  $f_{v,i}$  were taken from the “optimum” geometry 4-7.5. This is an assumption, as the notch geometries tested in the 4-point bending tests had notch front angles of  $\alpha = 0^\circ$  and  $\alpha = -5^\circ$  and are therefore different from the notch front angle  $\alpha = -7.5^\circ$  in the optimum geometry. However, the connection stiffness of all these geometries is in a range where slight alterations have a negligible influence on the effective bending stiffness of the composite beam. The slip modulus for one micro-notch on the specimen width  $b = 580 \text{ mm}$  used for the following analytical and numerical models is:

$$K = 656 \text{ kN/mm/m} \cdot 580 \text{ mm} = 380 \text{ kN/mm} \quad (4.1)$$

Two different values were considered for the shear strength of the micro-notches: the yielding shear strength and the maximum shear strength. They were determined from the load-slip curves of local push-out tests according to SIA 265 [149] (Fig. 3.6). Fig. 4.12 shows the two reference points on the load-slip curve for specimen PO2 4-7.5. The yielding shear strength of the micro-notches is:

$$f_{v,y} = 0.74 \text{ N/mm}^2 \quad (4.2)$$

The maximum shear strength of the micro-notches is:

$$f_{v,max} = 1.16 \text{ N/mm}^2 \quad (4.3)$$

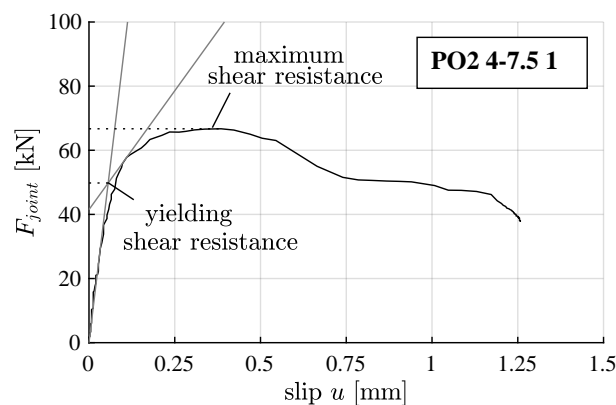


Fig. 4.12: Load-slip behaviour of micro-notches, specimen PO2 4-7.5 1

The MOE of timber was tested for every timber element. The mean MOE of all BST elements was  $E_2 = 10\,583\text{ N/mm}^2$  with a standard deviation of  $508\text{ N/mm}^2$ , resulting in a low CoV of 4.8%. This scattering was considered admissible and the mean MOE assumed valid for all specimens with BST elements.

### 4.3.2 Analytical approach with the $\gamma$ -method

#### Modelling assumptions and inaccuracies for the $\gamma$ -method

The analytical evaluation was conducted with the  $\gamma$ -method as described in Chapter 2.2.2. The boundary conditions of the bending test series were:

- single span, simply supported beam
- constant cross-section dimensions along the span
- assumed constant material properties of the components timber and concrete along the span
- assumed continuous connection along the span (area without micro-notches is around one third of the span and not subjected to shear, thus negligible)
- point loads

The support conditions and the constant material and connection properties fulfil the requirements for an accurate application of the  $\gamma$ -method. The material-related variability of the MOE can be neglected. The arrangement of the micro-notches on approximately two thirds of the span on both sides near to the supports represents a good approximation to a continuous connection. The point loads, however, might lead to inaccurate results.

Cracking of concrete occurs when the tensile stresses in concrete exceed the tensile strength. The cracked concrete decreases the effective cross-section and stiffness of the concrete. The cracked height  $h_{cr}$  and the resulting effective stiffness  $EI_{eff}$  of the composite beam are derived in Appendix C. The transition from uncracked to cracked is assumed to be abrupt. It is assumed that the whole concrete cross-section subjected to tensile stresses is cracked after reaching the critical cracking moment.

#### Different states of global behaviour of a TCC slab

The model presented to assess the global load-bearing behaviour of micro-notches is based on the model with notches developed by Boccadoro [8], addressing the different states of the global behaviour of a TCC slab using the moment-curvature relation. In this study, ductility was not a primary goal, but rather the achievement of a stiff and economically viable connection system. As shown in Chapter 3, micro-notches are a very stiff, approximately rigid connection system. The structural failure in practice is expected to be combined bending tension failure in the timber slab. The structural behaviour of the slab is linear elastic followed by a brittle failure. However, to assess the behaviour observed in the bending tests, the failure of the micro-notches was considered. Due to the position of the load application points, failure in the composite was the governing failure in the experimental tests. Furthermore, the timber cross-section is larger

than in the study of Boccadoro [8] and the concrete behaviour plays a minor role. Nevertheless, the influence of cracking of concrete is described and assessed in the following model with regard to the application in multi-span systems (Chapter 6).

The global behaviour of the experimentally tested TCC slab with BST elements and micro-notches can be described with the different states listed in Table 4.6 and displayed in a moment-curvature diagram in Fig. 4.13.

**Tab. 4.6:** Global behaviour of the experimentally tested TCC slabs with micro-notches

	timber	micro-notches	concrete	limit
State I	elastic	elastic	uncracked	concrete cracking (1cr)
State II	elastic	elastic	cracked	connection yielding + failure (MN yield + MN max)
State III	elastic	failed	cracked	bending tension failure in timber (2BT)

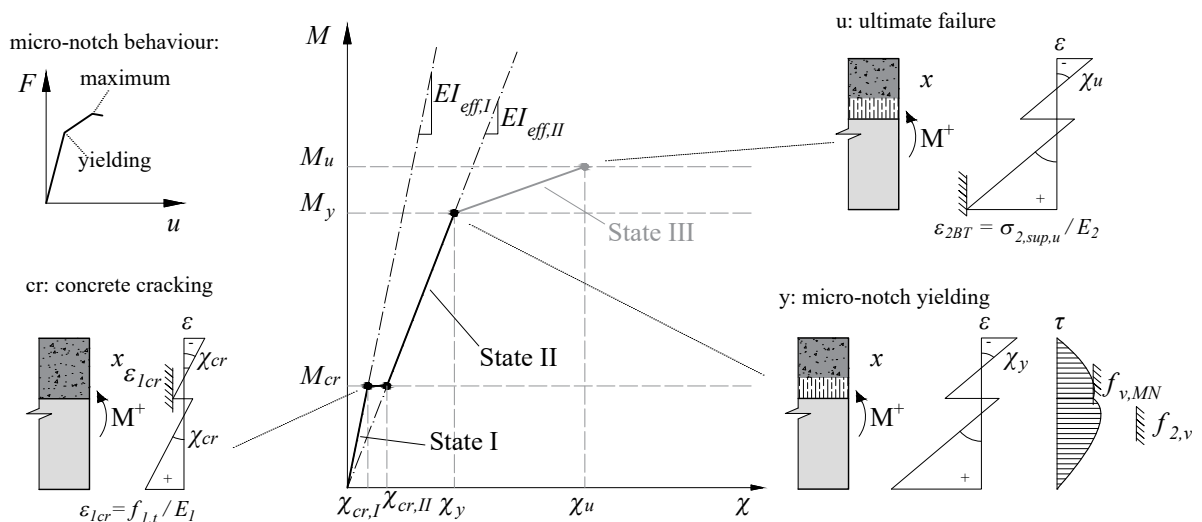


**Fig. 4.13:** Schematic illustration of the different states in the experimentally tested TCC beams with micro-notches

For TCC slabs in practice, the cross-sections of timber and concrete are defined by the requirements for the SLS verifications regarding the deflections or the vibrations. The loading situation with a uniformly distributed load leads to a higher ratio of bending stresses on the cross-sections compared to the shear stresses on the composite joint. For TCC slabs in practice, State III with compromised connection (yielded or failed micro-notches) does not exist. State II ends directly in bending tension failure in timber. The different states and the transition points at the limits are described in detail below.

a) **State I: cross-section intact**

The composite beam is assumed to be elastic in all components. The components' section properties result from the entire heights  $h_1 = h_{1,I}$  and  $h_2$  of the cross-sections of concrete and timber. For solid timber spanning in one direction, such as BST elements, the whole cross-section is considered. For the CLT element, the section properties were determined according to [165].

The  $\gamma$ -method according to Möhler [113] and EC5 [21] was applied with the slip modulus  $K = 380 \text{ kN/mm}$  and  $s$  as the length of the micro-notches  $l_{MN}$ :

$$\gamma_{1,I} = \frac{1}{1 + \frac{\pi^2 \cdot E_1 A_{1,I} s}{K l^2}} \quad (4.4)$$

The effective bending stiffness results from the effective moment of inertia  $I_{eff}$  determined with  $\gamma_{1,I}$  as described in Chapter 2.2.2:

$$EI_{eff,I} = E_2 \cdot I_{eff,I} \quad (4.5)$$

The corresponding curvature for the bending moment  $M$  at the applied load  $F$  or  $q$  is:

$$\chi_I = \frac{M}{EI_{eff,I}} \quad (4.6)$$

The strains and stresses in the cross-section as well as the internal forces and the deflection of the beam can be calculated as described in Chapter 2.2.2.

b) **Concrete cracking**

The stresses at the concrete bottom edge due to bending and normal forces in the concrete cross-section at mid-span are:

$$\sigma_{1,inf,I} = \frac{M}{I_{eff,I}} \cdot \left( \gamma_{1,I} \cdot n_1 a_{1,I} - \frac{h_{1,I}}{2} \right) \quad (4.7)$$

Cracking of concrete occurs if the tensile stresses at the concrete bottom is reached:

$$\sigma_{1,inf,I} = f_{1,t} \quad (4.8)$$

The critical bending moment for cracking is:

$$M_{cr} = \frac{f_{1,t}}{I_{eff,I}} \cdot \left( \gamma_{1,I} \cdot n_1 a_{1,I} - \frac{h_{1,I}}{2} \right) \quad (4.9)$$

The corresponding curvature is:

$$\chi_{cr,I} = \frac{M_{cr}}{EI_{eff,I}} \quad (4.10)$$

c) **State II: concrete cross-section partially cracked**

The uncracked concrete height  $h_{1,II} = x$  can be derived on the basis of an equilibrium consideration of the cross-section. The equilibrium considers all forces resulting from the cross-sections of timber, concrete, reinforcement, and the applied bending moment. This derivation of the uncracked concrete height  $x$  and the cracked concrete height  $h_{cr}$  is detailed in Appendix C. The corresponding effective bending stiffness  $EI_{eff,II}$  can also be derived directly from equilibrium considerations. The curvature of the beam right after the assumed abrupt cracking of the concrete is:

$$\chi_{cr,II} = \frac{M_{cr}}{EI_{eff,II}} \quad (4.11)$$

The concrete cross-section is partially cracked. The components' section properties result from the uncracked concrete height  $x$ . The effective bending stiffness  $EI_{eff,II}$  is directly derived from the equilibrium considerations. Table 4.7 shows a comparison of the uncracked effective bending stiffness  $EI_{eff,I}$  and the cracked effective bending stiffness  $EI_{eff,II}$ :

**Tab. 4.7:** Influence of concrete cracking on the effective bending stiffness of the beam on the example of the system used in the experiments (timber height  $h_2 = 120$  mm).

	concrete	eff. concrete height	eff. bending stiffness	
		$h_{1,i}$ [mm]	$EI_{eff,i}$ [Nmm <sup>2</sup> ]	[%]
State I	uncracked	80	$6.7061 \cdot 10^{12}$	100
State II	cracked	69.4	$6.6985 \cdot 10^{12}$	99.9

In the system used in the experimental tests with concrete height  $h_1 = 80$  mm and timber height  $h_2 = 120$  mm, the reduction of the bending stiffness due to cracking of concrete was only 0.1 %. In fact, the cracking of concrete has a very small influence on the stiffness and thus on the forces in the cross-sections and the deflections. The influence of concrete cracking can therefore be neglected for TCC beams with timber cross-sections considerably larger than the concrete section.

The method of the direct derivation of the bending stiffness  $EI_{eff,II}$  allows to divide the beam into segments and apply the uncracked or cracked effective bending stiffness to them. In this way, the internal forces can be calculated more accurately along the beam span. This is useful to consider the influence of concrete cracking on the system more accurately. For single-span beams with the low influence of concrete cracking as shown above, it is assumed that the cracked effective bending stiffness  $EI_{eff,II}$  applies to the whole span.

The curvature in State II is then:

$$\chi_{II} = \frac{M}{EI_{eff,II}} \approx \chi_I \quad (4.12)$$

d) **Micro-notches yielding**

The shear stress in the joint in the decisive area of the highest shear load near the support is:

$$\tau_{MN} = \frac{V(x=0, l) \cdot S_{II}(x=0, l)}{I_{eff,II} \cdot b_2} \quad (4.13)$$

Micro-notch failure occurs if the shear strength of the micro-notches is exceeded. Assuming that the micro-notches start to fail at the yielding strength  $f_{v,y}$  defined in the local shear tests, the yielding stress in the composite joint is:

$$\tau_{MN} > f_{v,y} \quad (4.14)$$

The critical shear force for micro-notch yielding results:

$$V_{cr,y} = \frac{f_{v,y} \cdot S_{II}(x=0, l)}{I_{eff,II} \cdot b_2} \quad (4.15)$$

e) **State III: concrete cracked, composite action compromised**

The concrete cross-section is partially cracked and the micro-notches yielded. The effective cross-sections are still the same as in State II with the uncracked concrete height  $h_{1,II} = x$ . The connection, however, is compromised and the slip modulus  $K$  and the corresponding composite action are much lower. State III occurred in the experimental 4-point bending tests as a very short phase comprising yielding and eventual failure of the micro-notches, the subsequent loss of composite action, and the following ultimate failure in the timber due to bending tension. The propagation of connection stiffness during this state is non-linear and difficult to assess. This state is also not relevant for planar TCC slabs designed for practice. On these grounds, no detailed analysis of state III was conducted. The connection stiffness during this state is somewhere between the connection stiffness of intact micro-notches  $K = 380 \text{ kN/mm}$  and no connection  $K = 0$  and decreases with increasing load. An approach to find a prescriptive fit to the experimental data is described in detail in Chapter 4.3.4.

d) **Ultimate failure in timber cross-section**

The effective moment of inertia  $I_{eff}$  during State III is a function of the decreasing slip modulus  $K$ . The stress at the timber bottom edge due to bending moments in the timber cross-section at mid-span is:

$$\sigma_{2,sup,III}(M) = \frac{M(x=l/2)}{I_{eff,III}} \cdot \left(0 - \frac{h_2}{2}\right) \quad (4.16)$$

The stress at the timber bottom edge due to normal forces in the timber cross-section at mid-span is:

$$\sigma_{2,sup,III}(N) = \frac{M(x=l/2)}{I_{eff,III}} \cdot a_{1,III} \quad (4.17)$$



Combined bending and tension failure occurs when:

$$\frac{\sigma_{2,sup,III}(M)}{f_{2,m}} + \frac{\sigma_{2,sup,III}(N)}{f_{2,t}} > 1 \tag{4.18}$$

**Findings of the assessment with the  $\gamma$ -method**

The detailed assessment of the different states showed that the global load-bearing behaviour can be described with a linear elastic model for planar TCC slabs with the approximately rigid connection stiffness and brittle failure behaviour of the micro-notches. The cracking of concrete does not have a significant influence on the effective bending stiffness of the beam. The failure load in the elastic range found for the yielding of micro-notches was  $F_{MN,y} = 55.4\text{ kN}$  and for failure due to bending tension in the timber  $103.2\text{ kN}$ . After failure of the micro-notches, the connection stiffness decreases rapidly, the forces redistribute into the timber and concrete cross-section and the failure due bending and tension in the timber follows shortly after. The exact progression of this State III (see Fig. 4.13) is not assessed in detail, as it does not occur in practice and is of no importance for the design. The moment-curvature diagram used for the assessment of the experiments (Fig. 4.13) can be simplified for the use in practice as shown in Table 4.8 and Fig. 4.14:

**Tab. 4.8:** Global behaviour of TCC slabs with micro-notches designed for practice

	timber	micro-notches	concrete	limit
State I	elastic	elastic	uncracked	concrete cracking (1cr)
State II	elastic	elastic	cracked	bending tension failure in timber (2BT)

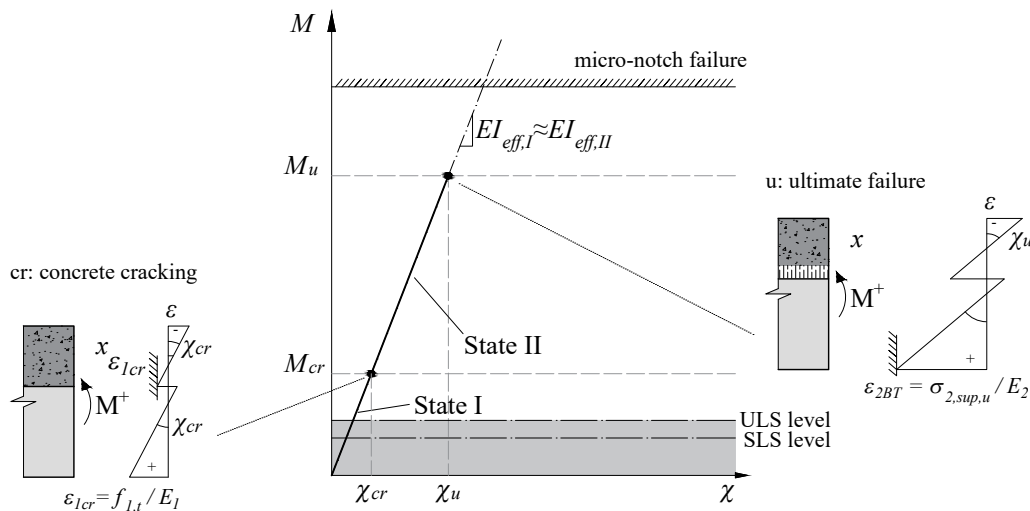


**Fig. 4.14:** Schematic illustration of the different states for the design of planar TCC slabs with micro-notches

The cracking of concrete does not influence the effective bending stiffness  $EI_{eff}$  and can be neglected. The micro-notch failure is not decisive for uniformly distributed loads and cross-section thicknesses with a 1:2 ratio of concrete to timber as common in practice. The decisive failure is the combined bending and tension in the timber cross-section. Fig. 4.14 also shows the range for the loads in ULS and SLS for the cross-sections investigated. The service loads do not lead to concrete cracking for the span of 3.7 m of the tests.

### 4.3.3 Numerical approach with the strut-and-tie model

#### Modelling assumptions and inaccuracies for the strut-and-tie model

The strut-and-tie model was implemented based on the method described in Chapter 2.2.3. For small and constant distances  $s$  between the connectors, the influence of the chord stiffness can be neglected (Fig. 2.10). The effective bending stiffness  $EI^*$  of the connection elements was calculated with equation 2.37 and the slip modulus  $K = 380 \text{ kN/mm}$  for the specimen width of 0.58 m.

#### Implementation

The strut-and-tie model was implemented using the Dlubal software RSTAB. The timber and concrete cross-section were modelled as beams with the heights  $h_1$  and  $h_2$  for the uncracked State I and heights  $h_{1,II} = x$  and  $h_2$  for the cracked State II. The material properties for the concrete beam are the measured MOE and strength values for concrete of class C30/37 (see Chapter 4.2.1). The material properties for the timber beam are the determined MOE (Table 4.2) and the mean values for timber of class C24 according to JCSS [75]. The distance between the two beams is the distance  $e$  between the centroids of the components. In the areas without micro-notches, the connection was realised as rigid beam elements with hinges every 30 mm connected to the timber and concrete beams. In the areas with micro-notches, the connection was realised as beam elements of type “Definable Stiffness...”, rigidly connected to the timber and the concrete beam, and a hinge at the position of the composite joint. The bending stiffness  $EI$  of a connector element (at the location of one micro-notch) is:

$$EI^* = \frac{K}{3} \cdot (z_1^3 + z_2^3) = \frac{K}{3} \cdot \left( \left(\frac{h_1}{2}\right)^3 + \left(\frac{h_2}{2}\right)^3 \right) \quad (4.19)$$

The shear stiffness and the axial stiffness of the connector elements is infinite. The geometry and self-weight of all connector elements of type “Definable Stiffness...” is zero.

For State II with cracked concrete, the concrete beam is altered: the height of the beam is changed to the uncracked height  $h_{1,I} = x = 69.4 \text{ mm}$  and the distance  $e$  between the chords increases with the cracked height  $h_{cr}$  to

$$e_{cr} = \frac{h_2}{2} + h_{cr} + \frac{h_1}{2} \quad (4.20)$$

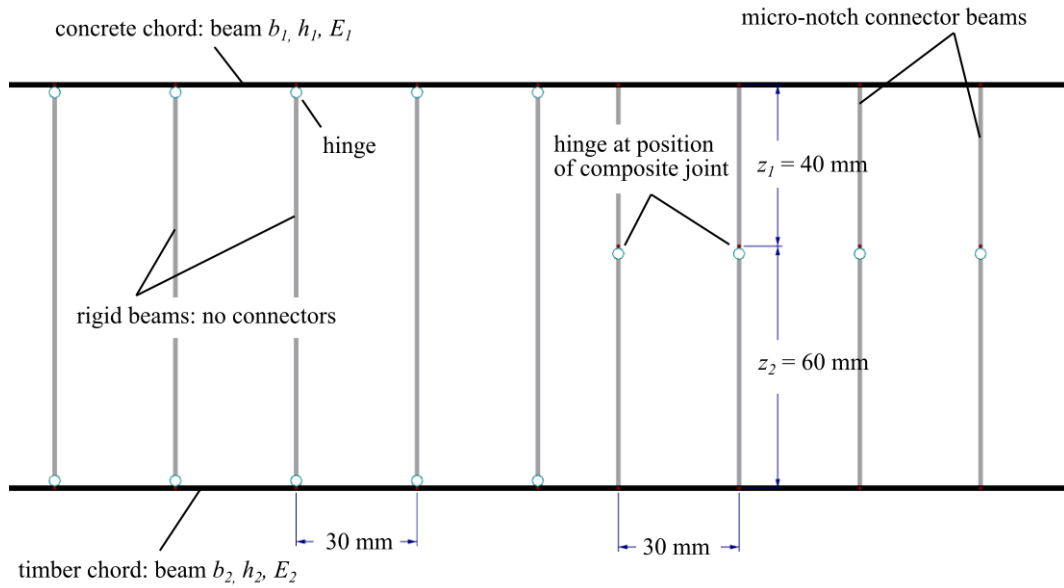


Fig. 4.15: Section of strut-and-tie model in RSTAB

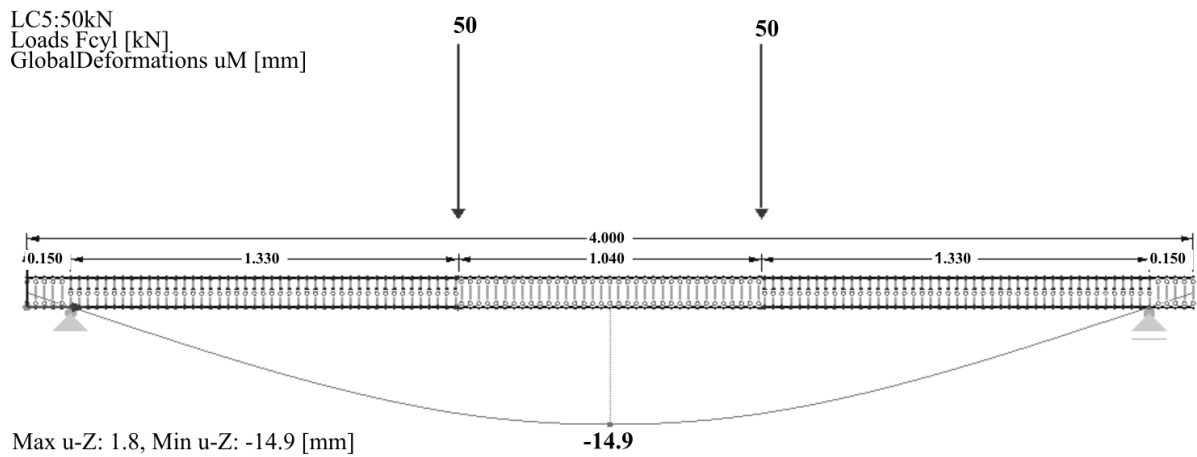


Fig. 4.16: Strut-and-tie model of the tested 4-point bending beams in RSTAB

The position of the hinges in the connection beams stays the same. Table 4.9 lists the effective bending stiffness of the composite beam  $EI_{eff}$  back-calculated from the deflection at different load levels for both State I and State II.

Tab. 4.9: Influence of concrete cracking on the effective bending stiffness of the beam on the example of the system used in the experiments (timber height  $h_2 = 120$  mm)

	concrete	eff. concrete height $h_{1,i}$ [mm]	eff. bending stiffness $EI_{eff,i}$	
			[Nmm <sup>2</sup> ]	[%]
State I	uncracked	80	$6.6466 \cdot 10^{12}$	100
State II	cracked	69.4	$6.6098 \cdot 10^{12}$	99.4

Table 4.9 shows that cracking of concrete has a negligible influence on the effective bending stiffness of the composite beam.

The strut-and-tie model gives the internal forces for the concrete beam, the timber beam, and connection elements. The stresses on the components can then be calculated directly from these forces and the cross-sections. Using the yield shear strength  $f_{v,y} = 0.74 \text{ N/mm}^2$  for the beginning of the micro-notch failure and assuming the shear distribution over the effective shear length  $l_v$  as described in Chapter 3.3, the critical shear force  $V_y$  results:

$$V_y = f_{v,y} \cdot l_v \cdot b \quad (4.21)$$

The effective shear length  $l_v$  for the notches used in the experiments equals the length of the notches  $l_{MN} = 30 \text{ mm}$  and thus the distance between the connector elements in the strut-and-tie model.

The stresses in the timber section are determined from the internal normal force  $N_2$  and the internal bending moment  $M_2$ :

$$\sigma_2(N) = \frac{N_2}{A_2} \quad (4.22)$$

$$\sigma_2(M) = \frac{M_2}{I_2} \cdot \frac{h_2}{2} \quad (4.23)$$

Combined bending and tension failure occurs when:

$$\frac{\sigma_2(M)}{f_{2,m}} + \frac{\sigma_2(N)}{f_{2,t}} \geq 1 \quad (4.24)$$

### Findings of the assessment with the strut-and-tie model

The strut-and-tie model assessment of planar TCC slabs with micro-notches for different load levels shows a linear elastic load-bearing behaviour. The strut-and-tie model confirms that cracking of concrete does not have a significant influence on the effective bending stiffness of the beam (Table 4.9). The failure load in the elastic range found for the yielding of micro-notches was  $F_{MN,y} = 58 \text{ kN}$  and for failure due to bending tension in the timber  $F_{2BT} = 105 \text{ kN}$ . State III with failed composite joint was not investigated further in the strut-and-tie model.

#### 4.3.4 Comparison of models and validation of experimental results

##### Analysis in States I and II

Fig. 4.17 shows the comparison of the measured load-deflection curves of the experimental 4-point bending tests, the failure loads, and corresponding deflections obtained with the analytical approach using the  $\gamma$ -method (Fig. 4.17a) and with the numerical approach using the strut-and-tie model (Fig. 4.17b).

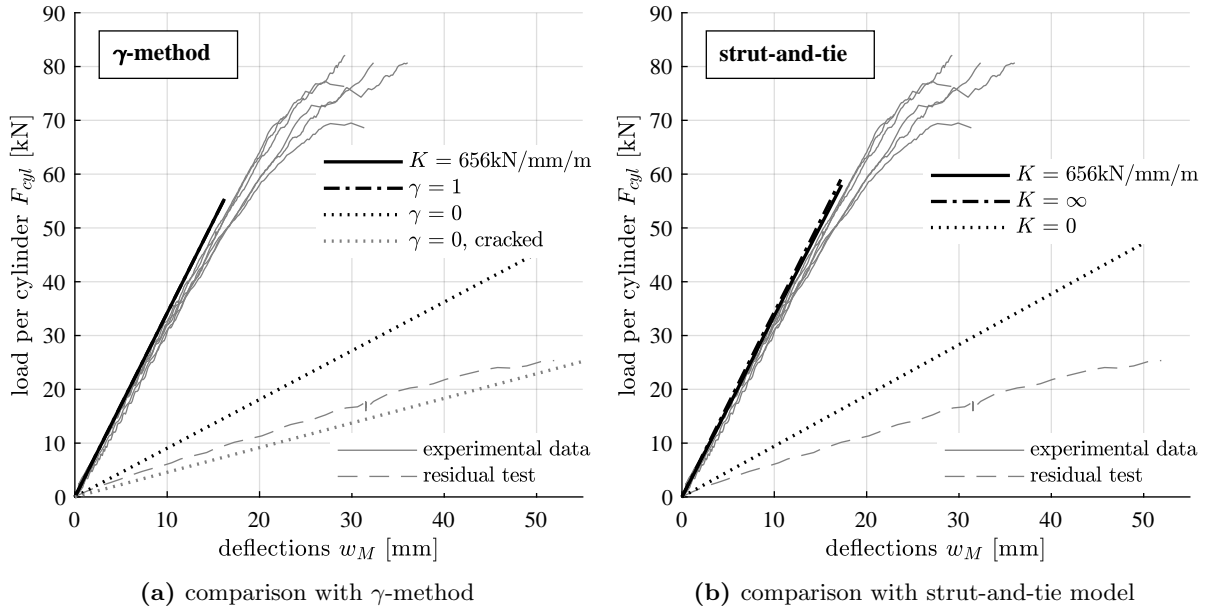


**Fig. 4.17:** Comparison of experimental data with models

Both models are in good agreement with the experimental data regarding the slope of the load-deflection curve. The slopes for a rigid connection (slip modulus  $K = \infty$  or  $\gamma = 1$ ) and the slopes obtained with the connection properties from the push-out tests (slip modulus  $K = 656 \text{ kN/mm/m}$ ) are approximately congruent. Especially for the area with lower loads (i.e. up to 20 kN), the models predict the load-bearing behaviour accurately. At higher load levels, the experimental data shows a slightly less stiff load-bearing behaviour and a non-linear behaviour. It should be noted that this approximately rigid connection behaviour in the experiments was obtained with micro-notches arranged on the entire area subjected to shear forces. If a large-area arrangement cannot be assumed, it is advisable to take a closer look on the stiffness.

As a lower boundary, the load-bearing behaviour of the investigated TCC beams with no connection are also plotted (slip modulus  $K = 0$  or  $\gamma = 0$ ). The failure of unconnected beams as seen with specimen H0-residual occurred first as cracking of the concrete at the bottom edge, then possible concrete compression failure of the concrete at the top edge, followed by bending tension failure in the timber bottom edge. The residual load-bearing behaviour of test H0-residual can be reconstructed with the assumption of  $\gamma = 0$  and a cracked concrete cross-section.

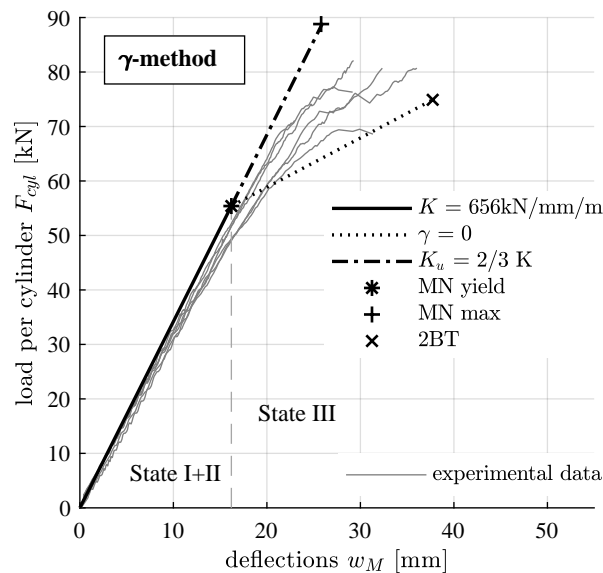
In contrast to the good agreement regarding connection stiffness, the failure loads predicted with the yielding shear strength  $f_{v,y}$  with the models are lower than the measured failure loads in the experimental tests. From the test curves, however, it can be seen that around the yielding load of the micro-notches, the connection stiffness begins to decrease.

### Analysis in State III

In State III, the composite action is compromised with non-linear regression of the slip modulus  $K$  until ultimate failure of the micro-notches (MN max) or bending tension failure in the timber (2BT). The failure loads of those two failure modes depend strongly on the present slip modulus. The load-bearing behaviour in State III can be reconstructed by assuming two limit states after yielding of the connection (MN yield):

- The micro-notches fail at the yielding strength  $f_{v,y}$ : the composite action is lost, the effective bending stiffness significantly decreased. The specimen deflects substantially until the ultimate failure due to bending tension failure in the timber at  $F_{2BT} = 74.9$  kN.
- The micro-notches yield, but not the whole composite action is lost. Assuming  $K_u = 2/3 \cdot K$  as for ductile connection systems, the shear strength  $f_{v,max}$  for the micro-notches is reached at  $F_{MN,max} = 88.8$  kN. At this ultimate failure of the micro-notches, the composite action will be lost and the bending tension failure in timber occurs abruptly.

The actual course of the connection stiffness is between these two limit states (Fig. 4.18). It can be seen that some of the specimens draw near to the complete loss of composite action ( $\gamma = 0$ ), others follow the almost rigid connection stiffness up to 70 kN. The maximum shear strength  $f_{v,max}$  determined from the local push-out tests overestimates the failure loads. The assumption of  $K = K_u = 2/3 \cdot K$  and linear connection stiffness during State III is not realistic.



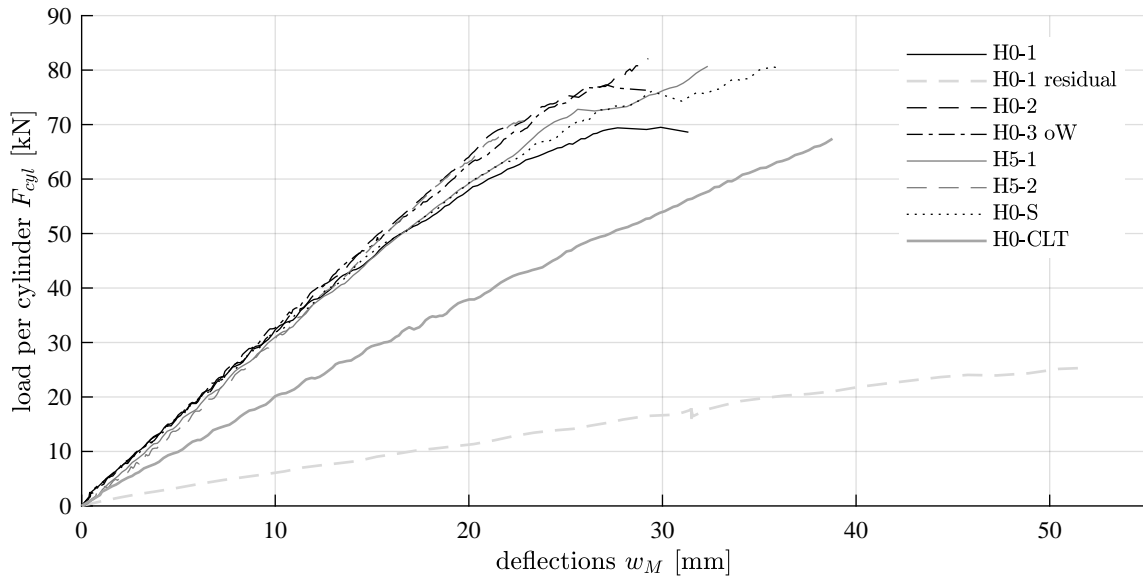
**Fig. 4.18:** Limit states in State III calculated with the  $\gamma$ -method

Fig. 4.18 also confirms that the connection stiffness of the micro-notches is so high that the transition from  $K$  to  $K_u = 2/3 \cdot K$  has no visible effect on the load-bearing behaviour: The slopes of  $K$  and  $K_u$  are the same.

## 4.4 Influence of different parameters

### 4.4.1 Comparison of global behaviour of all configurations

Fig. 4.19 shows the load-deflection curves of all tests in one plot. The influencing factors are discussed in the following subchapters.



**Fig. 4.19:** Load-deflection curves of all specimens tested in the 4-point bending tests

### 4.4.2 Notch front angle

Two different notch front angles  $\alpha$  were tested: specimens H0 with  $\alpha = 0^\circ$  (vertical notch front) and specimens H5 with  $\alpha = -5^\circ$  (notch front inclined inwards the notch = undercut notch). From the curves in Fig. 4.19 it can be seen that both micro-notch geometries have a linear elastic global behaviour. Some specimens such as H0-1 or H5-1 show a slight decrease of stiffness beginning at around 50 kN, others such as H0-2 or H5-2 have a constant stiffness up to shortly before failure. The notch front angle does not have an influence on this behaviour. The models (Fig. 4.17a and 4.17b) also show that a slight variation of  $K$  does not have a significant influence on the behaviour: The notch front angles  $\alpha = -5^\circ$  and  $-7.5^\circ$  were tested in local shear tests and had slip moduli of  $K = 693 \text{ kN/mm/m}$  and  $K = 656 \text{ kN/mm/m}$  respectively. The difference between these two slip moduli is negligible regarding the load-deflection behaviour. The connection efficiencies  $\eta_{C^*}$  according to equation 2.23 are 0.993 for  $\alpha = 0^\circ$  and 0.997 for  $\alpha = -5^\circ$ . Therefore, both micro-notch geometries can be assumed rigid. The vertical tensile stresses resulting from an inclined notch front seem to have no negative influence on the local or global load-bearing behaviour. Undercut notch fronts increase the friction forces and might help with a clamping effect, which can be useful during transportation or to help prevent separation of the timber and concrete but does not have any effect on the static structural behaviour.

### 4.4.3 Treatment of the timber surface

The timber surface of six specimens was watered before casting the concrete and the timber surface of one specimen (H0-3 oW) was not watered nor treated in any other way. Moulding oil was only applied to the side formwork, but not the top of the timber element. From the curves in Fig. 4.19 it can be seen that the non-watered specimen H0-3 oW has a very similar global load-bearing behaviour to the watered specimen H0-2 or the undercut, watered specimen H5-2. The influence of watering the timber surface was not investigated analytically or numerically. The experimental tests with realistic material properties deliver the most authentic results regarding this issue. The bending tests showed, as already the local tests, that the influence of watering the timber surface before concreting can be neglected. This neglect is, however, restricted to the performed tests on short-term local and global connection behaviour. Since the moisture content of the timber strongly influences the long-term behaviour, this issue has to be investigated further.

### 4.4.4 Additional screws

Specimen H0-S was equipped with 22 additional screws of type VB-48-7.5 X 100. From the curves in Fig. 4.19 it can be seen that the global load-bearing behaviour of this specimen is the same as for the other specimens with micro-notches only. The connection stiffness and the load-bearing capacity of composite beams cannot be increased by additional screws. This can also be shown in the models, where the increase of  $K$  for the already approximately rigid connection stiffness does not bring any more value. At the ultimate failure of the micro-notches MN max (or due to bending tension 2BT in practice-oriented design), the shear forces are abruptly transferred to the screws. Depending on the redundancy for bending tension failure in timber and on the shear resistance of the installed screws, it is possible that the screws could increase the load after the micro-notch failure and thus lead to plastic deformations. However, this was not observed in the experiments. The bending tension failure in timber occurs shortly after the partial loss of composite action. Regarding the influence on the ductility, it can be seen in Fig. 4.19 and Table 4.5 that the specimen H0-S has the highest maximum deformation. However, the difference of 4 mm and the results from only one specimen do not suffice to assign an increase in ductility to the screws. Furthermore, the separation of the concrete layer from the timber was not observed in any of the specimens during the tests until failure of the micro-notches. The additional screws in the specimen were not needed to prevent uplift. It should be noted, however, that this applies to the specific loading situation and chosen composite cross-section. The loading situation with two point loads is more likely to provoke uplift due to the local force transfer. It is expected, that the loading situation in practice (uniformly distributed loads) is less critical regarding uplift. In conclusion, the bending test with one specimen showed that additional screws in the micro-notch connection system did not increase the connection stiffness nor the failure load and were also not needed to prevent uplift before reaching the failure load.



#### 4.4.5 Duration of load / short-term creep

Specimens H0-2 and H5-2 were tested with increasing load levels over a total time span of 72 h. The first load level was held at 30 kN for 24 h, then the load was released and increased by 10 kN every 24 h. After three load levels, the specimen was loaded until failure. Fig. 4.20 shows the load procedure and the load-deflection curves. Table 4.10 lists the measured creep deformations during the held load levels and the back-calculated bending stiffness for the loading phase to the respective load level. As a reference, the specimens H0-1 and H5-1 with short duration of load are also listed.

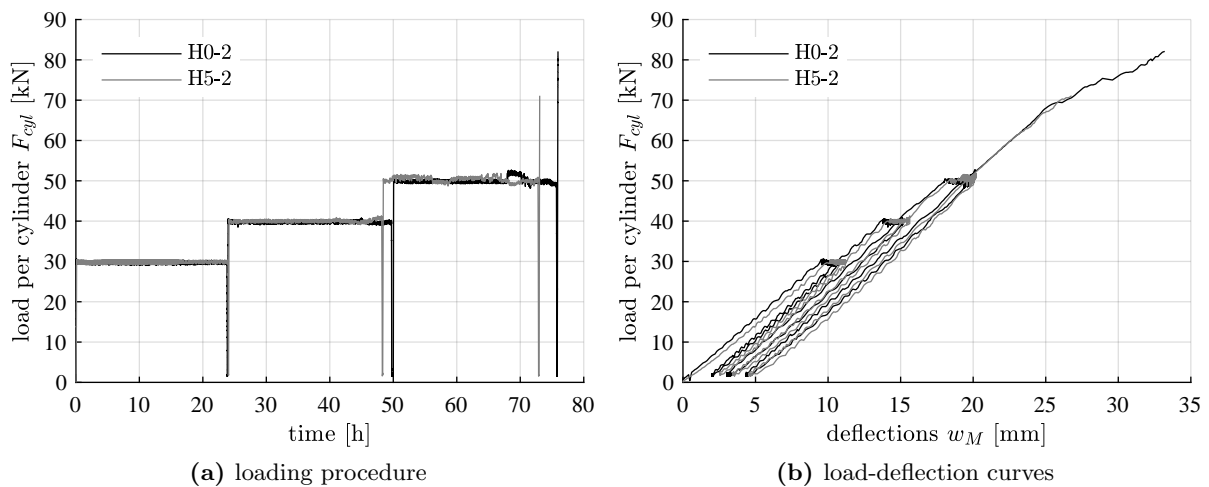


**Fig. 4.20:** Measurements of specimens H0-2 and H5-2 tested for 72 h

The charge at high load levels (the load levels 30 kN, 40 kN, and 40 kN correspond to approximately 40 %, 52 %, and 65 % of the failure load) did not compromise the composite beam regarding the bending stiffness or the reached failure load. The total creep deflection measured after 72 h was 4.30 mm for specimen H0-2 and 4.29 mm for specimen H5-2. The tests were not conducted long enough to allow a statement about the creep factor. For the specimens tested with one load level at 40 % of  $F_{max,est}$  (H0-1 and H5-1), the back-calculated effective bending stiffness  $EI_{eff}$  of the specimens decreased slightly from the first to the second loading phase. On the other hand, the specimens loaded over 72 h (H0-2 and H5-2) seem to slightly increase the effective bending stiffness. Especially the effective bending stiffness during the second loading phase is higher than in the first loading phase, whereas it decreases again in loading phase three and four. The results of these tests with only two specimens cannot be used to make general statements. However, it can be concluded that the charge with high load levels over a span of several days did not compromise the connection stiffness (see Table 4.10) nor shear resistance (see Fig. 4.19).

**Tab. 4.10:** Influence of short-term creep in specimens subjected to large load levels on effective bending stiffness and plastic deformations due to short-term creep

	load level	duration of load	creep deformations <sup>a</sup>				eff. bending stiffness <sup>b</sup>	
	$F_{cyl}$ [kN]	[s],[h]	$w_M$ [mm]	$v_M$ [mm]	$u_L$ [mm]	$u_R$ [mm]	$EI_{eff}$ [Nmm <sup>2</sup> ]	[%]
H0-1	24	30s	0.09	0.01	0.01	0.01	$5.97 \cdot 10^{12}$	100
	failure	-	-	-	-	-	$5.56 \cdot 10^{12}$	93.2
H0-2	30	24h	1.21	0.06	0.05	0.05	$6.03 \cdot 10^{12}$	100
	40	24h	1.49	0.09	0.02	0.02	$6.16 \cdot 10^{12}$	102.1
	50	24h	1.60	0.13	0.02	0.03	$6.06 \cdot 10^{12}$	100.5
	failure	-	-	-	-	-	$6.04 \cdot 10^{12}$	100.2
H5-1	24	30s	0.02	0.00	0.00	0.00	$5.89 \cdot 10^{12}$	100
	failure	-	-	-	-	-	$5.68 \cdot 10^{12}$	96.4
H5-2	30	24h	1.04	0.13	0.02	0.06	$5.64 \cdot 10^{12}$	100
	40	24h	1.56	0.18	0.04	0.13	$6.21 \cdot 10^{12}$	110.0
	50	24h	1.69	0.15	0.14	0.12	$6.10 \cdot 10^{12}$	108.2
	failure	-	-	-	-	-	$5.98 \cdot 10^{12}$	106.0

<sup>a</sup> plastic creep deformations measured from beginning to end of load level

<sup>b</sup> effective bending stiffness  $EI_{eff}$  of loading phase

#### 4.4.6 CLT element

The specimen H0-CLT with notch front angle  $\alpha = 0^\circ$  and CLT timber element with a total thickness of  $h_2 = 100$  mm showed, as expected, a much softer load-deflection behaviour than the specimens with BST elements with  $h_2 = 120$  mm. The specimen H0-CLT failed in a brittle manner due to bending tension in the timber cross-section. Unfortunately, the details of the production and thus the material properties of the CLT element were unknown. The element was stored in unknown conditions for several months before the test. The moisture content after concreting was very high at 22.3%. Signs of mould were visible on the timber (Fig. 4.21b). It is likely that the stiffness and strength properties of the wood have been affected during the storage time. The failure due to bending tension before failure in the micro-notches could be due to the inferior material. The results of this test should therefore not be used as quantitative results. However, the test showed that micro-notches can be applied to CLT elements and that the load-bearing behaviour is linear elastic. A comparison with the prognosis obtained with the model based on the  $\gamma$ -method shows a good agreement with the experimental data in terms of stiffness (Fig. 4.21a).

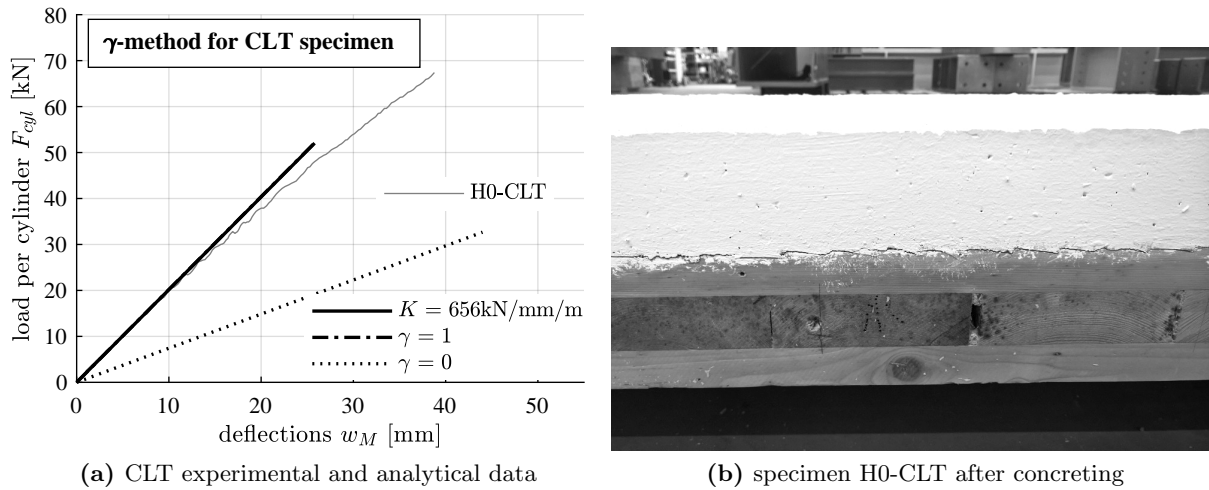


**Fig. 4.21:** Load-bearing behaviour and appearance of specimen H0-CLT

#### 4.4.7 Cracking of concrete

The calculated cracking moment of concrete ( $M_{cr}$ ) was at around a third of the moment at failure ( $M_u$ ). The propagation of cracks was not visible during the tests until failure of the micro-notches, followed shortly after by the ultimate failure due to timber bending tension failure. The failed specimens displayed visible cracks near to the two load application points and in the area between them. As shown in the assessment of the different states of the global load-bearing behaviour, the cracking of concrete has a negligible influence on the effective bending stiffness of the TCC slab.

### 4.5 Comparison of global and local load-bearing behaviour

The results for connection stiffness and shear resistance of the local push-out test series and the global 4-point bending test series were compared to each other. The shear force acting in the composite joint is calculated for the bending tests and plotted in Fig. 4.22 with the relative slip between timber and concrete. The relative slip is denoted with  $u$  for slip parallel to the composite joint and with  $v$  for slip perpendicular to the composite joint. This denotation is valid for both test setups. The relative slip was measured in the middle of the shear areas for both test setups. It is assumed that the specimen width does not influence the load-slip behaviour.

Fig. 4.22 shows a generally good agreement between the load-slip curves of the connection in the local test setup (PO2 specimens) and in the global test setup (HO and H5 specimens). However, the load situation of a shear-loaded composite joint in local shear tests does not represent the same situation as for a composite joint in global bending tests. According to Michelfelder [110], the shear test situation represent the composite joint situation near to a support. The direct shear transfer into the support is similar to the lateral constraint due to friction at the bottom supports of push-out tests. Fig. 4.22 therefore only shows a qualitative comparison neglecting the location of the micro-notches in the beam.

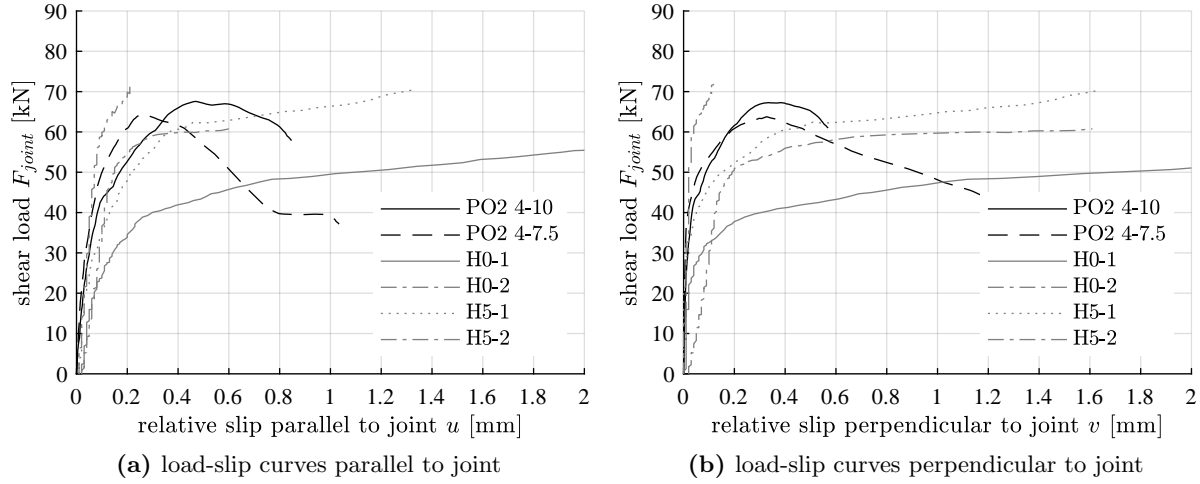


**Fig. 4.22:** Comparison of shear force on joint and relative slip for local and global experimental tests

#### 4.5.1 Connection stiffness

For the modelling of the global load-bearing behaviour, the connection properties of the local push-out tests were taken as a basis. However, the connection stiffness measured in the bending tests was lower than predicted with the slip modulus  $K = 656 \text{ kN/mm/m}$  resulting from the push-out test PO2 4-7.5 (see Table 3.6 and equation 4.1). Both local and global tests and models showed that micro-notches are an approximately rigid connection system for TCC slabs. These findings, however, are based on a continuous arrangement of the micro-notches. To ensure a realistic connection stiffness of micro-notches arranged in different ways, e.g. only in certain areas or in stripes along the span, the effective connection stiffness has to be considered to be on the conservative side. This is not the case with the slip modulus  $K = 656 \text{ kN/mm/m}$  resulting from the push-out tests. The apparent slip modulus  $K$  was back-calculated from the effective bending stiffness determined in the bending tests using the  $\gamma$ -method. In this manner, the slip modulus was adapted to  $K = 110 \text{ kN/mm/m}$  (Fig. 4.23a).

#### 4.5.2 Load-bearing capacity

The shear resistance of the micro-notches was determined as shear strength per area from the push-out tests PO2 4-7.5. The yielding shear strength  $f_{v,y} = 0.74 \text{ N/mm}^2$  determined from the turning point in the local load-slip curves slightly underestimates the failure load of the micro-notches, whereas the maximum shear strength  $f_{v,max} = 1.16 \text{ N/mm}^2$ , slightly overestimates the failure load of the micro-notches (Fig. 4.23a). Table 4.11 lists the shear strength values back-calculated from the observed failure loads in the specimens with BST elements. This data results in an average shear strength of  $f_{v,MN} = 0.87 \text{ N/mm}^2$  for micro-notches (mean value of 7 specimens). This average shear strength was then implemented in the calculation models. Fig. 4.23 shows the comparison of the experimental data with the models using the adaption of

values for the slip modulus  $K$  in the first step (Fig. 4.23a) and the shear strength  $f_{v,MN}$  in the second step (Fig. 4.23b).

**Tab. 4.11:** Values for shear strength of micro-notches obtained from experiments

specimen	$f_{v,MN}$ [N/mm <sup>2</sup> ]
H0-1	0.78
H0-2	0.91
H0-3 oW	0.93
H5-1	0.83
H5-2	0.88
H0-S	0.87

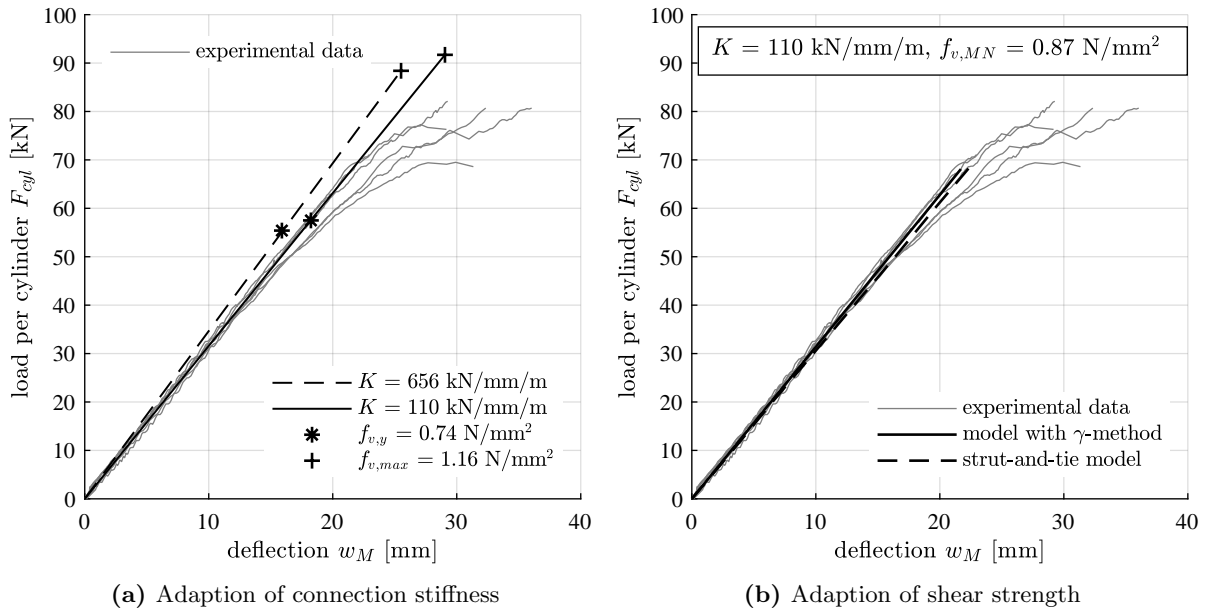


**Fig. 4.23:** Adaption of connection properties to fit global load-bearing behaviour

Fig. 4.23b shows that the load-deflection behaviour determined with the  $\gamma$ -method and the strut-ant-tie model using the adapted connection properties (slip modulus  $K$  and shear strength  $f_{v,MN}$ ) is in good agreement with the load-deflection behaviour observed in the experimental 4-point bending tests.

### 4.5.3 Ductility

Fig. 4.22 shows the load-slip curves in the composite joint for both local and global experiments. In both test setups, the micro-notches can take a deformation of a few millimetres before failing. However, the deformations are in a very low range compared to steel connectors, where much larger deformations can be observed. The deformations up to almost 4 mm horizontal slip in the bending tests are not a deformation capacity of the micro-notches but due to the abrupt failure of the composite joint and the subsequent movements of the detached concrete top layer. Furthermore, the main failure mode observed in both local and global experiments was shear failure in both concrete and timber notches. The low deformation capacity and the brittle failure mode lead to the statement, that the micro-notches cannot be considered a ductile connection system.

### 4.5.4 Discussion

The discrepancies of the connection properties in the local and global tests are in general small. The differences regarding connection stiffness and shear resistance are discussed below, followed by possible explanations for the discrepancies:

The connection stiffness observed in the global bending tests was lower than in the local tests. However, even though the slip modulus  $K$  is reduced by almost a factor of 6, this does not have a significant influence on the effective bending stiffness. The connection stiffness can still be considered as approximately rigid. The higher connection stiffness resulting from the local push-out tests could be due to the different cross-section thicknesses: The thicknesses in the local tests were 50 mm for concrete and 60 mm for timber, in the bending tests they were 80 mm for concrete and 120 mm for timber.

The maximum shear strength observed in the global bending tests ( $f_{v,MN}$ ) was slightly higher than the yielding shear stress in the local tests ( $f_{v,y}$ ). This is probably due to the definition of the yielding point in the local load-slip curves. Since the local load-slip behaviour was non-linear for most specimens, the assessment of valuable parameters depends strongly on the determination method. Another reason for the discrepancy could be the clamping effect due to the curvature in the bending tests. This effect has been found to have a non-negligible effect on the load-bearing behaviour [99]. Further, the observed ductility in the connection systems could have led to an increased global load-bearing capacity of the beam.

Another possible reason for the discrepancy could be the different direction of concreting in the local and global test specimens: The concrete part was cast parallel to the composite joint in the push-out tests and perpendicular to the composite joint in the bending tests. Inferior vibration of the concrete in the push-out tests could have led to inferior concrete in the lower part of the specimens. This would lead to inconsistent material properties along the length of the joint. The shear strength or the connection stiffness could be compromised if the concrete near to the joint was of inferior quality. However, the vibration of the concrete was executed carefully for both local and global test specimens. It can be assumed that the concrete quality was consistent.

## 4.6 Conclusions

The investigations on the global load-bearing behaviour of micro-notches as connection system for TCC slabs concerning the connection behaviour showed:

- The micro-notch connection system in TCC has a very high connection stiffness: The load-deflection curves of the experiments are comparable to the curves modelled with  $\gamma = 0$ . Therefore the composite action can be assumed rigid.
- The shear strength corresponds to a level between the yielding shear strength and maximum shear strength observed in the local shear tests.
- The TCC beams failed in a brittle manner due to bending tension in timber after a distinct linear elastic phase in the load-deflection behaviour and shortly after yielding of the composite joint.

Regarding the influence of different parameters, it can be concluded:

- The notch front angle  $\alpha$  has no apparent influence on the (short-term) load-bearing behaviour. Both vertical ( $\alpha = 0^\circ$ ) and undercut ( $\alpha < 0^\circ$ ) result in an approximate rigid connection stiffness and do not show any difference in shear resistance.
- The watering of the timber surface before concreting did not affect the (short-term) load-bearing behaviour of the tested TCC beams.
- Additional screws did not affect the connection stiffness or the shear resistance of the tested TCC beams. The tested specimen H0-S, however, resulted in the largest beam deflection at failure, with the advance on the next specimen being 4 mm.
- The application of high load levels over a period of 72 h did not compromise the connection stiffness nor the shear resistance of the micro-notches.
- The use of micro-notches on CLT elements is also possible and results in a linear-elastic load-deflection behaviour similar to the systems with BST elements. Unfortunately, no further findings were made, because only one specimen was tested and the timber element was of inferior quality.

The load-bearing behaviour observed in the global bending tests shows a slight discrepancy with the load-bearing behaviour observed in the local push-out tests. To fit the behaviour measured in the six specimens with BST elements, the connection stiffness per meter width was lowered from  $K = 656 \text{ kN/mm/m}$  to  $K = 110 \text{ kN/mm/m}$  and the shear strength set to  $f_{v,MN} = 0.87 \text{ N/mm}^2$  in between the locally determined yield shear strength  $f_{v,y} = 0.74 \text{ N/mm}^2$  and maximum shear strength  $f_{v,max} = 1.16 \text{ N/mm}^2$ .





## Chapter 5

# Long-term investigations of micro-notches

### 5.1 Introduction and literature review

#### 5.1.1 Overview

The local and global experimental tests and the corresponding global analytical and numerical models show excellent connection properties for micro-notches as a connection system for TCC slabs: Very high stiffness and a sufficient shear strength for high demands in practice have been demonstrated. These findings, however, only relate to the short-term behaviour of the TCC connection. In fact, the long-term behaviour of TCC slabs is of great importance since it affects the bending stiffness by influencing both the global deflections and the stresses in the composite cross-section. For this reason, an extensive experimental test series was installed to investigate the long-term behaviour on the micro-notches. In the frame of this thesis, the installation of the tests, the considerations behind the choice of dimensions and loading situations, and the first results after half a year of loading are reported.

#### 5.1.2 Rheological phenomena in timber and concrete

##### Shrinkage and swelling

Shrinkage and swelling describe a change in volume of a material that occurs independently of the load applied. The change of volume is a consequence of chemical and physical processes due to moisture changes in both timber and concrete or hydration reactions in concrete.

In timber, shrinkage and swelling indicate the increase and decrease of volume due to water absorption and release respectively. Timber is hygroscopic and in constant exchange with the environment. The relative humidity (RH) and temperature (Temp) of the environment lead to an equilibrium moisture content in the timber. Shrinkage and swelling of timber occurs only below the fibre saturation point at a moisture content of approximately 28 % [121]. Above this point, the cell walls of the timber are saturated and additional water is stored directly in the

lumina of the wood cells. The equilibrium moisture content in construction is dependent on the enclosure, the ventilation, and the heating of the premises. The equilibrium moisture content for spruce is around  $12\% \pm 3\%$  for timber components in closed and heated rooms and around  $17\% \pm 5\%$  for timber components partly sheltered from the weather in outdoor conditions [149]. The increase and decrease of volume due to shrinkage and swelling are equal in amount. Shrinkage and swelling in timber are dependent on the size of the component, the wood species, the density, the direction of grain, and the angle of the microfibrils. The shrinkage in longitudinal direction is approximately 10 times smaller than in radial direction and approximately 20 times smaller than in tangential direction [15; 121].

In concrete, there is only shrinkage, no swelling. Concrete shrinkage is due to different processes after concreting: Plastic shrinkage, drying shrinkage, autogeneous shrinkage, and carbonation shrinkage [138]. Plastic shrinkage can be largely prevented by proper curing. The share from carbonation shrinkage is proportionally negligible in comparison with the drying and autogeneous shrinkage. Drying and autogeneous shrinkage depend on the volume of the cement paste, the water to cement ratio, the type of cement used, and the size of the concrete surface exposed to the environment [150; 22]. Shrinkage can be reduced by shrinkage reducing admixtures.

## Creep

Creep describes the increase of strains and deformations over time at a constant level of applied stress.

In wood, creep occurs in the cell walls and in the middle lamella between the cells. The creep progression depends strongly on the stress level applied. The applied stress leads to several phenomena causing creep deformations [138; 56]. One phenomenon as described by Grossmann [59] is the displacement of the hydrogen bonds between the cellulose chains which are leading to deformations in the timber structure. Another phenomenon described by Boyd [11] is the deformation of a viscous gel embedded between the microfibrils. This viscous gel deforms in different ways depending on the stress direction applied as well as the angle between the applied load and the microfibril direction. The effect of these phenomena is called visco-elastic creep. Niemz [121] lists the different creep progression states depending on the stress level applied (Fig. 5.1): In the primary creep phase, the molecules are shifted, yet they can move less and less as the deformation increases. Deformations due to this primary creep are reversible. In the secondary creep phase, the first hydrogen bonds break, but can reconnect at a shifted position. However, the deformations due to secondary creep are irreversible. In the tertiary creep phase, more hydrogen bonds break that can reconnect and the creep deformations increase progressively until failure. The tertiary creep only occurs above a certain stress level. To avoid progressive deformations due to creep, the applied load should be kept below a limit stress level (denoted  $\sigma_{lim}$  in Fig. 5.1). The long-term loading of timber also negatively influences the strength. The reduction of the strength values in design is made by the factor  $k_{mod}$ . This factor  $k_{mod}$  is determined for timber by exposing the material to stresses above the stress limit

and recording the time to failure. Creep deformations in timber are also affected by the type of load, the moisture content, the force-grain angle, and varying moisture of the environment [121; 15].

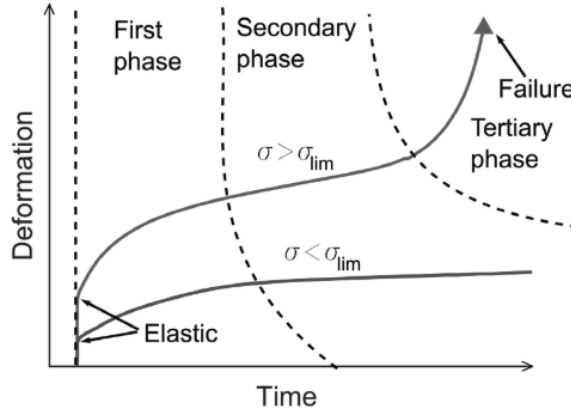


**Fig. 5.1:** Progression of creep strain  $\varepsilon(t)$  in timber [56]

The combination of shrinkage and swelling due to moisture changes and creep due to applied loads lead to a second, non-negligible effect in timber: the mechano-sorptive creep. The deformations of a loaded timber element are higher with moisture changes than under constant moisture. Even in heated indoor rooms, humid and dry phases cannot be avoided due to natural fluctuations of the relative humidity. The effect of mechano-sorptive creep must not be neglected.

Fig. 5.2 shows the different strains  $\varepsilon$  due to short-term loads and the effects of shrinkage/swelling, visco-elastic creep, and mechano-sorptive creep.

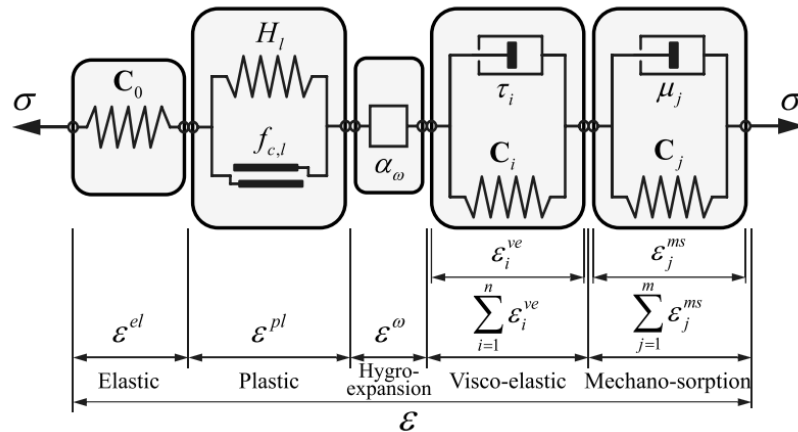


**Fig. 5.2:** Constitutive material model of wood after [65]

In concrete, creep is composed of a delayed elastic and a plastic part. The development of creep in concrete is fast at the beginning and then decrease with time. Similar to creep in timber, creep in concrete also progresses disproportionately if the stress level exceeds 40 % of the strength [99]. Deformations due to elastic creep are reversible, some delayed elastic deformations

disappear after a longer period of relief. The plastic part is irreversible and consists of two effects: basic shrinkage under sealed surfaces and drying shrinkage due to moisture emissions of the concrete. Concrete creep depends on the water to cement ratio, the cement type, the concrete age at the time of loading, the relative humidity, the type of cement, and the area of the concrete component exposed to the environment [138; 22].

### 5.1.3 Interaction in timber-concrete composite slabs

The rheological phenomena in timber and concrete have different intensities, influence factors, and time dependencies. By connecting a timber slab to a concrete slab with a flexible or rigid connection, the volume changes of the two materials are linked to one another at the connection. Additionally, the connection itself also is subjected to rheological phenomena. Therefore, long-term effects in TCC are very difficult to determine, but can have a major impact on deformations and stresses.

Because of the composite action, the deformations due to rheological phenomena in timber and concrete cross-section are coupled. Shrinkage and creep take place simultaneously in both components and influence each other. Fig. 5.3 shows the interaction due to different shrinkage behaviour. After concreting, the concrete top layer shrinks and contracts. Due to the composite action with timber, the timber constrains the free volume reduction of the concrete. This constraint leads to a tensile force in the concrete and a compressive force in the timber resulting in a positive bending moment on the TCC slab and an increase of sagging deflection (Fig. 5.3 top). The differential shrinkage can be caused by the chemical shrinkage described above, but also be due to temperature changes. Because of the higher temperature expansion coefficient of concrete, the situation described above occurs e.g. also when the temperature drops: the concrete top layer shrinks more than the timber layer and increased deflections occur. The reversed situation is shown in Fig. 5.3 below: the concrete expands more in relation to the timber, a negative bending moment results, and the sagging deflections decrease.

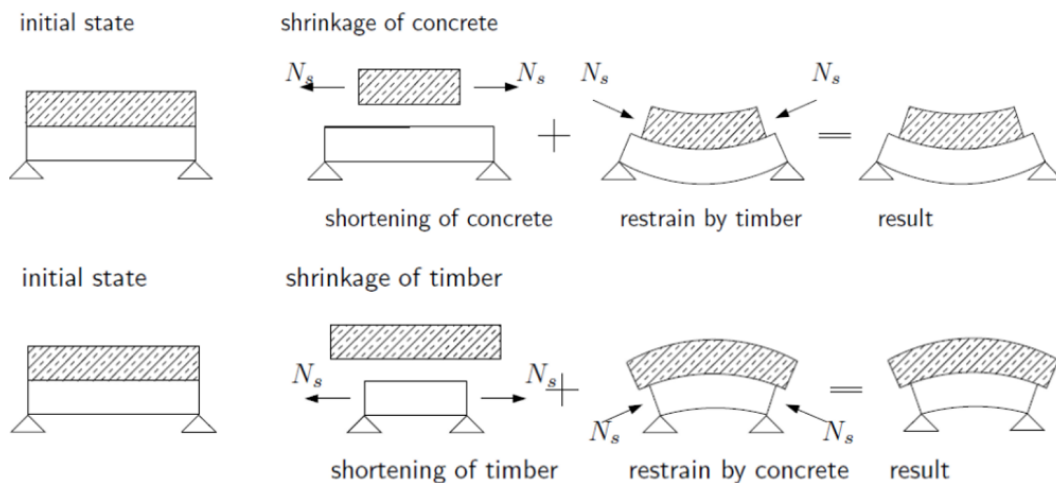


**Fig. 5.3:** Influence of differential shrinkage on the deflections of the TCC beams [98]

The stresses due to this interaction lead to an increased creep behaviour in addition to the load-induced visco-elastic creep. Through the higher creep, the concrete evades the stresses and transfers them to the timber cross-section, which leads to a higher creep in timber, followed by a transfer of stresses to concrete and so on. Because both shrinkage and creep occur at the same time in both concrete and timber, these processes constantly influence each other. The total bending moment, however, stays constant [97]. The creep factor  $\varphi_i$  of the materials is the ratio of creep deformations to the elastic deformations. Because the elastic deformations remain the same in the interaction processes described above, the effective creep factors in a composite beam depend on the bending stiffness ratios of the two components. If the concrete top layer is much stiffer, almost no stresses are transferred to the much softer timber cross-section. In this case, the effective creep factor of concrete corresponds approximately to the material creep factor  $\varphi_1$ . If the timber layer is much stiffer, the creep strain in concrete remains, while the stresses are transferred to the timber cross-section. This process is called relaxation. The effective creep coefficient or composite creep coefficient lies between the material creep coefficient and a creep coefficient corresponding to pure relaxation and depends on the stiffness of the connection. The stiffer the connection, the lower is the influence of the processes described above. However, the influence of connection stiffness is complex because the connection itself leads to the interaction in the first place.

Natterer and Hoefft [120] stated that the time course of the shrinkage and creep deformations is of no importance and that only the end of the service life needs to be proven. By contrast, Schänzlin [138] found that due to the mutual interaction of timber and concrete described above, the time-related development of creep and shrinkage are relevant. Concrete shrinks faster at the beginning and reaches approximately 90 % of its final shrinkage after 3 years, whereas timber at that time only reached around 50 % of its final shrinkage. Between 3 years and 7 years, the creep development is comparable for both materials. Fig. 5.4 shows the progression of the creep factors of both materials. It must be noted that the creep factors of both materials also depend strongly on the load level and moisture changes. During the time between 3 years and 7 years, the most stress is transferred from the already relatively soft concrete cross-section to the still relatively stiff timber cross-section. After 7 years, concrete creep is almost completed and the timber creep catches up. Schänzlin concluded, that the critical points in time for the deformations and stresses in a TCC slab are at the beginning ( $t = 0$ ), at the phase of large stress transfers ( $t = 3...7$  years) and at the end of the service life (often  $t = 50$  years), when both materials have experienced the most of their shrinkage and creep processes.

#### 5.1.4 Models and simplified approaches for codes

The development of the first models to assess the rheological phenomena in TCC slabs is described in detail by Blass [6]. The first models were developed around 1990 [18]. They implemented the influence of creep as a reduction of the MOE of both timber and concrete. Capretti and Ceccotti [16] determined the slip modulus for the serviceability limit state  $K_{ser}$  and a deformation factor  $k_{def}$  as a reduction factor for the MOE. The reduction factor  $k_{def}$

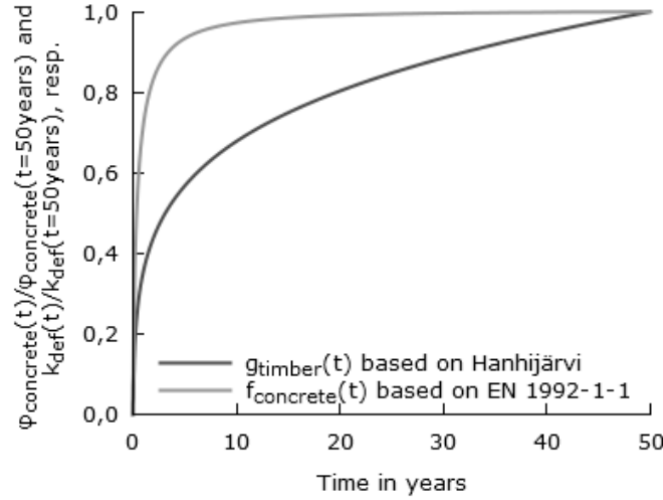


**Fig. 5.4:** Time-related development of creep in concrete and timber [31]

for connections is determined in experiments. This reduction of the MOE of timber, concrete and connection was adapted to Eurocode 5 [21]. The influence of shrinkage and other inelastic strains was taken into account by applying a fictitious load onto the composite cross-section. FE models were also used to simulate the influence of climate changes on the behaviour of TCC. Fragiacomò [42; 41] developed a model based on FE-method taking into account the rheological phenomena of concrete, timber, and the connection, as well as the moisture changes in timber. Khorsandia et al. [82] evaluated different test parameters, i.e. the influence of humidity cycles in a numerical model and verified the model on the basis of experimental data of long-term bending tests with timber-only beams and TCC beams.

Schänzlin [138] developed a detailed model to account for the different rheological phenomena of timber, concrete, the connection, and the interaction between them. He validated his model with existing experiments ([108] [68]), with measurements of deflections and strains of TCC slabs in a building in Germany as well as in own experiments [96]. He took into account not only the reduction of the MOE of the components and the constraints by inelastic strains, but also the interaction of shrinkage and creep depending on the connection stiffness. He implemented all effects in the differential beam equation and found a numerical solution using the difference method. With regard to the applicability in practice, he proposed a simplified model: The influence of creep deformations is covered with the creep factors  $\varphi_1$  for concrete,  $k_{def}$  for timber, and  $k'_{def}$  for the connection as well as extended by an additional factor  $\psi_i$  for every component to account for the interaction of creep and shrinkage depending on the connection stiffness. This additional factor  $\psi_i$  is calibrated with the  $\gamma$ -factor determined with the Möhler approach (Chapter 2.2.2). The influence of shrinkage and other inelastic strains can be taken into account by a fictitious load on the cross-section and a reduction of the bending stiffness depending on the  $\gamma$ -factor of the connection [44]. The state-of-the-art Technical Specification for TCC [30] adapted the proposed simplified model by Schänzlin. Detailed descriptions of the model are given in [139; 31].

### 5.1.5 Previous experimental research

A detailed overview of the long-term experimental and numerical research on TCC connections and TCC structural behaviour is given in [83] and [167]. The planning and realisation of experimental long-term tests is complex, space-consuming, and therefore expensive. However, they are essential for determining the correct system behaviour under creep and shrinkage effect. For flexible connections with low connection efficiencies such as screws, nail plates or glued-in rods, long-term shear tests are usually conducted to determine the creep coefficients  $k'_{def}$  of the connection. Such long-term shear tests were conducted inter alia by [110; 162; 167; 43; 40]. The structural long-term behaviour of TCC beams was investigated in studies with bending tests. In comparison with short-term TCC shear and bending tests, relatively few such studies have been conducted. Table 5.1 lists a selection of long-term bending test series. The list contains all kinds of long-term bending tests on TCC slabs with both linear and planar cross-sections, various connection systems, different timber to concrete ratios, and different timber or concrete properties. The information on test setup, installation, test parameters, measurements, monitoring, and other observations were used for the long-term test series described in the next Chapter 5.2.

The installation of long-term tests must be carefully planned to account for the various influences on the rheological phenomena of TCC slabs. As can be seen in Table 5.1, the loading situation in most series was a 4-point bending test setup. In most cases, the specimens and the test setup were chosen the same or similar as in short-term bending tests. The uniformly distributed load situation corresponds to the usual design loading situation. Depending on the objective of the experiment, this loading situation gives better insight into the practice-relevant structural behaviour. Further, the connection is of great importance, as its stiffness influences the interaction of the components. The span of most test series is chosen between 3.6 m and 8 m, according to common spans in office and residential buildings. Eisenhut & Seim [38] tested two beams with 10 m span and two beams with 12 m span for the application in bridges. The specimens in their study were stored outdoors over a river with no shelter. Equally, for the application in slabs for buildings, the specimens should be tested in a practice-relevant environment. The environmental conditions for such slabs are most likely to be in service class 1 for indoor, heated rooms. However, the aim of the tests can also be focused on the behaviour in a less favourable ambient situation. In many test series, this option was chosen because the test specimens take up a lot of space for a long time and are therefore often placed outside or in non-air-conditioned rooms. The load level is in most test series chosen as the service load for the serviceability limit state. This includes self-weight, superimposed loads, and the quasi-permanent share of the live loads and is around 20-30 % of the estimated failure load  $F_{max}$ . The duration of the tests listed in Table 5.1 is from a few weeks to more than six years. To assess for the seasonal fluctuations of temperature and moisture changes in winter and summer, at least one year of testing is reasonable. However, a longer testing period is needed in order to assess the behaviour during the critical point in time between 3 and 7 years as described in Chapter 5.1.3.

**Tab. 5.1:** Literature selection of long-term bending tests for TCC slabs.

source	type of test <sup>a</sup>	connection	span [m]	total load <sup>b</sup>	service class	no. of specimens	duration of tests
Natterer & Hoefft [120]	UL	screws inclined	5.2	24 kN	1	1	11w
Meierhofer&Kenel [81; 109]	4PB	screws crosswise	3.9	12 kN	2	3	5a
Höhmänn & Siemers [68]	UL	glued-in rods, joist hangers	5.8	SL	1	3	2a
Blass & Romani [7]	4PB	screws, notches + dowels, nailplates, reinforced notches	4.5	20-30% Fu	2	8	6.25a
Kuhlmann & Schänzlin [96]	4PB	notches + screws	5.3,7.3	SL	1	2	2a
Lehmann [99]	UL	alternating lamellas	4.8	SL	1	2	0.25a
Glaser [53]	4PB	notches	3.9	20	1	2	1a
Jorge [77; 76]	4PB	screws crosswise	5.4	30 % Fu	1	4	4a
Fragiacomo et al. [43]	4PB	notches + screws	3.6	SL	2	8	1a
Lukaszewska [102; 44]	4PB	steel plates, steel tubes	4.4	SL	2	2	1a
Yeoh [167]	UL	notches + screws	8.0	SL	1	1	1.4a
Kanocz&Bajzecerova [79]	4PB	crosswise screws, offset notches	5.0	?	?	2	4a
Eisenhut & Seim[38]	4PB	epoxy resin adhesive	10,12	21kN	3	2	2a
Tannert et al. [159]	4PB	adhesive	4,4.8	SL	1	2	4.5a
Tannert et al. [160]	4PB	ASSY VG, HBV mesh	6	SL	1	9	2.5a
Shi et al. [148]	4PB	notches + screws	4.5	30 % Fu	1	6	400d

<sup>a</sup> 4PB: 4-point bending tests, UL: bending tests with uniform load

<sup>b</sup> total load: in [kN] per specimen, in [%] of the failure load or SL = service load

## 5.2 Installation of a long-term test series

### 5.2.1 Objective of the experimental program

The long-term tests were installed as bending tests with 4-point as well as approximately uniform loading situations in a practice-oriented scale. The objective of the tests is the proof of concept of micro-notches as the only connection for a TCC system. The connection between timber and concrete of all specimens was realised without additional screws or dowels. Seven specimen in total were installed. The configurations of the test specimens were chosen so that as many parameters as possible could be independently assessed. The focus of the tests was on the applicability of micro-notches in TCC on the long-term. The tests should show if TCC beams with micro-notches as only connection system can withstand different unfavourable conditions such as high load levels, large spans, undersized dimensions, and shear transfer perpendicular to the grain over a long period. The tests will also be used to evaluate the influence of shrinkage and creep on the composite joint and on the structural behaviour.



## 5.2.2 Materials and methods

### Test setup

The test setup of the long-term tests were bending tests with different loading situations and different lengths. All specimens had a width of 1.16 m (two standard element widths) and were placed on two supports: a fixed support with hinge and a rolling support. The load was applied by means of static weight using concrete blocks. Six of the specimens (L1 to L6) were conducted as 4-point bending tests with the advantages described in Chapter 4.2. The cross-sections and load application points were designed to provoke failure in the composite joint, namely the micro-notches. The concrete blocks were placed on steel profiles that transferred the load onto the load-application points at approximately the thirds of the span. Fig. 5.5 shows the test setup and loading situation for specimens L1, L2, and L4. The test setup is the same for specimens L3, L5, and L6, but the loading situation is different. The seventh specimen L7 was loaded with four weights distributed evenly along the span (Fig. 5.6). This loading situation simulates a uniformly distributed linear load, but corresponds to a 6-point bending test.

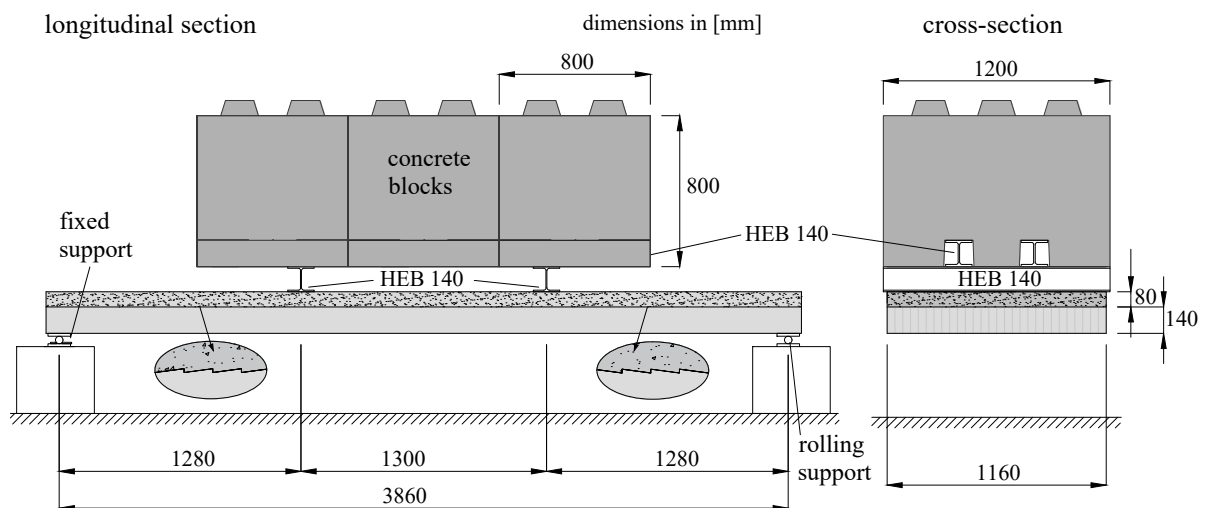


Fig. 5.5: Test setup for long-term tests, specimen L1, L2, and L4

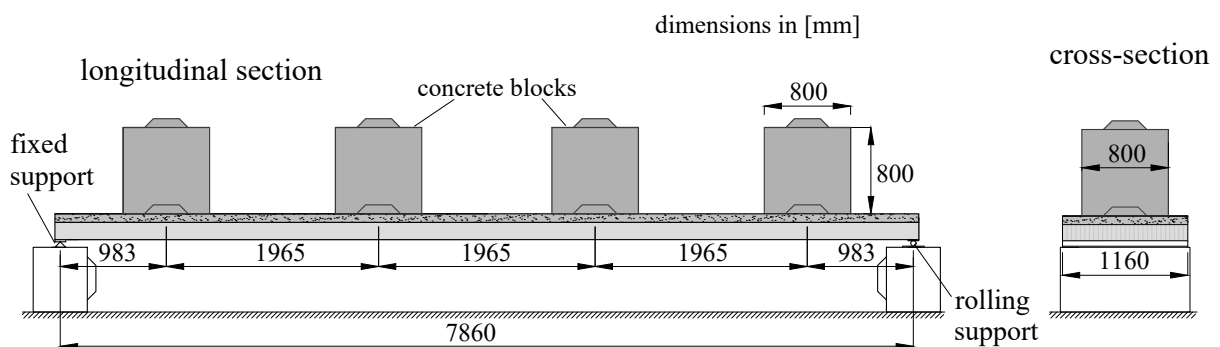


Fig. 5.6: Test setup for long-term tests, specimen L7

The testing room is a cellar, where the specimens are sheltered from the weather. The room is heated to imitate the climate in a indoor application in service class 1. However, for the first months, the room is unheated to imitate the construction state before the installation of the building services. The ambient conditions in this state can be assumed to be in service class 2.

### Specimens

The six specimens L1 to L6 had total length of 4 m and specimen L7 had a total length of 8 m. The design and dimensions of the specimens with a length of 4 m are shown in Fig. 5.7. The specimens L1 to L5 consist of a BST element with a total length of 4 m, height of 140 mm, and a width of 1.16 m composed of 28 lamellas of approximately 41 mm width each, connected by kiln-dried beech dowels. The specimen L6 consists of a CLT element with a total length of 4 m and a width of 1.16 m with an asymmetric layup of four layers: 4-4-4-4 (in [cm]) resulting in a total height of 160 mm. The concrete slab on top of all specimens with length 4 m (L1 to L6) has a thickness of 80 mm. The design and dimensions of the specimen L7 with length 8 m are shown in Fig. 5.8. Specimen L7 consists of a BST element with a total length of 8 m, height of 165 mm, and a width of 1.16 m composed of 28 lamellas of approximately 41 mm width each, connected by kiln-dried beech dowels. The concrete slab on top has a thickness of 110 mm.

The micro-notches are milled into the timber surface in the areas shown in Fig. 5.7 and 5.8. For the specimens L1 to L5, approximately 50 % of the 1.26 m length in the shear areas between the support and load application points on both sides of the beam were covered with micro-notches. The rest of the timber surface is planed evenly. For specimen L6, the micro-notches were arranged on the whole shear area on both sides between the load application points and the supports. For specimen L7, the micro-notches were arranged over a third of the span on both sides near the supports.

The materials used for the long-term test series were normal-strength concrete and spruce/fir timber lamellas for the BST and CLT elements. The specimens were produced in three steps: the production of the timber elements in the factories of the BST producer and the CLT producer respectively, milling of the micro-notches at the factory of the BST producer, and the casting of the concrete directly on site in the testing room.

In the first step, the timber elements were assembled. In this test series, the material properties were tested both on the lamellas used for the elements and the assembled timber elements. The material tests on the timber lamellas included the determination of moisture content by non-destructive moisture measuring devices, the raw density, and the MOE using ultrasound measurement for the BST lamellas and the Timber Grader MTG by Brookhuis for the CLT lamellas. The material tests on the assembled timber elements included the determination of moisture content by a non-destructive, resistance moisture meter and the determination of the MOE in 4-point bending tests according to EN 408 [36]. The mean material properties for the lamellas and timber elements are given per specimen in Table 5.2.

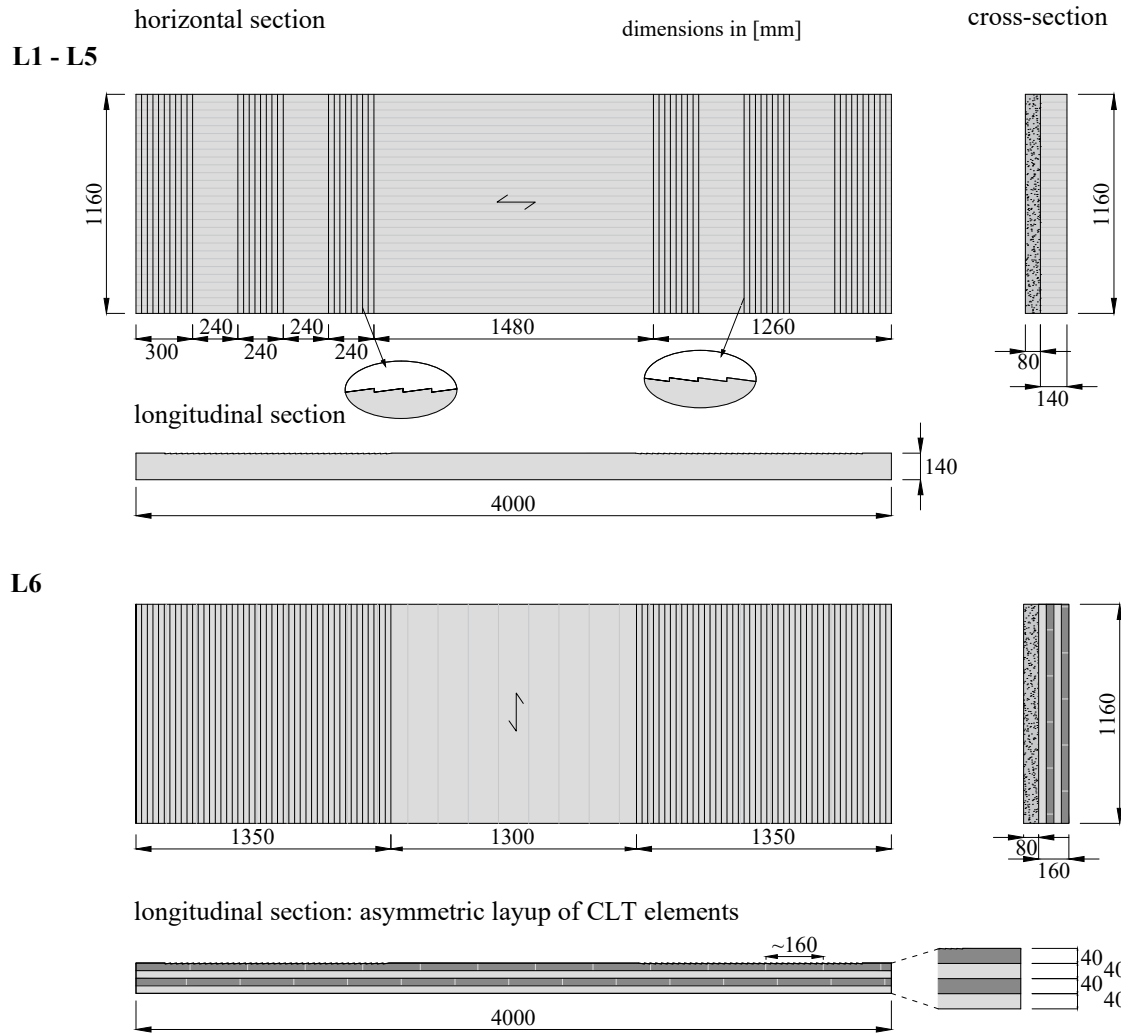


Fig. 5.7: Specimens with span 4 m for long-term tests

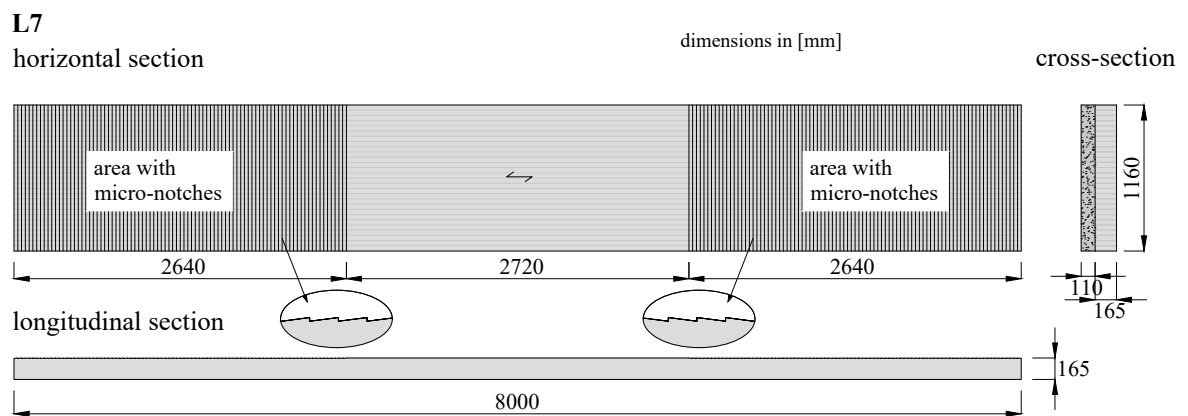


Fig. 5.8: Specimen with span 8 m for long-term tests

**Tab. 5.2:** Mean material properties of timber elements for long-term test series

	individual boards/lamellas			elements	
	moisture content	density	MOE		MOE
	[%]	$\rho$ [kg/m <sup>3</sup> ]	$E_2$ [N/mm <sup>2</sup> ]	$n$ [-]	$E_2$ [N/mm <sup>2</sup> ]
BST	9.3	446	11'522	6	10'233
CLT	10.1	407	11'136	1	12'040

In the second step, the micro-notches were milled by a CNC milling machine into the planed timber surface of the assembled timber elements. The micro-notches were milled in stripes of 8 micro-notches each. The notch geometry was the optimum geometry chosen from the push-out test series II: notch depth  $t_{MN} = 4$  mm, notch length  $l_{MN} = 30$  mm, and notch front angle of  $\alpha = -7.5^\circ$ . This geometry is comparable to the micro-notch geometry tested in the 4-point bending tests: the only difference in the short-term bending tests was the notch front angle of  $\alpha = 0^\circ$  or  $-5^\circ$ , which did not have an influence on the load-bearing behaviour. It can be assumed that the micro-notches used in this test series have the same connection properties as in the short-term bending tests.

In the third step, the concrete top is casted onto the timber elements. The concreting was carried out on site on the timber elements already installed on the test setup. A reinforcing mesh of type K335 was placed in the middle of the concrete height. The longitudinal reinforcement consisted of 4 bars of  $\varnothing 8$  mm resulting in a total area of  $A_{s,l} = 201$  mm<sup>2</sup>. The timber surface was watered one day before and approximately one hour before casting the concrete. The concrete mixture was prepared for a concrete strength class C25/30 with a maximum grain size of 16 mm. Air void content, flow spread, and density of the fresh concrete were determined to assess the quality of the concrete before casting. Concrete samples in form of ten cylinders were casted from the same batch as the specimens to assess the properties of the hardened concrete. The concrete samples were stored in the same room as the specimens. The concrete compressive strength determined from three hardened cylinder samples at age 37 d was  $f_{c,cyl} = 37.4$  N/mm<sup>2</sup>, the MOE 29 094 N/mm<sup>2</sup>, and the density 2326 kg/m<sup>3</sup>.

The configurations tested in the long-term test series are listed in Table 5.3. The main parameters to be tested were the load level and the treatment of the timber surface before concreting. As previously mentioned, a different span and different timber element were also tested with specimens L6 and L7. All tested parameters are listed below:

- The **load level** was the main test parameter of the long-term test series. The long-term deflections of a TCC slab are greatly affected by concrete shrinkage and creep of both materials. Shrinkage can be addressed with shrinkage admixtures in the concrete mixture or by prefabricating the elements. Creep, however, is dependent on the stresses applied and therefore significantly depending on the load level. For the specimens with BST elements and 4 span, three load levels were tested: 0 %, 40 %, and 70 % of the estimated short-term failure load  $F_{max}$ . This failure load  $F_{max}$  was determined with the  $\gamma$ -method using the

characteristic mean strength values after JCSS [75] and  $k_{mod} = 1$ . Specimen L5 (70%  $F_{max}$ ) is expected to be in the tertiary creep phase and reach creep failure as shown in Fig. 5.1. The reference load level was 40%  $F_{max}$ . Specimens L3 (0%  $F_{max}$ ), L4 (40%  $F_{max}$ ), and L5 (70%  $F_{max}$ ) are planned to be tested to failure after some years, if they do not break during the testing time. Specimens L6 and L7 were both tested at service load level. For these test specimens, the focus was not on the increased stress of the notches, but on feasibility of the system, namely the CLT element with notch front perpendicular to grain (L6) and the large span with slender cross-section (L7). In these scenarios, a load at service load level was applied. This service load consists of the design values for the superimposed load of a heavy floor structure ( $g_{A,k} = 1.8 \text{ kN/m}^2$ ) and the quasi-permanent share of the live load in an office building:  $\psi_2 \cdot q_{N,k} = 0.3 \cdot 3.0 \text{ kN/m}^2$ .

- The **treatment of the timber surface** with water before concreting was already investigated in the local shear tests and the bending tests. In these two short-term test series, the watering did not have a significant influence on the strength of the concrete near the composite joint, the local or global connection behaviour, nor the structural behaviour of the slab. The long-term tests are aimed to show if the watering influences the TCC slabs on the long term: Specimen L2 was not watered before casting the concrete. The rest of the specimens were watered one day before and one hour before concreting.
- The **timber elements** used in almost all tests in the frame of this research project were BST elements for uniaxial load situations. In the 4-point bending test series described in Chapter 4.2, one specimen was tested with a CLT element with shear transfer parallel to the grain in the notch front. Since the failure in this specimen did not occur and is also not expected to occur in the micro-notches in practice, testing the same configuration in long-term will offer no new insights. Therefore specimen L6 was installed with an asymmetric CLT element in the long-term test series. This specimen is to show the long-term behaviour of the micro-notches with shear transfer perpendicular to the grain.
- The **span** of the specimens L1 to L6 was approximately the same as in the short-term bending tests in the 4-point bending test series. Specimen L7 had a span of 8 m, which is around the upper limit of the usual range in practice. This test specimen is an illustrative test to show the deformation behaviour of very wide spanning slabs. Due to a production error, the timber cross-section is significantly undersized. The timber thickness  $h_2$  is 165 mm, but should be 200 mm to fulfil the SLS requirements of deflection and vibrations.

**Tab. 5.3:** Specimen configurations for long-term test series. Every row corresponds to one specimen.

Parameters altered in relation to the reference configuration are highlighted in gray

specimen	concrete thickness	timber thickness	timber	timber treatment <sup>a</sup>	direction of grain	beam width	span	load situation <sup>b</sup>	load level <sup>c</sup>	applied load	micro-notch arrangement
	$h_1$ [mm]	$h_2$ [mm]				$b$ [mm]	$l$ [m]			$F$ [kN]	
L1	80	140	BST	w		1160	3.9	4PB	40%	56.4	strips
L2	80	140	BST	-		1160	3.9	4PB	40%	56.4	strips
L3	80	140	BST	w		1160	3.9	4PB	0%	0	strips
L4	80	140	BST	w		1160	3.9	4PB	40%	56.4	strips
L5	80	140	BST	w		1160	3.9	4PB	70%	104.2	strips
L6	80	160	CLT	w	⊥	1160	3.9	4PB	SL	22.5	in full
L7	110	165	BST	w		1160	7.9	6PB	SL	49.2	in full
Total specimens in long-term test series											<b>7</b>

<sup>a</sup> treatment of the timber surface before concreting: w = water, - = no water

<sup>b</sup> load situation: 4PB = 4-point bending, 6PB = 6-point bending  $\approx$  uniformly distributed load

<sup>c</sup> load level: as part of the estimated failure load  $F_{max,est}$  in [%] or SL = service load

## Measurement points

The measurement points for the long-term test series are listed in Table 5.4. The position of the measurement points are shown in Fig. 5.9. The load  $F$  is applied statically by concrete blocks and the steel profiles to introduce the load approximately equally in the third points of the span. The global deflections  $w_i$  are measured in the middle of the beam width at mid-span  $w_M$  (see cross-section in Fig. 5.9). The deflections due to the self-weight of the timber element are not included in the measurements. The relative slip between timber and concrete is measured with linear variable differential transformers (LVDT) also in the middle of the beam width. The horizontal relative slip  $u_i$  is measured for both shear areas left  $u_{LM}$  and right  $u_{RM}$  as well as at the beam ends left  $u_L$  and right  $u_R$ . Additionally, strain gauges were installed at four points in the composite cross-section:  $\varepsilon_1$  on the top of the concrete,  $\varepsilon_2$  on the reinforcement,  $\varepsilon_3$  in the middle of the timber cross-section, and  $\varepsilon_4$  at the bottom of the timber cross-section. The relative humidity and the temperature in the room are continuously measured. The moisture content of timber is measured at four points in the timber cross-section by resistance moisture meters using screws as sensors. One pair of screws each inserted from the bottom of the timber cross-section measure the moisture content in different depths (see Fig. 5.9 bottom). The measurement program described above and illustrated in Fig. 5.9 is conducted completely for test pieces L1 and L2. For the rest of the specimen, only a part of the measurement program is conducted. Table 5.4 lists the measurements for every individual specimen.

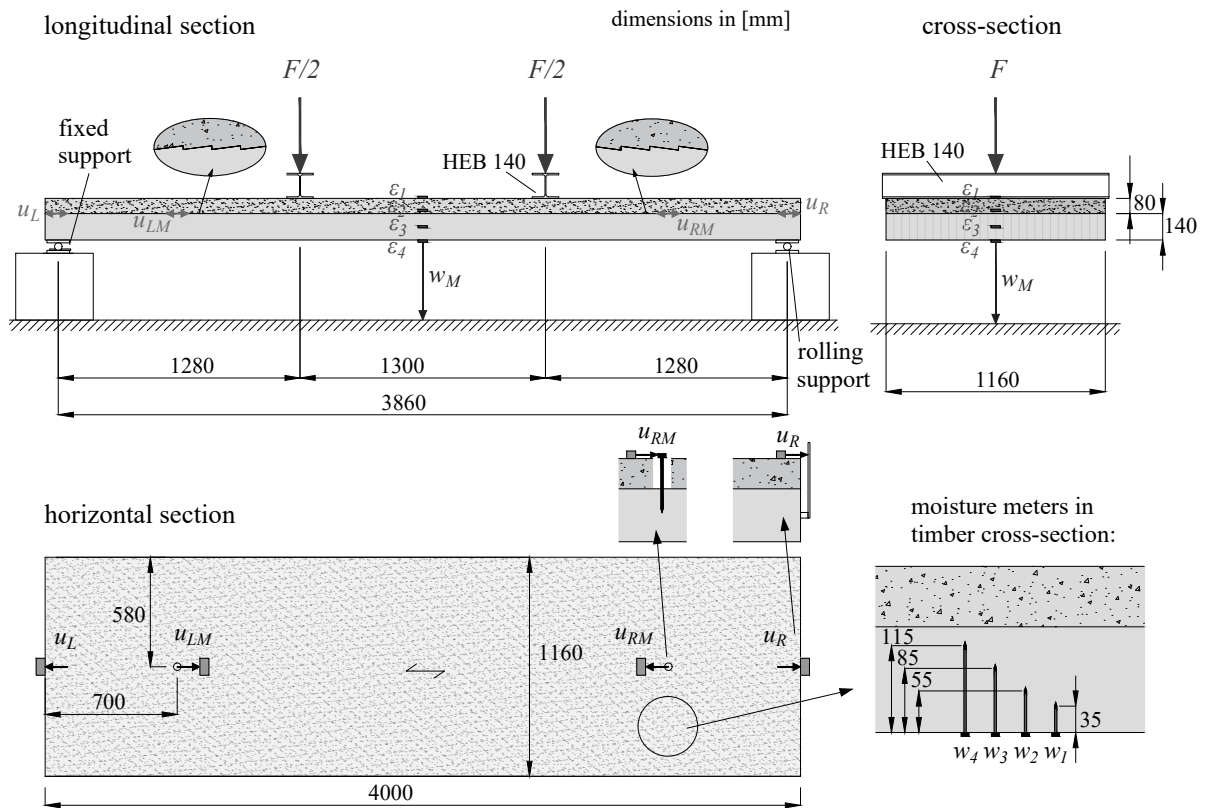


Fig. 5.9: Measurement points for long-term tests

Tab. 5.4: Measurement points for long-term tests

measurement	position	name								device	capacity	accuracy
			L1	L2	L3	L4	L5	L6	L7			
temperature	in room	$T$									$-20\text{ }^{\circ}\text{C} \dots 80\text{ }^{\circ}\text{C}$	$\pm 1\%$
rel. humidity	in room	RH									$0 \dots 100\%$	$\pm 1\%$
global deflection	mid-span	$w_M$	✓	✓	✓	✓	✓	✓	✓	LVDT	$\pm 50\text{ mm}$	$\pm 0.3\%$
horizontal slip	left end	$u_L$	✓	✓	-	-	✓	✓	-	LVDT	$\pm 25\text{ mm}$	$\pm 0.2\%$
	left shear area	$u_{LM}$	✓	✓	-	-	-	-	-	LVDT	$\pm 25\text{ mm}$	$\pm 0.2\%$
	right shear area	$u_{RM}$	✓	✓	-	-	-	-	-	LVDT	$\pm 25\text{ mm}$	$\pm 0.2\%$
	right end	$u_R$	✓	✓	-	-	✓	✓	-	LVDT	$\pm 25\text{ mm}$	$\pm 0.2\%$
strains	concrete top	$\varepsilon_1$	✓	✓	-	-	✓	-	-	SG	$1000\text{ }\mu\text{m/m}$	$\pm 0.2\%$
	reinforcement	$\varepsilon_2$	✓	✓	-	-	✓	-	-	SG	$1000\text{ }\mu\text{m/m}$	$\pm 0.2\%$
	timber center	$\varepsilon_3$	✓	✓	-	-	✓	-	-	SG	$1000\text{ }\mu\text{m/m}$	$\pm 0.2\%$
	timber bottom	$\varepsilon_4$	✓	✓	-	-	✓	-	-	SG	$1000\text{ }\mu\text{m/m}$	$\pm 0.2\%$
moisture		$w_{1-4}$	✓	✓	-	-	-	-	-	CM	$6 \dots 80\%$	$\pm 0.3\%$

### Testing procedure and Monitoring

The measurements of global deflections, moisture content of timber in specimens L1 and L2, and the temperature and the relative humidity of the room were started before concreting on top of the timber elements installed on the supports. Specimen L7 (with 8 m span) was propped during concreting. After 28 days, the props were removed. With the concrete hardened, the relative slip measurements and the strain gauges  $\varepsilon_1$  were installed on the concrete top.

#### 5.2.3 Results to date

The deflection and ambient condition measurements were started in December 2019. The load was applied in January 2020. So far, the ambient conditions and the deflection of all beams are evaluated for six months of measurement. The measurements are subject to certain leaps due to faulty measurement devices.

#### Ambient conditions

Fig. 5.10 shows the relative humidity and the temperature in the testing room. The temperature in the so far unheated room shows no major fluctuations. The winter months were mild above average and the measured temperatures are always well over  $0^\circ$ . The temperature fluctuations of day and night cycles are also visible. The humidity in the testing room fluctuates between less than 50% and more than 80%. The ambient conditions so far in the testing room can be classified as service class II. The continuously measured temperature and relative humidity will allow a detailed assessment of the rheological phenomena in the TCC slabs. Long time periods will show the seasonal fluctuations.

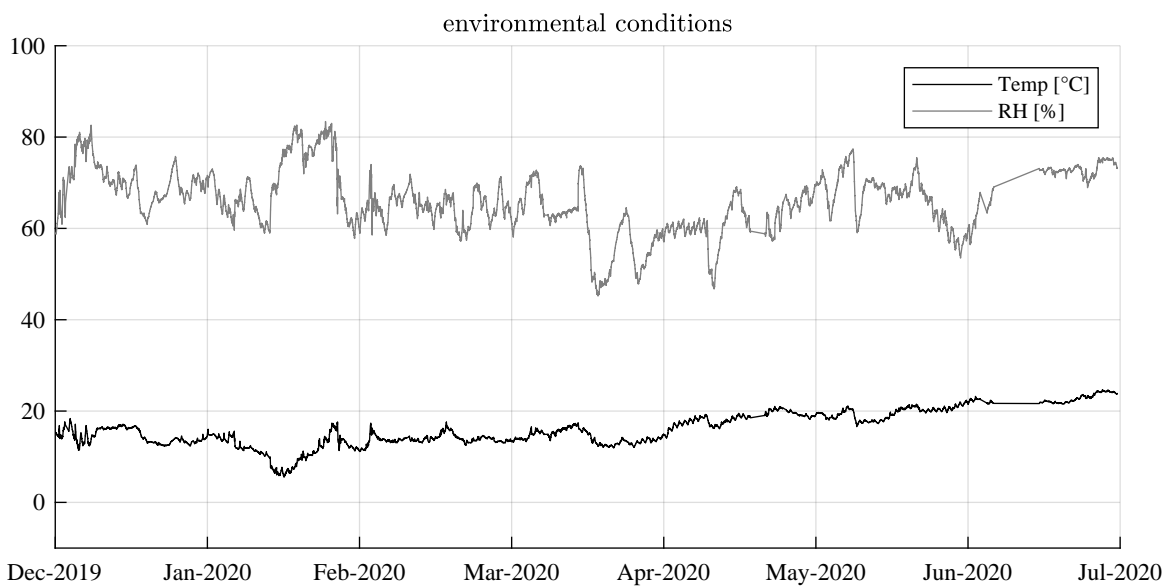


**Fig. 5.10:** Measurements of temperature and relative humidity



## Deflections

The deflections of the seven specimens are shown in Fig. 5.11 - 5.13. Fig. 5.11 shows the deflections of the three specimens L1, L2, and L4 subjected to 40 % of  $F_{max}$ . The weight of the concrete led to a mean deflection of 2.7 mm. This corresponds well with the calculated deflection of 2.4 mm due to the concrete weight. The deflections increased to around 6 mm during the 28 d of concrete hardening. The application of the load led to an additional deflection of around 4.2 mm. This is higher than the estimated 3.3 mm. Since then, the deflections have similarly increased for all specimens by approximately 10 mm. The deflection guideline value for SLS verification with  $w \leq \frac{l}{300}$  is 13 mm. Assuming that this span would not be propped in practice, the measured deflections of the beam already exceeded the SLS guideline value. The reasons for this have to be evaluated. The deflection curves are almost congruent for the three specimens. This was to be expected since the three specimens have the same geometry and loading situations and the material properties can be assumed to be similar as well.

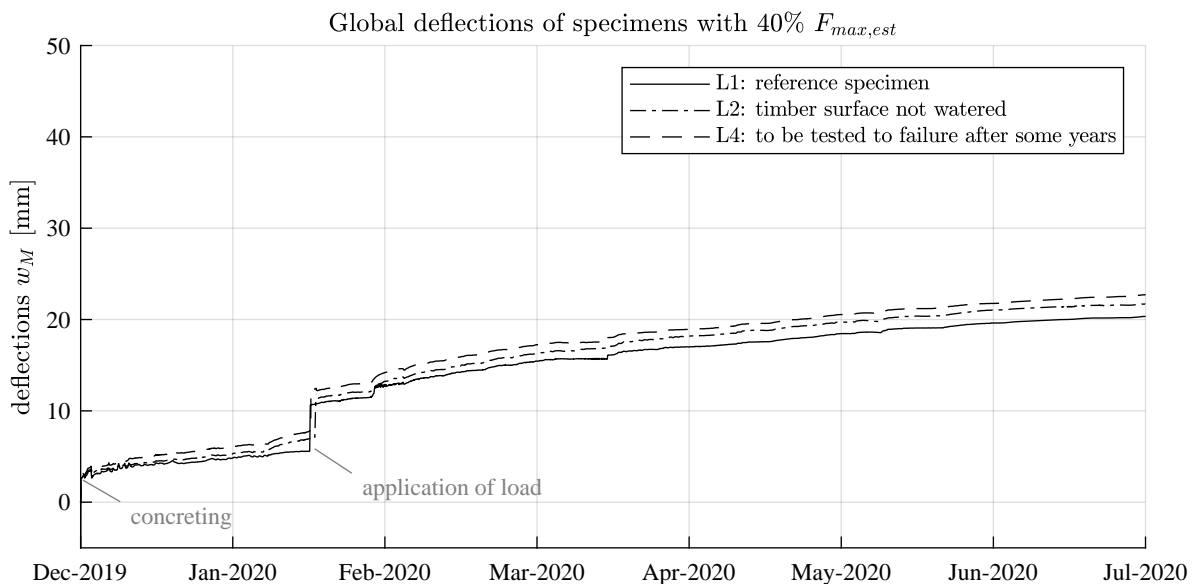


**Fig. 5.11:** Measurements of deflections for all specimens loaded with 40% of the estimated short-term failure load  $F_{max,est}$

Fig. 5.12 shows the deflections of the three specimens L3, L4, and L5 subjected to 0 %, 40 %, and 70 % of  $F_{max}$ . The deflection curve of specimen L3 shows the deflection solely due to self-weight of the concrete and due to creep deformations. In the six months since concreting, the unloaded specimen deflected around 10 mm. Specimen L5 deflects approximately 8 mm under the application of the concrete blocks. This is higher than the estimated 5.9 mm. The deflections of specimen L5 after application of the load are approximately 5.5 mm or 30% larger than the deflections of specimen L4. The deflections are proportional to the applied load and should therefore be 75% higher. This implies that the applied static load with concrete blocks has a lower influence on the deflections than expected. It is possible that the influence of the concrete self-weight is highly underestimated. Specimen L5 deflected approximately 12 mm

after the application of load and approximately 4 mm after concreting. The total approximately 16 mm deflections solely due to rheological processes are considerably higher than the deflections observed in the unloaded specimen L3. The part after the application of the load is comparable: specimen L3 deflected approximately 6 mm and specimen L5 deflected approximately 12 mm. The deflections due to rheological processes under a high load level of 70% of  $F_{max}$  are double over a period of 5.5 months compared to a non-loaded specimen. The deflections for all specimens are higher than estimated with short-term models. Even the deflections of the unloaded specimen L3 reach the guideline value for  $w \leq \frac{l}{300}$ . However, it has to be pointed out that the specimens as well as the setup were planned and dimensioned to evaluate the failure behaviour of the micro-notches, not to fulfil SLS requirements.

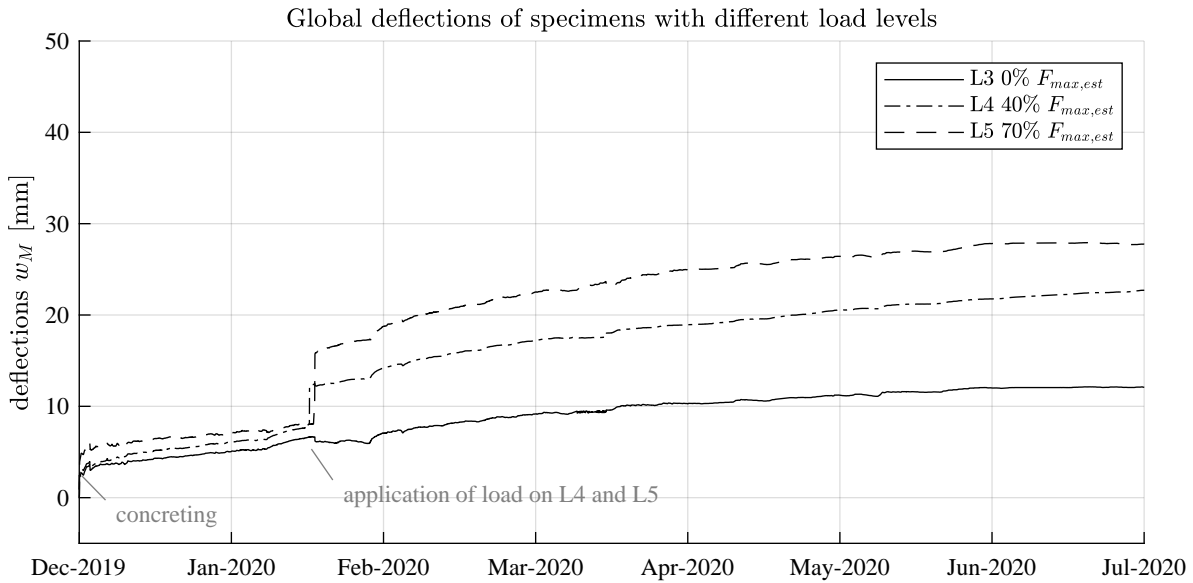


**Fig. 5.12:** Measurements of deflections for specimens loaded with different load levels in % of the estimated short-term failure load  $F_{max,est}$

Fig. 5.13 shows the deflections of the specimens L6 with CLT element and L7 with the large span and slender cross-section in reference to the deflections of specimen L1. The measurement curve of L6 shows some irregularities. However, the overall deflections are in the range of specimen L2. Specimen L7 was propped until one week before the application of the load. The removal of the propping resulted in an abrupt deflection increase of around 15 mm. The estimated deflections due to self-weight are considerably lower with 6 mm. However, the estimated deflections due to concrete self-weight were 33 mm. It must be assumed that the abrupt deflections after removal of the propping consist to a large part of deflections due to internal strains occurred during the load of concrete self-weight on the timber element. The application of the load led to another deflection increase of around 14 mm. The estimated deflection with short-term models was 15 mm. The deflections due to creep are very high: around 4 mm in the week between removal of the propping and application of the load and around 32 mm in the 5.5 months since the application of the load.

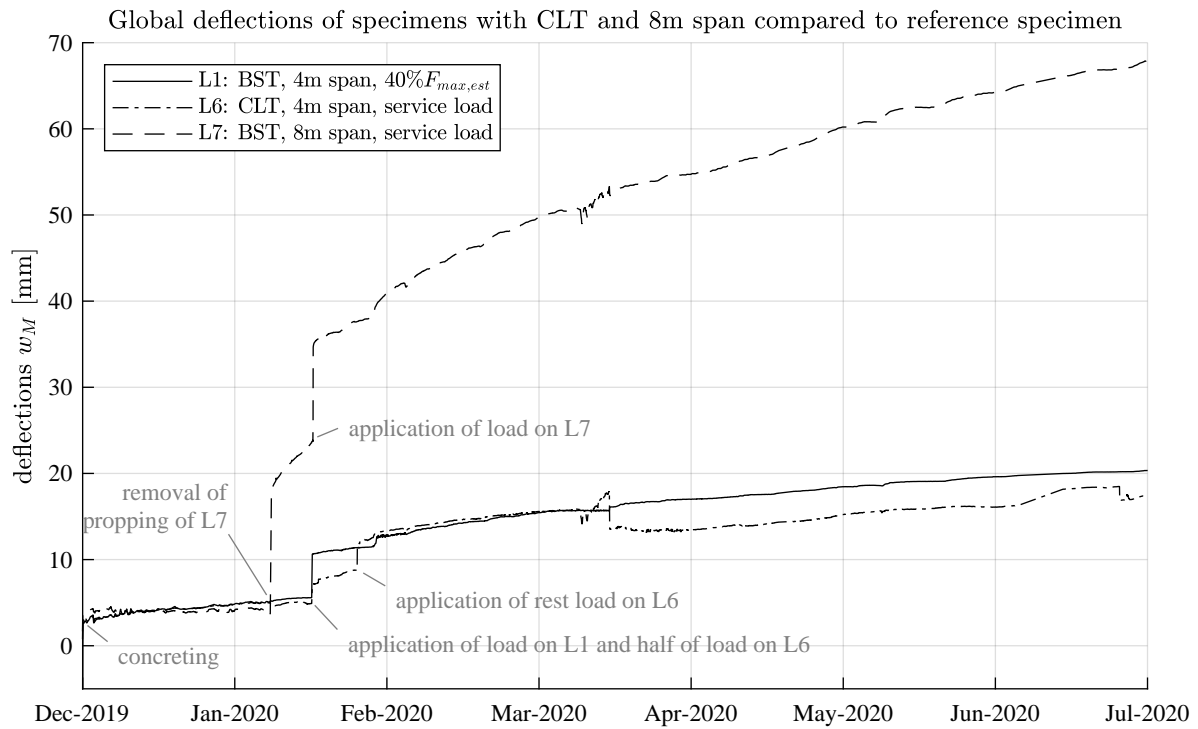


**Fig. 5.13:** Measurements of deflections for reference specimen L1 and special specimens with CLT timber element (L6) and long span of 8 m (L7)

The measured elastic deflections for all specimens are in general higher than the estimated values. No estimations were made yet for the creep deflections and the deflections due to shrinkage in concrete. The high relative humidity in the testing room indicates substantial creep in the timber cross-section. Further, the concrete shrinkage is assumed to be substantial as well due to the absence of shrinkage reducer in the mixture. The rheological phenomena are a probable cause for the large deflections.

### 5.3 Outlook

The aim of this long-term test series is to thoroughly document the properties of the material, the deflections due to different impacts, and the influence of different parameters on TCC slabs with micro-notches as the only connection system. The documentation of the material properties, the installation of the specimens, the concreting, and application of load has been completed. The measurements were started shortly before concreting and are constantly monitored. The deflections evaluated so far for each specimen make sense relative to each other. However, the measured deflections are in general higher than estimated with the short-term calculation models. The influence of shrinkage of concrete and creep under self-weight and under imposed loads already led to deflections in the double-digit range. The estimated deflection values need to be reevaluated carefully. The long-term effects need to be considered to make an accurate evaluation of the deflections observed so far. Due to the very high relative humidity of around 70%, the creep in timber was higher than expected. It is also possible that the high deflections observed are due to high concrete shrinkage because no shrinkage reducer was added. In the frame of this thesis, only the installation and the first results concerning the ambient conditions and the deflections can be presented. The processing of the gathered data and the comparison with the simplified models for long-term behaviour of TCC slabs according to Eurocode 5 [21] or the state-of-the-art extended model in the Technical Specification [30] are to be investigated in the next steps.

## Chapter 6

# Two-span TCC beams with micro-notches

### 6.1 Introduction and literature review

#### 6.1.1 Overview

The vast majority of slabs constructed in timber in buildings are simply-supported, single-span beams. The design is often dictated by the serviceability limit state (SLS), mostly because of large deflections. Continuous beams over multiple spans have the advantage of the deformation constraint in the middle support which leads to less deflection and enables load redistribution. However, continuous TCC beams are so far mostly used in bridge construction, such as the two-span TCC bridge in Rhupolding built in 2010 [1] or the TCC bridge spanning the Agger in Lohmar built in 2014 with three spans [111]. In Switzerland, TCC bridges have been constructed mainly as trussed bridges. The first TCC bridge was the trussed bridge with four spans over the Ronatobel in Furna, built in 1991 [131]. The few studies carried out to date on continuous TCC beams are described in the following chapter.

#### 6.1.2 Previous experimental and numerical research

**Marschall** [103] calculated and compared the slabs in a daycare center in Neckarsulm as single-span and two-span beams. He used both the  $\gamma$ -method and the strut-and-tie model for his calculations. The long-term effects were taken into account with the extended  $\gamma$ -method according to Schänzlin [30; 138]. To consider the length of the cracked concrete above the middle support, he chose a simplified approach from Eurocode 2 [22] for steel-concrete composite beams. According to this approach, the length of cracked concrete can be assumed as 15% of the span on each side of the middle support. His work shows that lower deflection is the main advantage of two-span beams over the single-span beams. The middle support acts as a constraint which lowers the rotation left and right of the middle support and thus decreases the deflections in the spans. He concluded that a TCC system designed as two-span beam instead of two single-span beams can be realised with more slender cross-sectional dimensions. However, the continuous

action has a negative effect on the ultimate limit state (ULS). Fig. 6.1 shows the shear forces and bending moment in a two-span beam subjected to a uniformly distributed load  $q$ . The negative bending moment over the middle support is generally unfavourable for TCC systems with timber at the bottom and concrete at the top. The tensile stresses in the concrete lead to cracks and thus to a reduction of the effective concrete cross-section and the stiffness of the composite beam. As a result, the timber cross-section is subjected to more stress and the overall load-bearing capacity is compromised. The shear forces over the middle support are significantly higher than the shear forces in single-span beams and also lead to higher shear stresses in the composite joint. On the other hand, due to the concrete cracking and the reduced stiffness, rearrangements of the internal forces from the middle support to the two spans occur. The cracking of concrete thus reduces the negative moment and the shear forces over the middle support.

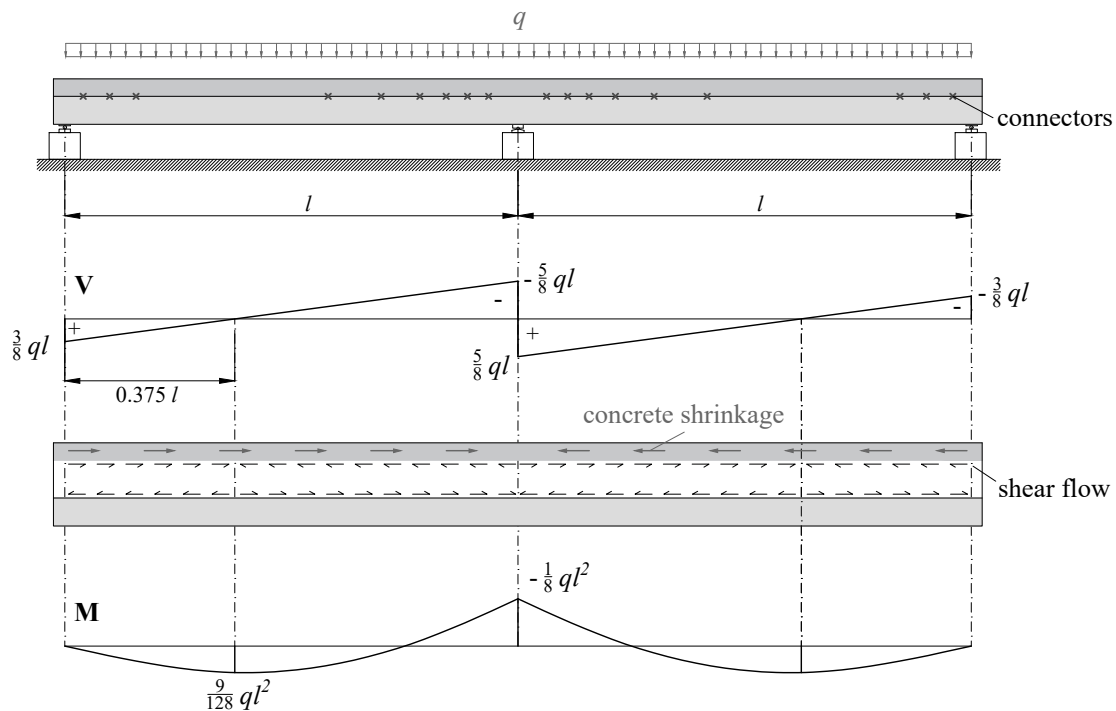


**Fig. 6.1:** Direction of shear flow and concrete shrinkage in two-span TCC beams

Marschall points out another disadvantage of the two-span system: the direction of the inelastic strains due to concrete shrinkage. In single-span beams, the inelastic strains due to concrete shrinkage are always in the opposite direction to the shear flow due to vertical loads and therefore have a relieving effect on the connection system. Fig. 6.1 shows the shear flow in the composite joint and the direction of the concrete shrinkage in two-span beams: the inelastic strains due to concrete shrinkage run towards the middle of the overall beam length, but the shear flow due to vertical loads changes over the middle support and runs in the same direction as the concrete shrinkage along the major part of the span length. The concrete shrinkage in

two-span beams has therefore a burdening effect on the connection system. As a consequence, the resulting shear stresses in the connection in two-span beams might be decisive in the long-term verifications. It is suggested to place more connectors in the area of the middle support to address this issue [50].

**Sebastian et al.** [146; 145] performed 3-point bending tests on an inverted TCC cross-section in order to investigate the structural behaviour of TCC beams under negative bending moments. The TCC cross-section was a 70 mm thick and 500 mm wide concrete top plate of class C32/40, reinforced with  $\varnothing$  12 mm rebars and a beech laminated veneer lumber rib of 200 mm height and 120 mm width. The connection was realised with perforated steel plates and additional two-component epoxy adhesive. The total span of the test setup was 4.6 m with the load applied in the middle of the span. Two specimens were tested, one specimen in a “sagging position” where the TCC beam is subjected to positive bending moments and the other specimen in a “hogging position” where the TCC beam is subjected to negative bending moments. The same test setup was used for both situations: for the “sagging position”, the TCC beam was installed with concrete on top and timber at the bottom, and for the “hogging position”, the TCC beam was inversely installed with the timber on top and the concrete at the bottom. For the “sagging” specimen, a failure load of 163 kN was reached with connection yielding as first failure mode and timber bending failure as the ultimate failure. For the “hogging” specimen, a failure load of 145 kN was reached. For this specimen, the study reports cracking of concrete, then yielding of the reinforcement steel, followed by timber and connection failure as ultimate failure. The connection stiffness was linear elastic until failure of the connection and the reinforcement for “sagging” and “hogging” respectively. Sebastian et al. state that ductile structural behaviour is possible for both situations due to the high ductility of the perforated steel plate connection and the reinforcement steel.

**Ghafari et al.** [52] performed vibration tests on a four-span TCC beam with joist hangers to evaluate the vibration susceptibility of multi-span TCC beams. Their modal testing included excitation by a shaker and an impact hammer. They tested the system with four-span, then cut the cross-section and also tested it as three-span, two-span, and single-span system. They recorded generally larger relative accelerations and deformations than they estimated. With regard to the number of spans, they could not detect any major differences in natural frequency and damping values. No tests on the load-bearing behaviour were performed.

**Schilliger** [142] performed 4-point bending tests and inverted 3-point bending tests on TCC with notches to simulate the areas with positive bending moments and with negative bending moments in a two-span beam respectively. All specimens had a total length of 5 m, width of 0.5 m, and consisted of a 100 mm thick concrete layer and a 160 mm thick CLT layer. The CLT layup consisted of 5 layers: 40-20-40-20-40 [mm]. The connection was realised with conventional notches (depth 20 mm, length 200 mm, notch front angles of  $\alpha = 0^\circ$ ) and one additional wafer-head screw arranged in the middle or in front of each notch. The test setup for the areas subjected to negative bending moments was a 3-point bending test over a length of 3.7 m. The surplus of 0.65 m on each side should act as a partial constraint. Three different configurations were tested in these inverted 3-point bending tests: three specimens with four notches on each

side, three specimens with three notches and three specimens with three notches and additional concrete lock at each end of the beam. The concrete locks were heavily reinforced concrete cross-sections over the whole beam height at both ends of the composite beam and should simulate a full constraint. The constructive reinforcement in all specimens was a reinforcement mesh K188 ( $\varnothing$  8 mm with distance 150 mm). The specimens subjected to negative bending moments had an additional reinforcement of 18 mm with distance 150 mm, and end anchoring. He reported the first failure in the notches, followed by rolling shear failure in the CLT cross-section. In addition, Schilliger conducted numerical investigations to assess the potential of force redistributions. Compared to single-span beams with the same span, he found a reduction of the deflections in the span by 50 % and a reduction of the bending moments in the span by 64 %. He concludes that using a continuous two-span beam instead of two single-span beams, the span could be increased by 26 % to still fulfil the SLS requirements and by 25 % to still fulfil the ULS requirements.

Each of the studies described above only covers a part of the issue of continuous action in TCC beams. No experimental data is available where both spans were tested in full. The  $\gamma$ -method and the strut-and-tie model used by Marschall [103] to investigate the load-bearing behaviour in continuous beams was based on a rough simplification of the length of the cracked concrete over the middle support.

The test series described in the following Chapter 6.2 had two objectives: to investigate the connection behaviour of micro-notches in the area of cracked concrete over the middle support and to investigate the structural behaviour of two-span TCC beams in general. Two models, used to assess the behaviour of the beams, also analyse and implement the length of cracked concrete in the area of the middle support and the subsequent redistribution of shear forces and bending moments.

## 6.2 Experimental two-span beam tests

### 6.2.1 Materials and methods

#### Test setup

The test setup was a two-span beam system with a total length of 12 m with two spans of 6 m each. The specimens had a width of 0.58 m and were placed on three supports: the vertically and horizontally fixed middle support with hinge and the rolling supports at both beam ends. The load situation was an approximated uniformly distributed load by four load application points in each span. The load was applied by eight hydraulic cylinders anchored in a strongfloor and transferring the load via a steel profile construction onto the beam (Fig. 6.2). The hydraulic cylinders were arranged in pairs on each side of the beam and the load per cylinder pair was transferred by steel profiles into the middle of the beam width and onto two linear load applications (Fig. 6.3).



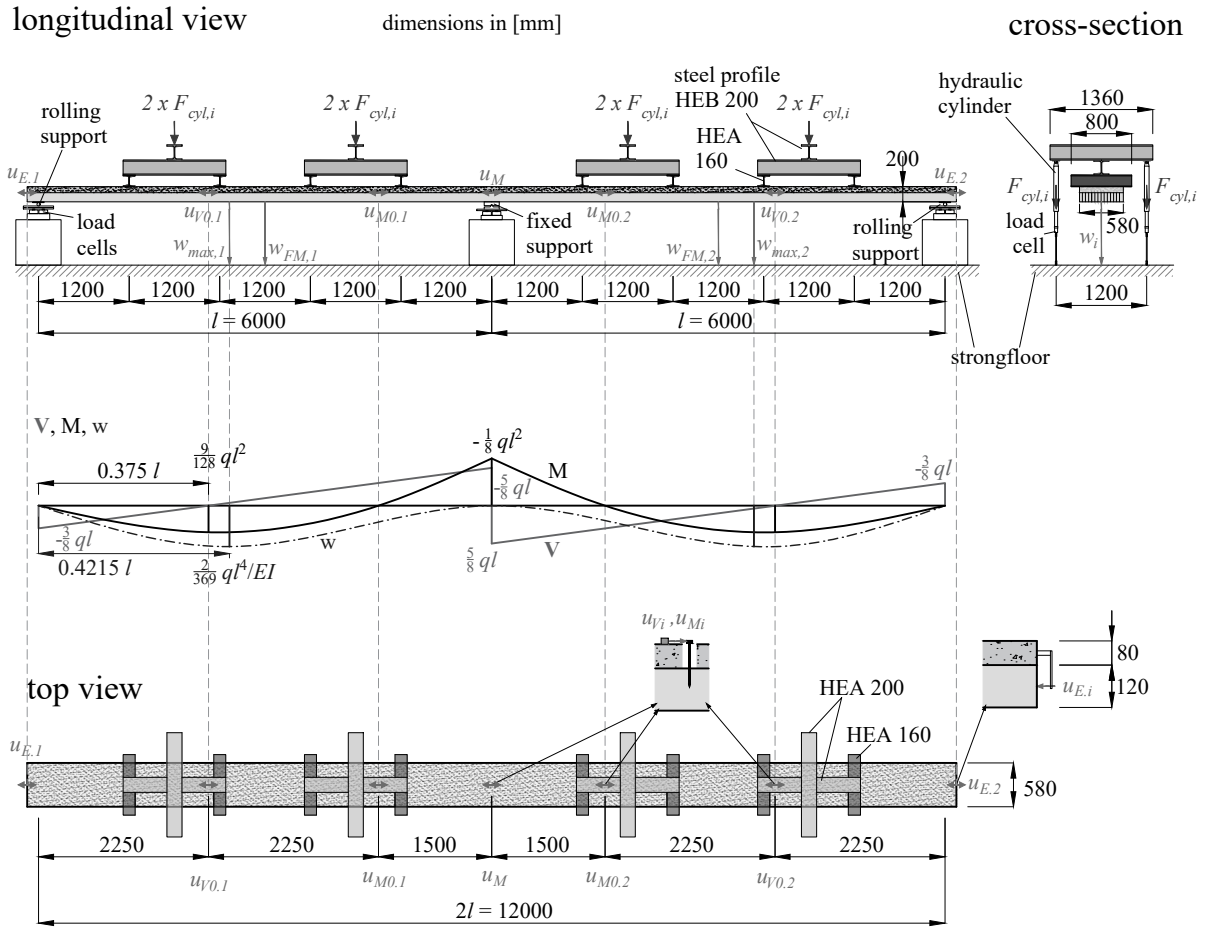


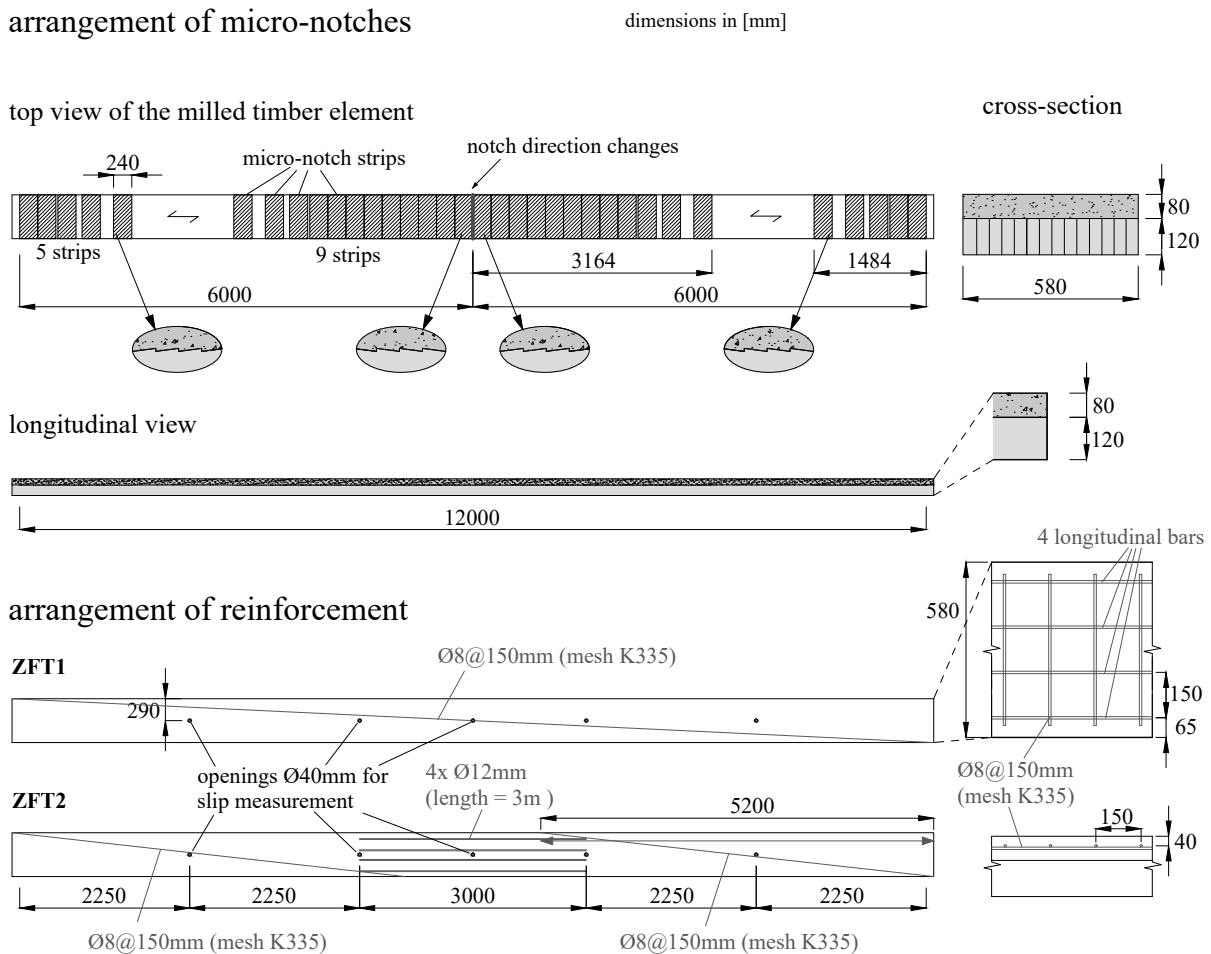
Fig. 6.2: Test setup and measurements for the two-span beam tests



Fig. 6.3: Specimen ZFT2 after failure in one span

**Specimens**

Two specimens were tested: ZFT1 and ZFT2. Both specimens had the same dimensions with total length of 12.1 m, width of 0.58 m, and consisted of a 120 mm thick BST element and a 80 mm concrete top layer. The connection was realised with micro-notches arranged in strips with 8 micro-notches each as shown in Fig. 6.4. The strips are arranged according to the shear force progression in the span (Fig. 6.1). The direction of the micro-notches is so that the notch front faces the shear flow, therefore the direction of micro-notches changes over the middle support. Table 6.1 shows the characteristics of the two specimens. Both specimens had a reinforcement mat of  $\varnothing$  8 mm rebars in distances of 150 mm (four bars over the width of the specimen) placed in the middle of the concrete height. For specimen ZFT1, the reinforcement mat was arranged on the whole length. For specimen ZFT2, the same reinforcement mat was arranged in the two spans. In the area of the middle support, the reinforcement mat was replaced with a larger reinforcement of  $\varnothing$  12 mm rebars in 150 mm distances (four bars over the width of the specimen). The reinforcement plan is shown in Fig. 6.4.



**Fig. 6.4:** Two-span beam specimens

**Tab. 6.1:** Specimen configurations for two-span beam test series. Every row corresponds to one specimen.

Parameters altered in relation to the reference configuration are highlighted in gray

name	concrete thickness	reinforcement in the fields	reinforcement over the middle support	timber thickness	timber	specimen width	spans	load situation <sup>a</sup>	micro-notch arrangement	notch depth	notch length	front angle
	$h_1$ [mm]	$A_{s,F}$ [mm <sup>2</sup> ]	$A_{s,M}$ [mm <sup>2</sup> ]	$h_2$ [mm]		$b$ [mm]	$l$ [m]			$t_{MN}$ [mm]	$l_{MN}$ [mm]	$\alpha$ [°]
<b>ZFT1</b>	80	201	201	120	BST	580	2 × 6	UL	strips	4	30	-7.5
<b>ZFT2</b>	80	201	452	120	BST	580	2 × 6	UL	strips	4	30	-7.5
Total specimens in two-span beam test series												<b>2</b>

<sup>a</sup> load situation: UL = uniform load

The materials used for the test series were normal-strength concrete and spruce/fir timber lamellas of strength class C24. The specimens were produced in two steps: the production of the timber elements and milling of the micro-notches in the company of the BST producer, as well as the casting of the concrete at the laboratories at ETH Zurich.

In the first stage, the timber lamellas were assembled, connected by beech dowels, and their surface was planed. The width of 580 mm corresponds to one standard element width. Then, the assembled beams were cut to length and the micro-notches were milled in strips of 8 micro-notches each using a special milling tool and a CNC milling machine into the planed timber surface. The fully prepared timber elements were then transported to ETH Zurich. The moisture content was determined with resistance moisture meters on five points along the beam on both sides. The MOE of the timber elements of both specimens ZFT1 and ZFT2 were determined on the test setup with the same loading situation. The timber elements were loaded up to 40% of the estimated failure load in two cycles. For the evaluation, the MOE was determined using a reference system with the same geometry and load application points in a structural analysis software. The deflections due to shear deformations in the timber cross-section were considered in the reference system with the shear modulus assumed as  $G = 650 \text{ N/mm}^2$ . The MOE was then derived from the load increment  $\Delta F$  and the corresponding deflection increment  $\Delta w$ . The mean moisture content at relevant points of time and the mean value of the MOE for all timber elements are given in Table 6.2.

In the second stage, the concrete was concreted on top. First, the reinforcement was placed in the middle of the concrete height. The timber surface was watered one day before and approximately one hour before casting the concrete. The concrete mixture was prepared for a concrete strength class C25/30 with a maximum aggregate size of 16 mm and the shrinkage reducer MasterLife SRA 895. Air void content, flow spread, and density of the fresh concrete

**Tab. 6.2:** Material properties of timber elements for two-span beam test series

element	mean moisture content				MOE $E_2$		
	upon arrival in the lab	before concreting	after stripping of formwork	on the test day	span 1	span 2	average whole beam
	[%]	[%]	[%]	[%]	[N/mm <sup>2</sup> ]	[N/mm <sup>2</sup> ]	[N/mm <sup>2</sup> ]
<b>ZFT1</b>	12.7	11.5	14.1	11.8	10'764	11'937	11'350
<b>ZFT2</b>	12.7	11.2	13.9	11.4	11'350	11'088	11'219

were determined to assess the quality of the concrete before casting. Concrete samples in form of cubes and cylinders were casted from the same batch as the specimens to assess the properties of the hardened concrete. The specimens and concrete samples were casted and stored indoors for 14 d, then stripped from the formwork. The concrete strength determined from the hardened cube and cylinder samples at age 32 d were for the cube compressive strength  $f_{c,cube} = 41 \text{ N/mm}^2$  and for the cylinder compressive strength  $f_{c,cylinder} = 36 \text{ N/mm}^2$ . The concrete corresponds to strength class C30/37 and is therefore one strength class higher than ordered. The measured MOE was  $31\,186 \text{ N/mm}^2$ . The mean value of concrete tension strength was  $f_{ctm} = 3.1 \text{ N/mm}^2$  determined in double-punch tests [23]. The concrete age at the time of testing was 40 d for specimen ZFT1 and 52 d for specimen ZFT2.

The configurations tested in the two-span beam test series are listed in Table 6.1. The main test parameter was the reinforcement of the concrete cross-section subjected to negative bending moments over the middle support:

- Specimen ZFT1 was reinforced over the whole length with a reinforcement mesh K335 ( $\varnothing$  8 mm with distance 150 mm). This reinforcement is constructively used to prevent cracks due to concrete shrinkage.
- Specimen ZFT2 was reinforced with the same shrinkage reinforcement over the whole length except for the length of 3 m over the middle support, where a larger reinforcement of four rebars with  $\varnothing$  12 mm was installed. In this area, the loading situation induces a negative bending moment and the concrete is subjected to tensile stresses.

### Measurement points and testing procedure

The measurement points for the two-span beam test series are listed in Table 6.3. The position of the measurement points are shown in Fig. 6.2. The induced pressure load  $F_{tot}$  is measured by the hydraulic hand pump. Additionally, every hydraulic cylinder was equipped with a load cell to measure the actual load  $F_i$  applied. The reactions in the three supports are measured by three load cells per support. The global deflections  $w_i$  are measured at the locations of the estimated maximum deflection  $w_{max,i}$  at  $0.4215 l$  distance from the support in every span and in the middle of each span  $w_{FM,i}$ . The relative horizontal slip between timber and concrete was measured in the middle of the specimen width. The measurement points were

at both ends of the specimens  $u_{E,i}$ , at the location of zero shear force in both spans  $u_{V0,i}$ , at the location of zero bending moments in both spans  $u_{M0,i}$ , and at the middle support  $u_M$ .

**Tab. 6.3:** Measurement points for two-span beam test series

measurement	position	name	device	capacity	accuracy
hydraulic pressure		$F_{tot}$	hydraulic hand pump		
force on cylinders	span 1	$F_{1-4}$	load cell	$\pm 150$ kN	$\pm 0.2$ %
	span 2	$F_{5-8}$	load cell	$\pm 150$ kN	$\pm 0.2$ %
support reactions	south rolling support	$S_{1,2,3}$	load cell	$\pm 250$ kN	$\pm 0.2$ %
	middle fixed support	$M_{1,2,3}$	load cell	$\pm 250$ kN	$\pm 0.2$ %
	north rolling support	$N_{1,2,3}$	load cell	$\pm 250$ kN	$\pm 0.2$ %
global deflections	span 1: $0.4125 \cdot l$	$w_{max.1}$	LVDT	$\pm 50$ mm	$\pm 0.3$ %
	span 1: $0.5 \cdot l$	$w_{FM.1}$	LVDT	$\pm 50$ mm	$\pm 0.3$ %
	span 2: $0.5 \cdot l$	$w_{FM.2}$	LVDT	$\pm 50$ mm	$\pm 0.3$ %
	span 2: $0.4125 \cdot l$	$w_{max.2}$	LVDT	$\pm 50$ mm	$\pm 0.3$ %
horizontal slip	end span 1	$u_{E.1}$	LVDT	$\pm 5$ mm	$\pm 0.2$ %
	shear force zero point	$u_{V0.1}$	LVDT	$\pm 5$ mm	$\pm 0.2$ %
	moment zero point	$u_{M0.1}$	LVDT	$\pm 5$ mm	$\pm 0.2$ %
	middle support	$u_M$	LVDT	$\pm 5$ mm	$\pm 0.2$ %
	moment zero point	$u_{M0.2}$	LVDT	$\pm 5$ mm	$\pm 0.2$ %
	shear force zero point	$u_{V0.2}$	LVDT	$\pm 5$ mm	$\pm 0.2$ %
	end span 2	$u_{E.2}$	LVDT	$\pm 5$ mm	$\pm 0.2$ %

Additionally, vibration tests were performed on the two specimens in two different support conditions. The specimens were set on the three main supports and two additional temporary supports in the middle of each span. The temporary supports were installed to prevent probable cracking in concrete over the middle main support due to the self-weight. With the temporary supports, no cracking was expected and using the vibration measurements, the stiffness of the beam could be determined. When removing the temporary supports, the system changed from a four-span to a two-span beam and the negative bending moment over the middle main support increased. The vibrations were measured using an impulse hammer and accelerometers placed in the middle of each span. The impulse strikes were executed with an impulse hammer in the middle of the beam width.

The tests with loads on the two-span TCC beam were conducted in different stages. In preliminary tests, the TCC beams were loaded in the elastic range using the steel profiles prepared for the load application. Both spans were loaded separately to investigate the load-bearing behaviour of asymmetric loaded two-span beams. In the main tests, the two-span TCC beams were loaded to failure. The loading procedure was executed in accordance with DIN EN 26891 [20] with a first loading cycle up to 40% of the estimated failure load, unloading, and reloading up to failure. The loading speed was held constant during the whole loading procedure.

## 6.2.2 Results

### Failure modes

Fig. 6.5 shows specimen ZFT2 after the test and removal of the steel profile constructions, load cylinders, and measurements.



**Fig. 6.5:** Specimen ZFT2 after failure

The observed failure propagation was for both specimens ZFT1 and ZFT2 the same and in the same order:

1. cracking of concrete over the middle support (Fig. 6.6a)
2. yielding of the reinforcement
3. bending tension failure in the timber in one of the spans, denoted as 2BT (Fig. 6.6b)

Due to the high slenderness of the beam, the concrete cross-section over the middle-support cracked at an early stage of the loading procedure. The first cracks appeared under self-weight after putting the specimen on the test setup. During application of the load, the crack width increased and new cracks appeared. The yielding of the reinforcement over the middle support occurred at around 50% of the estimated failure load and led to a significant decrease of the beam stiffness. With the stiffness decreased by the reduced active concrete cross-section and the yielded reinforcement, the forces were redistributed into the span. Eventually, the span with weaker material properties failed due to bending tension failure in the timber cross-section. Although the cross-section dimensions and the arrangement of the micro-notch strips were designed to provoke a failure in the micro-notches, no such failure was observed. The micro-notches stayed intact, which could be proven also inside the composite joint after separating the concrete from the timber element.

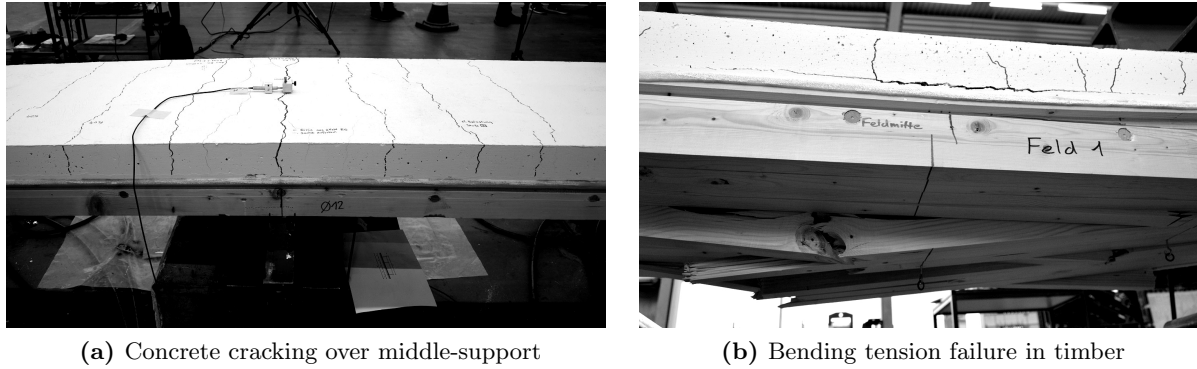


**Fig. 6.6:** Failure modes observed during 4-point bending tests

### Deflections

Fig. 6.7 shows the deflections at the position of the estimated maximum deflections  $w_{max,i}$  and at mid-span  $w_{FM,i}$  for both spans. The y-axis shows the load per cylinder  $F_{cyl}$ . The ultimate failure due to combined bending tension in timber occurred for specimen ZFT1 in span 1 and for specimen ZFT2 in span 2. The sudden apparent increase in force in Fig. 6.7a before failure is due to reaching the limit of the measurement device LVDT. For specimen ZFT2, they were installed with more measurement capacity.

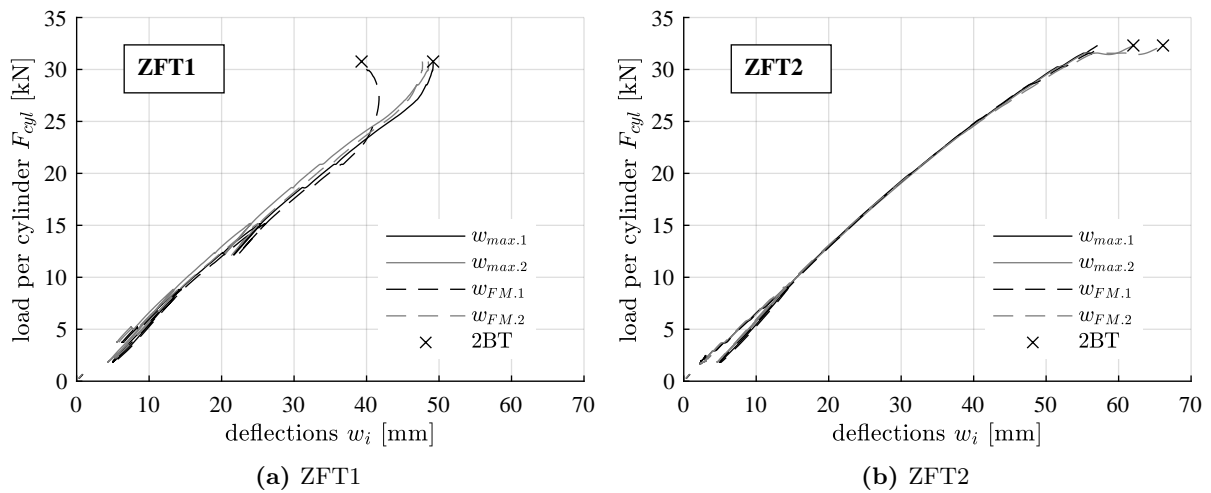


**Fig. 6.7:** Load-deflection curves of two-span beam tests

### Relative slip between timber and concrete

The relative horizontal slip  $u_i$  measured at five decisive points along the beam is shown in Fig. 6.8. The five decisive points were: each end of the beam ( $u_{E,i}$ ), at the position of the shear force zero point ( $u_{V0,i}$ ), at the position of the bending moment zero point ( $u_{M0,i}$ ), and over the middle support ( $u_M$ ) (see also Fig. 6.2). Fig. 6.8 top shows the slip convention.

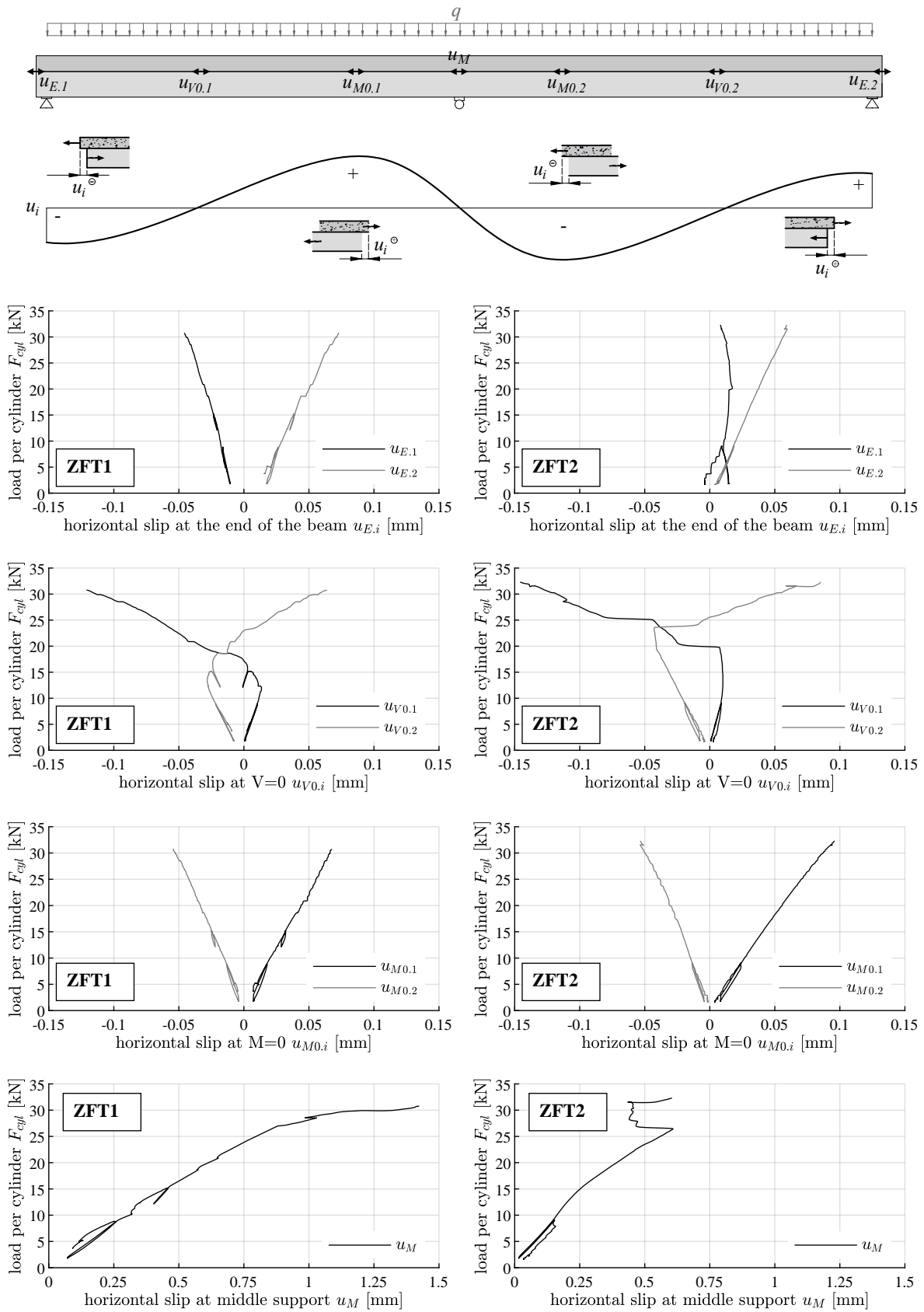


Fig. 6.8: Horizontal slip measurements of two-span beam tests



## Vibrations

The acceleration of the beams were measured for both specimens on a four-span and a two-span system. The excitation was conducted with an impulse hammer. The measured values were adjusted, signal noises cleaned, and the first natural frequency was determined as a mean value from the acceleration data from four impulse strikes.

## Summary of results

Table 6.4 lists the relevant measurement results and the observed failure modes per specimen. The natural frequency  $f_1$ , the failure load given as load per cylinder  $F_{cyl}$ , the corresponding deflections at the expected maximum  $w_{max,i}$  and at mid-span  $w_{FM,i}$ , and the horizontal slip at the beam ends  $u_{E,i}$  are listed.

**Tab. 6.4:** Selected results of two-span beam test series

Measurements in the failed span are highlighted in gray										
	natural frequency	failure load	deflection span 1 at expected maximum	deflection span 2 at expected maximum	deflection span 1 at mid-span	deflection span 2 at mid-span	hor. end slip span 2	hor. end slip span 1	hor. slip middle support	propagation of failure modes <sup>a</sup>
	$f_1$ [Hz]	$F_{cyl}$ [kN]	$w_{max.1}$ [mm]	$w_{max.2}$ [mm]	$w_{FM.1}$ [mm]	$w_{FM.2}$ [mm]	$u_{E.1}$ [mm]	$u_{E.2}$ [mm]	$u_M$ [mm]	
<b>ZFT1</b>	9.18	30.8	(49.2)	(48.6)	(41.7)	(47.7)	0.05	0.07	1.43	1cr, 1y, 2BT
<b>ZFT2</b>	8.58	32.3	57.2	62.2	57.8	66.1	-0.02	0.06	0.61	1cr, 1y, 2BT

<sup>a</sup> 1cr: cracking of concrete, 1y: yielding of reinforcement, 2BT: failure due to bending tension in the timber numbers in brackets have no absolute validity because the LVDT measurement limit was reached

The natural frequency measured for specimen ZFT2 is lower than for specimen ZFT1, even though their material properties (see Table 6.2) are comparable. The failure load of specimen ZFT2 with the larger reinforcement over the middle support is 6 % higher than the failure load of specimen ZFT1. The measured deflections for specimen ZFT1 were compromised due to reaching the limit of the LVDT (Fig. 6.7a). The deflections reached are therefore considerably lower than for specimen ZFT2. The relative slips show a similar progression for both specimens (Fig. 6.8). The slip measured at the shear force zero point  $u_{V0,i}$  indicates the load where the reinforcement yields: After yielding of the reinforcement, the cross-section over the middle supports forms a plastic hinge, and the forces redistribute. The horizontal slip changes the direction due to a transition from a two-span beam system to two single-span beam systems. The horizontal slip over the middle support  $u_M$  should in fact be zero. The measured displacements are due to the concrete cracking and subsequent displacements of the LVDT installed on the concrete top.

## 6.3 Modelling two-span TCC beams with micro-notches

### 6.3.1 General assumptions

The behaviour of TCC slabs with micro-notches in two-span beams was modelled with the  $\gamma$ -method and the strut-and-tie model (described in Chapter 2.2). The modelling of the two-span beams is based on the modelling of a single-span beam as described in Chapter 4.3. The extended models to predict and assess the behaviour of two-span TCC beams were developed in two Master theses [67; 135]. The models are based on the connection properties found in the local shear tests and adapted in the global bending tests. The slip modulus for one micro-notch on the specimen width  $b = 580$  mm used for the following models is:

$$K = 110 \text{ kN/mm/m} \cdot 580 \text{ mm} = 64 \text{ kN/mm} \quad (6.1)$$

The shear strength of the notches is the value resulting from the analysis of the global bending tests:

$$f_{v,MN} = 0.87 \text{ N/mm}^2 \quad (6.2)$$

### 6.3.2 Analytical approach with the $\gamma$ -method

#### Modelling assumptions and inaccuracies for the $\gamma$ -method

The boundary conditions of the two-span beam test series were:

- two-span beam
- constant cross-section dimensions
- assumed constant material properties of the components timber and concrete
- assumed continuous connection along the span: micro-notches are arranged in strips (see Fig. 6.4), but cover the majority of the spans, especially the areas subjected to considerable shear forces
- simulated uniformly distributed line load made of four point loads per span (see Fig. 6.2)

The  $\gamma$ -factor was developed from the solution of the differential beam equation for a single-span beam. The method can be adjusted for continuous beams by reducing the span  $l$  to the length  $l_{eff}$ . Schilliger [142] assumed the reduced span of  $l_{eff} = 0.85 l$  as proposed by SIA 262 [150]. Natterer and Hoefft [120] chose the adapted length  $l_{eff} = 0.8 l$  and conducted parametric studies on the influence of the reduction for the calculation of two-span beams. This length corresponds to the length of a single-span beam with the same deflections as a two-span beam with span  $l$ . They concluded that this assumption is on the unsafe side and that the forces in a two-span beam should be determined using the method of consistent deformations. The Eurocode 5 [21] also proposes  $l_{eff} = 0.8 l$ . Table 6.5 shows the influence of the chosen length  $l_{eff}$  to determine the  $\gamma$ -factor on the  $\gamma$ -factor itself and on the effective bending stiffness  $EI_{eff}$  for the cross-section used in the experiments. The reduction of the bending stiffness  $EI_{eff}$  by 2.4% is negligible. Therefore, in contrast to previous studies, the assumption of  $l_{eff} = 1.0 l$  was chosen for the model presented hereafter.

**Tab. 6.5:** Comparison of connection stiffness for  $l$  and  $l_{eff}$ 

reduction factor	$l$	$l_{eff}$	$\gamma^a$	$EI_{eff}$	
	[m]	[m]	[-]	[kNm <sup>2</sup> ]	[%]
1.0	6	6	0.839	6453	100
0.85	6	5.1	0.791	6344	98.3
0.8	6	4.8	0.770	6295	97.6

<sup>a</sup>  $\gamma$ -factor determined according to Möhler and EC5 [21], therefore no direct indicator of connection efficiency

The material-related variability of the MOE can be neglected, the mean MOE of both spans is assumed to be accurate for the whole beam. The arrangement of the micro-notch strips on the major part of the spans near to the supports represents a good approximation to a continuous connection. The point loads, however, do not comply with the boundary conditions of the  $\gamma$ -method and might lead to inaccurate results.

The cracking of concrete was considered the same way as in the modelling of single-span beams in Chapter 4.3.2. The cracked concrete decreases the effective cross-section and stiffness of the concrete. It is assumed that as soon as the tensile strength of the concrete is exceeded, the complete concrete height subjected to tensile stresses is cracked. Although the concrete does have a tensile strength, the appeared cracks and the shear peaks at the crack ends compromise the concrete subjected to tensile stresses below the tensile strength. The cracked concrete height  $h_{cr}$  and the resulting effective stiffness  $EI_{eff}$  of the composite beam are derived in Appendix C for both areas subjected positive bending moments and negative bending moments. Cracking of concrete in areas with positive bending moments (at mid-span of span 1 and 2) has no significant influence on the effective bending-stiffness and is therefore neglected. Cracking of concrete in the areas with negative bending moments needs to be considered. The cracked concrete cross-section and thus decreased effective bending stiffness  $EI_{eff}$  leads to a redistribution of forces in the beam. This redistribution was not considered for single-span beams, because concrete cracking could be neglected. For two-span beams, this redistribution of forces has to be considered.

### Implementation of the cracking of concrete over the middle support

The input parameter for the model using the  $\gamma$ -method are the geometry, the material and connection properties, the loads, and the reinforcement.

Due to the cracking of concrete in the areas with negative bending moments, the effective bending stiffness  $EI_{eff}$  in these areas is much lower. Because the length of these areas is also depending on the load level, the model calculates the effective bending stiffness  $EI_{eff}$  for individual sections of the beam. This is the biggest difference to the single-span beam, where the effective bending stiffness is constant over the whole span. In a first step, the possible states of the cross-section along the beam are determined. These cross-section states are:

- 1 cross-section with normal reinforcement, uncracked
- 2 cross-section with normal reinforcement, cracked (due to positive bending moments near mid-span)
- 3 cross-section with larger reinforcement over the middle support, uncracked
- 4 cross-section with larger reinforcement over the middle support, cracked (due to negative bending moments)

The four cross-sections have four different effective bending stiffnesses  $EI_{eff}$ . The cracking of concrete due to positive bending moments in the spans can be neglected, as was shown in Chapter 4.3. Therefore, cross-section 2 corresponds to cross-section 1. For the three remaining cross-sections, the  $\gamma$ -method is conducted and the effective moment of inertia  $I_{eff,i}$  and bending stiffness  $EI_{eff,i}$  are calculated. The critical cracking moment in cross-section 4 is determined from the stress at the concrete bottom edge  $\sigma_{1,inf}$  and the tensile strength of the concrete  $f_{1,t}$ :

$$\sigma_{1,inf} = \frac{M}{I_{eff,4}} \cdot \left( \gamma_1 \cdot n_1 a_1 - \frac{h_1}{2} \right) \quad (6.3)$$

$$M_{cr} = \frac{f_{1,t}}{I_{eff,4}} \cdot \left( \gamma_1 \cdot n_1 a_1 - \frac{h_1}{2} \right) \quad (6.4)$$

In the second step, the forces and bending moments are calculated for the individual sections of the beam. The section length in the area of the middle support is chosen smaller to assess the correct cracking length. Each section is then assigned one of the cross-sections described above. The bending moment of the section above the middle support is compared with the critical cracking moment  $M_{cr}$  to evaluate if cross-section 3 or 4 are applied. Fig. 6.4 shows the procedure described above.

The total length of all beam sections assigned to cross-section 4 result as the cracked length of the concrete cross-section over and near to the middle support. The bending stiffness along the cracked length of the concrete is approximately six times lower than the bending stiffness in the other sections of the beam. The loads in this area will redistribute and transfer to the spans. The load redistribution and the cracked length influence depend on each other. The load transfer therefore has to be calculated in an iterative way. To simplify the calculation, load transfer factors for the geometry used in the experiments were determined in structural analysis software for different loads and their corresponding cracked lengths.

In the third step with cross-sections assigned to every section and redistributed shear forces and bending moments determined, the stresses and deflections can be calculated.

### Limits of the model using the $\gamma$ -method

The model described above is based on the model of single-span beams in the linear elastic states with uncracked and cracked concrete (state I + II). At a certain load level, the reinforcement starts to yield and leads to a plastic behaviour in the beam. This decrease of the stiffness

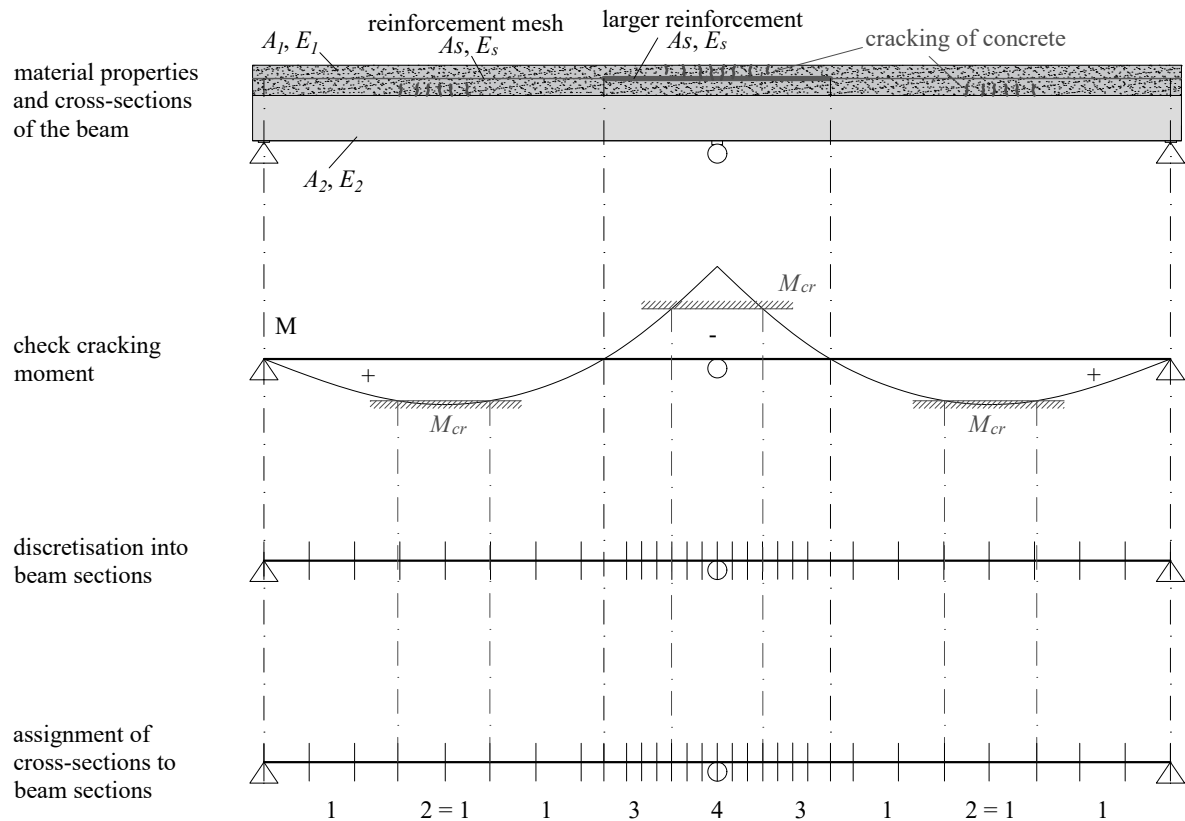


**Fig. 6.9:** Procedure to determine effective cross-sections in the two-span beam

was not considered in the model. After the reinforcement yielding load, the model overestimates the stiffness of the beam. The failure load predicted by the model will therefore be on the unsafe side. However, the model is accurate for the assessment of deflections at service load level.

The model is only applicable on one particular system because the load transfer factors have to be determined separately. The complexity of the model and the inflexible application make the calculation effort considerable.

The influence of creep can be considered by means of creep factors in the material properties. The correct separation of creep-effective loads and instantaneous loads as well as their assignment to the corresponding cross-sections is, however, not possible.

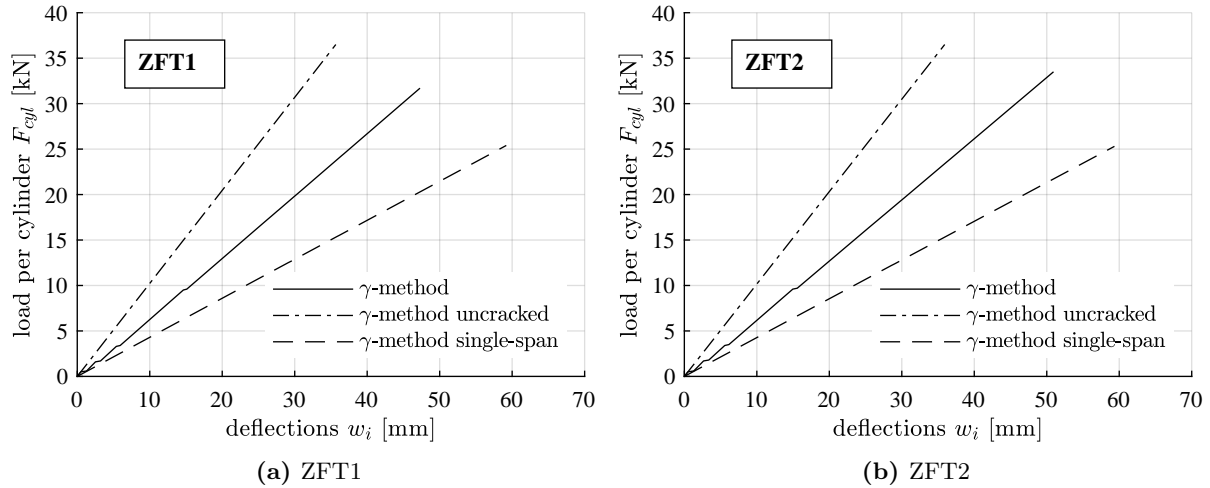
### Findings of the assessment with the $\gamma$ -method

The consideration of individual cracked concrete sections in a two-span beam is possible with the model based on the  $\gamma$ -method described above. Table 6.6 lists the predicted yielding load of the reinforcement, the ultimate failure load, and the corresponding deflection. The ultimate failure is predicted as combined bending tension failure (2BT) in one of the spans. However, the load-deflection behaviour after the reinforcement yielding determined with the model is expected to overestimate the actual stiffness.

**Tab. 6.6:** Prognosis of failure loads and deflections with the  $\gamma$ -method

specimen	reinforcement over middle support	reinforcement yielding [kN]	ultimate failure [kN]	deflection at ultimate failure [mm]
ZFT1	4 $\times$ $\varnothing$ 8 mm	14.0	31.7	47.3
ZFT2	4 $\times$ $\varnothing$ 12 mm	20.8	33.5	50.9

Fig. 6.10 shows the load-deflection curves predicted with the model using the  $\gamma$ -method for three scenarios: the model for two-span beams considering concrete cracking and redistribution of forces as described above, the model for two-span beams without considering the concrete cracking and the model for a single-span beam with the same span. The cracking of concrete and reduction in stiffness is visible as small steps in the curve of the  $\gamma$ -method. The scenario without this consideration is much steeper and overestimates the stiffness of the beam. The model for a single-span beam with the same span shows a much lower stiffness.

**Fig. 6.10:** Different scenarios predicted with the  $\gamma$ -method

### 6.3.3 Numerical approach with the strut-and-tie model

#### Modelling assumptions and inaccuracies for the strut-and-tie model

The strut-and-tie model of the two-span beam was implemented in RSTAB in the same way as the model for the single-span beam described in Chapter 4.3.3. The model has therefore already been validated using the single-span 4-point bending tests. The model consists of the lower beam with the timber dimensions and properties, the upper beam with the concrete dimensions and properties, and the vertical connection elements. The concrete beam in the software is automatically split into individual beam sections between the vertical connection beams. The micro-notches are modelled as connection element beams with the effective bend-

ing stiffness  $EI^*$  calculated with equation 2.37 and the slip modulus  $K = 110 \text{ kN/mm/m}$  (see Chapter 6.3.1). The position of connection beams was according to the arrangement in strips of eight micro-notches each (Fig. 6.4). The loads were implemented as point loads at the location of the cylinders.

### Implementation of the cracking of concrete over the middle support

The software RSTAB from Dlubal allows a direct dimensioning of the reinforcement in a separate concrete module. In this module, the cracking of concrete can be considered, but the cracked bending stiffness cannot be transferred to the main model. For a two-span beam, the bending stiffness over the middle support is crucial as it significantly affects the deflections. The implementation of the cracking of concrete must therefore be executed manually and in an iterative way. One iteration step includes:

1. Derive the effective concrete thickness  $x = h_{1,II}$  with a cross-sectional analysis in the concrete. The cross-sectional analysis is conducted on the reinforced concrete cross-section, including the internal normal force  $N_1$ , the internal bending moment  $M_1$ , and the reinforcement. From this effective concrete thickness  $x$ , the cross-section properties of the cracked concrete section are determined:  $A_{1,II}$  and  $I_{1,II}$ .
2. Check the individual concrete beam sections on concrete cracking:

$$\sigma_1 = \frac{N_1}{A_1} - \frac{M_1}{I_1} \cdot \frac{h_{1,II}}{2} \leq f_{1,t} \quad (6.5)$$

If the stress  $\sigma_1$  in this concrete beam section exceeds the tensile strength  $f_{1,t}$ , the beam section is considered as cracked.

3. Assign the cracked cross-section properties to all cracked concrete beam sections in the strut-and-tie model: the cracked bending stiffness  $EI_{1,II}$ , cracked axial stiffness  $EA_{1,II}$ , and cracked shear stiffness  $GA_{1,II}$ .
4. The model with adjusted stiffness outputs new internal forces  $N_1$  and bending moments  $M_1$ . The next iteration step begins.

The iteration was performed until the values obtained for the uncracked concrete height  $x$  reached an accordance of  $\pm 5\%$ . The cracked concrete length results as the total length of all concrete beam sections not fulfilling equation 6.5.

The cross-sectional analysis of the concrete is different for the location in the span and over the middle support. In the span, the reduction of the stiffness due to cracking of concrete can be neglected. Over the middle support, the cross-sectional analysis depends on the load level. Beyond a certain load, the whole concrete cross-section is cracked and only the reinforcement is effective. Below that load, a certain part of the concrete cross-section is still subjected to compressive stresses. The concrete height subjected to compressive stresses is the uncracked concrete height  $x$  and depends on the internal normal force  $N_1$ , the reinforcement, and the

concrete section subjected to compressive stresses:

$$x = \frac{A_s f_{s,k} - N_1}{0.85 \cdot b \cdot f_{1,c,k}} \quad (6.6)$$

where  $A_s$  cross-section of the reinforcement  
 $f_{s,k}$  characteristic strength of the reinforcement  
 $N_1$  internal normal force in concrete  
0.85 factor to account for compressive stress distribution  
 $b$  width of specimen  
 $f_{1,c,k}$  characteristic compressive strength of concrete

If the whole concrete cross-section is subjected to tensile stresses, only the reinforcement is effective. The cross-section properties of the beam are then defined:

$$A_{1,II} = A_s = n \cdot \left(\frac{\emptyset}{2}\right)^2 \cdot \pi \quad (6.7)$$

$$I_{1,II} = n \cdot \left(\frac{\emptyset}{2}\right)^2 \cdot \frac{\pi}{4} + A_s \cdot z_s^2 \quad (6.8)$$

where  $A_s$  cross-section of the reinforcement  
 $n$  number of reinforcement rebars  
 $\emptyset$  diameter of reinforcement rebars  
 $z_s$  distance of reinforcement centroid to concrete centroid

In this case, the stiffness of this beam section is clear and no iteration is needed.

### Implementation of the reinforcement yielding over the middle support

In case of a completely cracked concrete cross-section in the area of the middle support, only the reinforcement is effective. A further increase of the load leads at a certain point to the yielding of the reinforcement steel. From this point on, the reinforcement cannot take any additional normal forces. This limit of normal forces is:

$$N_{1,lim} = A_s \cdot f_{s,k} \quad (6.9)$$

In RSTAB, this limit normal force can be inserted directly as a limit to the concrete beam. Further normal forces are then transferred automatically to the spans.



### Limits of the strut-and-tie model

The concrete module in RSTAB is designed for four layers of reinforcement. Modelling only one longitudinal layer is possible, but the rebars cannot be positioned exactly in the middle of the concrete height. The error is small for the system investigated here.

The concrete module is also not linked to the main model in RSTAB. It is therefore not possible to transfer the calculations of cracked concrete to the main model. In the main model, cracking of concrete cannot be modelled directly since the software uses beam analysis and only considers the stresses in the centroid of the beams. The cracked length has to be determined manually as described above.

The model represents only one particular geometry with specific cross-section dimensions, materials, and arrangement of the connectors. The model is not suitable for parameter studies and the calculation of many different systems.

### Findings of the assessment with the strut-and-tie model

The strut-and-tie model can be used to predict the load-bearing behaviour of two-span beams. However, the implementation is time-consuming and complex due to the iterative process of finding the cracked concrete length and manual setting of the stiffness for each section of the concrete beam. For the prognosis of the load-deflection curve, the adjustment of the model was conducted for certain load levels. The output of the reinforcement yielding load, the ultimate failure load, and the deflection at failure load are listed in Table 6.7. The utilisation of the micro-notches in the composite joint near the beam ends, combined bending and tension stresses and combined bending and compression stresses in timber were all in the same range for the predicted ultimate failure load.

**Tab. 6.7:** Prognosis of failure loads and deflections with the strut-and-tie model

specimen	reinforcement over middle support	reinforcement yielding [kN]	ultimate failure [kN]	deflection at ultimate failure [mm]
<b>ZFT1</b>	4 × Ø 8 mm	13	30	53.5
<b>ZFT2</b>	4 × Ø 12 mm	19.5	33	47.3

Fig. 6.11 shows the load-deflection curves predicted with the strut-and-tie model in comparison with the model using the  $\gamma$ -method. Both models consider cracking of the concrete over the middle support and subsequent redistribution of forces. The strut-and-tie models additionally considers yielding of the concrete. This additional reduction in stiffness is visible as the offset between the two models.

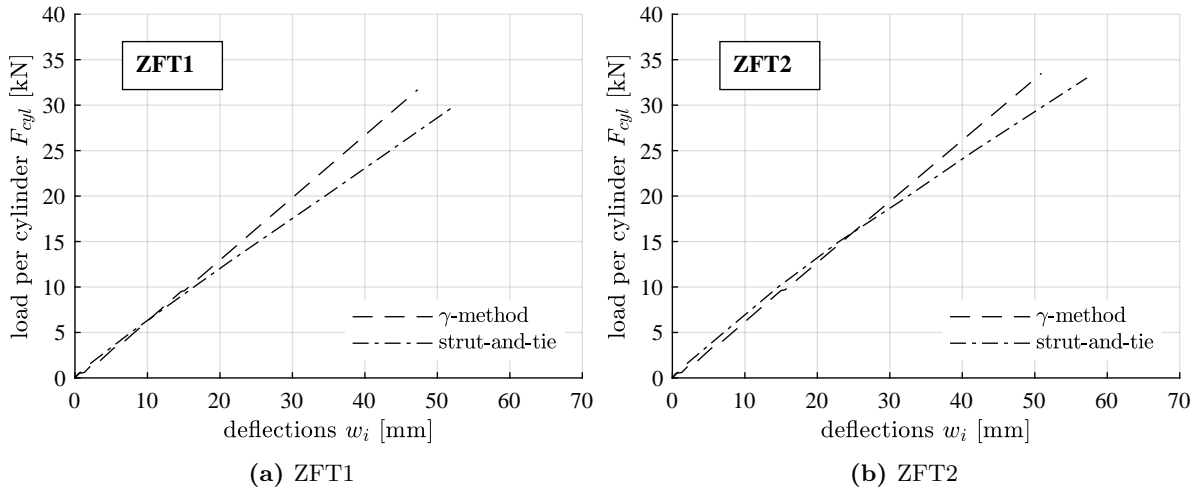


Fig. 6.11: Comparison of strut-and-tie model with  $\gamma$ -model

### 6.3.4 Comparison of the models and the experimental data

Fig. 6.12 and 6.13 show the load-deflection curves measured in both spans of the conducted two-span beam tests and obtained with the two models considering cracking of concrete, redistribution of forces, and, in the case of the strut-and-tie model, also the yielding of the reinforcement.

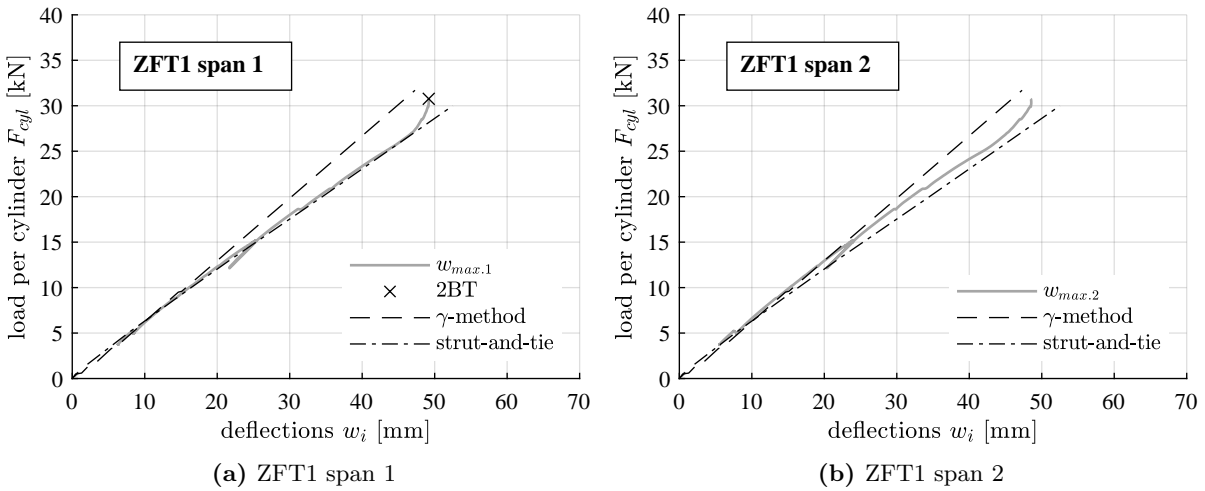
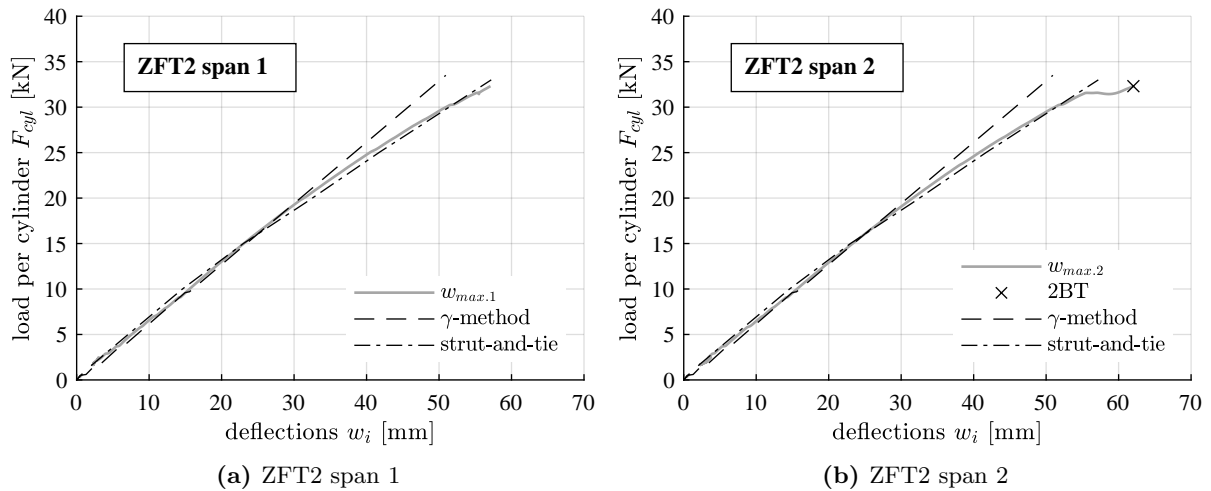


Fig. 6.12: Specimen ZFT1: comparison of experimental data with models

Both models show a good agreement with the experimental data in the lower range of the applied load. After reaching the reinforcement yielding (around 13 kN for ZFT1 and 20 kN for ZFT2), the stiffness of the beam decreases. Beyond this point, the  $\gamma$ -method overestimates the stiffness because it does not consider reinforcement yielding. The strut-and-tie model shows a better agreement after reinforcement yielding. The ultimate failure load was predicted accurately in both models. However, in the strut-and-tie model, the failure mode was not clear: the utilisation factor of bending tension failure in timber (2BT) was similar to failure due to



**Fig. 6.13:** Specimen ZFT2: comparison of experimental data with models

combined bending and compression in timber and failure in the micro-notches. Failure of the micro-notches did not occur and the failure due to combined bending and compression in the timber cross-section over the middle support was not visible.

## 6.4 Influence of different parameters

### 6.4.1 Comparison of configurations

Fig. 6.14 shows the measured load-deflection curves in the failed span for both specimens ZFT1 and ZFT2. In Fig. 6.14a, the load per cylinder  $F_{cyl}$  as installed in the experiments is plotted. In Fig. 6.14b, the total load of the eight cylinders is converted to a uniformly distributed load  $q$  over the total area of the beam ( $0.58 \text{ m} \cdot 12 \text{ m}$ ). As a reference, the service load levels for the SLS and the ULS with a heavy floor structure (superimposed load  $g_{A,k} = 1.8 \text{ kN/m}^2$ ) in an office building (live load  $q_{N,k} = 3.0 \text{ kN/m}^2$ ) are also plotted.

### 6.4.2 Reinforcement over the middle support

Both specimens ZFT1 and ZFT2 show a similar load-deflection behaviour for low load levels. In this load range up to the yielding of the reinforcement, the reinforcement installed in the concrete cross-section over the middle supports does not have a significant influence on the stiffness of the two-span beam. The use of larger reinforcement is therefore no measure to increase the stiffness and better fulfil the SLS requirements. However, the reinforcement yields earlier for specimen ZFT1 (around 13 kN) than for specimen ZFT2 (around 20 kN). After the reinforcement yielded, the beam stiffness decreased. The difference between the two curves after this point is caused by this. Larger reinforcement leads to a higher yielding load of the reinforcement. The reduction of the stiffness occurs at a higher load than with smaller reinforcement. Also, the specimen with larger reinforcement reaches a slightly higher ultimate failure load.

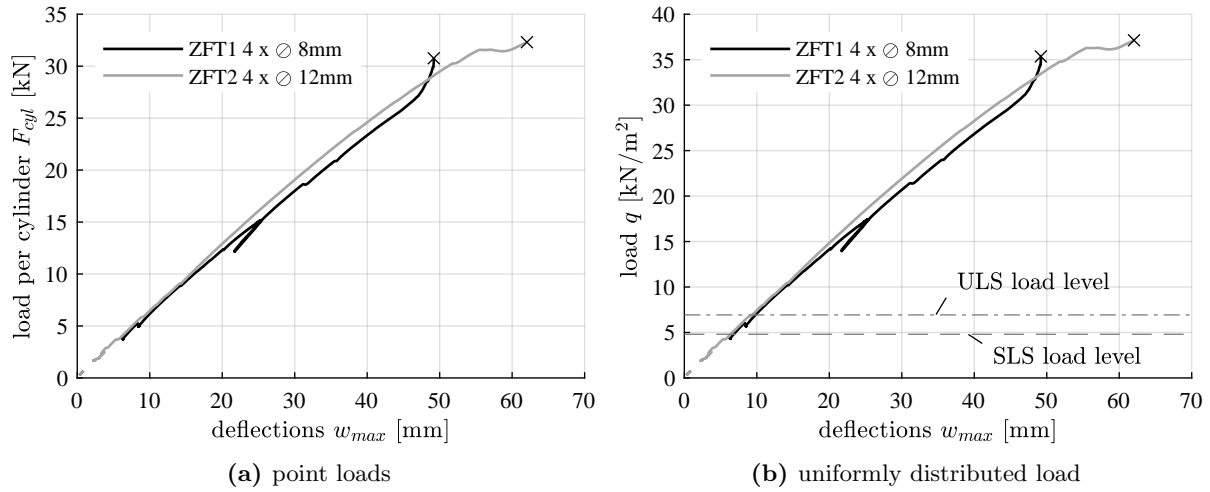


Fig. 6.14: Comparison of load-deflection curves of both specimens

### 6.4.3 MOE of the timber

Fig. 6.15 shows the measured load-deflection data in the load range up to  $q = 10 \text{ kN/m}^2$ . The data below  $1 \text{ kN/m}^2$  represents the placing of the steel profile construction. The data measurement of the load induced by the cylinders started at  $4 \text{ kN/m}^2$  for specimen ZFT1 and at  $2 \text{ kN/m}^2$  for specimen ZFT2. The missing range in between is due to the installation of the cylinders and errors in the data acquisition for specimen ZFT1. The offset for specimen ZFT1 at around  $6 \text{ kN/m}^2$  is due to the formation of a new crack above the middle-support.

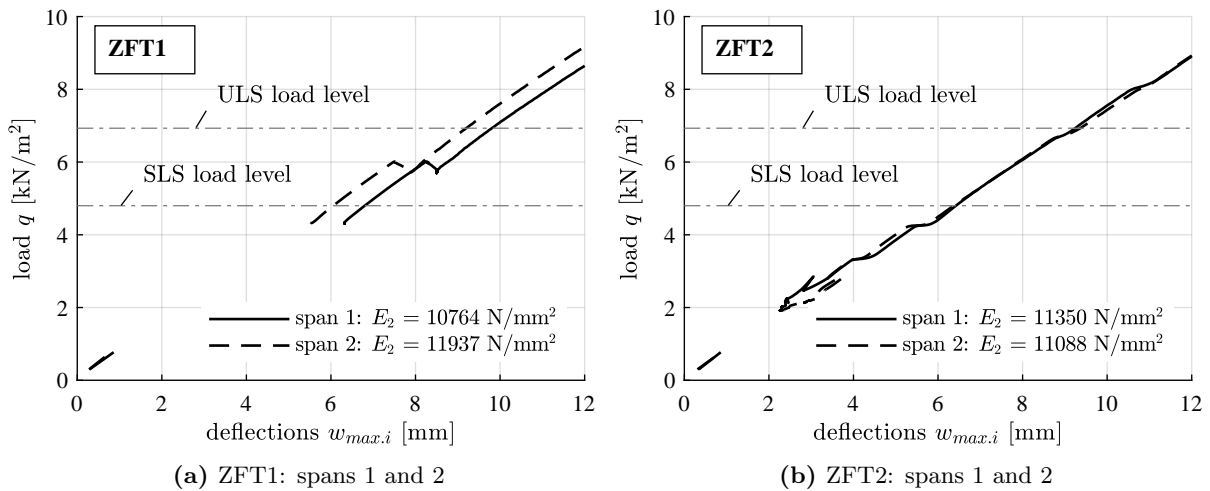


Fig. 6.15: Comparison of load-deflection curves in the service load range

Fig. 6.15 shows that in the range of the service loads for SLS and ULS, both specimens have a similar stiffness. For the SLS load level, the deflections are for ZFT1  $6.06 \text{ mm}$  in span 1 and  $6.84 \text{ mm}$  in span 2. For specimen ZFT2 the deflections at SLS load level are  $6.35 \text{ mm}$  and  $6.40 \text{ mm}$  respectively. The discrepancy of deflection in ZFT1 corresponds well with the

discrepancy of MOE of the timber element measured per span (see also Table 6.2 and legends in Fig. 6.15). The considerably smaller deflection in span 2 of ZFT1 is due to a higher MOE of the timber. For specimen ZFT2, the difference of timber MOEs in the two spans is smaller and the load-deflection curves are almost congruent.

In conclusion, the MOE of the timber per span has a significant influence on the stiffness of the beam. This can be found with the assumption that the MOE of concrete is approximately constant over the whole length of the beam. Apparently, the influence of the timber MOE is even greater than the amount of reinforcement installed over the middle support: the deflections of ZFT1 and ZFT2 at SLS level are comparable and thus not dependent on the reinforcement.

## 6.5 Conclusions

Fig. 6.16 summarises the load-deflection behaviour of TCC two-span beam with micro-notches as found in experimental tests and model analysis. Since only two test specimens were tested and analytically modelled, only statements about this particular system can be made.

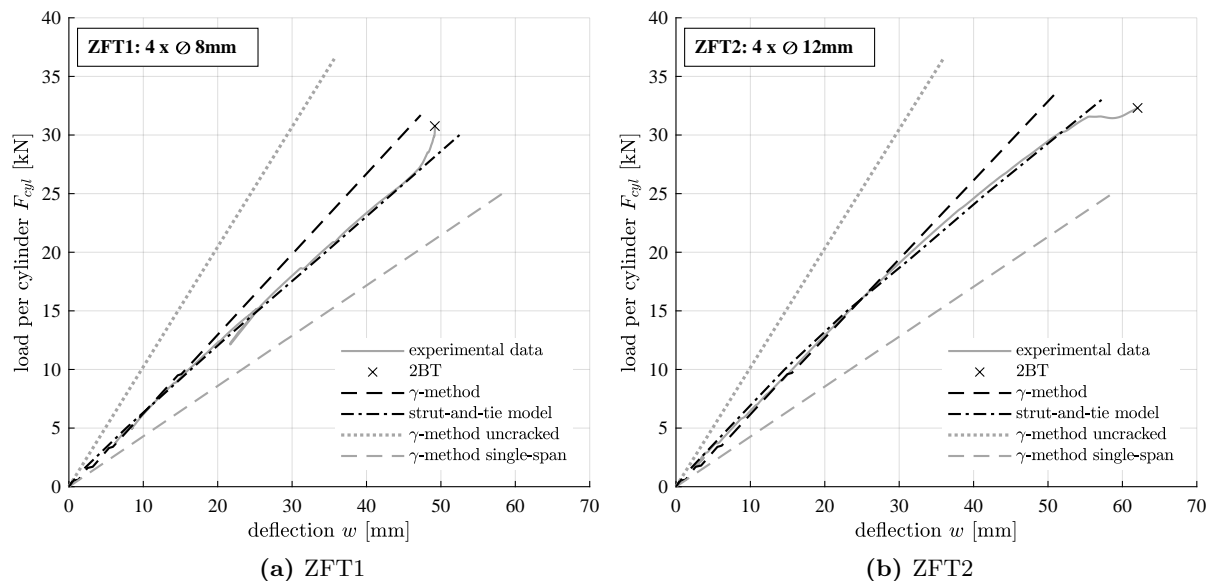


**Fig. 6.16:** Measured data and model scenarios of load-deflection curves

The investigations allow the following statements for the particular system of a TCC beam with micro-notches and two spans of 6 m each:

- The overall stiffness of a two-span beam is around 60% to 70% (depending on the load level) higher than the stiffness of a single-span beam. Therefore, the deflections can be reduced by using a two-span beam instead of two single-span beams. The cracking of concrete over the middle support was considered.
- The cracking of the concrete over the middle support and the yielding of the reinforcement lead to a significant decrease of the initial beam stiffness.

- At service load levels, the amount of reinforcement installed in the concrete over the middle support does not have an influence on the beam stiffness. At higher load levels, the larger reinforcement increases the yielding load of the concrete and thus delays the stiffness reduction. The ultimate failure load can also be increased slightly with larger reinforcement.
- More important for the beam stiffness at service load levels are the material properties, namely the MOE of the timber.
- The load-bearing behaviour of beams with negative bending moments can be modelled by an extended and adapted model using the  $\gamma$ -method or the strut-and-tie model. In both models, the determination of the cracked concrete length is complex and time-consuming. The  $\gamma$ -method needs an elaborate extension, section-wise calculation of the effective bending stiffness and forces, as well as additional support from structural analysis software to consider the redistribution of forces. The yielding of the reinforcement could not yet be taken into account. The strut-and-tie model is less time-consuming and more straightforward, because the cross-sections can be adapted directly in the model. However, the cracking of concrete needs to be checked manually and the cracked length can only be determined in an iterative way in the used software RSTAB. In contrast to the extended  $\gamma$ -model, the yielding of reinforcement can be accurately considered. Both models are designed for one particular system only, adjustments require a large investment of time.

## Chapter 7

# Design recommendations for TCC slabs with micro-notches

### 7.1 General information

In this chapter, the findings from the experimental tests as well as the analytical and numerical models are transferred to the application level. The characteristic values of the connection properties of micro-notches as a novel connection system for TCC slabs are converted for the use in design according to standards (SIA 265 [149], Eurocode 5 [21]). The findings on the structural behaviour are implemented in the necessary verifications for the ultimate limit state (ULS), the serviceability limit state (SLS), sound insulation, and fire safety.

The following recommendations for the design are based on a planar TCC system with a timber cross-section being larger than the concrete cross-section. It is generally recommended to choose the bending stiffness  $EI_1$  of the concrete slab to be lower than the bending stiffness  $EI_2$  of the timber slab to prevent uplift [100]. However, uplift of the concrete layer was never observed in the experiments before reaching ultimate failure, even in specimens with ratios near to 1:1 of concrete to timber.

### 7.2 Properties of the materials

#### 7.2.1 Timber

The following design recommendations are based on a system with spruce or fir BST or CLT elements. The local shear tests showed that the spruce or fir surface features a pronounced adhesion to the concrete cast on top. Hardwood such as beech and ash resulted in an initial slip and thus less stiff connection. The Technical Specification [30] explicitly recommends to not use e.g. larch in direct contact with concrete. The direct contact between timber and fresh concrete can lead to mutual damage: water-soluble extracts in highly resinous wood species compromise the hydration of the concrete and the alkaline substances in the concrete mixture lead to discoloration of the timber [120]. The discoloration of the spruce and fir timber surface

was observed in the experiments, but had no evident influence on the quality of the notches nor the composite action. No separating foil is recommended for the application of micro-notches, as the shear strength was determined including the adhesion in the joint. The treatment of the timber surface with water before concreting to saturate the timber could neither be proven to have a beneficial effect in the local shear tests, nor in the global bending tests, nor in the first six months of the long-term tests. The timber surface with micro-notches does not have to be treated in any special way before concreting to achieve the full composite action.

### 7.2.2 Concrete

The following design recommendations are based on findings made with normal-strength concrete of strength class C25/30 to C40/50. To achieve a good formation and full strength development of the concrete notches, careful vibration of the concrete is of great importance. Further, it is recommended to use a maximum aggregate size of  $D_{max} = 16$  mm.

Only in situ casting was investigated in the experimental tests conducted to develop the connection system. The prefabrication of the concrete slabs is also possible and even recommended, since it significantly decreases the deflections during construction state and due to shrinkage. However, the influence of the vibrations during transport of TCC slabs only connected with micro-notches is not investigated yet. During all the experimental work conducted, the relocating, and moving of specimens after one week of concrete hardening did not lead to uplift of the concrete layer or inferior composite action.

A constructive reinforcement against shrinkage is recommended. Additional reinforcement is recommended in systems with negative bending moments. In single-span beams, the influence of the cracked concrete is negligible. For systems with negative bending moments such as two-span or other continuous beams, cracking of concrete is of great importance.

## 7.3 Properties of micro-notches as a TCC connection system

According to the experimental, analytical, and numerical analysis of the local and global load-bearing behaviour of micro-notches as a connection system for uniaxial and planar TCC slabs, the following connection properties are proposed:

- **Slip modulus for serviceability limit state  $K_{ser}$  and for ultimate limit state  $K_u$**

The slip modulus of micro-notches is for both serviceability limit state and the ultimate limit state:

$$K = K_{ser} = K_u = 110 \text{ kN/mm/m} \quad (7.1)$$

This value is back-calculated from the connection stiffness measured in the global 4-point bending tests. The value denotes the slip modulus per micro-notch with a length of  $l_{MN} = 30$  mm and per 1 m slab width. Because of the high connection stiffness and linear load-deflection curves until brittle failure, the slip modulus  $K$  does not need to be reduced for the ULS. Both SLS and ULS are in the linear elastic, very stiff phase.



- **Distance between connectors**

In the discussed models using the  $\gamma$ -method and the strut-and-tie model, the distance between the individual connectors is an important input parameter. If micro-notches are used as continuous shear connection system, the distance between the connectors  $s$  equals the length of the micro-notches:

$$s = s_{eff} = l_{MN} = 30 \text{ mm} \quad (7.2)$$

- **Design value for shear strength**

The empirical value for the shear strength of micro-notches is back-calculated from the failure loads of the connection observed in the experimental 4-point bending tests described in Chapter 4.2. From these values, a design value was calculated using the direct conversion method described in EN 1990:2010 [35] Annex D7.3. The shear strength values are assumed to follow a log-normal distribution. The design value  $\chi_d$  is found directly as:

$$\chi_d = \eta_d \cdot \exp(m_y - k_{d,n}s_y) \quad (7.3)$$

where  $\eta_d$  factor to cover all uncertainties not covered by the tests  
 $m_y$  ln of mean value  
 $k_{d,n}$  determined according to EN 1990:2010 [35] Table D.2  
 $s_y$  standard deviation

The values back-calculated from the 4-point bending tests are listed in Chapter 4.5 in Table 4.11. The factor  $\eta_d$  to cover uncertainties was assumed as 0.7. The value  $m_y$  and the standard deviation  $s_y$  are:

$$m_y = \frac{1}{n} \cdot \sum \ln(x_i) \quad (7.4)$$

$$s_y = \sqrt{\frac{1}{n-1} \cdot \sum (\ln(x_i) - m_y)^2} \quad (7.5)$$

The proposed design value for the shear strength of micro-notches is then:

$$f_{v,MN,d} = 0.5 \text{ N/mm}^2 \quad (7.6)$$

This value is based on the results of six bending tests and does not necessarily satisfy statistical relevance.

## 7.4 Structural behaviour of TCC slabs with micro-notches

The analysis of the global load-bearing behaviour described in Chapter 4 showed that the structural behaviour of TCC slabs with micro-notches is characterised by a linear load-deflection behaviour followed by brittle failure. Accordingly, TCC slabs with micro-notches are to be verified in the same way as TCC slabs with other very stiff connection systems such as conventional notches.

Fig. 7.1 shows two different arrangement of micro-notches: as continuous area or in strips of several notches. If the micro-notches are arranged as continuous connection system on a wide area, e.g. over one third of the span on each side, the connection efficiency according to equation 2.23 is approximately  $\eta_{C^*} = 1$  and the connection stiffness can be assumed as rigid. If the micro-notches are arranged in strips, the strips are assumed to act as local connectors. The slip modulus of one strip depends on the number of micro-notches  $n$  in the strip:

$$K_{strip} = n \cdot K \quad (7.7)$$

The distance  $s$  between the connectors then equals the distance between the micro-notch strips as shown in Fig. 7.1 right. In this case, the connection stiffness is given by the number of micro-notches in the strip and the distance  $s$  between the strips. The connection stiffness and thus the connection efficiency decreases with fewer micro-notches per strip and increasing distance between the strips.

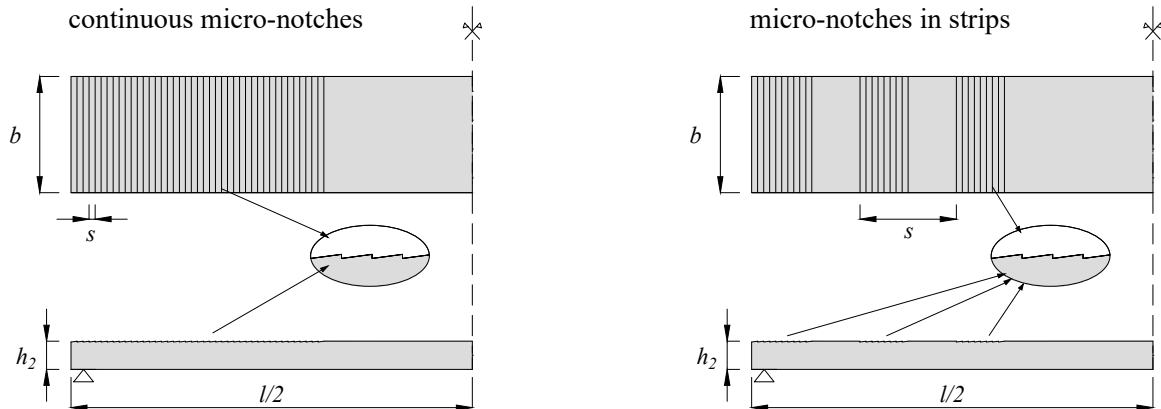


**Fig. 7.1:** Arrangement of micro-notches continuously or in strips

Suitable calculation models are both the analytical approach with the  $\gamma$ -method and the numerical approach with a strut-and-tie model for both continuous and strip arrangement of micro-notches. For systems with two spans, both modelling approaches lead to accurate results at service load level (see Chapter 6.3.4). The cracking of concrete needs to be taken into account for the areas subjected to negative bending moments. The reinforcement yielding can be neglected at service load levels.

The rheological phenomena due to temperature or moisture changes, shrinkage, and creep of the materials as well as the connection system have a considerable influence on TCC slabs (see Chapter 5.1.2). The stress and deflection analysis should be carried out at three decisive points in time: at the beginning of the service life of the component ( $t = 0$ ), at the time of maximum creep differences between the two materials ( $t = 3 \dots 7$  years), and at the end of the service life of the component ( $t \approx 50$  years).

## 7.5 ULS verifications

The stresses in the timber and concrete cross-section are to be determined as described in Chapter 2.2.2 for the  $\gamma$ -method and Chapter 2.2.3 for the strut-and-tie model. The verification of the stresses at the concrete bottom edge can be neglected in beams subjected to positive bending moments because the cracking of concrete only marginally influences the effective bending stiffness  $EI_{eff}$  of the composite cross-section. In beams subjected to negative bending moments, the cracking of concrete needs to be considered. The decisive verification in the ULS for planar TCC slabs with micro-notches subjected to a uniformly distributed load  $q$  is the combination of bending and tensile stresses at the timber bottom edge.

The verification of the combination of bending stresses  $\sigma_2(M)$  and tensile stresses  $\sigma_2(N)$  at the timber bottom edge reads:

$$\frac{\sigma_2(M)}{f_{2,m,d}} + \frac{\sigma_2(N)}{f_{2,t,d}} \leq 1 \quad (7.8)$$

The shear resistance of the connection system is not a decisive failure in practice-relevant cross-sections and loading situations. The verification of the shear stress  $\tau_v$  onto the micro-notches in the composite joint should nevertheless be conducted. It reads:

$$\tau_v \leq f_{v,MN,d} \quad (7.9)$$

## 7.6 SLS verifications

The SLS verifications include the compliance with deflection guidelines and the vibration behaviour. The structural behaviour of TCC slabs with micro-notches at service load level can be assumed to have a rigid connection.

### 7.6.1 Deflections

The deflections  $w$  of TCC slabs with micro-notches are to be determined according to SIA 265 [149] or Eurocode 5 [21]. The procedure is the same as for conventional TCC systems. The micro-notches have a positive effect on the effective bending stiffness  $EI_{eff}$  (in comparison with connection system such as notches, screws, dowels, metal plates). The approximately rigid composite action leads to smaller deflections.

### 7.6.2 Vibrations

The vibration verifications for TCC slabs with micro-notches are the same as for timber [63] or timber-concrete composite slabs with other connection systems [166]. The micro-notches do not affect the vibration behaviour.

## 7.7 Sound insulation

The vibration verifications for TCC slabs with micro-notches are the same as for TCC slabs with other connection systems [151; 143; 105]. The micro-notches do not affect the sound insulation behaviour.

## 7.8 Fire Safety

The behaviour of planar TCC slabs with micro-notches exposed to fire is comparable to the behavior of planar TCC slabs with other connection systems [73]. This system has been investigated in detail in [47; 45]. In planar TCC systems, the fire exposure is one-sided and the connection is protected [48]. It can be assumed that the temperatures in the composite joint remain low [84] and that the full composite action is active. TCC slabs with micro-notches have two advantages over comparable systems with other connection systems e.g. notches with additional screws or dowels:

- Nearly the complete timber thickness is available over the entire span because of the small notch depth of 4 mm.
- The connection is achieved with micro-notches without additional dowels, nails or screws. Metal parts in the composite beam facilitate heat introduction. The materials in the cross-section are only timber and concrete.

The design in case of fire can therefore be conducted according to SIA 265 [149] or EC5 [20] with the effective cross-section method. The fire safety is thereby verified by reducing the original cross-section to account for the charred and heated timber. The slip modulus  $K$  needs not to be reduced as long as 25 mm of timber thickness is remaining [48]. Furthermore, concrete spalling is mainly a problem for high-strength concretes [122; 107] and is prevented by the timber in planar TCC systems.

## 7.9 Conclusions

The design of planar TCC slabs with micro-notches is so far proposed for TCC with planar softwood BST or CLT elements and normal-strength concrete. The vibration of the concrete is of great importance. No special treatment of the timber surface before concreting is needed to ensure a good formation of the notches and full composite action.

The connection properties of the micro-notches were determined in local shear tests and adjusted using the findings of global bending tests. The connection with micro-notches arranged continuously in a wide area can be assumed rigid. For individual strips of several micro-notches, the slip modulus  $K$ , and the distance between the strips define the connection stiffness. The proposed design value for the shear strength was determined from the results of the bending tests and adapted to the design level.

The design verifications of planar TCC slabs with micro-notches are based on the design of planar TCC slabs with other connection systems such as notches with additional screws. For the ULS, the stress due to combined bending and tension in the timber bottom edge as well as the shear stress in the composite joint have to be verified. For the SLS, the deflection and vibration guidelines have to be verified. The long-term effects have to be taken into account. The decisive points in time are  $t = 0$ ,  $t = 3..7$  years, and  $t = \approx$  years (or end of the service life). The behaviour regarding the vibrations, sound insulation, and fire exposure are the same as for TCC slabs with other connection systems.



# Chapter 8

## Summary and conclusions

### 8.1 Overview

The objective of this research study was to develop a novel connection system for timber-concrete composite (TCC) slabs for residential and office buildings. In particular, the novel connection system should achieve a strong composite action based on the materials already available - timber and concrete - without additional metal connectors, such as screws or dowels. The relevant connection properties and production parameters should be elaborated and assembled in design and calculation guidelines.

Micro-notches are a rediscovery of the historical interlocking connection in timber: indentations with notch depths significantly smaller than the depth of conventional notches. In this research study, the concept of micro-notches was developed in an extensive experimental program accompanied by analytical and numerical investigations. The optimum production and design parameters were determined, and their influence on the connection behaviour was evaluated. The connection properties were determined by the slip modulus  $K$  and the shear resistance in form of a shear strength  $f_{v,MN}$ . The design with the most suitable properties for the application in slabs was selected for further investigations.

The micro-notch connection system was tested considering different features from practical applications. For example, the structural load-bearing behaviour of TCC slabs with micro-notches was investigated on single-span and two-span beams subjected to points loads. The experimental data obtained was used to validate and adapt calculation models based on the  $\gamma$ -method and the strut-and-tie model. Further, an extensive long-term test series was installed. The considerations regarding test setup, test parameters, and measurements, and results of the deflections for the first half year of testing were presented. The connection property values found in the short-term investigations were adapted to the design scale. Recommendations regarding the production of micro-notches as TCC connection system were made. The relevant design guidelines for the application as slabs were elaborated.

The most relevant conclusions drawn from the investigations of the four aspects are summarised and compared in the following chapters: local load-bearing behaviour, global load-bearing behaviour, long-term load-bearing behaviour, and behaviour in two-span beams.

## 8.2 Local and global load-bearing behaviour

The local and global load-bearing behaviour of the micro-notches was evaluated with shear tests and bending tests respectively. The materials and production procedure of the specimens used in both test series were comparable. The main properties investigated were the connection stiffness, the shear resistance, and the ductility.

The **connection stiffness** observed in the local push-out tests was very high: The determined values for the slip modulus  $K$  and the joint stiffness  $k$  for the optimum geometry indicate a rigid connection. The load-slip behaviour is linear elastic until the micro-notches yield. In the global bending tests, the observed load-bearing behaviour was linear elastic with brittle failure. The connection stiffness is very high and the composite action can be assumed rigid. However, the tests were performed with micro-notches arranged continuously over a wide area. The flexibility of the connection should be considered, if the micro-notches are arranged in individual strips of several micro-notches. On these grounds, the slip modulus  $K$  obtained in the local tests was compared to connection stiffness of the experimental data. The comparison showed that the connection stiffness in the global bending tests is smaller than the estimated stiffness. The slip modulus  $K$  was adapted accordingly to  $K = 110 \text{ kN/mm/m}$  per notch. Even though the adaption was significant in numbers, the effective bending stiffness was only marginally influenced because of the already very high joint stiffness  $k$  of the micro-notches.

The **shear resistance** was determined for two levels in the local shear tests: a yielding shear strength  $f_{v,y}$  and a maximum shear strength  $f_{v,max}$ . The yielding shear strength was used for the estimation of failure loads in the global bending tests. The calculated failure loads underestimated the measured failure loads by 23%. However, the calculated failure loads obtained with the maximum shear strength overestimated the measured failure loads by 26%. After adapting the slip modulus  $K$  as described above, the mean shear strength  $f_{v,MN} = 0.87 \text{ N/mm}^2$  was back-calculated from the results of the bending tests. The main failure mode observed in the push-out tests was shear failure in the concrete notches, combined with a lower share of shear failure in the timber notches. This failure mode was also observed as the main failure in the global bending tests.

The **ductility** behaviour of the micro-notches must be cautiously assessed. Although the failure modes observed in the local shear tests were brittle, the load-slip shows a yielding behaviour before reaching the maximum shear load (Fig. 4.12). Deformations of up to 1.5 mm were measured. However, this deformation capacity is low in comparison with steel connectors. Furthermore, the global load-bearing behaviour from the bending tests indicates brittle failure. The evaluation of slip measurements in the composite joints showed a similar load-slip behaviour as observed in the local shear tests. Deformations up to almost 4 mm were measured. However, these deformations occurred abruptly at the failure of the composite joint, shortly before the ultimate failure of the beam due to bending tension in timber. On these grounds, the micro-notches are assessed as a brittle connection system. However, it must be noted that all test series were designed to fail in the composite joint, provoking failure of the micro-notches as the first failure. In practice, the span, cross-sections, and loading situations lead to a bending



tension failure in timber at mid-span as first failure. Because this failure is brittle, the ductility of the micro-notches was not a primary criterion.

The influence of the different test setups, scales and loading situations should not be neglected. The local shear tests provided the connection properties for the prognosis of global load-bearing behaviour. But only the global bending tests are suitable to show the realistic structural behaviour of the TCC slab. The connection properties for micro-notches were therefore deduced from the bending tests.

### 8.3 Short-term and long-term behaviour

The short-term behaviour of micro-notches was tested in local shear tests and global bending tests in single-span and two-span beams. A variety of parameters concerning materials, production, and treatment of timber surface and concrete was investigated in the local shear tests. The treatment of the timber surface before concreting with water was further investigated in the global bending tests. The timber surface is usually watered before concreting because of the hygroscopic behaviour of the timber. However, neither the shear tests nor the bending tests showed an influence by this measure. It can be concluded that the watering of the timber surface is not needed in short-term to obtain a similar composite action as without watering. However, the watered or non-watered timber surface could have a significant effect on slabs in the long term.

The long-term test series was installed to investigate the influences on the rheological phenomena on the micro-notches subjected to static loads. The tests were designed to provoke the first failure in the micro-notches. This is necessary to correctly assess the long-term behaviour of the novel connection system instead of the behaviour of the TCC slab system as a whole. The composite action in the short-term bending tests was very high and can be assumed as rigid. However, the effect of shrinkage in concrete might have a significant influence on the micro-notches. Further, creep under high load levels usually affects the strength of the materials. Different load levels (0%, 40%, and 70% of  $F_{max,est}$ ) were applied to test the shear resistance of the micro-notches on the long term. All specimens were installed without additional screws. One specimen was installed with a large span of 8 m and a slender cross-section. The first results of the global deflections already show the influence of rheological phenomena. The deflections after concreting and after application of the load show a significant increase even under constant load. The evaluation of the measurements and comparison with long-term models will give more insight into the influence of shrinkage and creep on the shear resistance and connection stiffness of the micro-notches.

### 8.4 Single-span and two-span beams

In addition to the short-term 4-point bending tests and long-term bending tests on single-span beams, two large-scale beams over two spans were tested and analysed. The main objectives of these investigations were to test the performance of micro-notches in cracked concrete and to

evaluate the load-bearing behaviour of two-span TCC beams in general. Two specimens with a total length of 12 m on two equal spans of 6 m were tested under an approximately uniformly distributed load. The main test parameter was the reinforcement over the middle support. One specimen was tested with a minimum reinforcement ( $\varnothing = 8$  mm with a distance of 150 mm) over the whole length. The other specimen had a higher reinforcement ( $\varnothing = 12$  mm with a distance of 150 mm) in the area subjected to negative bending moments over the middle support. Both specimens showed a very similar load-bearing behaviour. The cracking of concrete over the middle support occurred at a low load level and reduced the overall stiffness of the beam. At a certain load, the reinforcement yielded and the stiffness of the beam decreased further. With increasing load, the cracked length over the middle support expanded. Due to the reduced stiffness over the middle support, the forces were redistributed into the spans until the timber in one of the spans failed from bending tension. The ultimate failure was brittle. A failure of the micro-notches was not observed.

The models based on  $\gamma$ -method and strut-and-tie model used for the evaluation of the single-span bending tests were extended and adapted for the two-span situation. Both models considered the cracking of concrete and the associated redistribution of forces. The strut-and-tie model also considered the reinforcement yielding. Both models show good agreement with the load-bearing behaviour observed in the experimental tests. The model based on the  $\gamma$ -method accurately predicts the behaviour in the lower load levels, but overestimates the stiffness after reinforcement yielding. The strut-and-tie model accurately predicts the whole load-bearing behaviour. Both models can be used for design at SLS and ULS.

The models were used to compare the load-bearing behaviour of the two-span beam with the behaviour of a system with two equal single-span beams subjected to the same load situation. The stiffness of the two-span beams strongly depends on the cracked concrete length over the middle support and decreases significantly after reinforcement yielding, but was still approximately 60-70% higher than the stiffness calculated for two single-span beams. Therefore, a two-span beam design significantly decreases the deflections and is beneficial for the fulfilment of the SLS requirements. The vibrations of the two-span beam were also tested. The experimental and analytical investigations showed that the reinforcement over the middle support plays a minor role. The stiffness of both beams was in the same range. The failure load in the specimen with larger reinforcement was slightly higher. More influence on the stiffness at the relevant service load levels showed the MOE of the timber element: the MOE of timber was different for both spans and this difference was visible in the deflections. Even though the strut-and-tie model predicted a high utilisation factor for the micro-notches, the connection did not fail and the micro-notches stayed intact. The cracked concrete did not compromise the good composite action achieved by micro-notches.

# Chapter 9

## Outlook

The concept of micro-notches as a novel connection system for TCC slabs was implemented and analysed on different aspects and fields of application. This thesis covers the most relevant aspects for planar TCC slabs with BST elements. However, there are still some issues to be resolved which are worthwhile for future investigations.

The **adhesion** between timber and concrete was not investigated in detail. It was concluded from testing different wood species, that spruce/fir BST elements show a good composite action with the concrete. The connection properties were determined including the surface effects of adhesion and friction. The quantitative share of adhesion was not determined. The quantification of this share on the shear resistance could give more insight on the use of undercutting (notch front angle  $\alpha < 0^\circ$ ) for the composite action and to prevent uplift.

In most experiments, the micro-notches were arranged in a wide area as a continuous connection system similar to a connection with adhesives. The production with a CNC milling machine allows for various arrangements. The arrangement in strips was tested in the two-span beams and was installed in the long-term test series. However, the **influence of the arrangement** on the global load-bearing behaviour was not yet quantified.

The **long-term tests** were installed and are being monitored beyond the work in this thesis. Not all data has been processed yet. The next step is to process all data and evaluate the data accumulated over these first months. The objective of the tests was at first the proof of concept of the micro-notches on the long term and under high load levels. Therefore, the long-term behaviour was not modelled yet. The ambient conditions and the moisture content measured in timber allow an accurate model of the deflection curve. The influence of concrete shrinkage and creep can be evaluated using these models. Three specimens with the load levels 0%, 40%, and 70% of  $F_{max,est}$  will be tested to failure after some years. The specimen loaded with 70% of  $F_{max,est}$  is expected to develop creep progression in the tertiary creep phase and eventually fail due to the compromised strength behaviour. The time until failure would give insight on the duration of load strength modification factor  $k_{mod}$ .

The investigations on **CLT elements** presented in this thesis consist of two single beams, one tested with inferior material properties in the 4-point bending tests and one installed in the long-term tests. The application of micro-notches on CLT is feasible and shows the same linear

elastic, very stiff behaviour with brittle failure caused by bending tension in timber. However, the implementation of micro-notches on CLT elements should be investigated in more depth to develop accurate design guidelines.

The application of micro-notches transferring shear forces **perpendicular to grain** was evaluated on three specimens in the local shear tests. This application is of special interest for the implementation in slabs bearing in two directions. The orientation of micro-notches is crucial, because only the notch front can take shear forces. Further investigations are also needed to develop arrangements suitable for systems other than slabs bearing in one direction.

# Appendix A

## Elastic bands as lateral supports for push-out test series II

This appendix describes the considerations and design calculations for the use of elastic bands as lateral supports for symmetric push-out tests as used for the push-out test series II.

### A.1 Transverse pressure on connections in TCC slabs

In TCC slabs, the composite joint between timber and concrete is exposed to transverse loads due to the self-weight of the concrete, the superimposed load of the floor construction and the live load. In local shear tests, this transverse component is usually not present, except for the horizontal slip-block test, where the self-weight of the concrete acts on the connection. The transverse loads on the slabs have a positive effect on the composite effect because the compressive forces can override tensile forces in the composite joint and thus increase the shear resistance of the connection.

The lower limit assumption of a transverse compressive stress on the connection of a TCC slab with a 80 mm concrete top layer, low superimposed loads, and no live loads as:

$$\begin{aligned}\sigma_Q &= g_{1,k} + g_{A,k} && \text{(A.1)} \\ &= 2 \text{ kN/m}^2 + 0.5 \text{ kN/m}^2 \\ &= 2.5 \text{ kN/m}^2 = 0.0025 \text{ N/mm}^2\end{aligned}$$

### A.2 Simulation of a realistic transverse force on the joints in the push-out tests

The shear area of the push-out series II is per joint:

$$A_{joint} = (350 \text{ mm} \cdot 160 \text{ mm}) = 56\,000 \text{ mm}^2 \quad \text{(A.2)}$$

The total transverse or lateral load on the two joints is:

$$LF_{real,tot} = 2 \cdot 56\,000 \text{ mm}^2 \cdot 0.0025 \text{ N/mm}^2 = 280 \text{ N} \quad (\text{A.3})$$

The total load is split on two elastic bands, the lower and the upper band. Because of the width of the specimen, the band remains on the timber surface in place and it is assumed that the two strands on side A and B transfer the force equally. The force on one strand of the elastic band is therefore:

$$LF_B = \frac{280 \text{ N}}{4} = 70 \text{ N} \quad (\text{A.4})$$

The dimensions of the elastic bands are given with band thickness  $t_B = 0.25 \text{ mm}$  and band width  $b_B = 254 \text{ mm}$ . The area of the elastic band is:

$$A_B = t_B \cdot b_B = (0.25 \text{ mm} \cdot 254 \text{ mm}) = 63.5 \text{ mm}^2 \quad (\text{A.5})$$

The required stress in the elastic bands to obtain the lateral force  $LF_B = 70 \text{ N}$  on the two joints of the push-out specimens is:

$$\sigma_B = \frac{70 \text{ N}}{63.5 \text{ mm}^2} = 1.1 \text{ N/mm}^2 \quad (\text{A.6})$$

To obtain this stress determined in equations A.1 to A.6, the elastic band has to be chosen according to its stiffness properties. The stiffness behaviour of elastic bands of the brand TheraBand<sup>®</sup> was determined in a study [133], see Fig. A.1. The elastic bands have a non-linear material behaviour with decreasing stiffness. The required stress can be reached with the black coloured TheraBand<sup>®</sup> at an elongation of approximately 14 mm on specimen length 75 mm, which corresponds to a strain  $\varepsilon_B$  of approximately 0.19, see Fig. A.1a.

The perimeter of the push-out specimens is:

$$U = 2 \cdot (160 \text{ mm} + 220 \text{ mm}) = 760 \text{ mm} \quad (\text{A.7})$$

The elastic band requires a prestressing to induce the strain  $\sigma_B$ . This prestressing is achieved by making the elastic band shorter by the strain  $\varepsilon_B$ :

$$\Delta l_B = U \cdot \varepsilon_B = 760 \text{ mm} \cdot 0.19 = 144 \text{ mm} \quad (\text{A.8})$$

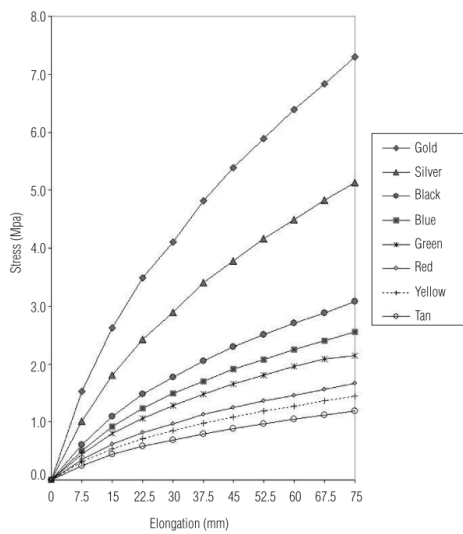
The required length of the elastic band results as:

$$l_B = U - \Delta l_B = 616 \text{ mm} \quad (\text{A.9})$$

The maximum horizontal slip in push-out series I was around 1.5 mm, see Fig. 3.18. This horizontal slip acts on the elastic band in four locations (left and right joint on front side A and front side B), so a maximum of 6 mm band elongation can be expected. However, this maximum horizontal slip was achieved with the very stiff lateral supports made of steel profiles

and rods in series I. Fig. A.1a can be used to determine the actual lateral load induced on the joints throughout using the development of the horizontal slip.

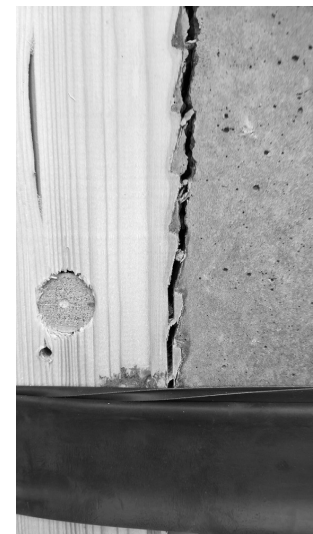
The elastic band width of 254 mm was too wide for the arrangement of two bands on the specimen height of 400 mm. Therefore, the band was folded twice. Fig. A.1b shows the final installation of one specimen of push-out series II with the upper and lower elastic bands installed. The elastic bands did not prevent any failure modes i.e. shear failure of the concrete notches as shown in Fig. A.1c.



(a) Stress-elongation behaviour of the different coloured TheraBands® for  $l=75\text{mm}$  [133]



(b) Elastic band installed on a specimen



(c) Close-up on the joint

**Fig. A.1:** Stress-elongation behaviour and implementation of elastic bands as lateral supports





## Appendix B

# Results for connection properties in push-out series I & II

Table B.1 lists the connection properties determined as described in Chapter 3.1.5 for each specimen of push-out series I. Table B.2 lists the connection properties for each specimen of push-out series II. The slip modulus was determined with three different approaches (listed in detail in Chapter 3.1.5).

**Tab. B.1:** Connection properties for push-out test series I

	width	no. of notches	yielding shear capacity	maximum shear capacity	vertical slip at $F_{max}$	maximum vertical slip	slip modulus (SIA 265)	slip modulus (1040)	slip modulus (EN 26891)
specimen	$b$ [mm]	$n$ [ ]	$F_y$ [kN]	$F_{max}$ [kN]	$u_{F_{max}}$ [mm]	$u_{max}$ [mm]	$K_{SIA}$	$K_{1040}$ [kN/mm]	$K_{EN}$
PO1 4-5 1	200	6	48.0	68.7	1.6	7.6	478	444	419
PO1 4-5 2	200	6	47.9	58.8	4.0	8.0	241	222	249
PO1 4-5 3	200	6	49.8	63.4	1.7	7.5	191	188	166
PO1 4-10 1	200	12	49.3	96.0	1.4	2.7	640	807	1038
PO1 4-10 2	200	12	73.1	109.0	0.8	3.6	758	856	684
PO1 4-10 3	200	12	62.8	91.6	2.3	3.8	505	428	428

**Tab. B.2:** Connection properties for push-out test series II

	width	no. of notches	yielding shear capacity	maximum shear capacity	vertical slip at $F_{max}$	maximum vertical slip	notch length	slip modulus (SIA 265)	slip modulus (1040)	slip modulus (EN 26891)
<b>specimen</b>	$b$ [mm]	$n$ [ ]	$F_y$ [kN]	$F_{max}$ [kN]	$u_{F_{max}}$ [mm]	$u_{max}$ [mm]	$l_{MN}$ [mm]	$K_{SIA}$	$K_{1040}$ [kN/mm]	$K_{EN}$
PO2 4-5 1	160	6	39.6	61.0	0.47	1.00	45	696	683	813
PO2 4-5 2	160	6	37.7	71.6	0.48	0.85	45	764	740	859
PO2 4-5 3	160	6	43.2	70.3	0.46	0.88	45	536	434	527
PO2 4-7.5 1	160	9	49.8	66.7	0.39	1.26	30	889	771	1143
PO2 4-7.5 2	160	9	36.3	63.4	0.27	1.05	30	921	1005	1267
PO2 4-7.5 3	160	9	38.0	64.1	0.24	1.04	30	1025	993	1537
PO2 4-10 1	160	12	61.6	81.7	0.27	0.43	22.3	817	768	891
PO2 4-10 2	160	12	79.2	93.4	0.30	0.41	22.3	574	507	533
PO2 4-10 3	160	12	61.6	79.4	0.14	0.28	22.3	1270	1166	1904
PO2 4-12.5 1	160	15	57.0	69.1	0.12	0.12	17.9	1105	1154	1657
PO2 4-12.5 2	160	15	51.5	54.1	0.08	0.17	17.9	865	721	1298
PO2 4-12.5 3	160	15	60.9	68.5	0.13	0.13	17.9	842	730	1027
PO2 6-7.5 1	160	9	39.6	72.3	0.60	1.15	45	608	542	619
PO2 6-7.5 2	160	9	37.7	68.0	0.36	0.78	45	572	530	582
PO2 6-7.5 3	160	9	43.2	85.5	0.63	1.11	45	414	414	366
PO2 10-7.5 1	160	9	39.6	108.9	0.68	1.01	45	454	449	392
PO2 10-7.5 2	160	9	37.7	103.5	0.84	1.39	45	404	378	345
PO2 10-7.5 3	160	9	43.2	99.7	0.59	1.01	45	351	323	299
PO2 oW 1	160	9	59.0	75.8	0.37	0.85	30	466	431	433
PO2 oW 2	160	9	51.0	73.2	0.31	1.08	30	781	801	878
PO2 oW 3	160	9	49.9	74.9	0.49	0.89	30	798	598	898
PO2 hP 1	160	9	29.5	34	0.36	1.08	30	494	415	680
PO2 hP 2	160	9	39.9	49.7	0.23	0.75	30	468	355	497
PO2 hP 3	160	9	27.6	34.1	0.09	0.58	30	778	681	2043
PO2 Bu	160	9	99.8	99.4	0.38	0.71	30	261	306	212
PO2 Es	160	9	53.8	56.9	0.42	0.78	30	198	219	166
PO2 nv	160	9	9.6	9.6	0.55	2.93	30	17	20	14
PO2 qF 1	160	7	10.4	17.8	0.78	3.42	40.9	189	224	213
PO2 qF 2	160	7	11.1	20	0.98	2.87	40.9	267	240	343
PO2 qF 3	160	7	11.6	17.7	1.89	2.63	40.9	109	117	101

# Appendix C

## Derivation of cracked concrete height

### C.1 Areas with positive bending moment

The following equations derive the uncracked concrete height  $x$  in cross-sections subjected to positive bending moments. In contrast to the approach mostly used in this thesis, the  $\gamma$ -factor was determined with the neutral axis in concrete as reference axis, see Chapter 2.2.2. The concrete cross-section is dependent on the cracked height and the  $\gamma_1$  determined with the neutral axis in timber axis as reference axis changes with the altering concrete cross-section. To take  $\gamma_1 = 1$  and  $\gamma_2$  according to [8] is therefore a mathematically necessary measure to find solutions for the uncracked concrete height  $x$ . Subsequently is  $\gamma_1 = 1$  and therefore not included in the equations.

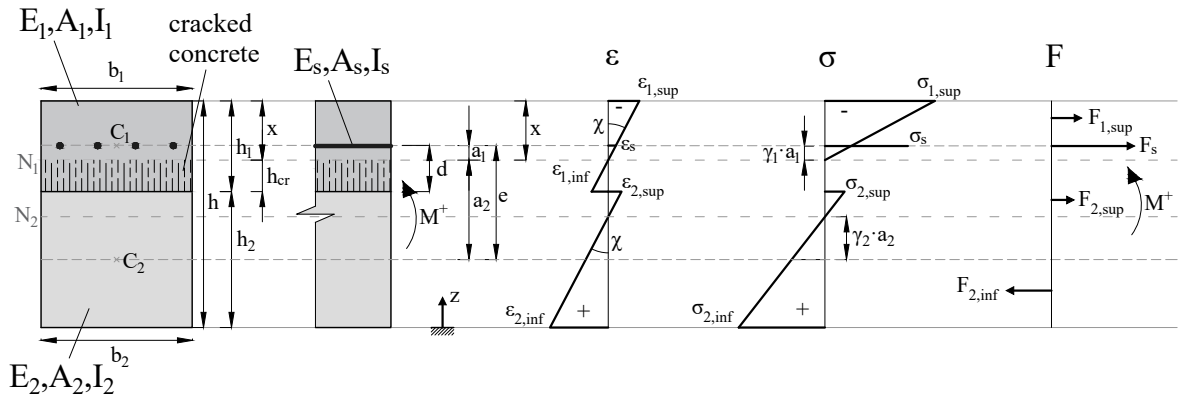


**Fig. C.1:** Strain and stress plane and forces on cracked composite cross-section subjected to positive bending moments

Assumption: The majority of the concrete height is uncracked:

$$x > \frac{h_1}{2} \quad (C.1)$$

**Tab. C.1:** Strains and stresses in a TCC cross-section subjected to positive bending moments

	<b>index</b> $i$	<b>position</b> $z_i$ [mm]	<b>strain</b> $\varepsilon_i$ [-]	<b>stress</b> $\sigma_i$ [N/mm <sup>2</sup> ]
concrete top	1, <i>sup</i>	$h_2 + h_1$	$\chi \cdot x$	$\varepsilon_{1, sup} \cdot E_1$
concrete bottom	1, <i>inf</i>	$h_2$	$\chi \cdot (h_1 - x)$	$\varepsilon_{1, inf} \cdot E_1$
reinforcement	$s$	$h_2 + d$	$\chi \cdot (d - h_1 + x)$	$\varepsilon_s \cdot E_s$
timber top	2, <i>sup</i>	$h_2$	$\chi \cdot (\frac{h_2}{2} - \gamma_2 \cdot a_2)$	$\varepsilon_{2, sup} \cdot E_2$
timber bottom	2, <i>inf</i>	0	$\chi \cdot (\frac{h_2}{2} + \gamma_2 \cdot a_2)$	$\varepsilon_{2, inf} \cdot E_2$

**Tab. C.2:** Forces in a TCC cross-section subjected to positive bending moments

	<b>index</b> $i$	<b>position</b> $z_{F,i}$ [mm]	<b>force</b> $F_i$ [kN]
concrete top	1, <i>sup</i>	$h_2 + h_1 - \frac{x}{3}$	$\chi \cdot \frac{x^2}{2} E_1 b_1$
reinforcement	$s$	$h_2 + d$	$\chi \cdot (d - h_1 + x) \cdot (E_s - E_1) \cdot A_s$
timber top	2, <i>sup</i>	$h_2 - \frac{x}{3} \cdot (\frac{h_2}{2} - \gamma_2 \cdot a_2)$	$\chi \cdot \frac{1}{2} (\frac{h_2}{2} - \gamma_2 \cdot a_2)^2 \cdot E_2 b_2$
timber bottom	2, <i>inf</i>	$\frac{x}{3} \cdot (\frac{h_2}{2} + \gamma_2 \cdot a_2)$	$\chi \cdot \frac{1}{2} (\frac{h_2}{2} + \gamma_2 \cdot a_2)^2 \cdot E_2 b_2$

Assuming that the cross-section is subjected to pure bending, equilibrium of forces states:

$$F_{2, inf} - F_{2, sup} - F_s - F_{1, sup} \stackrel{!}{=} 0 \quad (\text{C.2})$$

Solving equation C.2 with the forces from Table C.2, the uncracked concrete height  $x$  results:

$$x = \frac{1}{E_1 b_1} \cdot [(A_s E_1 - A_s E_s - A_2 E_2 \gamma_2 + \frac{1}{2} \cdot ((2A_s \cdot (E_1 - E_s) - 2b_2 E_2 h_2 \gamma_2)^2 + 4b_1 E_1 \cdot (2A_s \cdot (E_1 - E_s) \cdot (d - h_1) + A_2 E_2 \cdot \gamma_2 \cdot (2h_1 + h_2)))^{\frac{1}{2}}] \quad (\text{C.3})$$

Check, if assumption made in equation C.1 is true.

The equilibrium of moment states:

$$M + F_{2, inf} \cdot z_{F, 2, inf} - F_{2, sup} \cdot z_{F, 2, sup} - F_s \cdot z_{F, s} - F_{1, sup} \cdot z_{F, 1, sup} \stackrel{!}{=} 0 \quad (\text{C.4})$$

The effective bending stiffness  $EI_{eff, II}$  is:

$$EI_{eff, II} = \frac{M}{\chi} \quad (\text{C.5})$$

Solving equations C.4 and C.5 with the forces and positions from Table C.2, the effective bending stiffness  $EI_{eff}$  results:

$$EI_{eff} = \frac{1}{2} \cdot [2b_1E_1 \cdot (3h_1 + 3h_2 - x) \cdot x^2 - 12 \cdot A_s \cdot (E_1 - E_s) \cdot (d + h_2) \cdot (d - h_1 + x) + b_2E_2h_2^2 \cdot (h_2 - 3h_2\gamma_2 + 6\gamma_2 \cdot (x - h_1))] \quad (C.6)$$

## C.2 Areas with negative bending moment

In the following equations to derive the uncracked concrete height  $x$  in cross-section subjected to negative bending moments,  $\gamma_1$  is the  $\gamma$ -factor determined with the neutral axis in timber as reference axis, see Chapter 2.2.2. Subsequently is  $\gamma_2 = 1$  and therefore not included in the equations.

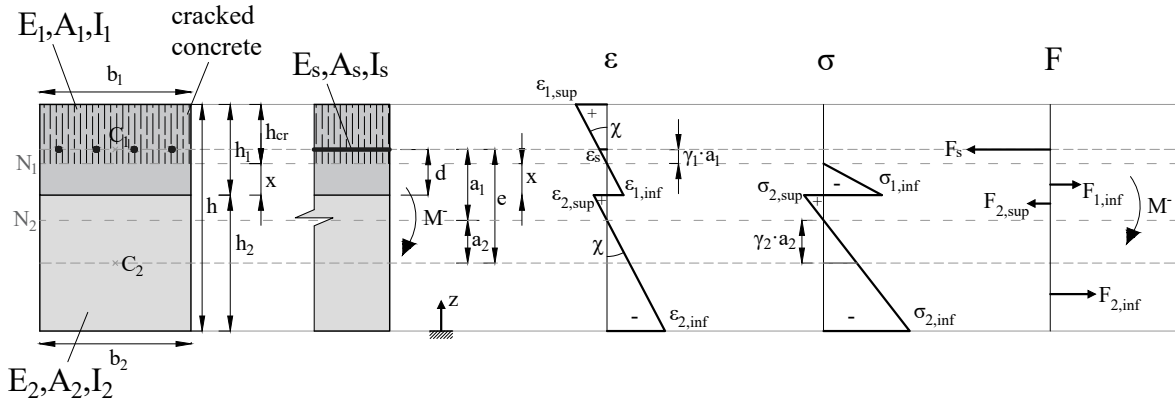


**Fig. C.2:** Strain and stress plane and forces on cracked composite cross-section subjected to negative bending moments

**Tab. C.3:** Strains and stresses in a TCC cross-section subjected to negative bending moments

	index	position	strain	stress
	$i$	$z_i$ [mm]	$\varepsilon_i$ [-]	$\sigma_i$ [N/mm <sup>2</sup> ]
concrete top	1, sup	$h_2 + h_1$	$\chi \cdot (h_1 - x)$	$\varepsilon_{1,sup} \cdot E_1$
concrete bottom	1, inf	$h_2$	$\chi \cdot x$	$\varepsilon_{1,inf} \cdot E_1$
reinforcement	$s$	$h_2 + d$	$\chi \cdot (d - x)$	$\varepsilon_s \cdot E_s$
timber top	2, sup	$h_2$	$\chi \cdot (\frac{h_2}{2} - a_2)$	$\varepsilon_{2,sup} \cdot E_2$
timber bottom	2, inf	0	$\chi \cdot (\frac{h_2}{2} + a_2)$	$\varepsilon_{2,inf} \cdot E_2$

Assuming that the cross-section is subjected to pure bending, equilibrium of forces states:

$$F_s + F_{2,sup} - F_{1,inf} - F_{2,inf} \stackrel{!}{=} 0 \quad (C.7)$$

**Tab. C.4:** Forces in a TCC cross-section subjected to negative bending moments

	<b>index</b>	<b>position</b>	<b>force</b>
	$i$	$z_{F,i}$ [mm]	$F_i$ [kN]
concrete bottom	$1, inf$	$h_2 + \frac{x}{3}$	$\chi \cdot \frac{x^2}{2} E_1 b_1$
reinforcement	$s$	$h_2 + d$	$\chi \cdot (d - x) \cdot E_s \cdot A_s$
timber top	$2, sup$	$h_2 - \frac{1}{3} \cdot (\frac{h_2}{2} - a_2)$	$\chi \cdot \frac{1}{2} (\frac{h_2}{2} - a_2)^2 \cdot E_2 b_2$
timber bottom	$2, inf$	$\frac{1}{3} \cdot (\frac{h_2}{2} + a_2)$	$\chi \cdot \frac{1}{2} (\frac{h_2}{2} + a_2)^2 \cdot E_2 b_2$

To find a viable solution, it is assumed that the entire concrete height is under tension and  $F_{1,inf} = 0$ . The equilibrium of forces is now:

$$F_s + F_{2,sup} - F_{2,inf} \stackrel{!}{=} 0 \quad (C.8)$$

Solving equation C.8 with the forces from Table C.4, the uncracked concrete height  $x$  results:

$$x = \frac{2A_s d E_s \gamma_1 - A_2 E_2 \cdot (h_1 \cdot (\gamma_1 - 1) + h_2 \gamma_1)}{2 \cdot (A_2 E_2 + A_s E_s \gamma_1)} \quad (C.9)$$

The equilibrium of moment states:

$$M + F_{2,inf} \cdot z_{F,2,inf} - F_{2,sup} \cdot z_{F,2,sup} - F_s \cdot z_{F,s} \stackrel{!}{=} 0 \quad (C.10)$$

The effective bending stiffness  $EI_{eff,II}$  is:

$$EI_{eff,II} = \frac{M}{\chi} \quad (C.11)$$

Solving equations C.10 and C.11 with the forces and positions from Table C.4, the effective bending stiffness  $EI_{eff}$  results:

$$EI_{eff} = \frac{1}{12 \cdot (A_2 E_2 + A_s E_s \gamma_1)} \cdot [A_2 E_2 \cdot (b_2 E_2 h_2^3 + A_s E_s \cdot (12d^2 + h_2 \cdot (3h_1(\gamma_1 - 1) + 4h_2 \gamma_1) + 6d \cdot (h_1 \cdot (\gamma_1 - 1) + h_2 \cdot (\gamma_1 + 1))))] \quad (C.12)$$



# Nomenclature

## Abbreviations

<i>eff</i>	Effective
BST	<i>Brettstapel</i> , in North America called dowel-laminated timber or DLT
CLT	Cross-laminated timber
CoV	Coefficient of Variation
FE	Finite Element
LVDT	Linear voltage displacement transducer
max	Maximum (value)
min	Minimum (value)
MOE	Modulus of Elasticity
RH	Relative Humidity
SD	Standard deviation
SG	Strain gauge
SLS	Serviceability Limit State
TCC	Timber-concrete composite
ULS	Ultimate Limit State

## Upper-case roman letters

$A$	Cross-section area
$A_i$	Cross-section area of component $i$
$A_s$	Cross-section area of the longitudinal reinforcement
$E_i$	Modulus of elasticity of component $i$
$F$	Force; load
$F_{cyl}$	Load of one hydraulic cylinder
$F_{joint}$	Load on composite joint
$G_i$	Shear modulus of component $i$
$I_i$	Moment of inertia (second moment of area) of component $i$
$K$	Slip modulus
$K_{ser}$	Slip modulus of connection at SLS level
$K_u$	Slip modulus of connection at ULS level
$M$	Bending moment
$M_i$	Internal bending moment of component $i$
$M_{cr}$	Critical bending moment that leads to cracking of concrete



$N$	Normal force
$N_i$	Internal normal force of component $i$
$R_F$	Frictional force
$S_i$	Statical moment (first moment of area) of component $i$
$V$	Shear force
$W$	Section modulus

## Lower-case roman letters

$a$	Distance between support and force application
$a_i$	Distance of the centroid of component $i$ and the centre of gravity of the composite cross-section
$b$	Width
$e$	Distance between the centroids of the components; excentricity
$f_1$	Natural frequency
$f_{i,c,d}$	Design compressive strength of component $i$
$f_{i,c,k}$	Characteristic compressive strength of component $i$
$f_{i,t,d}$	Design tensile strength of component $i$
$f_{i,t,k}$	Characteristic tensile strength of component $i$
$f_{s,k}$	Characteristic strength of the reinforcement
$g$	Self-weight
$g_{d,A}$	Design value of superimposed load
$g_{k,A}$	Characteristic value of superimposed load
$h$	Total height of component
$h_i$	Height of component $i$
$k$	Joint stiffness
$k_{def'}$	Deformation factor of the connection
$k_{def}$	Deformation factor of timber
$l$	Span
$l_N$	Length of notches N
$l_v$	Shear length
$l_{MN}$	Length of micro-notches MN
$n_i$	Ratio of the MOE of component $i$ to the MOE of the reference component
$q$	Distributed load
$q_{d,N}$	Design value of live load
$q_{k,N}$	Characteristic value of live load
$s$	Spacing between connectors
$t$	Time; thickness of interlayer
$t_N$	Depth of notches N
$t_{MN}$	Depth of micro-notches MN
$u$	Relative slip between timber and concrete parallel to the composite joint
$v$	Relative slip between timber and concrete perpendicular to the composite joint
$w$	Global deflection of a beam
$x$	Uncracked concrete height
$z_i$	Distance of centroid of componen $i$ to edge or other centroid

## Lower-case greek letters

$\alpha$	Angle between notch front and a normal perpendicular to the longitudinal axis of the beam
$\beta$	Angle between notch bottom and longitudinal axis of the beam
$\chi$	Curvature
$\eta$	Friction coefficient
$\eta_C$	Connection efficiency according to equation 2.22
$\eta_{C^*}$	Connection efficiency according to equation 2.23
$\gamma_i$	Reduction factor for the effective bending stiffness considering the stiffness of the connection for component $i$
$\psi_2$	Quasi-permanent part of load
$\rho$	Density
$\sigma$	Axial stress
$\tau$	Shear stress
$\varepsilon$	Strain
$\varphi_i$	Creep coefficient of component $i$

## Indices

1	Concrete
2	Timber
3...7a	time span at 3...7 years
$\infty$	time at the end of service life (usually 50 years)
	parallel to the grain
$\perp$	perpendicular to the grain
$c$	compression
$cr$	cracking
$d$	design value
$Ecc$	eccentricity
$I$	State I: concrete uncracked
$II$	State II: concrete cracked
$III$	State III: concrete cracked, connection compromised
$inf$	lower beam edge
$joint$	composite joint
$k$	characteristic value
$m$	bending
$mean$	mean value
$MN$	Micro-notches
$sup$	upper beam edge
$t$	tension
$u$	ultimate failure
$y$	yielding

## Other symbols

$\emptyset$	Diameter
-------------	----------

# Bibliography

- [1] BAHMER, R. Holz-Beton-Verbundbrücke Chiemgauarena Ruhpolding. In *16. Internationales Holzbau-Forum* (Garmisch-Partenkirchen, 2010), pp. 1–12.
- [2] BATHON, L. A., BLETZ, O., AND KOCHER, D. Holz-Beton-Verbund als starre und duktile Verbindung. In *Internationales Holzbau-Forum* (2004), pp. 1–17.
- [3] BATHON, L. A., AND GRAF, M. A continuous wood-concrete-composite system. In *WCTE 2000 - World Conference on Timber Engineering (Whistler)* (2000).
- [4] BERGFELDER, J. Näherungsverfahren zur Berechnung allgemeiner zusammengesetzter hölzerner Biegeträger mit elastischem Verbund. *Der Bauingenieur* 49 (1974).
- [5] BLANK, L. *Bending Resistance and Deformation Capacity of Fibre Reinforced Glulam Beams*. Dissertation, ETH Zürich, 2018.
- [6] BLASS, H. J., EHLBECK, J., VAN DER LINDEN, M., AND SCHLAGER, M. Trag- und Verformungsverhalten von Holz-Beton-Verbundkonstruktionen. Tech. rep., KIT, Karlsruhe, 1995.
- [7] BLASS, H. J., AND ROMANI, M. Langzeitverhalten von HB-Konstruktionen. Tech. rep., Versuchsanstalt für Stahl, Holz und Steine, Karlsruhe, 2002.
- [8] BOCCADORO, L. *Timber-concrete composite slabs made of beech laminated veneer lumber with notched connection*. Dissertation, ETH Zürich, 2016.
- [9] BOCCADORO, L., AND FRANGI, A. Experimental investigations on timber-concrete composite slabs made of beech laminated veneer lumber with notched connection Test report. Tech. rep., Institute for Structural Engineering, Zurich, 2016.
- [10] BOCCADORO, L., STEIGER, R., ZWEIDLER, S., AND FRANGI, A. Analysis of shear transfer and gap opening in timber-concrete composite members with notched connections. *Materials and Structures/Materiaux et Constructions* 50, 5 (2017), 1–15.
- [11] BOYD, J. D. An Anatomical Explanation for Visco-Elastic and Mechano-Sorptive Creep in Wood and Effects of Loading Rate on Strength. In *New Perspectives in Wood Anatomy. Forestry Sciences, vol 1.*, B. P., Ed. Springer, Dordrecht, 1982, pp. 171–222.

- [12] BRANDNER, R., RINGHOFER, A., AND GRABNER, M. Probabilistic models for the withdrawal behavior of single self-tapping screws in the narrow face of cross laminated timber (CLT). *European Journal of Wood and Wood Products* 76, 1 (2018), 13–30.
- [13] BRAUN, H.-J., SCHAAL, W., AND SCHNECK, F. Der Brettstapel als Verbundelement - Vorschlag für einen Berechnungsansatz. *Bautechnik* 75, 8 (1998), 539 – 547.
- [14] BRUNNER, M., ROMER, M., AND SCHNÜRIGER, M. Timber-concrete-composite with an adhesive connector (wet on wet process). *Materials and Structures* 40, 1 (2007), 119–126.
- [15] BURGERT, I. Holzphysik Vorlesungsunterlagen, 2015.
- [16] CAPRETTI, S., AND CECCOTTI, A. Service Behaviour of Timber-Concrete Composite Beams: a 5-Year Monitoring and Testing Experience. In *International Wood Engineering Conference 3* (New Orleans, 1994).
- [17] CECCOTTI, A. *Timber Engineering STEP2: Composite Structures*. STEP / Eurofortech, Centrum Hout, Almere, 1995.
- [18] CECCOTTI, A., AND COVAN, C. Behaviour of timber and concrete composite load-bearing structures. In *IUFRO Timber Engineering Group Meeting* (Saint John, New Brunswick, Canada, 1990).
- [19] CECCOTTI, A., FRAGIACOMO, M., AND GIORDANO, S. Long-term and collapse tests on a timber-concrete composite beam with glued-in connection. *Materials and Structures* 40, 1 (2007), 15–25.
- [20] CEN EUROPEAN COMMITTEE FOR STANDARDIZATION. EN 26891: Timber Structures - Joints made with mechanical fasteners: General principles for the determination of strength and deformation characteristics, 1991.
- [21] CEN EUROPEAN COMMITTEE FOR STANDARDIZATION. EN 1995-1-1:2010 - Eurocode 5: Design of timber structures - Part 1-1: General - Common rules and rules for buildings, 2010.
- [22] CEN EUROPEAN COMMITTEE FOR STANDARDIZATION. DIN EN 1992-1-1 - Eurocode 2: Bemessung und Konstruktion von Stahlbeton und- Spannbetontragwerken, 2011.
- [23] CHEN, W. F. Double Punch Test for Tensile Strength of Concrete. *Fritz Laboratory Reports* 67, 12 (1973), 993–995.
- [24] CLOUSTON, P., BATHON, L. A., AND SCHREYER, A. Shear and Bending Performance of a Novel Wood - Concrete Composite System. *Journal of Structural Engineering* 131, September (2005), 1404–1412.
- [25] COLLING, F. *Holzbau: Grundlagen und Bemessung nach EC 5*. Springer Vieweg, Wiesbaden, 2004.

- [26] CROCETTI, R., SARTORI, T., AND TOMASI, R. Innovative Timber-Concrete Composite Structures with Prefabricated FRC Slabs. *Journal of Structural Engineering* 141, 9 (2015).
- [27] DESTRO, R., BOSCATO, G., MAZZALI, U., RUSSO, S., PERON, F., AND ROMAGNONI, P. Structural and thermal behaviour of a timber-concrete prefabricated composite wall system. *Energy Procedia* 78 (2015), 2730–2735.
- [28] DEUTSCHES INSTITUT FÜR BAUTECHNIK. Europäische Technische Bewertung ETA-13/0699: SFS VB Schrauben, 2018.
- [29] DIAS, A. M. P. G. *Mechanical behaviour of timber-concrete joints*. Dissertation, TU Delft, 2005.
- [30] DIAS, A. M. P. G., FRAGIACOMO, M., HARRIS, R., KUKLIK, P., RAJCIC, V., AND SCHÄNZLIN, J. Technical Specification CEN/TC 250/SC 5, TS TCC, final draft, 2020.
- [31] DIAS, A. M. P. G., SCHÄNZLIN, J., AND DIETSCH, P. *Design of timber-concrete composite structures - COST Action FP1402*. Shaker Verlag GmbH, 2018.
- [32] DIAS, A. M. P. G., SKINNER, J., CREWS, K., AND TANNERT, T. Timber-concrete-composites increasing the use of timber in construction. *European Journal of Wood and Wood Products* 74, 3 (2016), 443–451.
- [33] DIN GERMAN INSTITUTE FOR STANDARDIZATION. DIN 52182: Prüfung von Holz - Bestimmung der Rohdichte, 1976.
- [34] DIN GERMAN INSTITUTE FOR STANDARDIZATION. DIN 52183: Prüfung von Holz - Bestimmung des Feuchtigkeitsgehaltes, 1977.
- [35] DIN GERMAN INSTITUTE FOR STANDARDIZATION. DIN EN 1990:2010 - Eurocode 0: EN 1990: Basis of structural design, 2010.
- [36] DIN GERMAN INSTITUTE FOR STANDARDIZATION. DIN EN 408: Timber Structures - Structural timber and glued laminated timber - Determination of some physical and mechanical properties, 2012.
- [37] DUBAS, P. Zusammengesetzte Holzstäbe mit unsymmetrischem zweiteiligem Querschnitt. *Schweizer Ingenieur und Architekt* 106, 9 (1988), 243–245.
- [38] EISENHUT, L., SEIM, W., AND KÜHLBORN, S. Adhesive-bonded timber-concrete composites - Experimental and numerical investigation of hygrothermal effects. *Engineering Structures* 125 (2016), 167–178.
- [39] FONROBERT, F. *Grundzüge des Holzbaues im Hochbau*. Ernst & Sohn GmbH & Co. KG, Berlin, 1942.

- [40] FRAGIACOMO, M., AMADIO, C., AND MACORINI, L. Short- and long-term performance of the "tecnaria" stud connector for timber-concrete composite beams. *Materials and Structures/Materiaux et Constructions* 40, 10 (2007), 1013–1026.
- [41] FRAGIACOMO, M., BALOGH, J., TO, L., AND GUTKOWSKI, R. M. Three-Dimensional Modeling of Long-Term Structural Behavior of Wood-Concrete Composite Beams. *Journal of Structural Engineering* 140, Toratti 1992 (2014), 1–11.
- [42] FRAGIACOMO, M., AND CECCOTTI, A. Long-Term Behavior of Timber-Concrete Composite Beams. I: Finite Element Modeling and Validation. *Journal of Structural Engineering* 132, 1 (2006), 901–913.
- [43] FRAGIACOMO, M., GUTKOWSKI, R. M., BALOGH, J., AND FAST, R. S. Long-term behavior of wood-concrete composite floor/deck systems with shear key connection detail. *Journal of Structural Engineering-Asce* 133, 9 (2007), 1307–1315.
- [44] FRAGIACOMO, M., AND LUKASZEWSKA, E. Time-dependent behaviour of timber-concrete composite floors with prefabricated concrete slabs. *Engineering Structures* 52 (2013), 687–696.
- [45] FRANGI, A. *Brandverhalten von Holz-Beton-Verbunddecken*. Dissertation, ETH Zürich, 2001.
- [46] FRANGI, A. *Grundzüge des Holzbaus*. Institut für Baustatik und Konstruktion ETH Zürich, Zürich, 2020.
- [47] FRANGI, A., AND FONTANA, M. Versuche zum Tragverhalten von Holz-Beton- Verbunddecken bei Raumtemperatur und Normbrandbedingungen. Tech. rep., ETH Zürich, 2000.
- [48] FRANGI, A., AND FONTANA, M. Charring rates and temperature profiles of wood sections. *Fire and Materials* 27, 2 (2003), 91–102.
- [49] FRANGI, A., AND FONTANA, M. Elasto-plastic model for timber-concrete composite beams with ductile connection. *Structural Engineering International: Journal of the International Association for Bridge and Structural Engineering (IABSE)* 13, 1 (2003), 47–57.
- [50] GEROLD, M. Ausgewählte HBV - Projekte des Hoch - und Brückenbaus aus Deutschland. In *S-WIN 2018 - 50. Fortbildungskurs: Verbundkonstruktionen im Holzbau* (Weinfelden, 2018), pp. 77–90.
- [51] GESTESCHI, T. *Der Holzbau*. Springer-Verlag Berlin Heidelberg GmbH, 1926.
- [52] GHAFAR, N. H. A., DEAM, B., AND FRAGIACOMO, M. Vibration Susceptibility of Multi-Span Lvl-Concrete Composite Floors. In *WCTE 2010 - World Conference on Timber Engineering* (Vienna, 2010).

- [53] GLASER, R. *Zum Kurz- und Langzeitverhalten von Holz-Beton-Verbundkonstruktionen*. Dissertation, Brandenburgische Technische Universität Cottbus, 2005.
- [54] GODYCKI, T., PAWLICA, J., AND KLESZCZEWSKI, J. Verbunddecke aus Holzrippen und Betonplatte - Forschungsergebnisse und Ausführungsbeispiele. *BauIngenieur* 59 (1984), 477–483.
- [55] GOTTGETREU, R. *Lehrbuch der Hochbau-Konstruktionen - Zweiter Theil: Die Arbeiten des Zimmermannes. Atlas*. Ernst & Korn, Berlin, 1882.
- [56] GRANELLO, G., AND PALERMO, A. Creep in Timber : Research Overview and Comparison Between Code Provisions. *New Zealand Timber Design Journal* 27, 1 (2019), 6–22.
- [57] GROSSE, M. *Zur numerischen Simulation des physikalisch nichtlinearen Kurzzeittragverhaltens von Nadelholz am Beispiel von*. Dissertation, Bauhaus-Universität Weimar, 2005.
- [58] GROSSE, M., HARTNACK, R., LEHMANN, S., AND RAUTENSTRAUCH, K. Modellierung von diskontinuierlich verbundenen Holz-Beton-Verbunddecken. *Bautechnik* 80 (2003), 534–541.
- [59] GROSSMANN, P. U. A. Mechano Sorptive Behaviour. *General Constitutive Relations of Wood and Wood-Based Materials* (1978).
- [60] GUTKOWSKI, R. M., BALOGH, J., AND SÀ RIBEIRO, R. A. Modeling and Testing of Composite Wood-Concrete Deep Beam Specimens. *Structural Faults and Repair*, July (2001).
- [61] GUTKOWSKI, R. M., BROWN, K., ETOURNAUD, P., AND THOMPSON, W. Shear Key for Strengthening Bridges. Tech. Rep. August, Colorado State University, 2001.
- [62] GUTKOWSKI, R. M., BROWN, K., SHIGIDI, A., AND NATTERER, J. Laboratory tests of composite wood-concrete beams. *Construction and Building Materials* 22, 6 (2008), 1059–1066.
- [63] HAMM, P. Schwingungsnachweise von Holzdecken auf Unterzügen. *10. Europäischer Kongress EBH* (2017), 1–14.
- [64] HARTMANN, H. Begleitende Untersuchungen zur Ausführung einer Holz-Beton-Verbundkonstruktion beim Engelbert-Kämpfer-Gymnasium in Lemgo. *Der Bauingenieur* 72, 6 (1997), 297–304.
- [65] HASSANI, M. M., WITTEL, F. K., HERING, S., AND HERRMANN, H. J. Rheological model for wood. *Computer Methods in Applied Mechanics and Engineering* 283 (2015), 1032–1060.
- [66] HEIMESHOFF, B., AND KÖHLER, N. Untersuchung über das Tragverhalten von zimmermannsmäßigen Holzverbindungen. Tech. rep., Lehrstuhl für Baukonstruktion und Holzbau, Technische Universität München, München, 1989.

- [67] HITZ, X. *Holz-Beton-Verbund - Zweifeldträger: Fokus Gebrauchstauglichkeit*. Masterthesis, ETH Zürich, 2019.
- [68] HÖHMANN, R., AND SIEMERS, M. Untersuchungen zum Trag- und Verformungsverhalten von Holz-Beton-Verbundträgern. *Bautechnik* 75, 11 (1998), 922–929.
- [69] HOLSCHMACHER, K., RUG, W., PLUNTKE, T., AND SORG, J. Holz-Beton-Verbund. *Holzbauforum* (2001).
- [70] HOLSCHMACHER, K., SELLE, R., SCHMIDT, J., AND KIESLICH, H. *Holz-Beton-Verbund*. Ernst & Sohn GmbH & Co. KG, Leipzig, 2013.
- [71] HOLZER, S. M. *Statische Beurteilung Historischer Tragwerke Band 2: Holzkonstruktionen*. Ernst & Sohn, Berlin, 2015.
- [72] HOLZER, S. M. Hölzerne Brücken in der Schweiz. Tech. Rep. Brunner 1925, Institut für Denkmalpflege und Bauforschung (IDB), ETH Zürich, 2017.
- [73] HOZJAN, T., BEDON, C., OGRIN, A., CVETKOVSKA, M., AND KLIPPEL, M. Literature Review on Timber-Concrete Composite Structures in Fire. *Journal of Structural Engineering (United States)* 145, 11 (2019), 1–12.
- [74] JAARANEN, J., AND FINK, G. Frictional behaviour of timber-concrete contact pairs. *Construction and Building Materials* 243 (2020).
- [75] JCSS JOINT COMMITTEE ON STRUCTURAL SAFETY. JCSS Probabilistic Model Code Part 3: Resistance Models, 3.5 Properties of Timber, 2006.
- [76] JORGE, L. F. C., SCHÄNZLIN, J., LOPES, S. M. R., CRUZ, H. M. P., AND KUHLMANN, U. Time-dependent behaviour of timber lightweight concrete composite floors. *Engineering Structures* 32, 12 (2010), 3966–3973.
- [77] JORGE, L. F. D. C. *Estruturas mistas madeira-betão com a utilização de betões de agregados leves*. Dissertation, Universidade de Coimbra, 2005.
- [78] JUNG, P. Der gedübelte Brettstapel. 6. *Internationales Holzbau Forum* (2000).
- [79] KANÓCZ, J., AND BAJZECEROVÁ, V. Influence of rheological behaviour on load-carrying capacity of timber-concrete composite beams under long term loading. *Procedia Engineering* 40 (2012), 20–25.
- [80] KAUFMANN, W. Lecture "Stahlbeton I: 2 - Materialverhalten", 2016.
- [81] KENEL, A., AND MEIERHOFER, U. A. Holz / Beton-Verbund unter langfristiger Beanspruchung. *Forschungs- und Arbeitsbericht EMPA* (1998).



- [82] KHORSANDNIA, N., SCHÄNZLIN, J., VALIPOUR, H., AND CREWS, K. Time-dependent behaviour of timber-concrete composite members: Numerical verification, sensitivity and influence of material properties. *Construction and Building Materials* 66, January (2014), 192–208.
- [83] KHORSANDNIA, N., VALIPOUR, H. R., SHRESTHA, R., GERBER, C., AND CREWS, K. Review on long-term behaviour of timber-concrete composite floors. *From Materials to Structures: Advancement Through Innovation - Proceedings of the 22nd Australasian Conference on the Mechanics of Structures and Materials, ACMSM 2012*, June 2014 (2013), 1053–1058.
- [84] KLIPPEL, M., BOCCADORO, L., KLINGSCH, E., AND FRANGI, A. Fire tests on timber-concrete composite slabs using beech laminated veneer lumber. In *WCTE 2016 - World Conference on Timber Engineering* (2016).
- [85] KNEIDL, R., AND HARTMANN, H. Träger mit nachgiebigem Verbund. Eine Berechnung mit Stabwerksprogrammen. *Bauen mit Holz* 4 (1995), 285–290.
- [86] KÖNIG, G., HOLSCHMACHER, K., AND DEHN, F. *Holz-Beton-Verbundbau Innovationen im Bauwesen. Beiträge aus Praxis und Wissenschaft*. Bauwerk Verlag Berlin, 2004.
- [87] KOSTIĆ, S., MEIER, S., CABANE, E., AND BURGERT, I. Enhancing the performance of beech-timber concrete hybrids by a wood surface pre-treatment using sol-gel chemistry. *Heliyon* 4, 9 (2018).
- [88] KREIS, B. Friction based connections in timber-concrete composite structures. In *COST Action FP 1402 / WG4* (2016).
- [89] KREIS, B. Zweiachsig tragende Holz-Beton-Verbunddecken aus Buchenfurnierschichtholz. In *S-WIN 2018 - 50. Fortbildungskurs: Verbundkonstruktionen im Holzbau* (2018).
- [90] KREUZINGER, H. Verbundkonstruktionen aus nachgiebig miteinander verbundenen Querschnittsteilen. In *Tagung Ingenieurholzbau, Karlsruher Tage 2000* (Karlsruhe, 2000), Bruderverlag.
- [91] KUDLA, K. Notched Connections for TCC structures as part of the standard. Tech. rep., 2015.
- [92] KUDLA, K. *Kerven als Verbindungsmittel für Holz-Beton-Verbundstraßenbrücken*. Dissertation, Universität Stuttgart, 2017.
- [93] KUDLA, K., MÖNCH, S., KUHLMANN, U., VOLK, D., AND GÖTZ, T. Investigations on the slip modulus of a notched connection in timber-concrete composite floors. In *WCTE 2016 - World Conference on Timber Engineering* (2016), Vienna University of Technology.

- [94] KUHLMANN, U., AND ALDI, P. Schubübertragung in Brettstapei-Beton-Verbunddecke ohne mechanische Verbindungsmittel zur Abhebesicherung. Tech. rep., Institut für Konstruktion und Entwurf, Universität Stuttgart, 2008.
- [95] KUHLMANN, U., AND ALDI, P. Simulation of grooved connections in Timber-Concrete Composite beams considering the distribution of the material properties. *WCTE 2008 - World Conference on Timber Engineering 2008 1* (2008), 286–293.
- [96] KUHLMANN, U., AND SCHÄNZLIN, J. Erweiterung des Anwendungsbereichs von Holz-Beton-Verbunddecken durch Erfassung des Kriechens und des Schwindens am Beispiel der Brettstapel-Beton-Verbunddecke. Tech. rep., Institut für Konstruktion und Entwurf, Universität Stuttgart, Stuttgart, 2002.
- [97] KUHLMANN, U., SCHÄNZLIN, J., AND MICHELFELDER, B. C. Berechnung von Holz-Beton-Verbunddecken. *Beton- und Stahlbetonbau* 99, 4 (2004), 262–271.
- [98] KUPFERLE, F., DIAS, A. M. P. G., SEBASTIAN, W., SCHÄNZLIN, J., FRAGIACOMO, M., AND FERREIRA, M. COST Action FP1402 Training School on TCC, 2018.
- [99] LEHMANN, S. *Untersuchungen zur Bewertung von Verbundbauteilen aus Brettstapelelementen im Flächenverbund mit mineralischen Deckschichten*. PhD thesis, Bauhaus-Universität Weimar, 2004.
- [100] LEHMANN, S., GROSSE, M., AND RAUTENSTRAUCH, K. Neuartige Schubverbindung für Brettstapel-Beton-Verbunddeckenplatten. *Bautechnik* 80, 6 (2003), 385–392.
- [101] LOEBUS, S., AND WINTER, S. Zweiachsige Tragwirkung bei Holz- Entwicklung von Bemessungsverfahren und Konstruktionsdetails für zweiachsige Lastabtragung bei der Holz-Beton-Verbundweise. Tech. rep., 2017.
- [102] LUKASZEWSKA, E. *Development of Prefabricated Timber-Concrete Floors*. Dissertation, Lulea University of Technology, Lulea, 2009.
- [103] MARSCHALL, J. *Untersuchung von Holz-Beton-Verbunddecken als Mehrfeldsystem*. Master thesis, Hochschule für Forstwirtschaft Rottenburg, 2018.
- [104] MARTI, P. *Baustatik: Grundlagen, Stabtragwerke, Flächentragwerke*, 1. ed. Ernst & Sohn GmbH & Co. KG, Berlin, Germany, 2012.
- [105] MARTINS, C., SANTOS, P., ALMEIDA, P., GODINHO, L., AND DIAS, A. M. P. G. Acoustic performance of timber and timber-concrete floors. *Construction and Building Materials* 101 (2015), 684–691.
- [106] MCCULLOUGH, C. B. Oregon Tests on Composite (Timber-Concrete) Beams. *ACI Journal Proceedings* 14, 5 (1943), 429–440.

- [107] MEENA, R., SCHOLLMAYER, M., AND TANNERT, T. Experimental and Numerical Investigations of Fire Resistance of Novel Timber-Concrete-Composite Decks. *Journal of Performance of Constructed Facilities* 28, 6 (2014).
- [108] MEIERHOFER, U. A. A Timber/Concrete Composite System. *Structural Engineering International* 3, 2 (1993), 104–107.
- [109] MEIERHOFER, U. A. Long term performance of timber concrete composite structural elements. Tech. rep., EMPA, 1997.
- [110] MICHELFELDER, B. C. Trag- und Verformungsverhalten von Kernen bei Brettstapel-Beton-Verbunddecken. *Dissertation* (2006).
- [111] MIEBACH, F., NIEWERTH, D., WOLF, F., AND LARAKI, J. Holz-Beton-Verbundbrücken Erfahrungen und Perspektiven. Tech. rep., Qualitätsgemeinschaft Holzbrückenbau e.V., Frielzheim, 2018.
- [112] MIKOSCHEK, M. Brettstapel-Beton-Verbunddecken mit Schubübertragung durch Buchenholzdübel. In *Doktorandenkolloquium Stuttgart* (2020).
- [113] MÖHLER, K. *Über das Tragverhalten von Biegeträgern und Druckstäben mit zusammengesetztem Querschnitt und nachgiebigen Verbindungsmitteln*. Habilitation, TH Karlsruhe, Karlsruhe, 1956.
- [114] MÖHLER, K., AND HERRÖDER, W. Obere und untere Reibbeiwerte von sägerauhem Fichtenholz. *Holz als Roh- und Werkstoff: European Journal of Wood and Wood Industries* 37, 1 (1979), 27–32.
- [115] MÖNCH, S., AND KUHLMANN, U. Investigations on the effects of geometry in timber-concrete composite push-out tests with notched connections. In *WCTE 2018 - World Conference on Timber Engineering* (2018), World Conference on Timber Engineering (WCTE).
- [116] MÜLLER, A. Holz-Beton-Verbundsysteme: Überblick und Ausblick, 2013.
- [117] MÜLLER, K., AND FRANGI, A. 4-Point Bending Tests of Timber-Concrete Composite Slabs with Micro-Notches. In *WCTE 2018 - World Conference on Timber Engineering* (Seoul, 2018).
- [118] MÜLLER, P. Patent DE334431C: Decke aus hochkantig stehenden Holzbohlen oder Holzbrettern und Betondeckschicht, 1921.
- [119] MUSTER, M. *Holz-Beton-Verbunddecken mit Brettstapel*. Master thesis, ETH Zürich, 2015.
- [120] NATTERER, J., AND HOEFT, M. Zum Tragverhalten von Holz-Beton-Verbundkonstruktionen. Tech. Rep. 1345, Lehrstuhl für Holzkonstruktionen EPFL, Lausanne, 1987.

- [121] NIEMZ, P., AND SONDEREGGER, W. *Holzphysik: Physik des Holzes und der Holzwerkstoffe*. Carl Hanser Verlag GmbH & Co. KG, 2017.
- [122] O'NEILL, J., CARRADINE, D., MOSS, P., FRAGIACOMO, M., DHAKAL, R., AND BUCHANAN, A. Design of timber-concrete composite floors for fire resistance. *Journal of Structural Fire Engineering* 2, 3 (2011), 231–242.
- [123] PALMA, P., AND STEIGER, R. SC-5 WG-10 N45 Figure slip moduli connections, 2019.
- [124] PAULT, J. D. Composite Action in Glulam Timber Bridge Systems. Tech. rep., Colorado State University, Fort Collins, 1977.
- [125] POLLMEIER FURNIERWERKSTOFFE. ETA-14 / 0354: Glued laminated timber made of hardwood - Structural laminated veneer lumber made of beech, 2015.
- [126] POSTULKA, J. Strengthening of wooden ceiling constructions. In *IAEBSE Symposium 1983* (1983), pp. 441–447.
- [127] RAUTENSTRAUCH, K. Baupraktische Dimensionierung von Holz-Beton-Verbunddecken. In *6. Informationstag des IKI, Bauhaus-Universität Weimar* (2003).
- [128] RICHARD, P., ZUOWEI, L., DESCAMPS, T., AND SIKORA, K. S. Effect of concrete modification on shear of connections for Timber Concrete Composites. *Proceedings of the Institution of Civil Engineers - Structures and Buildings* 173, 5 (2020), 326–339.
- [129] RICHART, F., AND WILLIAMS, C. B. Tests of composite timber and concrete beams. Tech. Rep. 38, University of Illinois, 1943.
- [130] RODRIGUES, J. N., DIAS, A. M. P. G., AND PROVIDÊNCIA, P. M. Timber-Concrete Composite Bridges: State-of-the-Art Review. *BioResources* 8, 4 (2013), 6630–6649.
- [131] RUG, W., AND LISSNER, K. Holz-Beton-Verbundbauweise in der Praxis. *Beton- und Stahlbetonbau* 99, 7 (2004), 578–586.
- [132] RUG, W., THOMS, F., GRIMM, U., EICHBAUM, G., AND ABEL, S. Untersuchungen zur Biegetragfähigkeit von verzahnten Balken. *Bautechnik* 89, 1 (2012), 26–36.
- [133] SANTOS, G. M., TAVARES, G. M., DE GASPERI, G., AND BAU, G. R. Mechanical evaluation of the resistance of elastic bands. *Revista Brasileira de Fisioterapia* 13, 6 (2009), 521–526.
- [134] SÁRIBEIRO, R. A., AND SÁRIBEIRO, M. G. Composite Wood-Concrete Structural Floor System with Horizontal Connectors. *International Journal of Concrete Structures and Materials* 9, 1 (2015), 61–67.
- [135] SCHACHER, M. *Holz-Beton-Verbund - Zweifeldträger: Fokus Tragsicherheit*. Masterthesis, ETH Zürich, 2019.

- [136] SCHÄFERS, M. *Entwicklung von hybriden Bauteilen aus Holz und hochfesten bzw. ultrahochfesten Betonen*. Dissertation, Universität Kassel, 2010.
- [137] SCHÄFERS, M., AND SEIM, W. Geklebte Verbundbauteile aus Holz und hoch- bzw. Ultrahochfesten Betonen. *Bautechnik* 88, 3 (2011), 165–176.
- [138] SCHÄNZLIN, J. *Zum Langzeitverhalten von Brettstapel-Beton-Verbunddecken*. Dissertation, Universität Stuttgart, 2003.
- [139] SCHÄNZLIN, J. Ausblick auf die zukünftige Bemessung von Holz-Beton-Verbunddecken. In *VPI-Arbeitstagung* (Baden-Baden, 2017), Hochschule Biberach Fakultät Bauingenieurwesen Institut für Holzbau.
- [140] SCHAUB, O. Patent US1792040A: Wood Reinforced Concrete Structural Member, 1931.
- [141] SCHAUB, O. Patent DE673556C: Verbunddecke aus Holzrippen und Betonplatte, 1939.
- [142] SCHILLIGER, M. *Durchlaufwirkung bei Holz-Beton-Verbunddecken*. Bachelor thesis, BFH Biel, 2019.
- [143] SCHMID, M. Acoustic performance of timber and timber-concrete composite floors. In *inter.noise Environmental Noise Control* (Rio de Janeiro, 2005).
- [144] SCHÖNBORN, F. *Holz-Beton-Fertigteilelemente*. Dissertation, Leopold-Franzens-Universität Innsbruck, 2006.
- [145] SEBASTIAN, W. Multi-span Timber-Concrete Composite structures. In *COST FP 1402 / WG4 Final Conference* (Munich, 2018).
- [146] SEBASTIAN, W., SMITH, A., AND LAWRENCE, A. Commentary : The potential for multi-span continuous timber-concrete composite floors. *Structures and Buildings* 171, 9 (2018), 661–662.
- [147] SEILER, J. F., AND KEENEY, W. D. New type of composite beam and design of composite slab highway bridge deck. *Wood Preserving News Vol. XI* (1933), 144–157.
- [148] SHI, B., LIU, W., YANG, H., AND LING, X. Long-term performance of timber-concrete composite systems with notch-screw connections. *Engineering Structures* 213, February (2020), 110585.
- [149] SIA SWISS SOCIETY OF ENGINEERS AND ARCHITECTS. SIA 265: Holzbau, 2012.
- [150] SIA SWISS SOCIETY OF ENGINEERS AND ARCHITECTS. SIA 262: Betonbau, 2013.
- [151] SIDLER HOLZ AG. Technische Dokumentation Sidler Holz AG.
- [152] SIKORA, K. S., AND LIU, Z. Shear strength of different connection and concrete types for Timber Concrete Composites (TCC). In *WCTE 2018 - World Conference on Timber Engineering* (2018), World Conference on Timber Engineering (WCTE).

- [153] SIMON, A. *Analyse zum Trag- und Verformungsverhalten von Straßenbrücken in Holz-Beton-Verbundbauweise*. Dissertation, Bauhaus-Universität Weimar, 2008.
- [154] STAUDACHER, E. *Der Baustoff Holz - Beiträge zur Kenntnis der Materialeigenschaften und der Konstruktionselemente*. PhD thesis, ETH Zürich, 1936.
- [155] STEPHAN, R. *Beitrag zur Spannungsermittlung beim Versatzanschluss im Holzbau*. PhD thesis, TH Hannover, 1950.
- [156] STEURER, A. *Grundzüge des Holzbaus: Autographie zur Vorlesung Holzbau ETH Zurich*. Institut für Baustatik und Konstruktion ETH Zürich, 2004.
- [157] STÜSSI, F. Beiträge zur Berechnung und Ausbildung zusammengesetzter Vollwandträger. *Schweizerische Bauzeitung* 61, 8/9 (1943), 87–89 + 102–103.
- [158] STÜSSI, F. Zusammengesetzte Vollwandträger. *IABSE publications* 8 (1947).
- [159] TANNERT, T., ENDACOTT, B., BRUNNER, M., AND VALLÉE, T. Long-term performance of adhesively bonded timber-concrete composites. *International Journal of Adhesion and Adhesives* 72, October 2016 (2017), 51–61.
- [160] TANNERT, T., MPIDI BITA, H., SHAHNEWAZ, M., EBADI, M. M., AND GERBER, A. Long-term performance of timber concrete composite floors. *WCTE 2018 - World Conference on Timber Engineering*, August (2018).
- [161] TIMMERMANN, K., AND MEIERHOFER, U. A. Berechnung von Holz-Beton-Verbundbalken mit der Differenzmethode. *Schweizer Ingenieur und Architekt* 112, 45 (1994), 931–936.
- [162] VAN DE KUILEN, J. W. G., AND DIAS, A. M. P. G. Long-term load-deformation behaviour of timber-concrete joints. *Proceedings of the Institution of Civil Engineers - Structures and Buildings* 164, 2 (2011), 143–154.
- [163] VAN DER LINDEN, M. Timber-concrete composite floor systems. Dissertation, Technische Universiteit Delft, Delft, 1999.
- [164] WACKER, J. P., DIAS, A. M. P. G., AND HOSTENG, T. K. 100-Year Performance of Timber-Concrete Composite Bridges in the United States. *Journal of Bridge Engineering* 25, 3 (2020), 04020006.
- [165] WALLNER-NOVAK, M., KOPPELHUBER, J., AND POCK, K. *Information Brettsper Holz Bemessung Grundlagen für Statik und Konstruktion nach Eurocode*. 2013.
- [166] WINTER, S., HAMM, P., AND RICHTER, A. Schwingungs- und Dämpfungsverhalten von Holz- und Holz-Beton-Verbunddecken. Tech. rep., Institut für Baustoffe und Konstruktion, Lehrstuhl für Holzbau und Baukonstruktion, TU München, 2010.

- [167] YEOH, D. *Behaviour and design of timber-concrete composite floor system*. Dissertation, University of Canterbury, 2010.
- [168] YEOH, D., FRAGIACOMO, M., DE FRANCESCHI, M., AND BOON, K. H. State of the Art on Timber-Concrete Composite Structures: Literature Review. *Journal of Structural Engineering* 137, 10 (2011), 1085–1095.
- [169] ZÖLLIG, S. Holz / Beton-Verbund mit vorgefertigten Brettstapel-Modulen. In *SAH-Kurs* (1999), pp. 197–199.

